Optomechanical enhancements for applications in metrology

Giovanni Guccione

A thesis submitted for the degree of
Doctor of Philosophy in Physics
The Australian National University

September 2017

Declaration

This thesis is an account of research undertaken between February 2012 and September 2016 at the Department of Quantum Science, Research School of Physics & Engineering, The Australian National University (ANU), Canberra, Australia.

The research presented here was supervised at all stages by Prof. Ping Koy Lam and Dr. Ben C. Buchler. The investigations presented in Chap. 4–8 were performed jointly with Dr. Mahdi Hosseini. The work in Chap. 7, 11, and 12 would not have been possible without the contribution of Harry J. Slatyer. Except where acknowledged in the customary manner, the material presented in this thesis is, to the best of my knowledge, original and has not been submitted in whole or part for a degree in any university.

Giovanni Guccione
May 2017

Acknowledgments

This research would not have been possible without the guidance and support of the many people who helped me throughout my permanence at the Australian National University.

In particular, I could not have asked for better supervisors than Ping Koy Lam and Ben Buchler. Ping Koy, I will always admire your insight in the many fields of physics. Ben, you were always ready to set me back on the right course regardless of how many wrong turns I would take. You both have my deepest gratitude and appreciation.

It is impossible to quantify how much I owe to Mahdi Hosseini. Mahdi, you have been an exceptional mentor, colleague, friend, and partner in crime. From quantum optics to tennis and even surfing, finding anything at which you do not excel is not easy. Thanks also to all the other members of the "optomechanics team" with whom I had the fortune of working with: Harry, Jeremy, Jinyong, Ruvi. Working with you has been both an honour and a pleasure.

Many thanks also go to the full quantum optics group, for the many moments of entertainment both inside and outside of the department. I will always treasure the memories of cultural dinners, quantum cakes, circus trampolines, Nowruz, camping, and cycling trips. And of all the things I learned in the past few years, proficiency in tying a figure-eight knot probably did not even figure in my list of expectations. Thanks to Geoff, Julien, Quentin, Oliver, Pierre, and the many other people that made me discover the excitement of the rock climbing scene in Australia.

Among all the people I have interacted with, special recognition goes to Alex, who had to put up with me both at home and around the lab. Sharing accommodation, trips, challenges, research, and philosophical conundrums with you has been a great part of this adventure. Should logic ever come back from km 21, I will let you know.

Most importantly, thanks to Simone, for being such a great part of my life. And thanks to my family, always with me even at such a great distance.

Abstract

The reciprocal interaction between light and matter has been attracting increasing interest in recent years thanks to the developments in the field of optomechanics. A typical optomechanical system can be exposed to the radiation pressure force thanks to the amplifying action of an optical cavity, which can increase the level of the interaction by several orders of magnitude. The extraordinary interplay between the light and the mechanical components of the cavity grants access to remarkably delicate applications, which include the cooling of an oscillator to its motional ground state, the generation of non-classical optical states, and refined quantum optical measurements.

A particular indicator of the capabilities of an optomechanical system is its mechanical quality factor, which gives a measure of the coherence time of the oscillator. High-quality oscillators are less susceptible to the interaction with the environment, thanks to the lower dissipation and reduced coupling of external noise. Thus, an optomechanical system with a very high quality factor enables more advanced operations. Levitated objects are particularly suitable for this, since their motional degrees of freedom are completely decoupled from any external reservoir. The levitation scheme introduced in this thesis takes the concept to extremes by considering fully coherent optical levitation of a cavity mirror. Such system would allow exceptionally pure tracking of the oscillator's position, which can be converted for example into accurate measurements of relative changes in the gravitational field.

Other approaches focusing on the improvement of the sensitivity in existing systems are also considered. Taking advantage of the incredible diversity of optomechanical structures, we show how enhanced signals can be extracted in systems as small as a nanowire or as big as an interferometer stretching over several kilometres. Each strategy is presented in relation to a specific application, while keeping the opportunity of generalizing to systems operating under very different conditions open.

Overall, the experimental and theoretical investigations presented in this thesis show that optomechanics is a valuable resource for the attainment of high-precision measurements of displacements, forces, accelerations, and other relevant physical quantities.

Contents

Part I

The framework of optomechanics

This Part covers the foundations of the topics treated in the rest of the manuscript, from the concept of an electromagnetic field to the full quantum treatment of the optomechanical interaction. Some of the material also focuses on more practical matters, such as locking of an optical resonator, with the aim of creating a reference point for users less experienced with modern techniques in experimental optics. Chapter 1 opens with a description of the subject of optomechanics, its origin, and the current state of advancement. It also outlines a few major incentives that motivate the interest behind the research in the field. This introduction aims to delineate a very general overview of the subject, and more detailed analysis of the relevant topics will be presented in the respective sections throughout the document. Chapter 2 covers some of the notions in quantum optics and other fields that are essential for the understanding of the topic. This opportunity is also used to introduce notions and conventions that will be presupposed throughout the thesis, and even though most of this preparatory material falls easily into the domain of common knowledge for a physicist this induction is still important for the establishment of a reference point for future chapters. Chapter 3 develops from the bases laid out in the previous chapter to formally describe the theory specific to optomechanics. Radiation pressure, optomechanical bistability, and the optical spring effect will develop naturally from the formalism introduced in this chapter.

In Greek mythology, light and progress are both associated with Prometheus, one of the four sons of Iapetus whose name literally means “forethought”. The Titan stole fire from the gods and gifted it to mankind, marking the beginning of technological advancement.

F. H. Füger, *“Prometheus bringt der Menschheit das Feuer”*

Chapter 1

Introduction

1.1 A historic tour of radiation pressure and optomechanics

Light is such a common premise to our daily experience that we often overlook its dominant role in many of the phenomena that lay the basis of our very existence. The energy from the Sun travels to Earth in the form of light, initiating photosynthesis and other photochemical processes indispensable for the sustenance of life. As a species, we evolved to probe the surrounding world with vision, a sense based on the reception and interpretation of the information carried by light. On the same principle we established astronomy and the exploration of the otherwise unreachable domains of the universe. The technological advancements based on different manifestations of light are uncountable, and the quest to understand its true nature has sparked some of the major revolutions in modern physics, from Maxwell's unification of electricity and magnetism to quantum mechanics and the standard model.

Among the discoveries that challenged our understanding of light was the existence of radiation pressure. Light impinging on a surface applies a force proportional to its intensity, establishing a direct form of interaction with matter. This force was first observed by Kepler, who noticed how the tail of comets always pointed away from the Sun rather than trailing behind in the comet's orbit. Today, we know that comets generally exhibit two tails corresponding to streams of neutral dust and ionized gas, driven by a combination of radiation pressure and solar winds. The first formulation for radiation pressure arrived only a few centuries after Kepler's discovery, with the development of Maxwell's theory of electromagnetism. The electromagnetic field carries its own energy and momentum, both capable of being transferred to a medium upon absorption or reflection. Light, being a manifestation of the electromagnetic field, makes no exception. With the advent of quantum mechanics and the quantization of the field, radiation pressure may be understood in terms of momentum transfer from a photon flux. Though the photon is itself a massless particle, it still carries a momentum that transfers to the target. Depending on whether the photon is reflected or absorbed, the process can be seen as equivalent to an elastic or an inelastic collision.

The first attempt to characterize radiation pressure in laboratory conditions was performed by Crookes in 1873. He envisioned a light-powered mill, with vanes enclosed in low vacuum and painted black on one side and white on the opposite. The net difference in radiation pressure due to the absorption or reflection of light on the two sides would power the mill and activate rotation around a low-friction spindle. However, while the rotation was expected to be observed with the white sides trailing backwards as they experienced a double momentum transfer, it was in fact observed in the opposite direction. The rotation originates from the thermal exchange of the residual gas molecules with the differently painted panels. The molecules bounce with greater velocity from the black sides, which are heated more by the light than the white ones, and specific air pressure conditions are needed to ensure a pressure imbalance on the two sides without the drag that would prevent the motion. This was confirmed in 1901 by Lebedev, who observed the rotation reducing and eventually ceasing in higher vacuum. Crookes' original idea was successfully implemented not long after by Nichols and Hull. They used a similar radiometer which allowed regulation of the air pressure to identify a regime where the gas heating and other thermal effects could reach a torsional balance. The apparatus could then be calibrated to obtain accurate

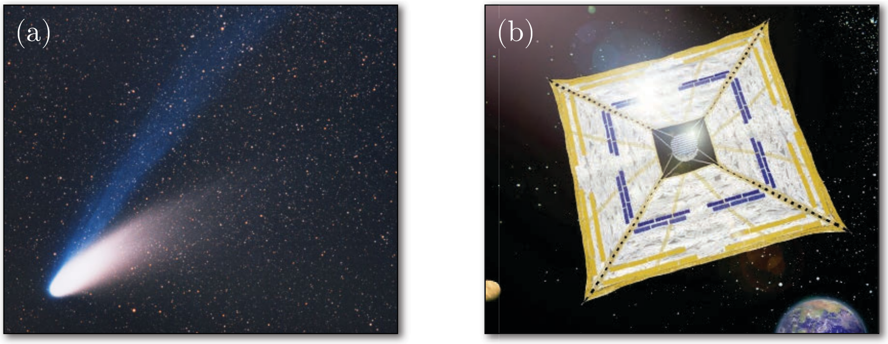

Figure 1.1: Examples of systems influenced by radiation pressure. **(a)** The comet Hale–Bopp was the brightest passing by Earth in recent years. The two tails that can be distinguished correspond to the white dust tail, fanning to the right, and the blue ion tail, pointing straight away from the Sun. Image credits: ESO (http://www.eso.org/). **(b)** Artist's impression of the IKAROS mission, propelled by the solar pressure on a large membrane acting as a solar sail. Image credits: JAXA (http://global.jaxa.jp/).

experimental measurements of radiation pressure force for the first time [1, 2].

Radiation pressure is generally very weak and hard to detect with conventional measurements. Sunlight, for example, exerts a pressure on the surface of the Earth on the order of a few micropascals, 10^{11} times smaller than the atmospheric pressure of air. Yet, the consequences of radiation pressure are identifiable in many different scenarios. Without question its largest manifestation occurs on the cosmic scale, where it is responsible for the dispersion of interstellar dust and the general redistribution of matter during formation processes. Within the solar system, the radiation pressure from the Sun exerts its influence by perturbing the orbits of large and small celestial bodies, including man-made probes or satellites [3]. It is even possible to harvest the energy received by solar pressure and use it as the main form of propulsion, as demonstrated by the solar sail mission of IKAROS (Interplanetary Kite-craft Accelerated by Radiation Of the Sun) on its way to Venus [4]. This mission made clever use of liquid-crystal panels that could change their reflectivity to steer the sail into the desired trajectory. In the last few decades radiation pressure became more easily accessible in laboratory conditions as well thanks to the much stronger optical intensities allowed by laser technology. Its impact is not always desirable: in gravitational-wave interferometers, for example, the sensitivity suffers from the laser noise that radiation pressure transmits to the test masses. Nevertheless, in different conditions it is often used to one's advantage for cutting edge light-matter interaction, with practical applications including laser cooling, trapping, and optical actuation.

The optical manipulation of mechanical systems and the reverse effect that material objects have on the propagation of light fall within the sphere of *optomechanics*. The origins of the field can be traced back to the early 1970s, when Braginsky and colleagues noticed and successively investigated the damping effects of light onto moving objects [5, 6]. Around the same period Ashkin started groundbreaking work on optical manipulation by levitating small microspheres using only the intensity of light. These two lines of research evolved into two major tools available to the optomechanical experimentalist: the optical spring effect, and optical tweezers. Fast-forwarding to the present day, optomechanics emerges as a fully mature discipline with a very active and prolific community that has recently accomplished exceptional milestones. These include the cooling of a mechanical oscillator to its quantum ground state [7], the generation of squeezed quantum states of light [8, 9], the slowing of light by optomechanically induced transparency [10, 11], and much more. With the race for most proof-of-principle demonstrations now over, the research in optomechanics is currently oriented towards the translation of these achievements into quantum-enabled technologies for practical applications (such as integrated quantum memories) but also for the investigation of fundamental physics (from quantum decoherence to tests of semiclassical models of gravity).

It should be mentioned that optomechanics does not strictly require the interaction between light and matter to be mediated by radiation pressure. A similar interplay between the two parts of the system can be achieved by thermal effects. These can arise for example in the form of bolometric forces, which apply to bimorph materials subject to thermal expansion, or in the form of photophoretic forces, occurring in fluid-suspended particles that exhibit a non-uniform distribution of temperature when irradiated by light. Depending on the system, these expressions of optomechanical interaction may benefit from a far greater strength than radiation pressure force. At the same time, however, they may not be as fast and direct as radiation pressure force and they could preclude the decoupling of thermal noise from the apparatus.

1.2 Motivation

A major benefit of optomechanics lies in its potential to investigate the quantum regime from a perspective that had been impossible until recently. With the assistance of laser cooling, even the collective motion of extremely large ensembles of atoms can be witnessed responding to the laws of quantum mechanics. Large systems, strong coherences, and close interactions with gravitational forces are all qualities that appeal to the modern physicist, as they can all test our understanding of the physical world.

Macroscopic quantum superpositions are required to observe predicted deviations from quantum physics [12,13]. This effort would necessarily involve adequate measures to isolate the system from environmental sources of noise and decoherence. One of the schemes proposed in the present work could be very promising in this respect: by levitating a milligram-scale mirror on top of a strong optical field, its centre-of-mass motion can be decoupled from any external degrees of freedom that would otherwise interfere with quantum operations [14]. The intrinsic role of gravity in the levitation process could also allow such system to act as a testbed to rule out certain semiclassical theories of gravitational quantum mechanics [15].

Optomechanics is also famed for state-of-the-art readings of displacements, which can be easily translated to other highly sensitive measurements in accelerometry, magnetometry, and atomic force microscopy thanks to the broad flexibility of mechanical platforms. This is also one of the possible scopes of the levitated mirror, along with the other schemes featured in this manuscript. At the nanoscopic level, it is shown that a sensitivity enhancement for impulsive forces is possible by applying periodic feedback to metallic nanowires [16]. At the opposite end of the scale, the optomechanical interaction is suggested as a means to push the sensitivity of kilometre-sized interferometric detectors for gravitational waves [17].

The purpose of this thesis is to present the investigations performed during the length of the author's doctoral candidature. The systems and techniques considered aim to promote the role of optomechanics for refined applications in metrology. The thesis is divided in four Parts. Part I offers a general overview of optics and optomechanics. Part II describes the investigations performed with nanowires for a sensitivity enhancement of impulsive forces. The levitating mirror scheme is developed in Part III. Finally, in Part IV we extend on the set of tools available thanks to optomechanics with the proposal of two schemes, one to engineer arbitrary optical potentials and one to enhance the sensitivity of interferometers with frequency-dependent squeezing.

Chapter 2

General premises

2.1 Notation and preliminary concepts

This section is meant to familiarize the reader with basic notions and conventions that will be used throughout the thesis. Even though most of these topics could easily fall into the domain of common knowledge of a physicist, an explicit introduction is still important to ensure acquaintance with the material and to act as a reference point for future chapters.

- **Physical and mathematical quantities**

  To facilitate navigation between the assorted topics covered in different parts of the thesis, a special endeavour was dedicated to maintain consistence of notation across different chapters. Naturally, exception is made for those variables or indices whose scope is manifestly local or illustrative for a specific context.

  The notation for physical quantities holding a universally accepted value, such as the speed of light and the Planck constant, is so widespread that it makes little sense to point them out individually every time they are being used. Table 2.1 reports here, for future reference, the symbols (and values) of the physical constants found throughout the main text, so that they can be used without further

Quantity	Symbol	Value
Reduced Planck constant	$\hbar$	$1.054\,57 \times 10^{-34}\,\mathrm{J\,s}$
Speed of light in vacuum	c	$299\,792\,458\,\mathrm{m\,s^{-1}}$
Vacuum permittivity	ε_0	$8.854\,187\,817 \times 10^{-12}\,\mathrm{F\,m^{-1}}$
Vacuum permeability	μ_0	$4\pi \times 10^{-7}\,\mathrm{N\,A^{-2}}$
Boltzmann constant	k_B	$1.380\,65 \times 10^{-23}\,\mathrm{J\,K^{-1}}$
Stefan–Boltzmann constant	σ_SB	$5.670\,39 \times 10^{-8}\,\mathrm{W\,m^{-2}\,K^{-4}}$

Table 2.1: Notation and values of the physical constants used in this text.

specification [18].

A similar argument applies to mathematical constants, of course. To avoid ambiguity, the symbol i is reserved for the imaginary unit and the symbol e is used only to indicate Euler's number. Other mathematical conventions include the use of bold-faced symbols to indicate vectors (e.g. $\mathbf{v}$), a double bar for its norm (e.g. $\|\mathbf{v}\|$), an asterisk (*) for complex conjugation, and a dagger (†) for the adjoint of an operator. Additionally, if the upper and lower bounds of an integral extend to infinity, for simplicity they may be omitted if they have been clearly specified at least once within the context.

- **Fourier analysis**

An essential mathematical tool in physics is the concept of *Fourier transform* [19]. As there are several possible conventions, however, it is imperative to clarify which particular transformation is in use. Given a generic function $f(t)$, with the assumption that all the necessary convergence conditions hold, we consider for the Fourier transform $\tilde{f}(\omega)$ the non-unitary transformation in terms of the "angular" conjugate variable ω:

$$\tilde{f}(\omega) := \int_{-\infty}^{+\infty} dt\, f(t) e^{-i\omega t}, \qquad f(t) = \int_{-\infty}^{+\infty} \frac{d\omega}{2\pi}\, \tilde{f}(\omega) e^{i\omega t}. \tag{2.1}$$

The use of an angular variable instead of the canonical one has the advantage of a lighter notation, as illustrated by the absence of 2π factors in the properties of the Fourier transform listed in Table 2.2. It is worth mentioning that the Fourier transform has the quality of being asymmetric with respect to complex

	Linearity	Translation		Scaling
$f(t)$	$a\, f(t) + b\, g(t)$	$f(t - t_0)$	$e^{i\omega_0 t} f(t)$	$f(at)$
$\tilde{f}(\omega)$	$a\, \tilde{f}(\omega) + b\, \tilde{g}(\omega)$	$\tilde{f}(\omega) e^{-i\omega t_0}$	$\tilde{f}(\omega - \omega_0)$	$\frac{1}{\lvert a\rvert} \tilde{f}(\omega / \lvert a\rvert)$

	Derivative		Convolution	
$f(t)$	$(\partial/\partial t)^n f(t)$	$(-it)^n f(t)$	$(f * g)(t)$	$f(t) g(t)$
$\tilde{f}(\omega)$	$(i\omega)^n \tilde{f}(\omega)$	$(\partial/\partial \omega)^n \tilde{f}(\omega)$	$\tilde{f}(\omega) \tilde{g}(\omega)$	$\frac{1}{2\pi} (\tilde{f} * \tilde{g})(\omega)$

Table 2.2: Properties of the Fourier transform.

conjugation:

$$[\tilde{f}(\omega)]^* = \tilde{f}^*(-\omega). \tag{2.2}$$

Note that the “tilde” used to denote the Fourier transform in this section will be dropped in the remainder of the thesis, in order to prevent the notation from becoming unnecessarily cumbersome.

- **Dirac delta**

  In the domain of distributions, one of the most singular Fourier transforms is the *Dirac delta function*,

  $$\delta(\omega) := \int_{-\infty}^{+\infty} dt \, \frac{e^{-i\omega t}}{2\pi}, \tag{2.3}$$

  which is obtained by transforming a constant function. The Dirac delta is an even distribution, null everywhere except at the origin where it is undefined, with the requirement that

  $$\int_{-\infty}^{+\infty} d\omega \; \delta(\omega) = 1. \tag{2.4}$$

  It also acts like the identity element for the convolution operation, an attribute that leads to the *sifting* of the value of other functions at the centre of the distribution (here taken to be some ω_0):

  $$\int_{-\infty}^{+\infty} d\omega \; f(\omega)\delta(\omega - \omega_0) = \int_{-\infty}^{+\infty} d\omega \; f(\omega_0)\delta(\omega - \omega_0) = f(\omega_0). \tag{2.5}$$

  It should be noted that the value of a generic integral involving the Dirac delta highly depends on the integration domain. The integration does not need to stretch to infinity for the above properties to hold, as long as the centre of the distribution is included within the limits of the integration. If, on the other hand, the centre of the distribution falls outside of the interval between the upper and lower bounds, the full integral vanishes. A particular case occurs when the centre of the distribution coincides with one of the two integration bounds:

  $$\int_{-\infty}^{\omega_0} d\omega \; \delta(\omega - \omega_0) = \frac{1}{2}, \qquad \int_{\omega_0}^{+\infty} d\omega \; \delta(\omega - \omega_0) = \frac{1}{2}. \tag{2.6}$$

- **Spectral density**

Often, when dealing with some time-dependent quantity $f(t)$, one might be concerned with the distribution of its frequency components across the spectrum. This task is performed effectively by the *power spectral density*, defined in terms of the Fourier transform by

$$S_f(\omega) := \langle |f(\omega)|^2 \rangle, \tag{2.7}$$

where the expectation value is taken over extended periods of time (i.e. greater than the inverse of the frequencies considered). The label of "power" comes from the fact that, thanks to Parseval's theorem, integrating the spectral density $S_f(\omega)$ over all frequencies is equivalent to integrating the squared absolute value of the original variable $|f(t)|^2$ over time, resulting in a quantity proportional to the "energy" of $f(t)$.

The power spectral density coincides with the Fourier transform of the auto-correlation function of f, i.e. $(f^* \star f)$, as

$$\begin{aligned} S_f(\omega) &= \int dt \int dt' \, \langle f^*(t) f(t') \rangle e^{i\omega(t-t')} \\ &= \int d\tau \int dt \, \langle f^*(t) f(t+\tau) \rangle e^{-i\omega\tau} \\ &= \int d\tau \, \langle (f^* \star f)(\tau) \rangle e^{-i\omega\tau}. \end{aligned} \tag{2.8}$$

This feature can be used to extend the definition of power spectral density to more than one quantity by use of their cross-correlation. Given a second quantity $g(t)$, its similarity to the first function $f(t)$ is measured by the *cross power spectral density*

$$S_{fg}(\omega) := \int d\tau \, \langle \mathrm{Re}[(f^* \star g)(\tau)] \rangle e^{-i\omega\tau}, \tag{2.9}$$

where the real part is considered to maintain the symmetry between the two functions.

Following directly from the definition, thanks to Eq. 2.2 we know that the power spectral density is always symmetric in frequency, i.e. $S_f(\omega) = S_f(-\omega)$. This property, however, is not always holding: if the quantity of interest, $f(t)$, is replaced with an operator $\hat{f}(t)$ belonging to a non-commutative algebra (as is the case of observables in quantum mechanics), the auto-correlation function is not guaranteed to be real. This renders the power spectral density asymmetric and leads to an inherently “quantum” interpretation of the spectrum [20], where one half describes the system’s capacity of absorbing energy from the environment and the other half measures how much energy is emitted by the system instead. The asymmetry in absorption and emission processes corresponds to the imbalance in the spectral density between negative and positive frequencies. Denoting the spectral density obtained by simple replacement of the classical functions with quantum operators as $S_f^{(\mathrm{Q})}(\omega)$, we consider a quantum power spectral density that more closely resembles its classical counterpart by applying a symmetrizing action:

$$\begin{aligned} S_f(\omega) &:= \int d\tau \; \langle \{ (\hat{f}^\dagger \star \hat{f})(\tau) \} \rangle e^{-i\omega\tau} \\ &= \int d\tau \; \frac{\langle (\hat{f}^\dagger \star \hat{f})(\tau) \rangle + \langle (\hat{f}^\dagger \star \hat{f})(-\tau) \rangle}{2} e^{-i\omega\tau} \\ &= \frac{1}{2} \left(S_f^{(\mathrm{Q})}(\omega) + S_f^{(\mathrm{Q})}(-\omega) \right) . \end{aligned} \tag{2.10}$$

The act of symmetrizing the quantum observables, indicated with curly brackets, resembles the act of taking the real part in the cross spectral density of Eq. 2.9. When probing the spectrum of an observable of the system with a classical measurement, this is the correct power spectral density to consider.

2.2 Quantum mechanics

Quantum mechanics [21], one of the biggest achievements of the 20th century, lays the foundations for an incredible variety fields. It is not surprising, then, to find it at the core of a relatively young field such as the one of optomechanics. Without laser light, for example, it would be hard to conceive a practical way to achieve the levels of interactions of a mechanical oscillator with an optical field observed today. Even more importantly, optomechanics has the possibility of exploring entirely new regimes that could help to answer some of the questions still open in quantum physics.

The name of this branch of physics originates from the fact that primary physical quantities, such as energy and angular momentum, are quantized and can hold only discrete values. This result can be predicted by Schrödinger’s equation, which is taken here as a postulate. In the customary *bra-ket* notation, Schrödinger’s equation takes the form

$$i\hbar\frac{\partial}{\partial t}|\psi(t)\rangle = \hat{\mathcal{H}}|\psi(t)\rangle, \tag{2.11}$$

where the quantum state with wave function $\psi(t)$ is indicated by the "ket" $|\psi(t)\rangle$ (and its dual by the "bra" $\langle\psi(t)|$). The operator $\hat{\mathcal{H}}$ denotes the system's Hamiltonian, governing the time evolution of the state.

Operators such as $\hat{\mathcal{H}}$, generally distinguished by an overhead circumflex, are an important part of the mathematical framework of quantum mechanics. Observables of the system are a special class of operators, with the property of being self-adjoint and thus admitting only real eigenvalues that represent the different values that can be measured for the particular variable under consideration. A crucial premise of quantum mechanics is that measurements might not be compatible: in the language of operators, this implies that the order in which different operators are applied is important, and in general two operators corresponding to two different measurements do not commute. One of the best examples is given by the position and momentum operators of an oscillator, $\hat{x}$ and $\hat{p}$, whose commutation relation is $\left[\hat{x},\hat{p}\right] = i\hbar$. An important consequence of non-commutativity is Heisenberg's uncertainty principle, which puts a bound to how well conjugate observables can be known at the same time. This is expressed as

$$\sigma_{\mathcal{O}_1}\sigma_{\mathcal{O}_2} \geq \frac{1}{2}\left|\langle[\hat{\mathcal{O}}_1,\hat{\mathcal{O}}_2]\rangle\right|, \tag{2.12}$$

where the uncertainty of the observable $\hat{\mathcal{O}}$ is represented by its standard deviation $\sigma_{\mathcal{O}} := \sqrt{\langle\hat{\mathcal{O}}^2\rangle - \langle\hat{\mathcal{O}}\rangle^2}$ and the angled brackets indicate the expected value over the state of the system. Observables corresponding to different degrees of freedom in the system are not affected by measurement incompatibility, however, and they always commute with one another. Specifically to optomechanics, for example, operators associated with the optical field unconditionally commute with any observable of the mechanical oscillator.

The formulation following from Schrödingers equation, where the temporal dynamics of the system are encoded in the state, is referred to as the *Schrödinger picture*. It is possible to use another formulation, called the *Heisenberg picture*, where the states are treated as constants and the time evolution is assigned to the operators. A generic operator $\hat{\mathcal{O}}(t)$, then, evolves according to the equation

$$\frac{d\hat{\mathcal{O}}(t)}{dt} = \frac{i}{\hbar}\left[\hat{\mathcal{H}},\hat{\mathcal{O}}(t)\right] + \frac{\partial\hat{\mathcal{O}}(t)}{\partial t} \tag{2.13}$$

(see Appendix A.2 for a detailed derivation). The two pictures are mathematically equivalent, and differ mainly in the interpretation attributed to the observables and the measuring process. However, sometimes one may seem more appropriate than the other for a convenient description of the dynamics. In quantum optics it is customary to work in the Heisenberg picture, where quantized fields are handled with more ease.

2.3 Quantum optics

Optics has been one of the main subjects of interest since the very early days of physics. History has seen many different interpretations and variants, slowly evolving into our modern understanding of the subject. From ray optics to beams and waves, it was only with the development of Maxwell's theory of electromagnetism that the entire picture started to come together. However, the advent of particle-wave duality in quantum mechanics demanded for a reformulation that ultimately gave rise to *quantum optics* and the concept of *photons*. The aim of this section is to highlight the major cornerstones of optics, from a classical understanding of electrodynamics [22] to the quantization of the electromagnetic field and the quantum properties of light [23].

2.3.1 Classical electrodynamics

Maxwell's equations establish a relation between the electric field **E** and the magnetic field **B**. In vacuum, in the absence of charges, they are:

$$\nabla \cdot \mathbf{E} = 0, \qquad \nabla \cdot \mathbf{B} = 0, \tag{2.14}$$

$$\nabla \times \mathbf{E} = -\partial_t \mathbf{B}, \qquad \nabla \times \mathbf{B} = \mu_0 \varepsilon_0 \, \partial_t \mathbf{E}, \tag{2.15}$$

where ε_0 and μ_0 are, respectively, the *electric constant* (or vacuum permittivity) and the *magnetic constant* (or vacuum permeability) [22]. Combining these equations together, we find that both **E** and **B** satisfy the wave equation:

$$\left(\nabla^2 - \frac{1}{c^2}\partial_t^2\right)\mathbf{E} = 0, \qquad \left(\nabla^2 - \frac{1}{c^2}\partial_t^2\right)\mathbf{B} = 0. \tag{2.16}$$

The waves propagate at velocity $c = 1/\sqrt{\mu_0 \varepsilon_0}$, corresponding to the speed of light in vacuum.

A specific class of solutions to the wave equations is obtained by considering the components of the field to be of the form $A(\mathbf{r})e^{-i\omega t}$, where the spatial dependence on the coordinates $\mathbf{r}$ is separated from the time dependence. Solutions of this form are known as *monochromatic waves*, since they are characterized by the presence of a single wave frequency, ω. Expressing Eq. 2.16 in terms of $A(\mathbf{r})$, we obtain the Helmholtz equation,

$$\left(\nabla^2 + k^2\right) A(\mathbf{r}) = 0. \tag{2.17}$$

The constant $k := \omega/c$ represents the wave number, which is linked to the wavelength λ by the well-known relation $k = 2\pi/\lambda$. To calculate the transfer of energy of a monochromatic wave, it should be observed that the rotating component is typically fast compared to an ordinary measurement time. This is especially true for optical waves, whose frequencies are typically in the scale of a few hundred terahertz. Therefore, it is reasonable to consider the average flow of energy over one or many cycles and obtain a result that is independent of time. The intensity of the field is then obtained by multiplying the average energy by the speed of the wave. With an appropriate choice of coordinates where $A(\mathbf{r})$ represents the full field amplitude, the intensity of the monochromatic wave is

$$I(\mathbf{r}) = \frac{c\varepsilon_0}{2} \left|A(\mathbf{r})\right|^2 . \tag{2.18}$$

In general, any solution of the wave equation can be expanded as a sum of monochromatic plane waves, i.e. monochromatic waves for which the field amplitude has uniform value across a plane orthogonal to some wave vector $\mathbf{k}$ which determines the direction of propagation of the wave. In these terms, the electric and magnetic fields are expressed as [23]

$$\mathbf{E}(\mathbf{r}, t) = \sum_{\mathbf{k}} \left(A_{\mathbf{k}} e^{i\mathbf{k}\cdot\mathbf{r} - i\omega_{\mathbf{k}} t} + A^*_{\mathbf{k}} e^{-i\mathbf{k}\cdot\mathbf{r} + i\omega_{\mathbf{k}} t}\right) \boldsymbol{\epsilon}_{\mathbf{k}}, \tag{2.19}$$

$$\mathbf{B}(\mathbf{r}, t) = \sum_{\mathbf{k}} \left(A_{\mathbf{k}} e^{i\mathbf{k}\cdot\mathbf{r} - i\omega_{\mathbf{k}} t} + A^*_{\mathbf{k}} e^{-i\mathbf{k}\cdot\mathbf{r} + i\omega_{\mathbf{k}} t}\right) \frac{\mathbf{k} \times \boldsymbol{\epsilon}_{\mathbf{k}}}{\omega_{\mathbf{k}}}, \tag{2.20}$$

where the sum is taken to run over all possible wave vectors $\mathbf{k}$. Each mode has a specific frequency $\omega_{\mathbf{k}} := c\,\|\mathbf{k}\|$, polarization orthogonal to the propagation and specified by the unit vector $\boldsymbol{\epsilon}_{\mathbf{k}}$, and amplitude $A_{\mathbf{k}}$ determined by the specific Fourier decomposition of the particular solution. The intensity of the field, proportional to the squared absolute value of the amplitude, is susceptible in this general case to the interference of different modes.

2.3.2 Radiation pressure

The electromagnetic field carries both momentum and energy, and is subject to the same conservation laws as mechanical systems [22]. The energy flux density is described by the Poynting vector,

$$\mathbf{\Pi} = \frac{1}{\mu_0}\mathbf{E} \times \mathbf{B}, \tag{2.21}$$

whose time-averaged magnitude corresponds to the fields intensity, $I = \langle \|\mathbf{\Pi}\| \rangle$. When the field is absorbed or reflected, the change in momentum results into the exertion of a pressure on the incident surface, known as *radiation pressure.*

An intuitive derivation for radiation pressure can be obtained by considering the Lorentz force applied by a monochromatic wave reflecting from a perfect conductor [24]. For convenience, assume the field to be propagating in the z direction, with the electric and magnetic components $\mathbf{E}$ and $\mathbf{B}$ aligned respectively to the x and y axis. and let the reflecting surface be aligned to a plane transversal to the direction of propagation. On reflection, the magnetic field outside of the conductor becomes a superposition of a forward and a backward-travelling wave. Within the conductor the magnetic field instead vanishes. The discontinuity at the interface generates a surface current along the x direction,

$$j_\mathrm{s} = \frac{1}{\mu_0}\left(0 - 2\left\|\mathbf{B}\right\|\right) = \frac{1}{\mu_0} \cdot \frac{2\left|A_0\right|}{c}\cos(\omega_0 t), \tag{2.22}$$

where $\left|A_0\right|/c$ is the amplitude of the incident magnetic field and ω_0 the frequency of oscillation of the waves. The Lorentz force applied by the magnetic field to an infinitesimal surface element of the conductor $d\Sigma$ is $dF = j_\mathrm{s}\left\|\mathbf{B}\right\| d\Sigma$, in the positive x direction. This corresponds to a force per unit area of $2\varepsilon_0\left|A_0\right|^2\cos^2(\omega_0 t)$ pushing on conductor. Considering ω_0 to be an optical frequency, one can average over multiple oscillations to directly obtain the radiation pressure

$$p_\mathrm{rad} := \left\langle \frac{dF}{d\Sigma} \right\rangle = \varepsilon_0 A_0^2 = \frac{2I}{c}. \tag{2.23}$$

In the last step, Eq. 2.18 was used to link the radiation pressure to the field's intensity.

A more formal derivation is possible in terms of the Poynting vector. Overall, radiation pressure depends on whether the field is reflected, absorbed, or transmitted by the material. The general expression for radiation pressure force, obtained by integration of p_{rad} over the surface, is

$$F_{\text{rp}} = \frac{Q_{\text{rad}} P}{c} \cos^2 \theta, \tag{2.24}$$

where P is the incident power, θ is the angle of incidence of the field on the surface, and Q_{rad} is a coefficient which determines how much pressure is applied ($Q_{\text{rad}} = 2$ when the field is fully reflected, 1 when fully absorbed, and 0 when fully transmitted).

2.3.3 Quantum electrodynamics

The electromagnetic field is quantized by identifying each mode's complex field amplitude $A_{\mathbf{k}}$ and its conjugate $A^*_{\mathbf{k}}$ as bosonic operators of a quantum harmonic oscillator (cf. Appendix B). As a result, the fields also become quantum operators:

$$\hat{\mathbf{E}}(\mathbf{r}, t) = \sum_{\mathbf{k}} \left(\hat{a}_{\mathbf{k}} e^{i\mathbf{k}\cdot\mathbf{r} - i\omega_{\mathbf{k}} t} + \hat{a}^\dagger_{\mathbf{k}} e^{-i\mathbf{k}\cdot\mathbf{r} + i\omega_{\mathbf{k}} t} \right) \mathcal{E}_0 \boldsymbol{\epsilon}_{\mathbf{k}}, \tag{2.25}$$

$$\hat{\mathbf{B}}(\mathbf{r}, t) = \sum_{\mathbf{k}} \left(\hat{a}_{\mathbf{k}} e^{i\mathbf{k}\cdot\mathbf{r} - i\omega_{\mathbf{k}} t} + \hat{a}^\dagger_{\mathbf{k}} e^{-i\mathbf{k}\cdot\mathbf{r} + i\omega_{\mathbf{k}} t} \right) \frac{\mathcal{E}_0}{\omega_{\mathbf{k}}} \left(\mathbf{k} \times \boldsymbol{\epsilon}_{\mathbf{k}} \right). \tag{2.26}$$

Here, $\hat{a}_{\mathbf{k}}$ and $\hat{a}^\dagger_{\mathbf{k}}$ are the annihilation and creation operators for the mode $\mathbf{k}$, normalized to satisfy the commutation relation $\left[\hat{a}_{\mathbf{k}}, \hat{a}^\dagger_{\mathbf{k}}\right] = 1$. Physically, the creation/annihilation refers to a quantum of excitation of the field, known as a *photon.* The dimensional component of the field amplitude is separated into a separate constant, $\mathcal{E}_0 := \sqrt{\frac{\hbar\omega_{\mathbf{k}}}{2\varepsilon_0 V}}$ [23], where V indicates the mode volume (for well-behaved modes, a consistent definition could be given in terms of energy as $V = \frac{\int d^3\mathbf{r}\ \varepsilon_0 |E(\mathbf{r})|^2}{\max(\varepsilon_0 |E(\mathbf{r})|^2)}$).

It is not uncommon to restrict the electromagnetic field to a single mode. This requirement is quite realistic for laser light, which is characterized by extremely good temporal coherence with a narrow spectral distribution centred around the carrier oscillation frequency of the field. The spectral linewidth of a laser depends on many factors, such as the width of the atomic transition used to generate the laser and the techniques used to achieve stability of the apparatus. The typical linewidth of a Nd:YAG laser with wavelength $\lambda = 1064\,\text{nm}$ ranges around a few tens of kilohertz, or a few parts in 10^{10}, and implementation of high-stability techniques can even achieve sub-hertz linewidths [25]. Under these premises, unless specifically declared otherwise in the following discussion the field will be implicitly assumed to consist of a single frequency mode. The index identifying the mode will be omitted: the annihilation and creation operators will simply be indicated by $\hat{a}$ and $\hat{a}^\dagger$, and ω_{o} will be the optical frequency of oscillation. The intensity of a single mode, originally described by Eq. 2.18, is reformulated as a photon flux as

$$I = \frac{c}{4V} \hbar\omega_\mathrm{o} \langle \hat{n} \rangle, \tag{2.27}$$

where $\langle \hat{n} \rangle = \langle \hat{a}^\dagger \hat{a} \rangle$ is the mean number of photons, each of energy $\hbar\omega_\mathrm{o}$.

2.3.4 Coherent states

The mode of a classical field is determined by the direction of propagation and the frequency of oscillation. Each mode, however, is not uniquely specified, unless its amplitude and phase are exactly known. In quantum optics, the amplitude and phase are two operators used to define two orthogonal quadratures of the field. They can be described by linear combinations of $\hat{a}$ and $\hat{a}^\dagger$ as

$$\hat{X}_1 := \hat{a} + \hat{a}^\dagger, \qquad \hat{X}_2 := -i\big(\hat{a} - \hat{a}^\dagger\big), \tag{2.28}$$

As conjugate observables, the amplitude and phase quadrature are subject to Heisenberg's uncertainty principle: $\sigma_{X_1}\sigma_{X_2} \geq 1$.

The vacuum state, corresponding to the ground state $|0\rangle$ of the field as a harmonic oscillator, has minimum uncertainty, i.e. $\sigma_{X_1}\sigma_{X_2} = 1$. The same is not true for the other number states which constitute the typical basis of a quantum harmonic oscillator. These, known as *Fock states* in connection with electromagnetic fields, are usually indicated by $|n\rangle$, where n is some integer number indicating how many quanta of excitations, or photons, the field carries. The uncertainty relation for a generic Fock state is $\sigma_{X_1}\sigma_{X_2} = 2n + 1$, which for $n > 0$ is always higher than the vacuum's.

The *coherent state*, $|\alpha\rangle$, is defined as the eigenstate of the annihilation operator: $\hat{a}|\alpha\rangle = \alpha|\alpha\rangle$. It can be expanded in terms of the Fock states basis as

$$|\alpha\rangle = e^{-\frac{|\alpha|^2}{2}} \sum_{n=0}^{+\infty} \frac{\alpha^n}{\sqrt{n!}} |n\rangle, \tag{2.29}$$

where the coefficients are determined by using the defining property and requesting unitary normalization. Formally, the same state can be obtained by applying the displacement operator $\hat{D}_\alpha := e^{\alpha\hat{a}^\dagger - \alpha^*\hat{a}}$ on the vacuum state, i.e. $|\alpha\rangle = \hat{D}_\alpha|0\rangle$ [23]. The parameter α is a complex number, and its squared absolute value is proportional to the mean number of photons:

$$\langle\hat{n}\rangle = \langle\hat{a}^\dagger\hat{a}\rangle = \langle\alpha|\hat{a}^\dagger \cdot \hat{a}|\alpha\rangle = |\alpha|^2 . \tag{2.30}$$

Like the vacuum, the coherent state has minimum uncertainty. In fact, $|\alpha\rangle$ is equivalent to a "displaced" vacuum state, with the same uncertainty but with a finite field amplitude equal to α. Coherent states exhibit maximum coherence, as opposed to *thermal states*—another class of displaced states characterized by an uncertainty larger than the vacuum's. Thanks to this remarkable feature, coherent states are often considered as "quasi-classical" states of the field and their use is widespread in quantum optics. For fields with high intensity, and thus a large number of photons, we can treat the coherent state as a classical field and let the operators $\hat{a}$ and $\hat{a}^\dagger$ be replaced by their counterparts α and α^*. This consideration might be performed implicitly in future chapters, but for now we will continue discussing about a quantum field.

Because the detection of each photon is independent from the others, the fluctuation in number of photons for any state different from a Fock state follows a specific probability distribution. Given a coherent state, from Eq. 2.29 we see that the probability of measuring n photons is

$$\Pr(n) = |\langle n|\alpha\rangle|^2 = \frac{|\alpha|^{2n}\, e^{-|\alpha|^2}}{n!}. \tag{2.31}$$

This is a Poisson distribution of mean $|\alpha|^2 = \langle n\rangle$. The variance of the photon-counting process is equal to its expectation value, meaning that the standard deviation grows as the square root of the mean number of photons. The relation between intensity and photon number given by Eq. 2.27 translates this fluctuation into an unavoidable measurement noise, known as *shot noise*, which originates from the quantized nature of the field.

2.3.5 Squeezed states

The shot noise designates a fundamental bound to the measurement of the intensity or the amplitude of the field [26]. However, there is a special class of states, known as *squeezed states*, that can push the shot noise limit even lower than the vacuum's by allowing a reduction in the photon-counting uncertainty at the expense of greater noise on different quadratures.

A squeezed state is obtained by applying the squeezing operator $\hat{S}_\rho := e^{\frac{1}{2}\left(\rho^*\hat{a}^2 - \rho\hat{a}^{\dagger 2}\right)}$ to a coherent state $|\alpha\rangle$, i.e $|\alpha, \rho\rangle := \hat{S}_\rho|\alpha\rangle$. The quantity ρ is the squeezing parameter, a complex number that specifies the degree of squeezing. Experimentally, squeezed states are achieved by exposing the field to non-linear processes that correlate different quadratures, for example by letting light propagate through an optical parametric oscillator. By doing so, conjugate quadratures such as amplitude and phase become engaged in a reciprocal interaction that can extract noise from one and cast it onto the other.

Photon-counting noise reduction is achieved by squeezing the uncertainty in the amplitude quadrature. In general, however, squeezing can be performed on any quadrature and does not have to be restricted to the two quadratures considered so far (amplitude and phase). It is convenient to define a quadrature parametrized by the angle θ that encompasses all possible choices:

$$\hat{X}_\theta := e^{-i\theta}\hat{a} + e^{+i\theta}\hat{a}^\dagger. \tag{2.32}$$

With this definition, the amplitude and phase quadrature correspond to $\hat{X}_0$ and $\hat{X}_{\pi/2}$, respectively. To understand how $\hat{X}_\theta$ generally responds to the uncertainty principle, we calculate its variance $\sigma^2_{X_\theta} := \langle \hat{X}^2_\theta \rangle - \langle \hat{X}_\theta \rangle^2$ on the squeezed state $|\alpha, \rho\rangle$. By specifying the squeezing parameter in terms of its polar coordinates as $\rho = re^{2i\varphi}$, and by using the operator properties $\hat{S}^\dagger_\rho \hat{a} \hat{S}_\rho = \hat{a}\cosh(r) - \hat{a}^\dagger e^{i\varphi}\sinh(r)$ and $\hat{S}^\dagger_\rho \hat{a}^\dagger \hat{S}_\rho = \hat{a}^\dagger \cosh(r) - \hat{a}e^{-i\varphi}\sinh(r)$ [27], we find

$$\sigma^2_{X_\theta} = \cosh(2r) - \cos(2(\theta - \varphi))\sinh(2r). \tag{2.33}$$

The quadrature corresponding to the squeezing angle, i.e. $\theta = \varphi$ (modulo multiple integers of π), is appointed as the squeezed quadrature thanks to the fact that it has minimum variance. The orthogonal quadrature, at the angle $\theta = \varphi + \pi/2$, has instead maximum variance and is designated as the anti-squeezed quadrature. The corresponding uncertainties are obtained from the square root of the variance,

$$\sigma_{X_\varphi} = e^{-r}, \qquad \sigma_{X_{\varphi+\pi/2}} = e^{+r}. \tag{2.34}$$

Squeezed states owe their title to the fact that one quadrature has reduced uncertainty relative to the conjugate one, unlike vacuum or coherent states where conjugate quadratures share the load of Heisenberg's uncertainty principle in equal measure. Any positive value of r brings the uncertainty of the squeezed quadrature lower than 1, which is the uncertainty value of any quadrature on the vacuum state. In this sense, a squeezed state is less noisy than vacuum itself, as long as the right quadrature is being observed; the noise is transferred onto the anti-squeezed quadrature, in such a way that $\sigma_{X_\varphi}\sigma_{X_{\varphi+\pi/2}} = 1$ and Heisenberg's uncertainty principle is still respected. Experimentally, some additional noise in the generation or propagation of the field typically leaks onto the state, and the product of the uncertainties of the squeezed and anti-squeezed quadratures may generally be greater than 1. The purity of the squeezed state [28], measured by

$$\mathcal{P} := \frac{1}{\sqrt{\sigma_{X_\varphi}\sigma_{X_{\varphi+\pi/2}}}}, \tag{2.35}$$

quantifies how close the squeezed state is to the states of minimum uncertainty discussed so far.

Squeezing of coherent states is an established technique [27] that has seen many breakthroughs over the past decades, with great improvements in efficiency and robustness. The current state-of-the-art is achieved by optical parametric oscillators, reported to accomplish up to 15 dB of shot noise reduction [29]. Current development is involved with the addressing of practical issues such as extension to new operating bandwidths [30], variation of the squeezed angle over frequency [31], and miniaturization of the source [32]. Original ideas are also pushing the subject to new frontiers, for example considering the involvement of non-linear entanglement for the generation of unconventional squeezed states [33] or by suggesting alternative methods of detection capable of detecting squeezing when the correlation between quadratures is complex [34]. The incredible interest attributed to squeezing is an indication of the importance it plays in several fields, from quantum information [35] to metrology beyond the standard quantum limit [36, 37]. In Chap. 12 we will examine the squeezing generated using optomechanics, how it presents frequency-dependent properties, and how this can be applied to enhance the sensitivity of interferometric gravitational-wave detectors.

2.4 Optical cavities

The optical resonator, or *cavity*, is an indispensable element of experimental optics [27, 38]. In its simplest form a cavity is composed by two mirrors aligned in front of each other, so that successive reflections of light can interfere and build up the field in the confined volume to a much greater power than that of the input field. This kind of optical cavity is known as the *Fabry–Pérot resonator*, or *etalon*, but many other different types are possible. For example one could consider a geometry with a greater number of mirrors, or there could be a non-linear medium in the intra-cavity path. Even completely different devices such as monolithic resonators are possible, where light is confined through total internal reflection [39, 40].

The applications of optical cavities are manifold. They can be employed as mode cleaners, purifying the spatial configuration of the mode, or also as frequency filters, narrowing the linewidth of a laser with low spectral coherence. They also have more distinctive uses for specific applications. For example, a resonator featuring a non-linear crystal can generate squeezing by correlating the amplitude and phase quadratures of the intra-cavity field.

Optomechanics often relies on the presence of an optical cavity. The reciprocal dependence between the position of the mirrors and the resonance condition of the cavity creates the opportunity for a strong interaction that could often be impossible by any other means.

2.4.1 Cavity field build-up

To derive an expression for the intra-cavity field we can start from the input field, with amplitude α_{in}, and follow its propagation within the cavity after entering from the first mirror. Let r_1, r_2 and t_1, t_2 be respectively the Fresnel reflection and transmission coefficients of the two end mirrors, which we identify by the subscript $i \in \{1, 2\}$. We then define the reflectivities $\mathcal{R}_i = |r_i|^2$ and the transmissivities $\mathcal{T}_i = |t_i|^2$, and consider each mirror to have other scattering or absorption losses described by $\mathcal{L}_i$ so that the relationship $\mathcal{R}_i + \mathcal{T}_i + \mathcal{L}_i = 1$ always holds true [41]. Also, let μ be the attenuation coefficient within the cavity. The distance between the two reflective surfaces determines the length of the cavity, L_0. A cavity resonates only when its length is an integer multiple of the half-wavelength $\lambda/2$, or else boundary conditions would not allow the fully resonant build-up of a stationary wave.

A diagram for the following discussion is provided in Fig. 2.1. Initially, the light inside the cavity is produced by the transmission of the input field through the input mirror (leading to $\alpha_0 = t_1 \alpha_{\text{in}}$). The light then propagates for the length of the cavity (gathering a phase shift equal to e^{ikL_0} and an attenuation of $e^{-\mu L_0}$), is reflected at the second mirror, propagates back to the first mirror, and is reflected once more (resulting into α_1). The total round-trip time of these steps is $\tau := 2L_0/c$. Multiple passes (α_n) keep repeating the same process until the field leaks outside of the resonator due to the losses and residual transmissivity of the mirrors. This is translated into the equations

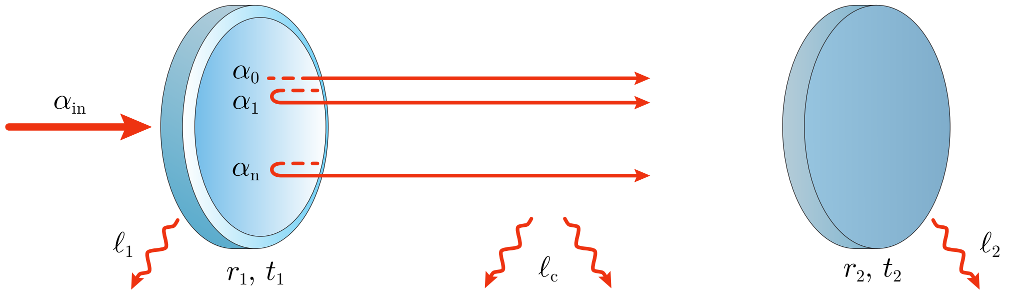

Figure 2.1: Schematic of a Fabry–Pérot cavity displaying resonance via the build-up of interference through subsequent passes.

for the field at the nth pass as

$$\begin{aligned}
\alpha_{\rm in} \;\to\; & \alpha_0 = t_1\alpha_{\rm in} \\
\to\; & \alpha_1 = r_1 e^{(-\mu+ik)L_0} r_2 e^{(-\mu+ik)L_0} t_1 \alpha_{\rm in} \\
& \dots \\
\to\; & \alpha_n = r_1^n e^{n(-\mu+ik)L_0} r_2^n e^{n(-\mu+ik)L_0} t_1 \alpha_{\rm in}. \qquad (2.36)
\end{aligned}$$

The phase accumulated after a single round trip is $\phi_0 := k \cdot 2L_0$, where $k := 2\pi/\lambda$ is the wave number. Analogously, the losses due to attenuation within the cavity are described by $\ell_{\rm c} := \mu \cdot 2L_0$. The total cavity field, as a consequence of the superposition principle, is given by the sum of each single pass contribution. The transmitted and reflected fields can also be obtained by using Fresnel conditions at the first and second mirror, respectively.

$$\alpha_{\rm cav} = \sum_{n=0}^{\infty} \alpha_n = \frac{t_1}{1 - r_1 r_2 e^{-\ell_{\rm c} + i\phi_0}} \alpha_{\rm in}, \qquad (2.37)$$

$$\alpha_{\rm tra} = t_2 \alpha_{\rm cav} = \frac{t_1 t_2}{1 - r_1 r_2 e^{-\ell_{\rm c} + i\phi_0}} \alpha_{\rm in}, \qquad (2.38)$$

$$\alpha_{\rm ref} = -r_1^* \alpha_{\rm in} + t_1^* r_2 e^{(-\mu+ik)2L_0} \alpha_{\rm cav} = \left(-r_1^* + \frac{r_2 \left|t_1\right|^2 e^{-\ell_{\rm c} + i\phi_0}}{1 - r_1 r_2 e^{-\ell_{\rm c} + i\phi_0}} \right) \alpha_{\rm in}. \qquad (2.39)$$

To infer the power, which we know is proportional to the absolute value of the corresponding field thanks to Eq. 2.18, we first introduce the *coefficient of finesse*

$$f := \frac{4\sqrt{\mathcal{R}_1 \mathcal{R}_2} e^{-\ell_{\rm c}}}{\left(1 - \sqrt{\mathcal{R}_1 \mathcal{R}_2} e^{-\ell_{\rm c}}\right)^2}, \qquad (2.40)$$

and then express everything in terms of the input power P_{in}:

$$P_{\text{cav}} = \frac{\mathcal{T}_1}{\left(1-\sqrt{\mathcal{R}_1\mathcal{R}_2}e^{-\ell_{\text{c}}}\right)^2\left(1+f\sin^2(\phi_0/2)\right)}P_{\text{in}}, \tag{2.41}$$

$$P_{\text{tra}} = \frac{\mathcal{T}_1\mathcal{T}_2}{\left(1-\sqrt{\mathcal{R}_1\mathcal{R}_2}e^{-\ell_{\text{c}}}\right)^2\left(1+f\sin^2(\phi_0/2)\right)}P_{\text{in}}, \tag{2.42}$$

$$P_{\text{ref}} = \frac{\mathcal{R}_1+\left(1-\mathcal{L}_1\right)^2\mathcal{R}_2e^{-\ell_{\text{c}}}+2\mathcal{T}_1\sqrt{\mathcal{R}_1\mathcal{R}_2}e^{-\ell_{\text{c}}}\cos(\phi_0)}{\left(1-\sqrt{\mathcal{R}_1\mathcal{R}_2}e^{-\ell_{\text{c}}}\right)^2\left(1+f\sin^2(\phi_0/2)\right)}P_{\text{in}}. \tag{2.43}$$

We can use the quantities introduced during the derivation to identify certain distinctive properties of the cavity field. The frequency-domain equivalent of the phase ϕ_0 accumulated at each pass, commonly referred to as *free spectral range*, can be defined from the inverse of the round-trip time τ,

$$\omega_{\text{FSR}} := \frac{2\pi}{\tau} = \frac{\pi c}{L_0}. \tag{2.44}$$

The free spectral range corresponds to the spacing in frequency between different resonances of the cavity, a direct consequence of the periodicity of Eq. 2.41. The coefficient of finesse gives a measure of the quality of the resonance, as large values of f correspond to a higher build-up of constructive interference into a narrower portion of the free spectral range. To have a measure of the spectral width of the resonance is, we can consider the phase for which the cavity power is half of its maximum resonant value, i.e. the ϕ that satisfies $P_{\text{cav}}|_{\phi_0=\phi} \equiv \frac{1}{2}\,P_{\text{cav}}|_{\phi_0=0}$. The equivalent of this phase in the frequency domain is the cavity half-linewidth,

$$\frac{\delta\omega}{2} := \omega_{\text{FSR}}\frac{\arcsin(1/\sqrt{f})}{\pi}. \tag{2.45}$$

Together, the free spectral range and the cavity linewidth can be used to define an optical analogue of a quality factor to indicate the number of reflections that light undergoes before escaping from the resonator. This is known as the *finesse*:

$$\mathcal{F} := \frac{\omega_{\text{FSR}}}{\delta\omega} = \frac{\pi}{2\arcsin(1/\sqrt{f})}. \tag{2.46}$$

The definition of Eq. 2.40 suggests that f, and consequently $\mathcal{F}$, can be specified by a unique parameter $\sqrt{\mathcal{R}_1\mathcal{R}_2}e^{-\ell_{\text{c}}}$. Having the loss factors corresponding to each mirror indicated by ℓ_i, chosen such that $e^{-\ell_i} = \sqrt{\mathcal{R}_i}$, we can define $\ell := \ell_1+\ell_2+\ell_{\text{c}}$ to represent

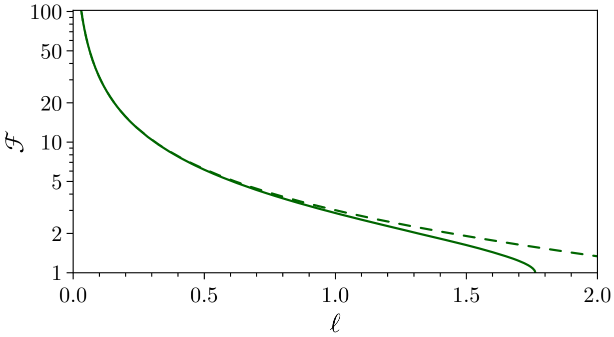

Figure 2.2: Finesse $\mathcal{F}$ as a function of total cavity losses ℓ. The approximated expression for $\mathcal{F}$ (dashed line) significantly diverges from the original definition only for $\ell \gtrsim 1$.

the total losses of the cavity. For $\ell \ll 1$, the finesse can then be approximated to

$$\mathcal{F} \simeq \frac{\pi\sqrt{e^{-\ell}}}{1-e^{-\ell}}. \tag{2.47}$$

In Fig. 2.2, where Eq. 2.46 and 2.47 are compared, we see that the approximation does not require extreme system purities to hold. As few as five reflections before the field leaks out of the cavity are enough to make the two results indistinguishable. In this approximation, the intra-cavity power can be expressed as

$$P_{\text{cav}} \simeq \frac{\mathcal{T}_1}{1+\frac{4\mathcal{F}^2}{\pi^2}\sin^2(\phi_0/2)}\frac{\mathcal{F}^2}{\pi^2}P_{\text{in}}. \tag{2.48}$$

The reduction induced by the necessarily low transmissivity of the input mirror is compensated by the square of the finesse, and as a rule of thumb the intra-cavity power scales as $\mathcal{F}$ times the input power.

The cavity dynamics obtained so far are general enough for regular purposes, but we may sometimes be interested in scanning through the cavity length (or equivalently the optical frequency) and the speed of the scan might be high enough that it might affect the regular build-up of resonance. To make provisions for the ring-down interference effects arising, we can look back at Eq. 2.36 and consider a length which is now dependent on the number of reflections of the light within the cavity. Using the initial cavity length L_0 as reference, we consider a scan actuated through motion of the input mirror at speed v. When light is reflected at the second mirror after traversing the cavity once, the length is altered to $L_0\,(1-v/c)$. When light has travelled again to return to the input mirror, the correction due to the back-and-forth reflection gives a revised length $L_1 = L_0\,(1-v/c)\,/\,(1+v/c)$, which can be linearized to

$L_1 \simeq L_0\,(1-2v/c)$ for a mirror travelling much slower than light. Successive iterations give a length $L_n \simeq L_0\,(1-2nv/c)$ at the nth pass. The field amplitude is revised to

$$\begin{aligned}\alpha_{\text{in}} \;&\rightarrow\; \alpha_0 = t_1\alpha_{\text{in}}\\ &\rightarrow\; \alpha_1 = r_1 e^{(-\mu+ik)L_0(1-2v/c)} r_2 e^{(-\mu+ik)L_0} t_1 \alpha_{\text{in}}\\ &\;\;\ldots\\ &\rightarrow\; \alpha_n = r_1 e^{(-\mu+ik)L_0(1-2nv/c)} r_2 e^{(-\mu+ik)L_0[1-2(n-1)v/c]}\alpha_{n-1}\\ &\qquad\;\; = t_1\,(r_1 r_2)^n\, e^{\left(n-n^2v/c\right)(-\ell_{\text{c}}+i\phi_0)}\alpha_{\text{in}}. \end{aligned} \tag{2.49}$$

The full series remains unresolved due to the quadratic exponent and the intra-cavity field cannot be expressed analytically. An accurate comparison with Eq. 2.37 can still be performed if we consider that after a number of reflections comparable to the finesse most of the light has escaped and the series can be truncated to the first leading terms. However, this method could prove computationally demanding and unappealing, especially in light of an alternative, more efficient method to describe the intra-cavity field presented in the next section.

2.4.2 Cavity field dynamics

A more flexible treatment for the intra-cavity field takes into account time, not the number of reflections, as the parametrizing variable. Considering the field at a time t, at any stage of its evolution, after a round-trip time τ it will undergo a reflection from both mirrors, will be attenuated by a factor $e^{-\ell_{\text{c}}}$ and will accumulate a propagation phase ϕ_0. Considering also the contribution from the travelling wave at the input of the cavity, the intra-cavity field becomes

$$\alpha_{\text{cav}}(t+\tau) = \left(\sqrt{\mathcal{R}_1\mathcal{R}_2}\alpha_{\text{cav}}(t) + \sqrt{\mathcal{T}_1\mathcal{R}_2}\alpha_{\text{in}}(t)\right) e^{-\ell_{\text{c}}+i\phi_0}. \tag{2.50}$$

Assuming small changes at each round trip, i.e. $\phi_0 \ll 1$ (modulo 2π), $\mathcal{R}_i \simeq 1$, and $\sqrt{1-\mathcal{L}_{\text{c}}} := e^{-\ell_{\text{c}}} \simeq 1$, the field can be expanded to first orders as

$$\begin{aligned}\alpha_{\text{cav}}(t) + \tau\dot{\alpha}_{\text{cav}}(t) &\simeq \sqrt{(1-\mathcal{T}_1-\mathcal{L}_1)\,(1-\mathcal{T}_2-\mathcal{L}_2)\,(1-\mathcal{L}_{\text{c}})}e^{i\phi_0}\alpha_{\text{cav}}(t) + \sqrt{\mathcal{T}_1}\alpha_{\text{in}}(t)\\ &\simeq \left(1-\frac{\mathcal{T}_1}{2}-\frac{\mathcal{T}_2}{2}-\frac{\mathcal{L}_1}{2}-\frac{\mathcal{L}_2}{2}-\frac{\mathcal{L}_{\text{c}}}{2}+i\phi_0\right)\alpha_{\text{cav}}(t) + \sqrt{\mathcal{T}_1}\alpha_{\text{in}}(t),\end{aligned} \tag{2.51}$$

and by introducing the stationary cavity field $\alpha := \sqrt{\tau}\alpha_{\text{cav}}$, normalized to the cavity lifetime, we obtain the differential equation

$$\dot{\alpha}(t) = \left(-\kappa + i\Delta_0\right)\alpha(t) + \sqrt{2\kappa_1}\alpha_{\mathrm{in}}. \tag{2.52}$$

Here, we use $\Delta_0 := \phi_0/\tau$ for the cavity detuning from resonance, $\kappa_i := \mathcal{T}_i/\left(2\tau\right)$ for the partial decay rates at the end mirrors and $\kappa := \kappa_1 + \kappa_2 + \left(\mathcal{L}_1 + \mathcal{L}_2 + \mathcal{L}_{\mathrm{c}}\right)/\left(2\tau\right)$ for the total decay rate of the cavity. The steady-state solution is

$$\alpha = \frac{\sqrt{2\kappa_1}}{\kappa - i\Delta_0}\alpha_{\mathrm{in}}, \tag{2.53}$$

and it corresponds to the zero-frequency component of the more general solution in the frequency domain,

$$\alpha(\omega) = \frac{\sqrt{2\kappa_1}\alpha_{\mathrm{in}}}{\kappa - i\left(\Delta_0 - \omega\right)}. \tag{2.54}$$

Using the boundary conditions set by the relation between the input field α_{in} and the transmitted and reflected fields, α_{tra} and α_{ref},

$$\alpha_{\mathrm{tra}} = \sqrt{\mathcal{T}_2}\alpha_{\mathrm{cav}} \simeq \sqrt{2\kappa_2}\alpha, \tag{2.55}$$

$$\alpha_{\mathrm{ref}} = -\sqrt{\mathcal{R}_1}\alpha_{\mathrm{in}} + \sqrt{\mathcal{T}_1}\alpha_{\mathrm{cav}} \simeq -\alpha_{\mathrm{in}} + \sqrt{2\kappa_1}\alpha, \tag{2.56}$$

and, remembering that $\alpha_{\mathrm{cav}} = \alpha/\sqrt{\tau}$, we can infer the steady-state solutions for the travelling waves:

$$\alpha_{\mathrm{cav}} = \frac{\sqrt{2\kappa_1/\tau}}{\kappa - i\Delta_0}\alpha_{\mathrm{in}}, \tag{2.57}$$

$$\alpha_{\mathrm{tra}} = \frac{\sqrt{4\kappa_1\kappa_2}}{\kappa - i\Delta_0}\alpha_{\mathrm{in}}, \tag{2.58}$$

$$\alpha_{\mathrm{ref}} = \frac{2\kappa_1 - \kappa + i\Delta_0}{\kappa - i\Delta_0}\alpha_{\mathrm{in}}. \tag{2.59}$$

The steady-state power of each travelling wave is proportional to the squared absolute

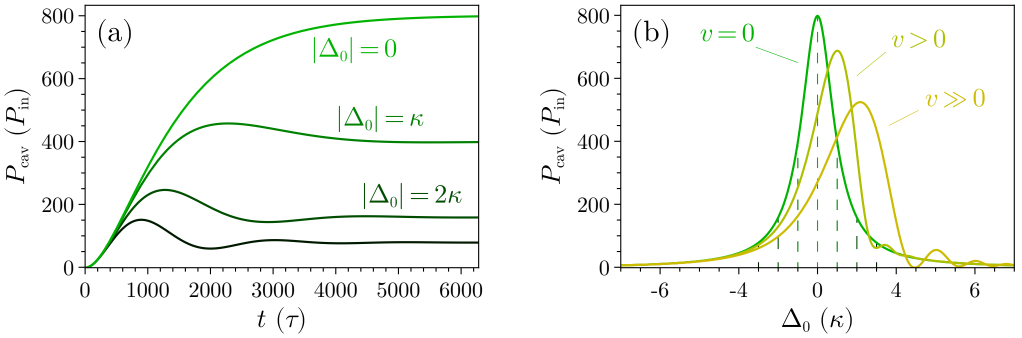

Figure 2.3: Intra-cavity power for a cavity of length $L_0 = 0.185\,\mathrm{m}$ with $\mathcal{R}_1 = \mathcal{R}_2 = 99.90\,\%$ and $\mathcal{T}_1 = \mathcal{T}_2 = 0.08\,\%$. The finesse corresponding to these parameters is $\mathcal{F} = 3140$. **(a)** Time-domain evolution of the intra-cavity power at different detunings, from $|\Delta_0| = 0$ (bright) to $|\Delta_0| = 3\kappa$ (dark) in intervals of κ. The horizontal axis is in units of the cavity round-trip time τ, and the vertical axis is normalized to the input power P_{in}. **(b)** Intra-cavity power in the frequency domain. The horizontal axis is in units of the cavity decay rate κ and the vertical axis is again normalized to the input power P_{in}. Vertical dashed lines indicate the detunings used in (a), and for each the value of the power corresponds to the steady-state level in the time domain. The asymmetric traces show how the intra-cavity field is affected by a scan speed $v \neq 0$. They have been obtained at scan speeds $v = 50 \times 10^{-6}\,\mathrm{m\,s^{-1}}$ and $v = 150 \times 10^{-6}\,\mathrm{m\,s^{-1}}$, corresponding to scan frequencies of 50 Hz and 150 Hz for a 1 µm stroke.

value of the corresponding field. In terms of the input power P_{in}, they are:

$$P_{\mathrm{cav}} = \frac{2\kappa_1/\tau}{\kappa^2 + \Delta_0^2} P_{\mathrm{in}}, \tag{2.60}$$

$$P_{\mathrm{tra}} = \frac{4\kappa_1\kappa_2}{\kappa^2 + \Delta_0^2} P_{\mathrm{in}}, \tag{2.61}$$

$$P_{\mathrm{ref}} = \frac{(2\kappa_1 - \kappa)^2 + \Delta_0^2}{\kappa^2 + \Delta_0^2} P_{\mathrm{in}}. \tag{2.62}$$

An example of how the intra-cavity power evolves in time before reaching the steady state is shown in Fig. 2.3a. After a total time equal to the time of a single round-trip times the finesse ($\approx 3000\,\tau$ in the case at hand), the evolution starts to converge to its steady-state value given by Eq. 2.60. In the frequency domain (Fig. 2.3b) the power follows a Lorentzian profile.

To see how the scan speed affects the intra-cavity field, we now consider a cavity length changing linearly in time as $L(t) = L_0 + vt$ because of one end mirror moving at speed v. For the field, the change in length translates into a time-dependent detuning $\Delta(t) = (k \cdot 2L(t))/\tau = 2k\,(L_0 + vt)/\tau = \Delta_0 + 2kv \cdot t/\tau$. Equation 2.52 is then modified to

$$\dot{\alpha}(t) = \left[-\kappa + i\left(\Delta_0 + 2kv \cdot t/\tau\right)\right]\alpha(t) + \sqrt{2\kappa_1}\alpha_{\mathrm{in}}. \tag{2.63}$$

The non-constant nature of the new coefficient in front of $\alpha(t)$ prevents us from directly solving it in the frequency domain, as it was done for Eq. 2.54. Instead, the Fourier transform of the field amplitude answers to the differential equation

$$\alpha'(\omega) = \frac{\tau}{2kv}\left[\left(-\kappa + i\Delta_0 - i\omega\right)\alpha(\omega) + \sqrt{2\kappa_1}\alpha_{\mathrm{in}}\right], \tag{2.64}$$

where the prime indicates derivation relative to the Fourier variable. The effects of the scan are shown in Fig. 2.3b. Compared to the Lorentzian solution at zero speed, the solutions at speed $v \neq 0$ show signs of asymmetry due to the end mirror moving in a particular direction. Self-interference of the field causes lower peak powers and additional ripples at the tails. Note that these self-interference effects are highly dependent on the optical quality of the cavity [42]: at high finesse, the cavity lifetime $2\pi/\kappa$ is longer and the light interacts with the moving mirror more extensively than it would at low finesse. In other words, the extent of self-interference can be characterised by the dimensionless quantity $2kv \cdot 2\pi/\kappa$. If this quantity is small, which could either be because the scan speed is slow enough or because the cavity lifetime is short, then the correction term in Eq. 2.63 has less weight and the behaviour is closer to the solution described by the original differential equation without the correction term (Eq. 2.52).

On a final note, it should be mentioned that both the total cavity decay rate κ and the cavity half-linewidth $\delta\omega/2$ of Eq. 2.45 are a measure of the losses in the cavity, and even if they have a different definition they are technically the same quantity. For losses $\ell \ll 1$, the asymptotic congruence of κ and $\delta\omega/2$ can be proved as follows:

$$\begin{aligned}
\frac{\delta\omega}{2} &:= \omega_{\mathrm{FSR}}\frac{\arcsin(1/\sqrt{f})}{\pi} & \kappa &:= \frac{(\mathcal{T}_1 + \mathcal{L}_1) + (\mathcal{T}_2 + \mathcal{L}_2) + \mathcal{L}_{\mathrm{c}}}{2\tau} \\
&\simeq \frac{\omega_{\mathrm{FSR}}}{2\pi}\frac{2}{\sqrt{f}} & &= \frac{(1-\mathcal{R}_1) + (1-\mathcal{R}_2) + \mathcal{L}_{\mathrm{c}}}{2\tau}, \\
&= \frac{1}{\tau}\frac{1-e^{-\ell}}{e^{-\ell/2}} & &= \frac{\left(1-e^{-2\ell_1}\right) + \left(1-e^{-2\ell_2}\right) + \left(1-e^{-2\ell_{\mathrm{c}}}\right)}{2\tau} \\
&\simeq \frac{\ell}{\tau}, & &\simeq \frac{\ell}{\tau}.
\end{aligned} \tag{2.65}$$

This congruence makes the original solutions found via successive reflections (Eq. 2.37–2.39) agree with the solutions of the cavity equation (Eq. 2.57–2.59).

2.4.3 Impedance matching

The relationship between the input, the output and the intra-cavity fields is conditioned by the losses at each mirror. From Eq. 2.59 we can see that, for example, if $\kappa_1 = \kappa$ the reflected field differs from the input field only by a phase shift. This particular example also implies $\kappa_2 = 0$, which corresponds to a perfect reflectivity for the second mirror. Another possible configuration could be given by $\kappa_1 = \kappa_2 = \kappa/2$, in which case

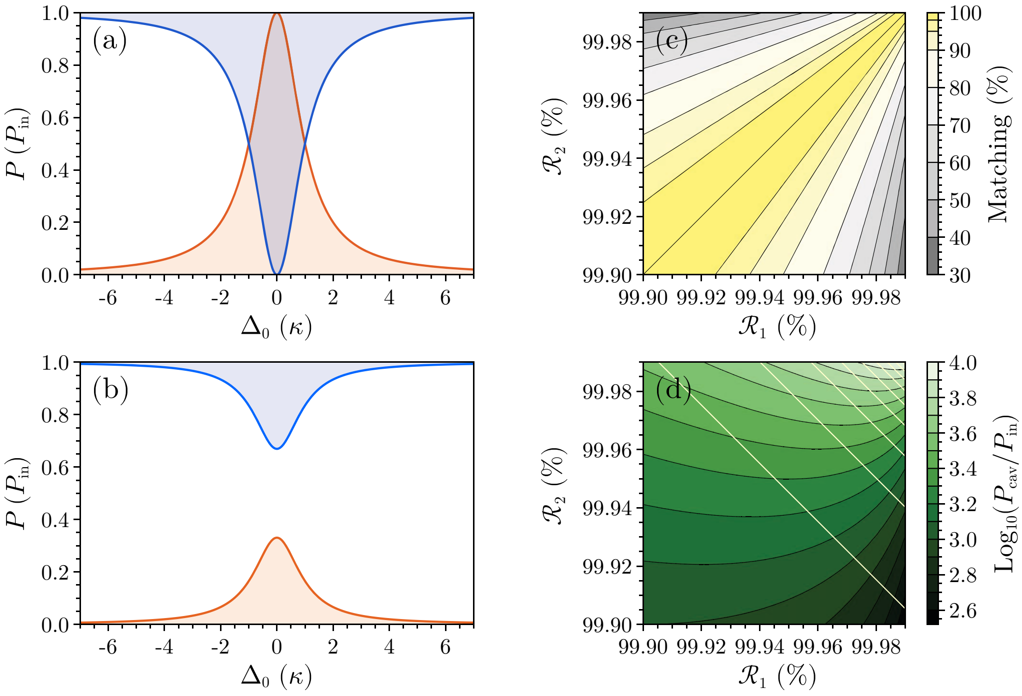

Figure 2.4: Impedance matching of a Fabry–Pérot cavity. All plots assume no losses in the cavity, and mirror 1 used as the input port. **(a)** Response of the reflected (blue) and transmitted (red) fields during a scan across resonance. The reflectivity is chosen to be 99.90 % for both mirrors, corresponding to a finesse of 3140. On resonance there is no reflection and the field is fully transmitted, implying optimal (100 %) impedance matching for the cavity. **(b)** Same as (a), but now one of the mirrors is chosen with a reflectivity of 99.99 %. The finesse in this instance is 5710, and the intra-cavity power depends on whether the higher reflectivity is assigned to the first or the second mirror. In either case, on resonance only part of the input field is transmitted and the impedance matching of the cavity is ineffective (33 %). **(c)** Impedance matching as a function of the reflectivities of the two mirrors. The level of impedance matching is determined by the proportion of the input field being transmitted rather than reflected back. Perfect impedance matching conditions are achieved when $\mathcal{R}_1 = \mathcal{R}_2$. **(d)** Intra-cavity power as a function of the reflectivities of the two mirrors. A higher reflectivity for the input mirror implies less power coupled into the cavity. The symmetrical situation, with the reflectivity of the input mirror swapped with the other one, has the same finesse but higher circulating power. The bright lines denote constant finesse, from 6000 to 30000 at increments of 3000.

on resonance the reflected field completely vanishes and the input is fully transmitted through the cavity. These are only two examples of a broader set of circumstances determined by all possible values of κ_1 and κ_2. The selection of specific values for the decay rates of the two mirrors in order to satisfy one's requirements is known in resonator optics as *impedance matching.*

Some examples of different impedance matching conditions are presented in Fig. 2.4. The first example (Fig. 2.4a) shows the power of the reflected and transmitted fields when the cavity has no losses and the two mirrors have the same reflectivity. The second example (Fig. 2.4b) considers the same lossless cavity where the reflectivity is higher for one of the two mirrors is higher while it is unchanged for the other. Assuming the mirror with unchanged reflectivity to be the input port, the amount of power coupled into the cavity is the same. As the total intra-cavity power also depends on the finesse which is now higher, however, there is more energy circulating within the cavity. Despite this, the response of the output fields on resonance is more moderate, as the discrepancy between the reflectivities of the two mirrors creates a mismatch from optimal impedance conditions. Since impedance matching is symmetrical with respect to $\mathcal{R}_1$ and $\mathcal{R}_2$ (see Fig. 2.4c), the response of the output fields would be exactly the same if the reflectivities of the two mirrors were to be swapped, thus associating the higher reflectivity to the input mirror. In this case, however, less field is transmitted from the input into the cavity, and the intra-cavity power would be lower despite the finesse being the same. This situation is better described in Fig. 2.4d, where the intra-cavity power is seen to be asymmetrical with respect to the reflectivity of the input and the output mirrors.

2.4.4 Gaussian modes

So far the analysis has involved only one of the three spatial dimensions, the one longitudinal to the direction of propagation of light. A realistic treatment needs to account for the transverse directions as well, since the optical mode might be diverging or converging and the cavity might not fully satisfy the requirements bringing for a stable, complete interference. It is therefore important to determine a solution to Maxwell's equations that well approximates the idea of a ray of light, in terms of its propagation and divergence properties.

The Helmholtz equation introduced in Chap. 2.3.1 describes the profile of an optical mode, with the assumption that the time dependence of the wave can be separated from its spatial features. In making the further assumption of a planar wave propagating along a specific direction z, representing the optical propagation axis, the generic wave profile $A(\mathbf{r})$ can be further separated into

$$A(\mathbf{r}) := \bar{A}(\mathbf{r}) e^{-ikz}. \tag{2.66}$$

The spatial properties of the complex envelope $\bar{A}(\mathbf{r})$ are assumed to vary slowly compared to the scale determined by the wavelength $\lambda = 2\pi/k$, i.e. $\partial_z \bar{A} \ll \bar{A}/\lambda$, so that the monochromatic nature of the wave is preserved along the propagation [38]. The argument can also be extended to the second derivative, and we request $\partial_z^2 \bar{A} \ll \partial_z \bar{A}/\lambda$. Substituting the new expression into Eq. 2.17, we can use the two assumptions on $\bar{A}(\mathbf{r})$ to find an approximation of the Helmholtz equation, called the *paraxial Helmholtz equation* [43]:

$$\left(\nabla_{\mathrm{T}}^2 - 2ik\partial_z\right) \bar{A}(\mathbf{r}) = 0. \tag{2.67}$$

The paraxial approximation does not affect the transverse degrees of freedom, which still feature in terms of the transverse Laplacian $\nabla_{\mathrm{T}} := \partial_x^2 + \partial_y^2$.

A spherical wave, given by $A(\mathbf{r}) = (A_0/r)e^{-ikr}$, can be approximated to be paraxial if $\sqrt{x^2+y^2} \ll |z|$, i.e. the transverse coordinates are much smaller than the longitudinal one. The approximation results into the paraboloidal wave, with a propagating profile

$$\bar{A}(\mathbf{r}) = \frac{A_0}{z} e^{-ik\frac{x^2+y^2}{2z}}. \tag{2.68}$$

It can be easily verified that this represents a solution to the paraxial Helmholtz equation, and it will still be one if the entire wave is shifted along the direction of propagation. Interestingly, an imaginary shift $z \to z + iz_0$ also produces a solution of Eq. 2.67. The paraxial wave obtained in this case is the *Gaussian beam*, which is expanded as

$$\begin{aligned}
\bar{A}(\mathbf{r}) &= \frac{A_0}{z+iz_0} e^{-ik\frac{x^2+y^2}{2(z+iz_0)}} \\
&= A_0 \frac{z-iz_0}{z^2+z_0^2} e^{-ik\left[\frac{x^2+y^2}{2}\left(\frac{z-iz_0}{z^2+z_0^2}\right)\right]} \\
&= \frac{A_0}{\sqrt{z^2+z_0^2}} \frac{(-i)\left(z_0+iz\right)}{\sqrt{z^2+z_0^2}} e^{-ik\frac{x^2+y^2}{2z(1+z_0^2/z^2)}} e^{-\frac{2\pi}{\lambda}\frac{x^2+y^2}{2z_0(1+z^2/z_0^2)}} \\
&= \frac{A_0}{z_0} \frac{1}{\sqrt{1+z^2/z_0^2}} e^{-i\left(\frac{\pi}{2}-\arctan\left(z/z_0\right)\right)} e^{-ik\frac{x^2+y^2}{2z(1+z_0^2/z^2)}} e^{-\frac{\pi}{\lambda z_0}\frac{x^2+y^2}{(1+z^2/z_0^2)}}.
\end{aligned} \tag{2.69}$$

We can define the Gouy phase shift,

$$\zeta(z) := \arctan\Big(\frac{z}{z_0}\Big), \tag{2.70}$$

the wavefront radius,

$$R(z) := z\left(1 + \frac{z_0^2}{z^2}\right), \tag{2.71}$$

and the beam width,

$$W(z) := W_0\sqrt{1 + \frac{z^2}{z_0^2}}, \tag{2.72}$$

which depends on the beam waist $W_0 := \sqrt{\lambda z_0/\pi}$ and corresponds to the distance from the peak of the field distribution where the field amplitude decays to a $1/e$ factor of its maximum value. The field amplitude of the Gaussian beam can be expressed in terms of these parameters as

$$A(\mathbf{r}) = \frac{A_0}{z_0}\frac{W_0}{W(z)} e^{-\frac{x^2+y^2}{W(z)^2}} e^{-i\frac{\pi}{2}+i\zeta(z)-ik\left(\frac{x^2+y^2}{2R(z)}+z\right)}. \tag{2.73}$$

The name of this particular solution of the paraxial Helmholtz equation originates from the Gaussian profile of its intensity,

$$I(\mathbf{r}) = \frac{c\varepsilon_0}{2}\left|A(\mathbf{r})\right|^2 = I_0\left(\frac{W_0}{W(z)}\right)^2 e^{-2\frac{x^2+y^2}{W(z)^2}}. \tag{2.74}$$

Each cross section along the longitudinal direction follows a two-dimensional Gaussian envelope which has a width determined by $W(z)$ and a peak value of $I_0 := c\varepsilon_0\left|A_0\right|^2/(2z_0^2)$ at the origin. The brightness is inversely proportional to $W(z)$, and the total power in each transverse plane,

$$P(z) = \iint dx\, dy\; I(\mathbf{r}) = \frac{1}{2}\pi W_0^2 I_0, \tag{2.75}$$

is independent of z. Even though, technically, the intensity profile extends infinitely in the transverse directions, one can use the beam width as an appropriate measure of the dimensions of the beam, since more than 86 % of the power is contained in a circle of radius $W(z)$. Propagation makes the beam expand to a width of $\sqrt{2}W_0$ when $|z| = z_0$, and when $|z| \gg z_0$ the width increases linearly in z. The angular spread of

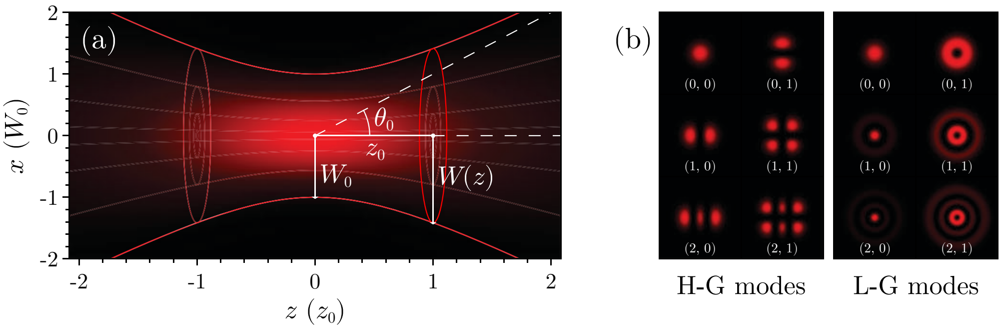

Figure 2.5: Illustration of the intensity distribution of Gaussian modes. **(a)** Longitudinal cross section of a Gaussian beam. The main parameters characterizing the beam are outlined: the Rayleigh range z_0, the beam waist W_0, the beam width $W(z)$ and the angular spread θ_0. **(b)** Transverse cross sections of Hermite–Gaussian modes (left) and Laguerre–Gaussian modes (right). The indices denoting the order of the mode are, respectively, (m, n) and (p, l).

the beam in the far-field region is

$$\theta_0 := \lim_{z \to +\infty} \frac{W(z)}{z} = \frac{W_0}{z_0} = \frac{\lambda}{\pi W_0}. \tag{2.76}$$

The Gouy phase shift $\zeta(z)$ makes the wavefronts propagate at a different velocity than those of a plane wave. The curvature also varies with propagation, as described by $R(z)$: at $z = 0$ the wavefront is flat, progressively getting more curved as the beam propagates until it can be considered spherical at $|z| \gg z_0$. The parameter z_0, known as the Rayleigh length, gives a measure of the range in which the beam can be considered to be collimated. The far-field limit of the Gaussian beam is a paraboloidal wave. A conceptual vision of the Gaussian beam and its main parameters is provided in Fig. 2.5a.

The Gaussian beam belongs to a broader class of orthogonal solutions of the Helmholtz paraxial equation, the *transverse electromagnetic* (TEM) *modes* [38]. These solutions, obtained by having the mode amplitude A_0 a function of coordinates before solving Eq. 2.67, are a combination of the Gaussian beam with particular orthogonal polynomials, which depend on the symmetry of the system. Generally, their intensity distribution is different from a Gaussian function. However, they share the same paraboloidal wavefronts of the Gaussian beam, meaning that they can be reflected off a curved mirror or transmitted through lenses in a similar way. When reflection in the system occurs with rectangular symmetry in the transverse plane, the polynomials used to describe higher-order modes are the Hermite polynomials. The solutions, typically referred to as *Hermite–Gaussian modes*, are described by

$$A_{mn}(\mathbf{r}) = \frac{A_0}{z_0}\frac{W_0}{W(z)} H_m\Big(\frac{\sqrt{2}x}{W(z)}\Big) H_n\Big(\frac{\sqrt{2}y}{W(z)}\Big) \\ \times e^{-\frac{x^2+y^2}{W(z)^2}} e^{-i\frac{\pi}{2}+i(1+m+n)\zeta(z)-ik\left(\frac{x^2+y^2}{2R(z)}+z\right)}, \tag{2.77}$$

with integers indices m and n representing the horizontal and vertical directions of the transverse plane, respectively, and $H_n(x) := (-1)^n e^{x^2} \frac{d^n}{dx^n}(e^{-x^2})$ for integer n. When the symmetry of the system is cylindrical, the generalized Laguerre polynomials are used instead. The solutions, called *Laguerre–Gaussian modes*, have the form

$$A_{pl}(\mathbf{r}) = \frac{u_0}{z_0}\frac{W_0}{W(z)} \left(\frac{\sqrt{2}\rho}{W(z)}\right)^{|l|} L_p^{|l|}\Big(\frac{2\rho^2}{W(z)^2}\Big) \\ \times e^{-\frac{\rho^2}{W(z)^2}} e^{-i\frac{\pi}{2}+i(1+2p+|l|)\zeta(z)+il\phi-ik\left(\frac{\rho^2}{2R(z)}+z\right)}, \tag{2.78}$$

where we use cylindrical coordinates $\mathbf{r} = \{\rho, \phi, z\}$, radial and azimuthal indices p and l, and $L_n^a(x) := \frac{e^x x^{-a}}{n!}\frac{d^n}{dx^n}(e^{-x}x^{n+a})$ for integers n and a. The intensity distribution of both kinds of higher-order modes is shown in Fig. 2.5b. In both cases, the mode u_{00} corresponds to the Gaussian beam of Eq. 2.73. The difference in Gouy phase shift between modes of different orders results in different resonance conditions, and during the cavity scan each mode can usually be independently identified.

The optical resonators used for the production of laser light generally employ mirrors with spherical curvature wrapped around the gain medium, imposing a very specific boundary condition on the resonant modes. Gaussian modes can satisfy this condition thanks to their almost-spherical wavefronts, and they are the typical optical modes used in experimental setups. A Gaussian beam with a waist $W_0 = 1\,\mathrm{mm}$ can be regarded as collimated in a range of at least $3\,\mathrm{m}$ for most optical wavelengths, thus being suitable for table-top experiments. Collimation over an even greater extent can be obtained by increasing the beam waist: for example, $W_0 = 2\,\mathrm{cm}$ ensures collimation over more than $1\,\mathrm{km}$, which is convenient for experiments on a larger scale [44–46]. Gaussian modes are not the only solutions to the paraxial Helmholtz equation, though, and other optical modes are possible if the experiment requires different characteristics. One example is given by the Bessel beam, which maintains a planar wavefront during the entire propagation (as opposed to the almost spherical wavefronts of the Gaussian beam) but has a non-uniform, unbounded intensity profile which would require infinitely extended boundary conditions to be faithfully reproduced. Despite the possible complications, Bessel beams have particularly useful applications as optical tweezers [47], since their diffraction properties make them robust over long distances and even against obstacles. The use of other optical modes goes beyond the scope of this thesis, however, and a Gaussian mode will always be implicitly assumed unless otherwise specified.

2.4.5 Mode matching and optical stability

We now examine the procedure that reveals how to match a Gaussian mode to the optical resonant mode of a cavity. The idea is to find appropriate beam parameters that allow the wavefronts to be reflected off the end mirrors of the cavity without distortion [38].

Consider two spherical mirrors, aligned along the z axis at positions $-z_1$ and z_2, and take their radii of curvature R_1 and R_2 to be positive if they look concave from within the cavity. Recalling the functional form of the wavefront of a Gaussian beam from Eq. 2.71, and adjusting the sign convention to parallel the one for the mirrors, so that a converging wave has a negative wavefront, we can request a match between the wavefront profile and the curvature of the mirror to obtain the conditions

$$R_1 = -R(-z_1) = z_1 \left(1 + \frac{z_0^2}{z_1^2}\right), \tag{2.79}$$

$$R_2 = R(z_2) = z_2 \left(1 + \frac{z_0^2}{z_2^2}\right), \tag{2.80}$$

$$L_0 = z_1 + z_2. \tag{2.81}$$

The three equations can be solved for z_1, z_2, and z_0 with simple algebraic manipulation. Introducing the stability parameters

$$g_1 = 1 - \frac{L_0}{R_1}, \qquad g_2 = 1 - \frac{L_0}{R_2}, \tag{2.82}$$

the positions of the two mirrors have solutions

$$z_1 = \frac{L_0\,(R_2 - L_0)}{R_1 + R_2 - 2L_0} = L_0 \frac{(1 - g_1)\,g_2}{g_1 + g_2 - 2g_1 g_2}, \tag{2.83}$$

$$z_2 = \frac{L_0\,(R_1 - L_0)}{R_1 + R_2 - 2L_0} = L_0 \frac{(1 - g_2)\,g_1}{g_1 + g_2 - 2g_1 g_2}, \tag{2.84}$$

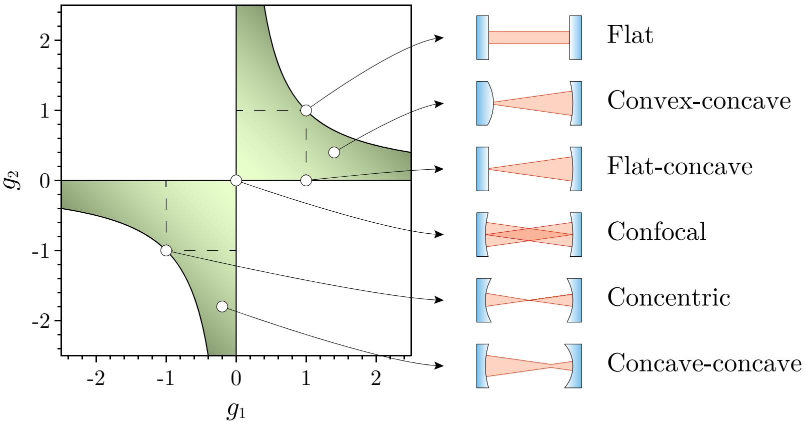

Figure 2.6: Stability diagram of an optical resonator. The illustrations on the right show some possible cavity configurations: in order from top to bottom, these correspond to $R_1, R_2 \to \infty$ (flat), $R_1 < 0$ and $R_2 > 0$ (convex-concave), $R_1 \to \infty$ and $R_2 > 0$ (flat-concave), $R_1 = R_2 = L_0$ (confocal), $R_1 = R_2 = L_0/2$ (concentric), $R_1 > 0$ and $R_2 > 0$ (concave-concave).

and the Rayleigh range of the beam is

$$\begin{aligned} z_0 &= \sqrt{\frac{L_0\left(R_1 + R_2 - L_0\right)\left(R_1 - L_0\right)\left(R_2 - L_0\right)}{\left(R_1 + R_2 - 2L_0\right)^2}} \\ &= L_0\sqrt{\frac{\left(1 - g_1 g_2\right) g_1 g_2}{\left(g_1 + g_2 - 2g_1 g_2\right)^2}}. \end{aligned} \tag{2.85}$$

The mode has a real solution only when the argument within the square root of Eq. 2.85 is positive, which is accomplished when

$$0 \leq g_1 g_2 \leq 1. \tag{2.86}$$

This is the stability condition that an optical cavity needs to satisfy in order to guarantee the existence of a resonant mode. The separation between two mirrors of given curvature needs to lie in a very specific range, or otherwise after reflection the beam might be diverging or converging too much for the other mirror to compensate, and the field would escape the cavity.

The simplicity of Eq. 2.86 inspires an intuitive visual representation of all the possible stable configurations for a resonator, as presented in Fig. 2.6. Configurations close to the edge of the stability region are usually avoided, since they require additional precision in mode matching and cavity length that is otherwise unnecessary in most common applications. Moreover, when $g_1 g_2 \simeq 1$ the resonator is particularly sensitive to misalignment and even small angular displacements can make the optical axis fall out of the cavity boundaries determined by the finite dimensions of the mirrors [48]. Concave-concave configurations are probably the most common in experimental setups, as they are stable under a wide range of parameters and allow flexibility in terms of the possible lengths for the cavity. This is particularly convenient if one needs to operate with given mirrors and different cavity linewidths are required. However, convex-concave configurations are also a viable option in terms of optical stability, and one remarkable example is found in the optical levitation system proposed in Chap. 8.

2.5 Experimental techniques

A successful quantum optics experiment relies on a number of standard techniques [27]. The aim of this section is to present some of the practises employed systematically which will also feature in the two major investigations presented in this thesis.

2.5.1 Homodyne and heterodyne detections

Homodyne detection is a very versatile technique based on interferometry that can be used to measure specific attributes of the field that would be otherwise unaccessible. It is performed by combining the field $\hat{a}$, in the role of the signal to be detected, with a stronger reference field $\hat{a}_{\mathrm{LO}}$, acting as a local oscillator. The name (derived from the ancient Greek words *homós*, “same”, and *dýnamis*, “power”) hints that the two fields oscillate at the same frequency, ω_{o}, and to guarantee temporal coherence the same source is often used for both. The intensity of the local oscillator is typically high to enhance the interferometric component, and can thus be modelled as a classical coherent field α_{LO}.

The signal and the local oscillator are combined at a beam splitter (as shown in Fig. 2.7), resulting in the two output fields

$$\hat{d}_1 = t\,\alpha_{\mathrm{LO}} + r\,\hat{a}, \tag{2.87}$$

$$\hat{d}_2 = r^*\alpha_{\mathrm{LO}} - t^*\hat{a}, \tag{2.88}$$

where r and t are the reflection and transmission coefficients of the beam splitter, related by the conditions $|r|^2 + |t|^2 = 1$ and $r^*t + rt^* = 0$ [49]. A photodetector after the first output port of the beam splitter records an intensity proportional to

$$\langle \hat{d}_1^\dagger \hat{d}_1 \rangle = |t|^2 \left|\alpha_{\mathrm{LO}}\right|^2 + |r|^2 \langle \hat{a}^\dagger \hat{a} \rangle + rt^* \langle \alpha_{\mathrm{LO}}^* \hat{a} - \alpha_{\mathrm{LO}} \hat{a}^\dagger \rangle. \tag{2.89}$$

The interference of the two fields is represented by the last term on the right-hand side of the equation. This makes the reading depend not only on the intensity but also on the complex amplitude of the signal. The large amplitude of the local oscillator enhances the interference and could make even weak signals easier to detect. As the intensity of the field grows quadratically with the amplitude, however, the measurement in the case of the single photodetector of Fig. 2.7a might become overly tainted and information on the signal could be swamped by the local oscillator instead of being boosted. This problem is easily circumvented by the use of another photodetector on the second output port (as in Fig. 2.7b), whose measurement would be proportional to

$$\langle \hat{d}_2^\dagger \hat{d}_2 \rangle = |r|^2 \, |\alpha_{\mathrm{LO}}|^2 + |t|^2 \, \langle \hat{a}^\dagger \hat{a} \rangle - r t^* \langle \alpha_{\mathrm{LO}}^* \hat{a} - \alpha_{\mathrm{LO}} \hat{a}^\dagger \rangle. \tag{2.90}$$

The two readings can then be subtracted, analogically or digitally, to obtain

$$\begin{aligned} \langle \hat{d}_2^\dagger \hat{d}_2 \rangle - \langle \hat{d}_1^\dagger \hat{d}_1 \rangle = {} & \big(2\,|r|^2 - 1\big)\, |\alpha_{\mathrm{LO}}|^2 + \big(1 - 2\,|r|^2\big) \langle \hat{a}^\dagger \hat{a} \rangle \\ & + 2\,|r| \sqrt{1 - |r|^2} e^{-i\frac{\pi}{2}} \langle \alpha_{\mathrm{LO}}^* \hat{a} - \alpha_{\mathrm{LO}} \hat{a}^\dagger \rangle. \end{aligned} \tag{2.91}$$

Here the condition $r^* t + r t^* = 0$ was used to infer that the relative phase between r and t is $\pi/2$ [49]. The terms related to the intensity of the two fields are then easily eliminated by choosing $|r|^2 = |t|^2 = 1/2$, corresponding to a 50:50 beam splitter. The subtracted output in this case is proportional to

$$\langle \hat{d}_2^\dagger \hat{d}_2 \rangle - \langle \hat{d}_1^\dagger \hat{d}_1 \rangle = |\alpha_{\mathrm{LO}}| \, \langle e^{-i\left(\theta_{\mathrm{LO}} + \frac{\pi}{2}\right)} \hat{a} + e^{i\left(\theta_{\mathrm{LO}} + \frac{\pi}{2}\right)} \hat{a}^\dagger \rangle, \tag{2.92}$$

where the phase of the local oscillator was specified by writing $\alpha_{\mathrm{LO}} = |\alpha_{\mathrm{LO}}| \, e^{i\theta_{\mathrm{LO}}}$ in the frame rotating at the optical frequency of both fields. This is precisely the quadrature $\hat{X}_{\theta_{\mathrm{LO}}+\pi/2}$ of the signal field, as defined in Eq. 2.32. Therefore, any quadrature of the field can be revealed by homodyne detection after an appropriate choice of the local oscillator's phase, whereas the amplitude of the local oscillator acts as an effective gain for the measurement.

Heterodyne detection (from the ancient Greek *héteros*, “different”) is based on very similar principles to those of homodyne detection, with the only difference being in the local oscillator frequency, ω_{LO}, which is not restricted to be the same as that of the signal. The difference induces a beating component, and the measurement of

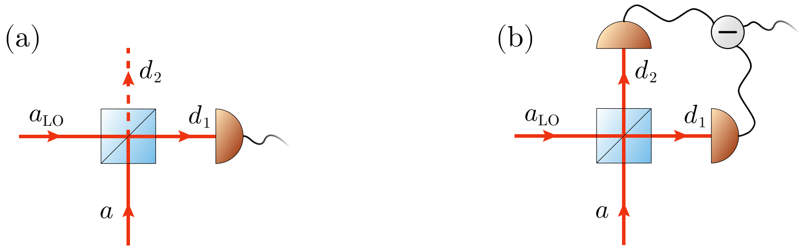

Figure 2.7: Schematic of a homodyne/heterodyne detection setup. **(a)** Combination and detection of the signal field with a reference local oscillator. **(b)** A clean quadrature measurement is obtained after subtracting the read-outs of photodetectors at both ports.

$\langle \hat{d}_2^\dagger \hat{d}_2\rangle - \langle \hat{d}_1^\dagger \hat{d}_1\rangle$ results centred around a carrier frequency $|\omega_{\rm LO} - \omega_{\rm o}|$:

$$\langle \hat{d}_2^\dagger \hat{d}_2\rangle - \langle \hat{d}_1^\dagger \hat{d}_1\rangle = |\alpha_{\rm LO}| \, \langle e^{-i\left(\theta_{\rm LO}+\frac{\pi}{2}\right)} e^{-i(\omega_{\rm LO}-\omega_{\rm o})} \hat{a} + e^{i\left(\theta_{\rm LO}+\frac{\pi}{2}\right)} e^{i(\omega_{\rm LO}-\omega_{\rm o})} \hat{a}^\dagger \rangle. \tag{2.93}$$

In the presence of low-frequency background noise, this feature can be very useful as the information coming from the signal may be shifted to a different spectral region, clear of contamination.

Both detection methods are very effective for the measurement of the quadrature of the signal field, whether this is another coherent state like the local oscillator, or a single photon, or even a squeezed vacuum state. It should be emphasized one more time, however, that the analysis presented assumes a high-power local oscillator. Although this is sufficient for the scope of this thesis, a more complete treatment is required [27] to extend the concept to general interference of two quantum fields.

2.5.2 Feedback and control theory

Many disciplines, from navigation and aeronautics to mechanical engineering, rely on control theory as a measure against deviations of the system from a desired state. Quantum optics makes no exception, and feedback loops are commonly applied to lasers and cavities to stabilize the frequency. Another application, more specific to optomechanics, involves the use of feedback to cool down a specific mode of oscillation of the resonator. This is known as feedback cooling, and it will be a central topic in Part II. In this section we focus on the basics of control theory [50] in order to encompass a broader class of systems, including for instance the cavity locking schemes discussed in the next section.

At the core of every system in control theory is the *plant*, which is the element we want to keep in a certain state. Internal dynamics or external elements may cause

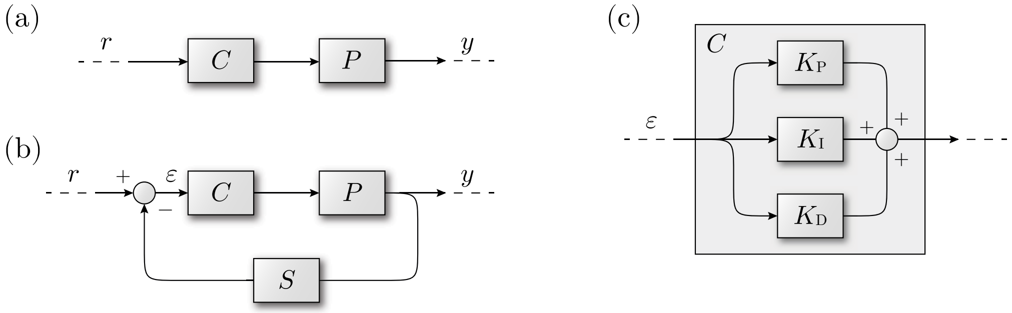

Figure 2.8: Simple examples of control systems. **(a)** Open-loop control: the controller C directly acts on the input to the plant P in order to obtain an output y as close as possible to the reference signal r. **(b)** Closed-loop control: some sensors S are used to feed back the output and compare it to the reference in order to create the error signal ε. **(c)** The proportional-integral-derivative controller.

deviations from this state, and another module, the *controller*, is normally required to restore the desired conditions. In order to know how to act to bring the system closer to the target, rather than further away, it is essential to have the appropriate *sensors* to register the current state of the system. Control theory is represented well by block diagrams, where each block represents a part of the system (plant, control, etc.) and inputs and outputs are the measurable signals. In time domain the input is transformed into an output by a convolution operation, and in Fourier or Laplace domain this becomes equivalent to a multiplication. A good control should make the transfer function, given by the ratio of the output and the input of the total system, as close to unity as possible.

A relatively unsophisticated method of implementing control is outlined in Fig. 2.8a. The plant, P, has an output y that we would like to get as close to the reference r as possible. The controller, C, uses the reference to change the input to the plant, and therefore the final output as well. This scheme makes no use of sensors, and relies on prior modelling of the system to implement control. The transfer function for this example is

$$\frac{y}{r} = PC, \tag{2.94}$$

and it is straightforward to infer that a control acting like the inverse of the plant, i.e. $C = P^{-1}$, would achieve the result sought. Unfortunately this simple, open-loop method is useful only for very predictable systems, and is not robust against arbitrary swings that are not covered by the modelling.

A closed-loop feedback control, as in Fig. 2.8b, does not suffer from the same issue. The key lies in the *error signal*, which is proportional to the difference between the state of the system and the reference. The aim of the control system is to maintain the error signal as close to zero as possible. The outline of the setup includes some sensing devices, S, that send the information recorded back in order to create and update the error signal, which is obtained by subtracting the measured output from the reference. Feeding a non-vanishing error into the controller prompts a reaction that modifies the plant's input. The changes applied through this negative feedback loop are expected to oppose the causes of the non-vanishing error in the first place, thus restoring the system to balance. With the output depending on the error as $y = PC\varepsilon$, and the error depending on the output as $\varepsilon = r - Sy$, the transfer function obtained by closing the loop is

$$\frac{y}{r} = \frac{PC}{1 + SPC}. \tag{2.95}$$

Even though this transfer function might seem harder to bring close to unity than Eq. 2.94, it represents a much better choice for most practical applications since there is no need to model the plant perfectly. Any disturbance, whether internal or external, is handled directly by the feedback.

There is a special type of controller that accounts for the vast majority of applications because of its versatility: the *proportional-integral-derivative* (PID) *controller* (Fig. 2.8c). Starting from the error signal, the PID controller produces an output given by three terms proportional to the error itself and its integral and derivative over time:

$$(C * \varepsilon)(t) = K_{\mathrm{P}}\, \varepsilon(t) + K_{\mathrm{I}} \int_0^t d\tau\ \varepsilon(\tau) + K_{\mathrm{D}} \frac{d\varepsilon(t)}{dt}. \tag{2.96}$$

The reason for the presence of the proportional term is clear. If the error signal is different from 0, the controller has to act to restore the system with a strength proportional to the magnitude of the deviation. Responding only to what the error signal indicates at the present instant might not be enough, however. This is where the integral and derivative terms play their part. The integral of the error signal can detect patterns in the history of the feedback and is particularly sensitive to slow and periodic disturbances. Thanks to the accumulation over time, it is more sensitive to a constant offset than the proportional gain and it is therefore useful to dynamically compensate for possible deviations from the steady state. The derivative of the error signal, on the other hand, anticipates what the disturbances might be in the near future. It can predict fast or sudden events, but it is rarely used because it could easily become unmanageable if the system is too erratic. The proportionality constants K_P, K_I and K_D designate the gains associated with each operation, and should be tuned independently to best account for the requirements of the system.

2.5.3 Pound-Drever-Hall locking

The resonance condition of a cavity is particularly sensitive to the effective path of the light within the resonator, as we have seen in Chap. 2.4. Variations can occur because of independent fluctuations of the cavity mirrors, or because of subtle changes in the refractive index due for example to air currents. Most of these problems can be tackled by robust designs that manage to couple the motion of the end mirrors and prevent unwelcome air flows, but making the optical resonator impervious to any type of fluctuation is a rather challenging task, especially if the same conditions need to be met for extended periods of time. A solution is found in the implementation of active feedback control. If the variations of the round-trip path over time could be monitored, then one would be able to continuously adjust the effective length of the cavity to maintain resonance. In linear resonators the adjustment can be performed by moving the end mirrors with a piezoelectric actuator, for example. In monolithic cavities, an analogous result is achieved by tuning the refractive index using electro-optic effects.

Monitoring the cavity length variations, however, is not a trivial task. One option to infer how the cavity drifts once the resonance condition is reached would be to monitor intensity fluctuations, since the resonance frequency depends on the round-trip path and a drop in intensity directly translates into a change in length. This side-of-fringe locking scheme unfortunately presents a few flaws. The cavity response is symmetric around resonance, and unless the lock is restricted to small fluctuations on one side of the resonance it is not possible to identify whether the cavity length needs to be increased or decreased. Additionally, the effectiveness of this procedure is limited by the impossibility of distinguishing the original intensity fluctuations from the frequency fluctuations of the cavity. Despite the simplicity and original popularity of this scheme, there are now more advanced alternatives that do not suffer from the same weaknesses.

The *Pound-Drever-Hall* (PDH) *locking* scheme [51,52], initially developed for applications in gravitational-wave interferometry, soon became the standard in most cavity or laser frequency stabilization applications. Intuitively, this technique relies on fast dithering of the input field's frequency to allow a comparison between this modulation and the variations in the intensity of the cavity field. The error signal produced is proportional to the derivative of the Lorentzian response of the cavity with respect to frequency, and is therefore antisymmetric with respect to resonance. Thus PDH locking overcomes both the major complications of side-of-fringe locking, and thanks to the fast modulation it also has the additional advantage of an extended bandwidth, which is usually limited by the other elements within the feedback loop (e.g. a relatively slow response of the piezoelectric actuator used to move one of the end mirrors of the cavity).

In practice the dithering is performed on the phase rather than the frequency of the input field [53]. A piezo-actuated mirror on the beam path can achieve phase modulation frequencies of up to a few tens of kilohertz. Electro-optic modulators, however, are a much more common choice since they can be driven by sinusoidal voltages of up to a few hundreds of megahertz, and can therefore dither over a spectral range that covers several multiples of the cavity linewidth. Regardless of the method chosen, the mathematical formulation of the sinusoidal phase modulation is identical. Indicating the modulation depth with M and the modulation frequency with ω_M, the oscillating component of the input field is changed as $\omega_\mathrm{o} t \rightarrow \omega_\mathrm{o} t + M \sin(\omega_M t)$. In the frame rotating at the optical frequency, assuming that the modulation depth M is small, we can linearize to obtain

$$\alpha_\mathrm{in} \rightarrow \alpha_\mathrm{in} \left[1 - \frac{M}{2} \left(e^{i\omega_M t} - e^{-i\omega_M t} \right) \right]. \tag{2.97}$$

The new rotating terms represent sidebands at ω_M relative to the carrier frequency of the field. The presence of the sidebands propagates to the cavity field, and the response of the cavity, originally described by Eq. 2.54, changes accordingly. Expressing everything in terms of the Airy function,

$$\mathcal{A}(\omega) := \left[\kappa - i \left(\Delta_0 - \omega \right) \right]^{-1}, \tag{2.98}$$

we have that the modulation changes the field amplitude as

$$\alpha = \mathcal{A}(\omega)\sqrt{\kappa}\alpha_\mathrm{in} \rightarrow \left[\mathcal{A}(\omega) - \frac{M}{2} \left(\mathcal{A}(\omega - \omega_M) e^{i\omega_M t} - \mathcal{A}(\omega + \omega_M) e^{-i\omega_M t} \right) \right] \sqrt{\kappa}\alpha_\mathrm{in}, \tag{2.99}$$

corresponding to an intra-cavity power

$$\begin{aligned}
P_{\text{cav}} = \frac{\kappa}{\tau} P_{\text{in}} \times \Bigg[&|\mathcal{A}(\omega)|^2 + \frac{M^2}{4}\left(|\mathcal{A}(\omega-\omega_M)|^2 + |\mathcal{A}(\omega+\omega_M)|^2\right) \\
&+ \frac{M}{2}\left(\mathcal{A}(\omega)\mathcal{A}(\omega+\omega_M)^* e^{i\omega_M t} - \mathcal{A}(\omega)^*\mathcal{A}(\omega-\omega_M)e^{i\omega_M t}\right. \\
&+ \left.\mathcal{A}(\omega)^*\mathcal{A}(\omega+\omega_M)e^{-i\omega_M t} - \mathcal{A}(\omega)\mathcal{A}(\omega-\omega_M)^* e^{-i\omega_M t}\right) \\
&- \frac{M^2}{4}\left(\mathcal{A}(\omega-\omega_M)^*\mathcal{A}(\omega+\omega_M)e^{2i\omega_M t} + \mathcal{A}(\omega-\omega_M)\mathcal{A}(\omega+\omega_M)^* e^{-2i\omega_M t}\right)\Bigg] \\
\simeq \frac{\kappa}{\tau} P_{\text{in}} \times \Bigg[&|\mathcal{A}(\omega)|^2 + \frac{M^2}{4}\left(|\mathcal{A}(\omega-\omega_M)|^2 + |\mathcal{A}(\omega+\omega_M)|^2\right) \\
&+ M\left(\text{Re}(\mathcal{S}(\omega))\cos(\omega_M t) + \text{Im}(\mathcal{S}(\omega))\sin(\omega_M t)\right)\Bigg]. \qquad (2.100)
\end{aligned}$$

The function introduced here,

$$\mathcal{S}(\omega) := \mathcal{A}(\omega)\mathcal{A}(\omega+\omega_M)^* - \mathcal{A}(\omega)^*\mathcal{A}(\omega-\omega_M), \qquad (2.101)$$

stands for the error signal needed to implement the feedback. It is important to ensure that the operating bandwidth of the photodetector used to collect the reflected or transmitted power has a cut-off higher than ω_M, since at this stage the information is encoded at this frequency. The terms rotating at $2\omega_M$ can be neglected because they are not going to be retrieved by the same demodulation procedure required for $\mathcal{S}(\omega)$. When two sinusoidal signals are multiplied together the result is equivalent to the sum of two sinusoidal components, oscillating at frequencies given by the difference and the sum of the original two. The photodetector signal is combined with a reference oscillating at ω_M on a frequency mixer in order to split the information on $\mathcal{S}(\omega)$ between 0 and $2\omega_M$. Filtering out higher frequencies, a signal proportional to $\text{Re}(\mathcal{S}(\omega))\cos(\phi) + \text{Im}(\mathcal{S}(\omega))\sin(\phi)$ is recovered, where ϕ indicates the phase between the sinusoidal components of Eq. 2.100 and the reference sine wave used. The mixed-down signal reflects the real part or the imaginary part of $\mathcal{S}(\omega)$, or a combination of the two, depending on the relative phase of the mixer's inputs.

A valid error signal, appropriately demodulated with the correct relative phase, will resemble one of the traces in Fig. 2.9 [53]. Which one it reflects should only depend on the modulation frequency: for a relatively slow modulation, such that $\omega_M \lesssim \kappa$, the modulation sidebands are located within the cavity linewidth and the error signal echoes the derivative of the typical Lorentzian; at faster modulation frequencies, $\omega_M \gg \kappa$, the sidebands separate from the cavity resonance and the error signal acquires a

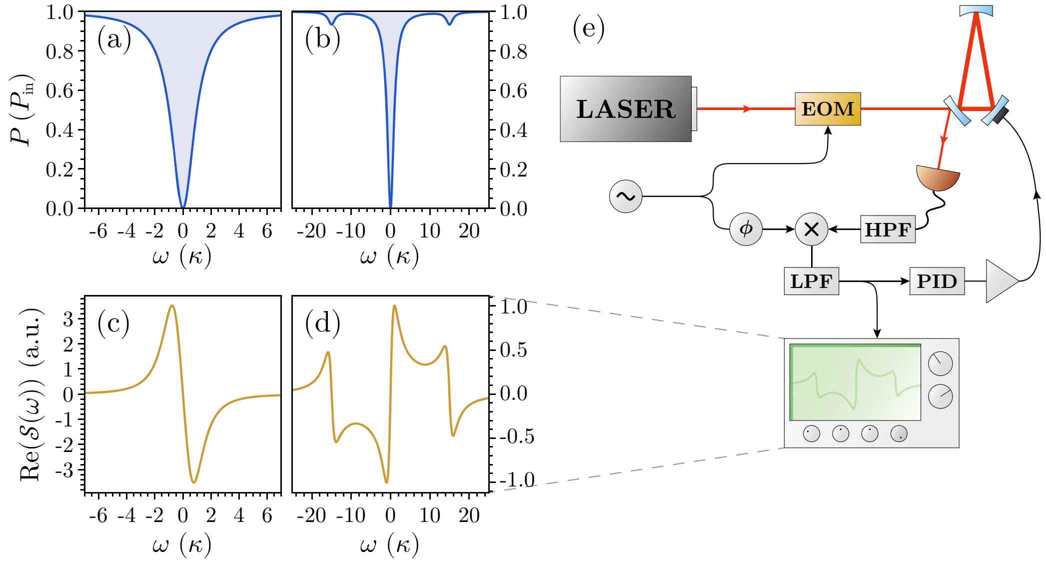

Figure 2.9: The PDH locking scheme. **(a–d)** Cavity output at reflection (a–b) and associated error signals (c–d) for low (left, $\omega_M = 0.5\,\kappa$) and high (right, $\omega_M = 15\,\kappa$) modulation frequencies. When the modulation is slow the sidebands are concealed within the cavity linewidth. Only at high modulation frequencies (ω_M) the two distinctive peaks become visible. **(e)** Schematic of the setup. A function generator (∼) is used to send a sinusoidal voltage to an electro-optic modulator (EOM) to modulate the phase of the laser. The function generator's output is split to send a similar sine wave through a phase shifter (ϕ) in order to use it as a reference for demodulation on a frequency mixer (×). The other input to the mixer is the read-out of the photodetector, in this example measuring the cavity's reflected power. A high-pass filter (HPF) or band-pass filter can be used to let only the information at the modulation frequency through. The output of the mixer is low-pass filtered (LPF) to obtain the error signal, which is fed to a proportional-integral-derivative controller (PID) to close the feedback loop. A high-voltage servo amplifier may be required after the PID controller to drive the piezo-actuator on one of the cavity mirrors.

much more distinctive appearance. From an operational point of view, both traces display an asymmetric, linear profile close to resonance that makes them perfectly viable choices for the feedback. The criteria to select what modulation frequency should be used mostly depend on other factors external to the feedback. For instance, a low modulation frequency that can be followed adiabatically by the cavity field would be desirable if the same modulation needs to be propagated further down the optical line. At the same time, modulating the phase of the field at a frequency close to the mechanical resonance in an optomechanical setup could lead to undesired excitations of the oscillator and thus be detrimental to the experiment. Whether a high or low frequency of modulation is needed depends entirely on the specific parameters of the system.

An implementation of the PDH locking scheme will typically resemble the diagram of Fig. 2.9e. The input beam, before entering the cavity, is sent through an electro-optic modulator to dither the phase. The response of the cavity to the modulated input field is recorded on a photodetector. Since the signal is encoded at ω_M, a high-pass or band-pass filter can be used to remove low-frequency noise. This signal is then directed to one port of a frequency mixer, where it is multiplied with a sine wave at the same frequency. This sine wave can be obtained from the same function generator used to drive the electro-optic modulator, although its phase needs to be adjusted separately for a result that is directly proportional to either the real or the imaginary part of $\mathcal{S}(\omega)$. Phase adjustments can be performed by the use of delay lines in the coaxial cables, or with analog/digital phase shifter modules. Alternatively, satisfactory results can be obtained by fine-tuning the modulation frequency. Amplifiers on the photodetector line or attenuators on the pure sine wave reference can also be included to ensure similar magnitudes of the two inputs. The output of the mixer contains the demodulated error signal, which is sent through a low-pass filter to eliminate residual components at ω_M, $2\omega_M$ or higher frequencies. A PID controller can make use of the error signal generated by this procedure to infer when the cavity drifts away and act to restore the resonance condition accordingly.

With the option to execute PID controls on traditional circuit boards, it is possible to carry out the entire operation purely on analog components. However, as field-programmable gate arrays (FPGAs) and system-design platforms such as LabVIEW or other programming environments matured into feasible and accessible technologies, it became possible to turn the PID controls into digital processes. This is a very flexible and cost-effective strategy that, simply by changing a few lines of code, can be adapted to a variety of systems with different parameters. A one-time expense for the FPGA and an annexed input-output breakout box to convert signals from analog to digital and vice versa replaces the need to design and build new hardware for each individual system. With everything set up appropriately, one could extend the adaptation to digital to other parts of the locking scheme as well, including the generation and processing of the error signal. The author is gratefully indebted to B. M. Sparkes and S. Armstrong [54, 55] for their efforts into the establishment of digital PDH locking in the Australian National University's quantum optics laboratories.

Chapter 3

Optomechanics: the theoretical perspective

3.1 Hamiltonian formalism

The theory of optomechanics finds an elegant presentation in the Hamiltonian formalism, which offers a unified description for the variety of systems developed in the last few decades. We begin this section with the dynamics of a mechanical oscillator, then treat the field also as a harmonic oscillator to derive the quantum version of the cavity equations. For a formal treatment, it will be necessary to describe the external noise using the quantum Langevin equations, whose application will also be pertinent to a general optomechanical system. Once the background for each part of the system is outlined, we simply need to assemble the pieces together to unlock the full potential of optomechanics.

3.1.1 Mechanical Hamiltonian

We start by focusing on the "mechanical" part of the term *optomechanics*, trying to give a brief but exhaustive description of the dynamics behind a moving mirror.

Considering harmonic motion due to some unspecified restoring force, the Hamiltonian of the mechanical system $\hat{\mathcal{H}}_{\mathrm{M}}$ can simply be taken as that of a harmonic oscillator, given by a function of the position and momentum of the mirror described by the Hermitian observables $\hat{x}$ and $\hat{p}$:

$$\hat{\mathcal{H}}_{\mathrm{M}} = \frac{\hat{p}^2}{2m} + \frac{1}{2} m\omega_{\mathrm{m}}^2 \hat{x}^2. \tag{3.1}$$

The quantities m and ω_{m} represent the effective mass of the oscillator and the frequency of its oscillation, respectively. The first of the Hamiltonian terms describes the kinetic energy of the mirror. The second term corresponds to the potential energy due to the restoring force behind the oscillation, whose nature could be elastic (spring), gravitational (pendulum) or, as we will see in Chap. 3.3, even optical.

Position and momentum are conjugate observables, and as such the corresponding operators are subject to a non-zero commutation relation:

$$\left[\hat{x}, \hat{p}\right] = i\hbar. \tag{3.2}$$

This can be used to expand Heisenberg's equations of motion (see Appendix A.2):

$$\dot{\hat{x}}(t) = \hat{p}(t)/m, \tag{3.3}$$
$$\dot{\hat{p}}(t) = -m\omega_{\mathrm{m}}^2\hat{x}(t). \tag{3.4}$$

Even if we are considering the case of a harmonic oscillator, it is clear from the dynamics that the limit for a free mass can be immediately recovered by taking $\omega_{\mathrm{m}} \to 0$.

New variables for the system offer a deeper insight on the nature of the quantum harmonic oscillator. We can define the two conjugate observables

$$\hat{b} := \frac{1}{\sqrt{2\hbar m\omega_{\mathrm{m}}}}\left(m\omega_{\mathrm{m}}\hat{x} + i\hat{p}\right), \tag{3.5}$$
$$\hat{b}^\dagger := \frac{1}{\sqrt{2\hbar m\omega_{\mathrm{m}}}}\left(m\omega_{\mathrm{m}}\hat{x} - i\hat{p}\right). \tag{3.6}$$

These quantities are called respectively the lowering and raising operators, or alternatively the ladder operators, for the quantum harmonic oscillator. They act on the eigenstates of the Hamiltonian to lower or raise the energy of the system, making the state jump to the next energy level available (Appendix B offers more details on the topic). From their definition it can be seen that they are not Hermitian, and using the canonical commutation relation of $\hat{x}$ and $\hat{p}$ (Eq. 3.2) we know that

$$\left[\hat{b}, \hat{b}^\dagger\right] = 1. \tag{3.7}$$

An alternative interpretation of $\hat{b}$ and $\hat{b}^\dagger$ considers them as the annihilation and creation operators for the quantum of mechanical oscillation, a quasi-particle known as *phonon*. In this regard, the operator $\hat{b}^\dagger\hat{b}$ describes the number of phonons of the system, and we can rewrite the Hamiltonian as

$$\hat{\mathcal{H}}_{\mathrm{M}} = \hbar\omega_{\mathrm{m}}\left(\hat{b}^\dagger\hat{b} + \frac{1}{2}\right). \tag{3.8}$$

The ground state of the system has a fundamental energy of $\hbar\omega_{\mathrm{m}}/2$, and each phonon adds a quantum of $\hbar\omega_{\mathrm{m}}$ to the total energy.

3.1.2 Optical Hamiltonian

Although the cavity equations have already been introduced in Chap. 2.4, their reformulation in terms of quantum operators requires a formal treatment of the dissipation terms due to the inescapable coupling with the environment [56]. In view of this, we can identify three terms to describe the Hamiltonian concerned with the optics side of the system: one for the cavity, one for the external bath, and one for the interaction between the two:

$$\hat{\mathcal{H}}_{\mathrm{O}} = \hat{\mathcal{H}}_{\mathrm{cav}} + \hat{\mathcal{H}}_{\mathrm{ext}} + \hat{\mathcal{H}}_{\mathrm{int}}. \tag{3.9}$$

Instead of treating the optical field as a sum of harmonic oscillators, we can assume a single-mode input and reduce the analysis to a single frequency of the cavity, ω_{c}. The cavity resonance is taken to be the multiple of the free spectral range nearest to the optical frequency of the impinging field, ω_{o}, with the difference between the two corresponding to the cavity detuning, $\Delta_0 \equiv \omega_{\mathrm{o}} - \omega_{\mathrm{c}}$. The cavity's Hamiltonian in terms of the field annihilation and creation operators $\hat{a}$ and $\hat{a}^\dagger$ is, therefore,

$$\hat{\mathcal{H}}_{\mathrm{cav}} := \hbar\omega_{\mathrm{c}} \left(\hat{a}^\dagger \hat{a} + \frac{1}{2} \right). \tag{3.10}$$

The external bath can be modelled as a reservoir of infinite modes denoted by the bosonic annihilation and creation operators, $\hat{\epsilon}_\omega$ and $\hat{\epsilon}^\dagger_\omega$, subject to the commutation relation $\left[\hat{\epsilon}_\omega, \hat{\epsilon}^\dagger_{\omega'}\right] = 2\pi\delta(\omega - \omega')$:

$$\hat{\mathcal{H}}_{\mathrm{ext}} := \int_{-\infty}^{+\infty} \frac{d\omega}{2\pi}\, \hbar\omega \hat{\epsilon}^\dagger_\omega \hat{\epsilon}_\omega. \tag{3.11}$$

The interaction is taken to be linear in $\hat{\epsilon}_\omega$ and $\hat{\epsilon}^\dagger_\omega$, and identified by a coupling term ζ:

$$\hat{\mathcal{H}}_{\mathrm{int}} := \int_{-\infty}^{+\infty} \frac{d\omega}{2\pi}\, i\hbar\zeta(\omega) \left(\hat{a}^\dagger \hat{\epsilon}_\omega - \hat{a}\hat{\epsilon}^\dagger_\omega \right). \tag{3.12}$$

The two terms describe the processes by which each bath mode can extract a photon out of the cavity or bring one inside. The coupling with the environment is necessary to have an external drive, but this cannot happen without introducing dissipation. It is convenient to express the dynamics of the field relative to the optical frequency. To do so we consider the unitary transformation $\hat{U}(t) = e^{-i\omega_\mathrm{o}\hat{a}^\dagger\hat{a}t}$ (see Appendix A.1), moving the Hamiltonian to a frame where the field is rotating at frequency ω_o. This transformation would make the interaction term dependent on time. In order to have a time-independent Hamiltonian, the rotation needs to be counterbalanced by a transformation for each bath mode, $\hat{U}_\omega(t) = e^{-i\omega_\mathrm{o}\hat{\epsilon}_\omega^\dagger\hat{\epsilon}_\omega t}$. With all the variables in the rotating frame, the new Hamiltonian is

$$\hat{\mathcal{H}}_\mathrm{O} = -\hbar\Delta_0\left(\hat{a}^\dagger\hat{a} + \frac{1}{2}\right) + \int\frac{d\omega}{2\pi}\,\hbar\left(\omega - \omega_\mathrm{o}\right)\hat{\epsilon}_\omega^\dagger\hat{\epsilon}_\omega + \int\frac{d\omega}{2\pi}\,i\hbar\zeta(\omega)\left(\hat{a}^\dagger\hat{\epsilon}_\omega - \hat{a}\hat{\epsilon}_\omega^\dagger\right). \tag{3.13}$$

The equations of motion for $\hat{a}$ and $\hat{\epsilon}$ in the Heisenberg picture are

$$\dot{\hat{a}}(t) = i\Delta_0\hat{a}(t) + \int\frac{d\omega}{2\pi}\,\zeta(\omega)\hat{\epsilon}_\omega(t), \tag{3.14}$$

$$\dot{\hat{\epsilon}}_\omega(t) = i\left(\omega_\mathrm{o} - \omega\right)\hat{\epsilon}_\omega(t) - \zeta(\omega)\hat{a}(t). \tag{3.15}$$

We can directly solve for the external bath relative to some initial time t_0,

$$\hat{\epsilon}_\omega(t) = \hat{\epsilon}_\omega(t_0)e^{i(\omega_\mathrm{o}-\omega)(t-t_0)} - \int_{t_0}^{t}dt'\,\zeta(\omega)\hat{a}(t')e^{i(\omega_\mathrm{o}-\omega)(t-t')}. \tag{3.16}$$

Under the first Markov approximation [56], according to which ζ can be assumed uniform across all modes and therefore independent of ω, we can use Eq. 3.16 together with 2.3 and 2.6 to rewrite Eq. 3.14 as

$$\dot{\hat{a}}(t) = \left(-\frac{\zeta^2}{2} + i\Delta_0\right)\hat{a}(t) + \zeta\int\frac{d\omega}{2\pi}\,\hat{\epsilon}_\omega(t_0)e^{i(\omega_\mathrm{o}-\omega)(t-t_0)}. \tag{3.17}$$

A comparison with the intra-cavity field amplitude obtained in Chap. 2.4.2 (Eq. 2.52) suggests the following identifications:

$$\zeta \;\leftrightarrow\; \sqrt{2\kappa}, \tag{3.18}$$

$$\int\frac{d\omega}{2\pi}\,\hat{\epsilon}_\omega(t_0)e^{-i\omega(t-t_0)} \;\leftrightarrow\; \hat{a}_\mathrm{in}(t)e^{-i\omega_\mathrm{o}t}. \tag{3.19}$$

The decay rate of the cavity mediates the exchange between the system and the environment, manifested in two terms: one accounting for the losses and one representing the external drive of the field. The Fourier transform of the external modes can be seen as a driving field in the time domain, in the same rotating frame as the cavity modes. In our case we take this to be the coherent field at the input of the cavity, but one could include the contribution of the vacuum or of scattering elements in the same fashion. The quantum operator of the cavity field evolves according to the equation

$$\dot{\hat{a}}(t) = (-\kappa + i\Delta_0)\,\hat{a}(t) + \sqrt{2\kappa}\hat{a}_{\mathrm{in}}(t). \tag{3.20}$$

3.1.3 Quantum Langevin equation

The advantage of the derivation above is that it does not restrict to an optical field [57], and one can immediately generalize to generic bosonic operators $\hat{\mathcal{O}}$ and $\hat{\mathcal{O}}^\dagger$ satisfying the commutation relation $\left[\hat{\mathcal{O}}, \hat{\mathcal{O}}^\dagger\right] = 1$ and whose dissipation is determined by some coefficient η. Modelling the external bath as a reservoir of infinite modes indicated by $\hat{\epsilon}$ and $\hat{\epsilon}^\dagger$, as before, we can then distinguish the operator $\hat{\mathcal{D}}(t) := \int \frac{d\omega}{2\pi}\ \hat{\epsilon}_\omega e^{-i\omega t}$ as the driving element for $\hat{\mathcal{O}}$. In the previous section this was taken to be the input of the cavity, but it could also be a thermal bath or any other operator that could act as a driving factor. In optomechanics, the most common use for $\hat{\mathcal{D}}$ is as an operator describing the Brownian noise that couples the mechanical oscillator to a thermal bath of phonons. The coupling with the external bath is mediated by the dissipation mechanisms. Instead of considering the Hamiltonians for the external bath and the coupling, one can employ a variant of the Heisenberg's equation of motion (Eq. 45) to directly include the conventional decay term $-\eta\hat{\mathcal{O}}(t)$ and the additional drive term $\sqrt{2\eta}\hat{\mathcal{D}}(t)$. This variant, known as the *quantum Langevin equation*, takes the general form

$$\dot{\hat{\mathcal{O}}}(t) = \frac{i}{\hbar}\left[\hat{\mathcal{H}}_{\mathrm{S}}, \hat{\mathcal{O}}(t)\right] - \eta\hat{\mathcal{O}}(t) + \sqrt{2\eta}\hat{\mathcal{D}}(t), \tag{3.21}$$

where it should be remembered that here $\hat{\mathcal{H}}_{\mathrm{S}}$ is the Hamiltonian of the system only, and the interaction with the bath is introduced directly into the equation of motion.

3.1.4 Optomechanical Hamiltonian

An optomechanical system considers an optical cavity whose length depends on the state of the mechanics. The typical implementation consists of a Fabry–Pérot cavity where one of the end mirrors is free to oscillate, but it is possible to have many different variants based on the same principle. For example, in whispering gallery mode resonators the variation in length can be obtained because of the mechanical oscillations around the perimeter, where the optical modes propagate. Even though it will be convenient to work around the assumption of linear optical cavity with an oscillating mirror, any specific assumptions about the system will be limited to keep the following derivation as general as possible.

The complete picture of optomechanics is obtained by considering the independent optical and mechanical sub-systems and introducing the interaction between the two, arising from the dependence of the cavity resonance on the position of the oscillating mirror. Defining

$$G_0 := -\left.\frac{\partial \omega_{\mathrm{c}}(x)}{\partial x}\right|_{x=0}, \tag{3.22}$$

we can expand the resonant frequency of the cavity for small displacements:

$$\omega_{\mathrm{c}}(x) \simeq \omega_{\mathrm{c}}(0) - G_0 \hat{x}. \tag{3.23}$$

For simplicity, from now on we will refer to the zero-displacement cavity frequency $\omega_{\mathrm{c}}(0)$ simply as ω_{c}. The quantity G_0 represents the *optomechanical coupling strength.* For a Fabry–Pérot cavity, where the resonant frequency is inversely proportional to the distance between the two mirrors, the coupling strength is $G_0 = +\omega_{\mathrm{c}}/L_0 = 2\omega_{\mathrm{FSR}}/\lambda$. For the sake of generality, however, a specific expression for the coupling will not be used unless strictly necessary. Moreover, the following discussion is abstract enough that it can be extended beyond the simple processes due to radiation pressure force and be applied to alternative sources of coupling between the oscillator and the optical field. An example is given by photothermal effects, where the thermal absorption of light can induce a reaction in the mechanical system that could be analogous or opposite to those of radiation pressure force, depending on the nature of the response [58]. Therefore, G_0 could adopt either positive or negative values, depending on whether an increase of optical power results in shortening or lengthening of the cavity.

The optomechanical Hamiltonian is a combination of the Hamiltonians of the two sub-systems, $\hat{\mathcal{H}}_{\mathrm{O}}$ and $\hat{\mathcal{H}}_{\mathrm{M}}$, plus one additional term describing the interaction:

$$\hat{\mathcal{H}}_{\mathrm{OM}} = \hat{\mathcal{H}}_{\mathrm{O}} + \hat{\mathcal{H}}_{\mathrm{M}} + \hat{\mathcal{H}}_{\mathrm{int}}. \tag{3.24}$$

The two sub-systems are taken with their own independent external drives/baths, coupled to the main variables through the damping rates κ for the optics and γ_{m} for the mechanics. For simplicity the corresponding terms will be omitted from the Hamiltonian and will be introduced into the equations of motion by using the quantum

Langevin equations. Following from Eq. 3.23, the interaction term takes the form

$$\hat{\mathcal{H}}_{\text{int}} = -\hbar G_0 \left(\hat{a}^\dagger \hat{a} + \frac{1}{2} \right) \hat{x}, \tag{3.25}$$

from which we can identify the radiation pressure force acting on the oscillator,

$$\hat{F}_{\text{rp}} := \hbar G_0 \left(\hat{a}^\dagger \hat{a} + \frac{1}{2} \right), \tag{3.26}$$

and see that $\hat{\mathcal{H}}_{\text{int}} = -\hat{F}_{\text{rp}}\hat{x}$. Despite its simple form, the interaction Hamiltonian holds all the information on the reciprocal coupling between the optical field and the mechanical oscillator, and it will be instructive to see how it can be manipulated to address different aspects of the optomechanical interaction.

Considering the field operators in the same rotating frame as the driving field, the equations of motion obtained from $\hat{\mathcal{H}}_{\text{OM}}$ are

$$\dot{\hat{a}}(t) = \left[-\kappa + i \left(\Delta_0 + G_0 \hat{x}(t) \right) \right] \hat{a}(t) + \sqrt{2\kappa}\hat{a}_{\text{in}}(t), \tag{3.27}$$

$$\dot{\hat{x}}(t) = \hat{p}(t)/m, \tag{3.28}$$

$$\dot{\hat{p}}(t) = -m\omega_{\text{m}}^2 \hat{x}(t) - \gamma_{\text{m}} \hat{p}(t) + \hat{F}_{\text{rp}}(t) + \hat{F}_{\text{th}}(t). \tag{3.29}$$

These equations include the drive and decay terms from the quantum Langevin equation. For the cavity field, the coupling to the environment is once more represented by the input field $\hat{a}_{\text{in}}$, with expectation value $\langle \hat{a}_{\text{in}}(t) \rangle = \alpha_{\text{in}}(t)$. The mechanics are driven by a Brownian force $\hat{F}_{\text{th}}$, deriving from thermal fluctuations and with mean value $\langle \hat{F}_{\text{th}} \rangle = 0$. At thermal equilibrium at temperature T, this force has spectral density [57]

$$S_F^{(\text{th})}(\omega) = m\gamma_{\text{m}} \hbar\omega \coth\left(\frac{\hbar\omega}{2k_{\text{B}}T} \right). \tag{3.30}$$

Considering the phonon thermal occupation number $n_{\text{th}}(\omega) = 1/\left(e^{\hbar\omega/k_{\text{B}}T} - 1 \right)$, we find that $S_F^{(\text{th})}(\omega) = m\gamma_{\text{m}}\hbar\omega \left(2n_{\text{th}}(\omega) + 1 \right)$ and can see that the magnitude of the Brownian motion is proportional to the number of phonons. Also, in the regime of high temperature one can recover the limit $S_F^{(\text{th})}(\omega) \to 2m\gamma_{\text{m}} k_{\text{B}} T$, corresponding to white thermal noise.

In Eq. 3.27 the interaction is expressed as a correction to the phase term of the cavity field dependent on the position of the mirror and proportional to the optomechanical coupling strength. The mirror motion is also subject to back action from the light, manifested through the radiation pressure force term in Eq. 3.29 that affects the momentum rate together with the thermal noise and the regular restoring force. The cross-coupling is still evident in the steady-state solutions of the expectation values of the operators:

$$\alpha_{\mathrm{s}} := \langle \hat{a} \rangle|_{\partial_t \to 0} = \frac{\sqrt{2\kappa}\alpha_{\mathrm{in}}}{\kappa - i\left(\Delta_0 + G_0 x_{\mathrm{s}}\right)}, \tag{3.31}$$

$$x_{\mathrm{s}} := \langle \hat{x} \rangle|_{\partial_t \to 0} = \frac{F_{\mathrm{rp}}}{m\omega_{\mathrm{m}}^2}, \tag{3.32}$$

$$p_{\mathrm{s}} := \langle \hat{p} \rangle|_{\partial_t \to 0} = 0. \tag{3.33}$$

When the cavity is resonating, the mean cavity field α_{s} produces a mean radiation pressure force $F_{\mathrm{rp}} := \langle \hat{F}_{\mathrm{rp}} \rangle$ that displaces the mirror by a constant offset x_{s}. The displacement affects the resonance condition of the cavity on account of the position-dependent frequency shift, which is now also constant. It would seem like the argument is circular: the position of the mirror depends on how much light resonates in the cavity, and the resonance condition depends on the position of the mirror. This is the principle behind optomechanical bistability, which should be seen at this stage as a positive feedback loop under specific parameter regimes, which will be analysed in detail in Chap. 3.2. The optical spring effect is based on a similar principle that originates from the fluctuations of the mirror around its equilibrium point rather than from the constant displacement of the steady-state solution, which is always positive in sign. In Chap. 3.3 we will see how to use the bigger parameter space to achieve positive (unstable) or negative (stable) feedback.

Considering coherent states for the optical fields, we can separate their quantum properties from their mean values, which are simply considered as classical displacements:

$$\hat{a} \to \alpha_{\mathrm{s}} + \delta\hat{a}, \tag{3.34}$$

$$\hat{a}_{\mathrm{in}} \to \alpha_{\mathrm{in}} + \delta\hat{a}_{\mathrm{in}}. \tag{3.35}$$

Because the displacement terms are classical, the fluctuation operators inherit the non-commutativity of the original variables and satisfy the same commutation relations, so that $\left[\delta\hat{a}, \delta\hat{a}^\dagger\right] = 1$. The phase of the complex field amplitudes α_{s} and α_{in} is related by Eq. 3.31, but as long as this condition is preserved it can be set arbitrarily. While we could assume the cavity field amplitude to be real ($\alpha_{\mathrm{s}} = \alpha_{\mathrm{s}}^*$) and let the input field be complex, or vice versa, for the sake of generality we will treat both as complex quantities while keeping in mind this possibility for later application. In the linearizing approximation, the interaction Hamiltonian can be separated into three parts:

$$\begin{aligned}\hat{\mathcal{H}}_{\mathrm{int}} &= -\hbar G_0 \left(|\alpha_{\mathrm{s}}|^2 + \frac{1}{2} \right) \hat{x} - \hbar G_0 \left(\alpha_{\mathrm{s}}^* \delta\hat{a} + \alpha_{\mathrm{s}} \delta\hat{a}^\dagger \right) \hat{x} - \hbar G_0 \left(\delta\hat{a}^\dagger \delta\hat{a} \right) \hat{x} \\ &= \hat{\mathcal{H}}_{\mathrm{int}}^{(\mathrm{rp})} + \hat{\mathcal{H}}_{\mathrm{int}}^{(\mathrm{L})} + \hat{\mathcal{H}}_{\mathrm{int}}^{(\mathrm{NL})}. \end{aligned} \tag{3.36}$$

The first term, $\hat{\mathcal{H}}_{\mathrm{int}}^{(\mathrm{rp})}$, simply describes the effect of the constant radiation pressure force F_{rp}. The second term, $\hat{\mathcal{H}}_{\mathrm{int}}^{(\mathrm{L})}$, is linear in the field fluctuations and proportional to the cavity field amplitude. The last term, $\hat{\mathcal{H}}_{\mathrm{int}}^{(\mathrm{NL})}$, maintains the original non-linearity of the interaction, which is now of second order in the fluctuations. With the amplification provided by the field amplitude α_{s}, the linear interaction term, also called the many-photon interaction, has a much bigger effect on the dynamics than the residual non-linear interaction, which is usually neglected. The many-photon coupling constant,

$$G_\alpha := G_0 \alpha_{\mathrm{s}}, \tag{3.37}$$

is then acting as the effective strength of the interaction, and can be intensified simply by increasing the number of photons in the cavity. Ignoring the non-linear interaction, we can see that the radiation pressure force transforms as

$$\hat{F}_{\mathrm{rp}} \to F_{\mathrm{rp}} + \delta\hat{F}_{\mathrm{rp}} := \hbar G_0 \left(|\alpha_{\mathrm{s}}|^2 + \frac{1}{2} \right) + \hbar \left(G_\alpha^* \delta\hat{a} + G_\alpha \delta\hat{a}^\dagger \right). \tag{3.38}$$

The fluctuation approach can also be extended to the variables for the mechanics. We can treat the steady-state value of the position as no more than a constant offset and separate it from the time-dependent part of $\hat{x}$. Thus, we define the transformations

$$\hat{x} \to x_{\mathrm{s}} + \delta\hat{x}, \tag{3.39}$$

$$\hat{p} \to \delta\hat{p}, \tag{3.40}$$

$$\hat{F}_{\mathrm{th}} \to \delta\hat{F}_{\mathrm{th}}. \tag{3.41}$$

A fixed value of x_{s} also allows the use of an effective initial detuning

$$\Delta := \Delta_0 + G_0 x_{\mathrm{s}} \tag{3.42}$$

instead of the original detuning Δ_0. When all degrees of freedom are expressed in terms of fluctuations, the equations of motion become fully linear:

$$\delta\dot{\hat{a}}(t) = (-\kappa + i\Delta)\,\delta\hat{a}(t) + iG_\alpha \delta\hat{x}(t) + \sqrt{2\kappa}\delta\hat{a}_{\mathrm{in}}(t), \tag{3.43}$$

$$\delta\dot{\hat{x}}(t) = \delta\hat{p}(t)/m, \tag{3.44}$$

$$\delta\dot{\hat{p}}(t) = -m\omega_{\mathrm{m}}^2\delta\hat{x}(t) - \gamma_{\mathrm{m}}\delta\hat{p}(t) + \delta\hat{F}_{\mathrm{rp}}(t) + \delta\hat{F}_{\mathrm{th}}(t). \tag{3.45}$$

To draw a more symmetric picture of optomechanics, we can express the dynamics of the mechanical system in terms of the phononic annihilation and creation operators $\hat{b}$ and $\hat{b}^\dagger$. We directly consider their fluctuation terms $\delta\hat{b}$ and $\delta\hat{b}^\dagger$, which are related to the fluctuations of the position and momentum operators in an analogous way:

$$\delta\hat{x} = \sqrt{\frac{\hbar}{2m\omega_{\mathrm{m}}}}\left(\delta\hat{b} + \delta\hat{b}^\dagger\right), \tag{3.46}$$

$$\delta\hat{p} = -i\sqrt{\frac{\hbar m\omega_{\mathrm{m}}}{2}}\left(\delta\hat{b} - \delta\hat{b}^\dagger\right). \tag{3.47}$$

As for the original position operator $\hat{x}$, the normalization coefficient in front of $\delta\hat{x}$ is the amplitude of the zero-point fluctuations, $x_{\mathrm{ZPF}} = \sqrt{\hbar/(2m\omega_{\mathrm{m}})}$, representing the standard deviation of the position of an oscillator at the ground state (see Appendix B for more details). The zero-point fluctuations can be used to scale the optomechanical coupling strength so that it has the dimensions of a frequency:

$$g_0 := G_0 x_{\mathrm{ZPF}}, \tag{3.48}$$

$$g_\alpha := g_0\alpha_{\mathrm{s}}. \tag{3.49}$$

Ignoring all constant terms due to vacuum fluctuations and steady-state offsets, neglecting the higher-order terms in the fluctuations, absorbing the appropriate factors into the quantum Langevin equations, and choosing the phase of the input field so that α_{s} is real, the Hamiltonian in the rotating frame reads

$$\hat{\mathcal{H}}_{\mathrm{OM}} \simeq -\hbar\Delta\delta\hat{a}^\dagger\delta\hat{a} + \hbar\omega_{\mathrm{m}}\delta\hat{b}^\dagger\delta\hat{b} - \hbar g_\alpha\left(\delta\hat{a} + \delta\hat{a}^\dagger\right)\left(\delta\hat{b} + \delta\hat{b}^\dagger\right). \tag{3.50}$$

The optical and mechanical degrees of freedom are now perfectly counterbalanced in the interaction, as outlined schematically in Fig. 3.1. Each of the four terms obtained by expanding the product represents a different process which involves the creation or the annihilation of a photon or a phonon. From the physical point of view, the oscillation of the mirror modulates the phase of the cavity field at the mechanical frequency,

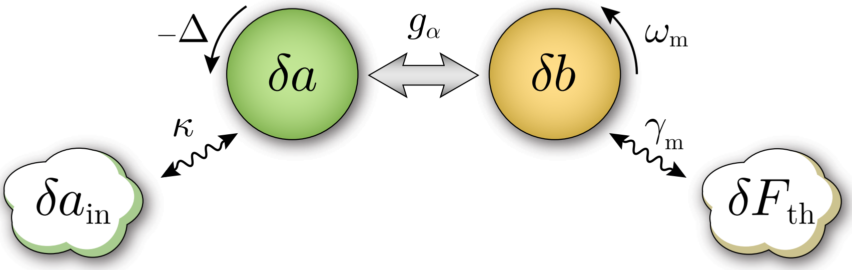

Figure 3.1: Schematic of the generic optomechanical system. The optical mode $\delta\hat{a}$, rotating at frequency $-\Delta$ in the chosen reference frame, and the mechanical mode $\delta\hat{b}$, rotating at frequency ω_m, are coupled by the normalized optomechanical coupling strength g_α. The cavity field is also coupled to the input driving field $\delta\hat{a}_\mathrm{in}$ through the cavity's optical damping rate κ. The mechanical oscillator is subject to Brownian forces $\delta\hat{F}_\mathrm{th}$ originating from the external thermal bath, and its response is mediated by the mechanical damping rate γ_m.

inducing two sidebands on the carrier frequency which interact with the motion by exchanging the energy between photons and phonons. Using terminology borrowed from Raman scattering, these are often referred to as Stokes ($\delta\hat{a}$) or anti-Stokes ($\delta\hat{a}^\dagger$) sidebands. Depending on the value of the detuning, the cavity resonance could enhance one sideband more than the other. Correspondingly, one pair of (conjugate) processes of creation/annihilation prevails over the other. This effect, illustrated in Fig. 3.2, can also be observed in the Hamiltonian by performing a rotating wave approximation in the refined rotating frame to neglect all terms oscillating at a frequency different from the resonant one. The approximation is much more effective in the *sideband-resolved regime*, $\omega_\mathrm{m} \gg \kappa$, where the separation between the sidebands is such that only one can resonate at the time. In terms of the interaction, then, we can distinguish three representative cases: when the detuning is equal to 0, $+\omega_\mathrm{m}$ or $-\omega_\mathrm{m}$.

- **On-resonance regime: $\boldsymbol{\Delta = 0}$.**

  When the input field is on resonance with the cavity, the interaction has the form of a *metrology Hamiltonian*:

  $$\hat{\mathcal{H}}_\mathrm{int} \simeq -\hbar G_\alpha \left(\delta\hat{a} + \delta\hat{a}^\dagger\right) \delta\hat{x}. \tag{3.51}$$

  From the equations of motion obtained from this Hamiltonian it can be seen that the evolution of the optical phase quadrature, $-i\left(\delta\hat{a} - \delta\hat{a}^\dagger\right)$, is directly proportional to the displacement of the mirror, $\delta\hat{x}$. Position metrology can then be performed using homodyne detection [59].

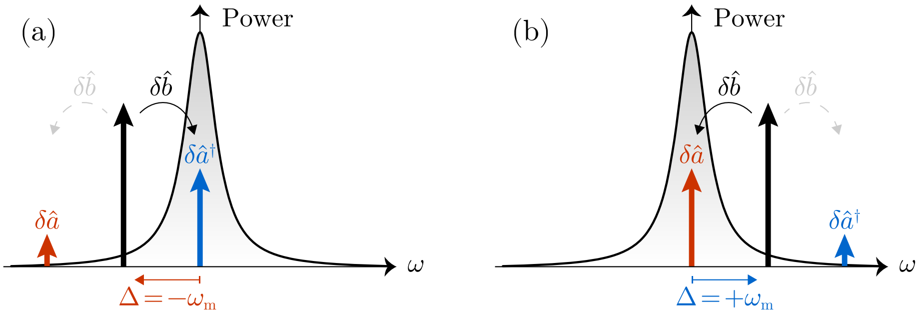

Figure 3.2: Diagram of the cavity response in the sideband representation of the optomechanical dynamics, in different detuning regimes. The black arrows correspond to the input field, while the Stokes and anti-Stokes sidebands are indicated by the red and blue arrows respectively. For simplicity, only the processes corresponding to the destruction of a phonon ($\delta\hat{b}$) are shown. **(a)** Red-detuned input field, with enhanced anti-Stokes processes. The destruction of a phonon is more likely to create a higher-energy photon ($\delta\hat{a}^\dagger$) than a lower-energy one. **(b)** Blue-detuned input field, with enhanced Stokes processes. The predominant event associated with the destruction of a phonon is the creation of a lower-energy photon ($\delta\hat{a}$).

- **Red-detuned regime:** $\boldsymbol{\Delta = -\omega_\mathrm{m}}$.

  When the input field has a negative detuning relative to the cavity resonance, the dominant terms of the interaction are those corresponding to anti-Stokes processes (Fig. 3.2a):

  $$\hat{\mathcal{H}}_\mathrm{int} \simeq -\hbar g_\alpha \left(\delta\hat{a}\,\delta\hat{b}^\dagger + \delta\hat{a}^\dagger\delta\hat{b}\right). \tag{3.52}$$

  The two conjugate terms describe events where the energy of the optical field becomes lower if a phonon is created, or higher if a phonon is annihilated. This is known as the *beam-splitter Hamiltonian*, and can be used to achieve state-swapping between the field and the mechanical oscillator [60], or even between different systems [61, 62]. In this detuning regime it is also possible to perform *sideband cooling* of the mechanical motion, a process where energy is subtracted from the oscillator and transferred to the light by the creation of higher-energy photons. This passive cooling method can prove extremely effective, and it has been used to reach the quantum ground state of the oscillations [7, 63].

- **Blue-detuned regime:** $\boldsymbol{\Delta = +\omega_\mathrm{m}}$.

  For positive detunings, the Stokes processes prevail in the interaction (Fig. 3.2b):

  $$\hat{\mathcal{H}}_\mathrm{int} \simeq -\hbar g_\alpha \left(\delta\hat{a}\,\delta\hat{b} + \delta\hat{a}^\dagger\delta\hat{b}^\dagger\right). \tag{3.53}$$

Now, the energy of the optical field becomes higher when a phonon is created and lower when a phonon is destroyed. Energy is still conserved, thanks to the fact that in the rotating frame the energy of a photon, $-\hbar\Delta$, is negative in this regime. This is the *parametric Hamiltonian*, resembling an optical parametric oscillator (OPO) generating two-mode optical squeezing [64], and it shows that it is possible to use an optomechanical system to correlate the noise of the optical field on different quadratures and generate *ponderomotive squeezing* [65, 66]. This property has recently been demonstrated experimentally [8,9] and will be discussed in more detail in Chap. 12. As is often implied by the possibility of squeezing, another potential application of this Hamiltonian could be in the generation of entanglement between the mechanical motion and the optical mode [67, 68]. This has already been achieved experimentally with techniques using pulsed light [69], although parametric instabilities of the blue-detuned regime (see Chap. 3.3) might impose limits to the extent of entanglement and hinder its realization with continuous waves.

3.2 Bistability

The relation between the steady-state position of the moving mirror, x_s, and the intracavity field, α_s, has a direct consequence: the radiation pressure force from the intracavity field displaces the mirror and causes the resonance of the cavity to be shifted. If the power is high enough, the shift can be more than one linewidth away relative to the original cavity resonance, and the response of the system can result in bistable behaviour.

The closed-loop relation between x_s on α_s can be explicitly revealed by expansion of the radiation pressure force term in Eq. 3.29:

$$x_\mathrm{s} = \frac{\hbar G_0}{m\omega_\mathrm{m}^2}\left(|\alpha_\mathrm{s}|^2 + \frac{1}{2}\right). \tag{3.54}$$

We can incorporate the cavity field steady-state solution of Eq. 3.31 to obtain a cubic relation for x_s (or equivalently $|\alpha_\mathrm{s}|^2$):

$$x_\mathrm{s}\left[\kappa^2 + (\Delta_0 + G_0 x_\mathrm{s})^2\right] = \frac{\hbar G_0}{m\omega_\mathrm{m}^2} 2\kappa\left(|\alpha_\mathrm{in}|^2 + \frac{1}{2}\right). \tag{3.55}$$

What this expression shows is that, under specific circumstances, the cavity can have three possible configurations at the same time. Specifically, the cubic equation can have

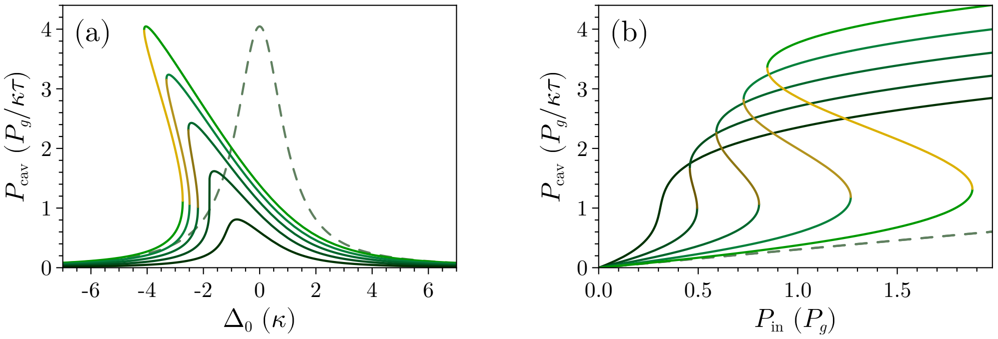

Figure 3.3: Effects of optomechanical bistability on the cavity. All the powers are normalized in terms of $P_g := \hbar\omega_{\rm c}\left|\alpha_{\rm s}\right|^2\Big|_{G_0 x_{\rm s}=\kappa} = \omega_{\rm c}\kappa^2 m\omega_{\rm m}^2/g^2$. The parameters of interest have the following values: $m = 1\,\text{kg}$, $\omega_{\rm m} = 2\pi\times 10\,\text{Hz}$, $\omega_{\rm c} \approx 2\pi\times 280\,\text{THz}$, $\mathcal{F} = 1000$. **(a)** Intra-cavity power as a function of detuning. The traces, from darker to lighter, correspond to the power $P_{\rm cav} = \hbar\omega_{\rm c}\left|\alpha_{\rm s}\right|^2$ at input power $P_{\rm in}$ between 0.2 and 1.0 P_g, at intervals of $0.2\,P_g$. **(b)** Intra-cavity power as a function of input power. Different traces now correspond to an increasingly more negative detuning Δ_0, ranging from $-1.5\,\kappa$ (darker) to $-3.5\,\kappa$ (lighter) at intervals of $0.5\,\kappa$. In both plots, in the presence of bistability, the unstable solution is represented in yellow. The dashed traces show what intra-cavity power would be obtained in the absence of optomechanical interaction at an input power $P_{\rm in} = P_g$ (a) or at a detuning $\Delta_0 = -3.5\,\kappa$ (b).

exactly three solutions if it is equipped with two stationary points, i.e. if its derivative has two distinct roots, a situation that occurs when $|\Delta_0| > \sqrt{3}\kappa$. The boundaries of the multi-stable region are thus determined by the mirror coordinates

$$x_\pm = \frac{\Delta_0}{3G_0}\left(-2 \pm \sqrt{1 - \frac{3\kappa^2}{\Delta_0^2}}\right). \tag{3.56}$$

The typical response of a cavity showing bistable behaviour is demonstrated in Fig. 3.3a. Optomechanical back-action shifts the resonance proportionally to the power within the cavity, resulting in a deformed Lorentzian response. When the input power is high enough the deformation tilts the top of the peak beyond its base, leading to three possible cavity configurations for a specific detuning range. Of these, only two are stable; the other solution will dynamically collapse the system to one or the other configuration. The overlap of the two stable solutions leads to hysteresis, meaning that the intra-cavity power experienced by the system depends on whether the overlapping region is adiabatically reached from more positive or more negative detunings. In general, bistability can only be observed at negative detunings. The maximum intra-cavity power occurs when $\Delta_0 = -\frac{\hbar G_0^2}{m\omega_{\rm m}^2}\frac{2|\alpha_{\rm in}|^2}{\kappa}$, a condition obtained after enforcing $\Delta_0 = -G_0 x_{\rm s}$ (or, in terms of the effective detuning, $\Delta = 0$) in Eq. 3.55. Hysteresis can also be witnessed if the intra-cavity power is treated as a function of input power rather than detuning, as in Fig. 3.3b. When the detuning is fixed at a value such that $|\Delta_0| > \sqrt{3}\kappa$ a region emerges where multiple stable solutions are possible, and of these only the two corresponding to increasing cavity power for increasing input power are stable.

The bistability described here is analogous to similar phenomena arising from cavity non-linearities of different origin, and a comparable hysteresis can be obtained in an optical system coupled to a single atom [70, 71] or a Bose-Einstein condensate [72]. In optomechanics, bistability has been reported since early experiments [73, 74], and has recently become more common to observe with the emergence of cavities with higher finesses.

3.3 Optical spring

The response of the mechanical system is directly affected by the interaction with the optical field [6]. Under appropriate conditions radiation pressure force displays restoring properties that operate jointly with the original elastic restoring force of the mechanical oscillator, providing a versatile technique that can be used to explore very diverse parameter regimes.

3.3.1 Semiclassical model

For an intuitive, preliminary approach [75] we consider the mean radiation pressure force from Eq. 3.26 in the semiclassical regime, where $\langle \hat{a}^\dagger \hat{a} \rangle \to |\alpha_{\mathrm{s}}|^2$:

$$F_{\mathrm{rp}} \simeq \hbar G_0 |\alpha_{\mathrm{s}}|^2 = \frac{2\hbar\omega_{\mathrm{c}} |\alpha_{\mathrm{s}}|^2}{c\tau}. \tag{3.57}$$

Between the first and second step we used the fact that for a Fabry–Pérot cavity the optomechanical coupling is $G_0 = \omega_{\mathrm{c}}/L_0$, and recalled the relationship between the length L_0 and the cavity lifetime τ from Eq. 2.44. Remembering that $\alpha_{\mathrm{s}} = \sqrt{\tau}\alpha_{\mathrm{cav}}$ and that $P_{\mathrm{cav}} = \hbar\omega_{\mathrm{c}} |\alpha_{\mathrm{cav}}|^2$, we see that the force is proportional to the intra-cavity power,

$$F_{\mathrm{rp}} = \frac{2P_{\mathrm{cav}}}{c}, \tag{3.58}$$

and as a consequence its dependence on the position of the mirror is Lorentzian:

$$F_{\mathrm{rp}}(x) = \frac{4P_{\mathrm{in}}}{c\kappa\tau} \frac{\kappa^2}{\kappa^2 + (\Delta_0 + G_0 x)^2}. \tag{3.59}$$

Combining this with the elastic force acting on the oscillator, $F_{\mathrm{el}}(x) = -m\omega_{\mathrm{m}}^2 x$, one can then derive an effective mechanical potential

$$V_{\mathrm{eff}}(x) = -\int dx\, \left(F_{\mathrm{el}}(x) + F_{\mathrm{rp}}(x)\right) = m\omega_{\mathrm{m}}^2 x^2 - \frac{4P_{\mathrm{in}}}{c\tau G_0} \arctan\left(\frac{\Delta_0 + G_0 x}{\kappa}\right). \tag{3.60}$$

The effective potential deviates from the typical parabola expected for a self-contained mechanical oscillator. The perturbation introduced by the radiation pressure force can lead to a secondary minimum, which is simply another manifestation of optomechanical bistability. An implication of the reshaping of the potential is that the spring constant of the system, determined by the concavity of V_{eff}, is also altered from its original value $m\omega_{\mathrm{m}}^2$. The correction term to this quantity is what is commonly referred to as the *optical spring*:

$$k_{\mathrm{os}}(x) = \frac{8G_0 P_{\mathrm{in}}}{c\tau} \frac{\kappa\,(\Delta_0 + G_0 x)}{\left[\kappa^2 + (\Delta_0 + G_0 x)^2\right]^2}. \tag{3.61}$$

As it should be expected of a property arising from the interaction of the mechanical system with the field, the optical spring is directly proportional to both the optical power and to the coupling strength. It can be either negative or positive, representing the restoring or the anti-restoring behaviour of F_{rp} depending on the detuning of the input field. The optical spring is maximum in magnitude when the slope of the Lorentzian force is maximum, i.e. when the force responds more acutely to small variations in position, and vanishes on resonance and in the far-detuning regime.

The result obtained by this simple model is already accurate enough to describe the data from experiments aiming at the characterization of the radiation pressure force [76]. However, this approach does not take into account the retardation effects existing in optical cavities due to the finite value of the speed of light.

3.3.2 Dynamical back-action

Since light needs a finite amount of time to traverse the full effective length of the optical resonator, the effects of radiation pressure force on the mirror are experienced with a delay. As a consequence, the mirror builds up a viscous-like response to the optical field, an outcome that can have extreme consequences for the stability of the system and is not accounted for in the previous model. For this reason it is necessary to utilize the full dynamical, quantum picture of the system to completely describe the impact of the optical spring [77].

We follow a derivation that regards the effective susceptibility of the mechanical system as it interacts with the optical field. We consider the linearized regime, since any higher order, non-linear response of the mechanical system can always be treated as an additional noise term. Thus, starting from the linearized equations of motion, Eq. 3.43–3.45, we look at the fluctuations of the field and of the mirror's position in the frequency domain:

$$\delta\hat{a}(\omega) = \frac{iG_\alpha}{\kappa - i(\Delta-\omega)}\delta\hat{x}(\omega) + \frac{\sqrt{2\kappa}}{\kappa - i(\Delta-\omega)}\delta\hat{a}_{\mathrm{in}}(\omega), \tag{3.62}$$

$$\delta\hat{x}(\omega) = \frac{1}{m\left(\omega_{\mathrm{m}}^2 - \omega^2 + i\gamma_{\mathrm{m}}\omega\right)}\left(\delta\hat{F}_{\mathrm{rp}}(\omega) + \delta\hat{F}_{\mathrm{th}}(\omega)\right). \tag{3.63}$$

The quantity

$$\chi_{\mathrm{m}}(\omega) := \left[m\left(\omega_{\mathrm{m}}^2 - \omega^2 + i\gamma_{\mathrm{m}}\omega\right)\right]^{-1} \tag{3.64}$$

can be recognized as the natural mechanical susceptibility, describing how the oscillator responds to the input forces applied. From the optomechanical point of view, however, the oscillator is regarded as a component of the extended system rather than as an apparatus on its own, and the effects of radiation pressure force can be included in an effective susceptibility instead of being considered as an external input. Recalling the relation between $\delta\hat{F}_{\mathrm{rp}}$ and $\delta\hat{a}$ from Eq. 3.38, the dependence of the field on position can be directly substituted in Eq. 3.63 to obtain

$$\frac{\delta\hat{x}(\omega)}{\chi_{\mathrm{m}}(\omega)} = \hbar G_\alpha^* \frac{iG_\alpha\delta\hat{x}(\omega) + \sqrt{2\kappa}\delta\hat{a}_{\mathrm{in}}(\omega)}{\kappa - i(\Delta-\omega)} + \hbar G_\alpha \frac{-iG_\alpha^*\delta\hat{x}(\omega) + \sqrt{2\kappa}\delta\hat{a}_{\mathrm{in}}^\dagger(\omega)}{\kappa + i(\Delta+\omega)} + \delta\hat{F}_{\mathrm{th}}(\omega). \tag{3.65}$$

Collecting the terms in $\delta\hat{x}$ together, we get

$$\left(\frac{1}{\chi_{\mathrm{m}}(\omega)} + \frac{1}{\chi_{\mathrm{os}}(\omega)}\right)\delta\hat{x}(\omega) = \delta\hat{F}_{\mathrm{sh}}(\omega) + \delta\hat{F}_{\mathrm{th}}(\omega), \tag{3.66}$$

where we introduced the radiation pressure force due to shot noise,

$$\delta\hat{F}_{\mathrm{sh}}(\omega) := \frac{\sqrt{2\kappa}}{\kappa - i\left(\Delta - \omega\right)}\hbar G_\alpha^* \delta\hat{a}_{\mathrm{in}}(\omega) + \frac{\sqrt{2\kappa}}{\kappa + i\left(\Delta + \omega\right)}\hbar G_\alpha \delta\hat{a}_{\mathrm{in}}^\dagger(\omega), \tag{3.67}$$

and an "optical spring" susceptibility due to the direct effect of the mean radiation pressure force on the position,

$$\chi_{\mathrm{os}}(\omega) := \left\{-i\hbar\left|G_\alpha\right|^2\left[\frac{1}{\kappa - i\left(\Delta - \omega\right)} - \frac{1}{\kappa + i\left(\Delta + \omega\right)}\right]\right\}^{-1}. \tag{3.68}$$

The optical spring is given by the inverse of $\chi_{\mathrm{os}}(\omega)$:

$$\begin{aligned} k_{\mathrm{os}}(\omega) &= -i\hbar\left|G_\alpha\right|^2\left[\frac{1}{\kappa - i\left(\Delta - \omega\right)} - \frac{1}{\kappa + i\left(\Delta + \omega\right)}\right] \\ &= \hbar\left|G_\alpha\right|^2\frac{2\Delta}{\kappa^2 + \Delta^2 - \omega^2 + 2i\kappa\omega} \\ &= \hbar\left|G_\alpha\right|^2\frac{2\Delta}{\kappa^2 + \Delta^2}\left[1 - \frac{\omega}{\kappa^2 + \Delta^2}\left(\omega - 2i\kappa\right)\right]^{-1}. \end{aligned} \tag{3.69}$$

The dependence of the optical spring on the position of the mirror is implicit in the effective detuning $\Delta = \Delta_0 + G_0 x$. A stricter resemblance to the result obtained by the previous model is achieved by carrying out an expansion of the leading coefficient, similarly to Eq. 3.57–3.59:

$$k_{\mathrm{os}}(\omega) = \frac{8G_0 P_{\mathrm{in}}}{c\tau}\frac{\kappa\Delta}{\left(\kappa^2 + \Delta^2\right)^2}\left[1 - \frac{\omega}{\kappa^2 + \Delta^2}\left(\omega - 2i\kappa\right)\right]^{-1}. \tag{3.70}$$

A direct conclusion is that the model of Eq. 3.61 is only adequate in the static limit $\omega \to 0$. The dynamical component of the optical spring turns it into a complex quantity: while the real part of the optical spring alters the mechanical eigenfrequency of the oscillator, the imaginary part acts like a viscous term that affects the damping of the system. The new effective parameters can be derived by combining the optically induced susceptibility with the original one into an effective susceptibility $\chi_{\mathrm{eff}}(\omega)$, satisfying $\chi_{\mathrm{eff}}(\omega)^{-1} = \chi_{\mathrm{m}}(\omega)^{-1} + \chi_{\mathrm{os}}(\omega)^{-1}$. Imposing an analogy with $\chi_{\mathrm{m}}(\omega)$, we request that the effective susceptibility satisfy an expression of the form $\chi_{\mathrm{eff}}(\omega) = \left[m\left(\omega_{\mathrm{eff}}^2 - \omega^2 + i\gamma_{\mathrm{eff}}\omega\right)\right]^{-1}$. This allows us to derive expressions for the effective mechanical frequency, ω_{eff}, and the effective mechanical damping, γ_{eff}, which are perturbed from the original parameters by the correction terms imparted by the optical spring, ω_{os} and γ_{os}, as follows:

$$\begin{aligned}\omega_{\mathrm{eff}}(\omega) &= \sqrt{\omega_{\mathrm{m}}^2 + \omega_{\mathrm{os}}(\omega)^2} = \sqrt{\omega_{\mathrm{m}}^2 + \frac{\mathrm{Re}(\chi_{\mathrm{os}}(\omega)^{-1})}{m}} \\ &= \sqrt{\omega_{\mathrm{m}}^2 + \frac{\hbar\,|G_\alpha|^2}{m}\left[\frac{\Delta-\omega}{\kappa^2+(\Delta-\omega)^2} + \frac{\Delta+\omega}{\kappa^2+(\Delta+\omega)^2}\right]}, \qquad (3.71) \\ \gamma_{\mathrm{eff}}(\omega) &= \gamma_{\mathrm{m}} + \gamma_{\mathrm{os}}(\omega) = \gamma_{\mathrm{m}} + \frac{\mathrm{Im}(\chi_{\mathrm{os}}(\omega)^{-1})}{m\omega} \\ &= \gamma_{\mathrm{m}} - \frac{\hbar\,|G_\alpha|^2}{m\omega}\left[\frac{\kappa}{\kappa^2+(\Delta-\omega)^2} - \frac{\kappa}{\kappa^2+(\Delta+\omega)^2}\right]. \qquad (3.72)\end{aligned}$$

Figure 3.4 shows the magnitude of the optically induced correction terms at a frequency equal to the mechanical eigenmode of the oscillator, as a function of detuning. In the unresolved sideband regime ($\omega_{\mathrm{m}} \lesssim \kappa$) the optical spring seems to follow the same trend as the derivative of the Lorentzian profile of the intra-cavity power with respect to the detuning. This is however not completely true. Comparing Eq. 3.70 to Eq. 3.61, we see that part of the functional behaviour just described is withdrawn from the optical stiffness to be embodied into the induced optical damping. This deviation from the behaviour expected from the static model is much more evident in the resolved sideband regime ($\omega_{\mathrm{m}} \gg \kappa$), as can be seen in Fig. 3.4e–f by comparing the lightest traces (corresponding to $\omega_{\mathrm{m}} = 2.5\,\kappa$) to the dashed ones, obtained using the static limit under the same parameters. In this regime the dynamics diverge considerably, and the role of the two sidebands created by the interaction becomes more crucial.

The expression for the optical spring given in Eq. 3.69 can be reformulated to give emphasis to the importance of the optomechanical sidebands. Introducing the Airy functions

$$\begin{aligned}\mathcal{A}_-(\omega) &:= [\kappa - i\,(\Delta-\omega)]^{-1} & \mathcal{A}_+(\omega) &:= [\kappa + i\,(\Delta+\omega)]^{-1} \\ &= \frac{\kappa + i\,(\Delta-\omega)}{\kappa^2+(\Delta-\omega)^2}, & &= \frac{\kappa - i\,(\Delta+\omega)}{\kappa^2+(\Delta+\omega)^2}, \qquad (3.73)\end{aligned}$$

standing for the anti-Stokes and the Stokes sidebands, respectively, and satisfying the property $(\mathcal{A}_-(\omega))^* = \mathcal{A}_+(-\omega)$, one can rewrite the full optical spring as

$$k_{\mathrm{os}}(\omega) = -i\hbar\,|G_\alpha|^2\,(\mathcal{A}_-(\omega) - \mathcal{A}_+(\omega)). \qquad (3.74)$$

The two sidebands act reciprocally: the sign of the detuning, determining which sideband resonates in the cavity, makes the optical spring display opposite behaviour, as

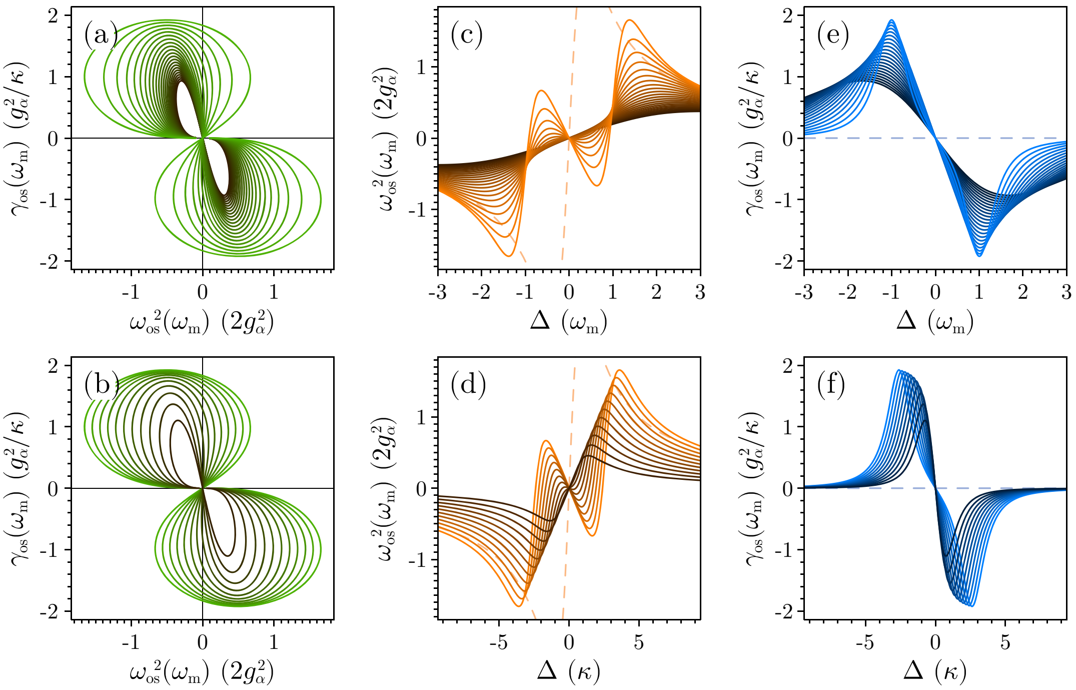

Figure 3.4: Modelling of the optical spring. The traces in the top row are calculated for a cavity linewidth κ ranging between $0.4\,\omega_{\mathrm{m}}$ (resolved sidebands regime, light traces) and $2.5\,\omega_{\mathrm{m}}$, (unresolved sidebands regime, dark traces) at intervals of $0.1\,\omega_{\mathrm{m}}$. The bottom row is instead obtained when the mechanical frequency ω_{m} is varied, from $0.4\,\kappa$ (unresolved sidebands regime, dark traces) to $2.5\,\kappa$ (resolved sidebands regime, light traces), at intervals of $0.2\,\kappa$. In all plots the frequency-dependent quantities are calculated at $\omega = \omega_{\mathrm{m}}$, with the assumption that the oscillator samples the optical field at its own resonant frequency. **(a–b)** Optical spring k_{os} in the complex plane, parametrized as a function of detuning Δ. The horizontal axis is rescaled as $\omega_{\mathrm{os}}^2 := \mathrm{Re}(k_{\mathrm{os}})/m$ to reflect the adjustment to the mechanical frequency due to the optomechanical interaction; similarly, the vertical axis is rescaled as $\gamma_{\mathrm{os}} := \mathrm{Im}(k_{\mathrm{os}})/(m\omega)$ to account for the correction term applied to the mechanical damping. **(c–d)** Squared frequency ω_{os}^2 as a function of detuning Δ. **(e–f)** Optically induced damping γ_{os} as a function of detuning Δ. In plots (c–f) the dashed traces indicate what would be obtained in the resolved sideband regime ($\omega_{\mathrm{m}} = 2.5\,\kappa$) if the contribution of dynamical back-action were ignored.

can also be seen in Fig. 3.4. Looking at detunings bigger in magnitude than the spectral frequency under consideration, the optical stiffness, $m\omega_{\mathrm{os}}^2$, is positive or negative depending on the sign of Δ. This means that the force exerted by radiation pressure force is restoring at positive detunings (blue-detuned input) and anti-restoring at negative detunings (red-detuned input). A similar argument applies to the optical damping γ_{os}, which makes the system damped at negative detunings and anti-damped at positive detunings. This fits well with the sideband picture provided by Fig. 3.2: in the blue-detuned regime the anti-damping force channels energy from the optical field into the mechanical system, driving it into *parametric amplification* [78–83], whereas in the red-detuned regime the creation of higher-frequency photons is achieved by the optical damping, removing energy from the oscillator and performing *sideband cooling* [59, 79, 84–88].

Sideband cooling can be used to steer the optical spring in a stable regime [89]. When the optomechanical system is driven by a blue-detuned beam the oscillator experiences a force that is restoring, but at the same time anti-damping. To prevent parametrically unstable oscillations, one can introduce a second, red-detuned beam to oppose the anti-damping of the blue-detuned beam. The second beam would be set with specific parameters so as not to exceedingly alter the optical stiffness induced by the original beam: a lower power, for example, and most importantly a particular detuning chosen so that the negative stiffness induced is minimal (thus, minimal anti-restoring). On top of this application, the bare cooling obtained by optical damping can prove to be extremely effective [90], and to date many mechanical systems have even reached the quantum ground state of the oscillations using this technique [7, 59, 63, 91–93]. Unfortunately the effectiveness of cooling in the unresolved sideband regime is hindered by optomechanical bistability, as the regime of negative detunings coincides precisely with the region where bistability is observed. Phenomena analogous to parametric amplification and cooling by radiation pressure force have also been obtained by photothermal coupling [94, 95], although in these cases it is the nature of the interaction itself acting as the main obstacle to the observation of quantum effects.

Trapping, cooling and many other qualities make the optical spring a fascinating tool for the manipulation of mechanical oscillators [96], and entirely new systems are emerging [89, 97–100] which rely strongly, or entirely, on the optical spring effect for the creation of a stable optical trap. Part III of this thesis, in particular, focuses on the development of a system that relies on three optical cavities to fully trap a mirror and suspend it against its own weight [14] just by the use of optical springs.

Part II

Experimental interactions between light and nanowires

The content of this Part is dedicated to the investigations performed with crystalline nanowires to explore the effects of feedback control on sensitivity. An all-optical setup is devised to detect the mechanical modes, implement feedback cooling, and explore the effects of active control and post-processing filtering techniques on the sensitivity towards force measurements in the transient regime. Chapter 4 touches on the topic of precision sensing using nanomechanical devices and closes with a detailed description of the nanowires employed. In Chapter 5 the detection methods used to monitor the mechanical modes of the nanowires are explained, both with and without the aid of an optical cavity. Chapter 6 enters into the details of the feedback, the nature of its driving mechanism and its engagement in the cancellation of thermal fluctuations for cooling of the mechanical modes. Finally, in Chapter 7 we delineate the circumstances under which the abolition of thermal noise with feedback cooling can be advantageous, showing that the nanowires benefit from feedback-enhanced sensitivity for impulsive forces. Because feedback cooling can also be simulated off-line, the findings are compared to the results obtained with virtual feedback and with optimal Kalman filtering.

The research presented here has been featured in the following publication:

- [16] Hosseini, M., Guccione, G. et al., "Multimode laser cooling and ultra-high sensitivity force sensing with nanowires", *Nature Communications* **5**, 4663 (2014).

The impulsive forces acting on the nanowires are well represented by Menoetius, son of Iapetus and brother of Prometheus: he is known in Greek mythology as the Titan of rash action.

J. Jordaens, *"La Chute des Géants"*

Chapter 4

Nanomechanical oscillators as probes

4.1 Mass sensing, atomic-force microscopy, and more

Micro- and nano-scale oscillators, thanks to their typically high quality factors [101], serve as excellent metrological platforms. The smallest mass scales are hard to access for two-dimensional oscillators [102–104], but if a small area is sufficient to achieve the necessary interaction, then the solution is simple: one-dimensional oscillators, such as cantilevers, beams, tubes, strips, and wires are inherently lightweight and hold extraordinarily interesting attributes for metrology applications. The gallery in Fig. 4.1 displays only a small selection of all the nano-mechanical devices in existence. With interest growing in several areas, and the availability of faster, cheaper, and more precise fabrication techniques, nanoscopic probes are now established for ultra-fast, high-precision sensing in a variety of applications [105].

Mass sensing is perhaps one of the most successful specializations of nano-mechanical devices. From the detection of the smallest cells, particles, and molecules [106–111] to the achievement of atomic resolution [112, 113], most of the sub-picogram mass spectrum is accessible to investigation by nano-scale probes. A similar argument extends to force sensing, with the achievement of sub-attonewton resolution [114]. The popularity of nano-cantilevers for force measurements is largely due to the advancements in atomic-force microscopy [115]. This is a technique based on the detection of light reflected from the back of a cantilever, whose extremity is equipped with an atom-wide tip that is allowed to interact with the sample surface. With the capacity of revealing the structure of the surface down to a fraction of a nanometre, it is easy to understand how the interest in this practice quickly spread across many disciplines. The widespread extent of AFM cantilevers has been assisted by many refinements, such as the use of fre-

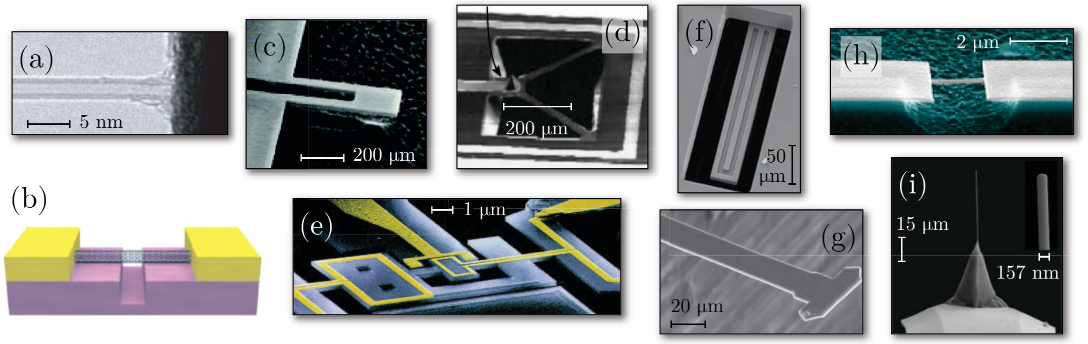

Figure 4.1: Nanomechanical devices come in a great variety of shapes, designs and applications. **(a)** The attachment of the carbon nanotubes used for mass sensing [112]. **(b)** Schematic of a similar carbon nanotube setup [113]. **(c)** Cantilever with integrated piezoresistive transducer for detection of gas particles [109]. **(d)** Accelerometer based on a nitride cantilever with a tunnelling tip [118]. **(e)** Torsional mechanical oscillator for charge sensing [120]. **(f)** Suspended microfluidic channel in a cantilever for biomass detection [107]. **(g)** Torsional cantilever used for inferring the structural flexibility of proteins [123]. **(h)** Doubly-clamped nanobeam for detection of single molecules [108]. **(i)** Nano-needle on top of an atomic-force microscopy cantilever, for viscosity [124] and visual force [125] measurements.

quency modulation [116], electromechanical feedback [117], and other forms of control for sensitivity enhancements. More sectors benefitting from the incredible resolution of nano-mechanical sensors are accelerometry [118, 119], charge sensing [120], and magnetometry [121], with tremendous implications for three-dimensional imaging thanks to the resolution of single-spin interactions.

These advancements are in high demand by disciplines other than physics. In biology, super-resolution allows monitoring of the properties of cells and proteins with unprecedented accuracy and adaptability. For example, it is now possible to weigh single cells [107], perform real-time tracking of single molecules [108], and interact with proteins by detecting their binding processes [122] and their structural flexibility within the time scale of conformational changes [123]. As the samples under investigation tend to be extremely sensitive to the environmental conditions, fast, low-power measurements such as the ones provided by nano-mechanical devices are in very high demand. Any slight improvement in resolution, especially that does not require cryogenic environments, might imply a significant breakthrough in biosensing. This is the aim of the investigations performed with crystalline nanowires presented in this thesis: can low-power optical feedback at room temperature be a practical technique for sensitivity enhancement by suppression of thermal fluctuations? We will see the answer in Chapter 7.

4.2 Crystalline nanowires

The investigations on methods to boost the force sensitivity of nano-probes discussed in this thesis involve the use of commercial crystalline nanowires[1] as nano-mechanical devices. Each nanowire is grown coaxially at the extremity of a tungsten needle, by a process that involves dipping of the silver-coated tip of the needle into a droplet of liquid gallium at room temperature. Slow retraction of the tip from the droplet allows the two metals to alloy into a long, uniform rod of Ag_2Ga crystallites [126] (cf. Fig. 4.2).

Similar nanowires have been used to quantify the surface tension, the viscosity, and other properties of fluids at the microscopic level [124], and to perform high-precision subsurface characterization of nano-structures with high dielectric constants [127]. Visual force sensing was also demonstrated by directly monitoring their buckling deformations [125]. In biology, they have been considered for the detection of edge-binding effects in proteins [122]. In most applications, however, the quality of the measurements in ordinary operating environments is compromised by the thermally induced vibrations of the nanowires. The work presented here analyses the effects of control techniques that aim to boost the sensitivity of the nanowires at room temperature conditions by physical or simulated influence on the transient dynamics of the oscillations.

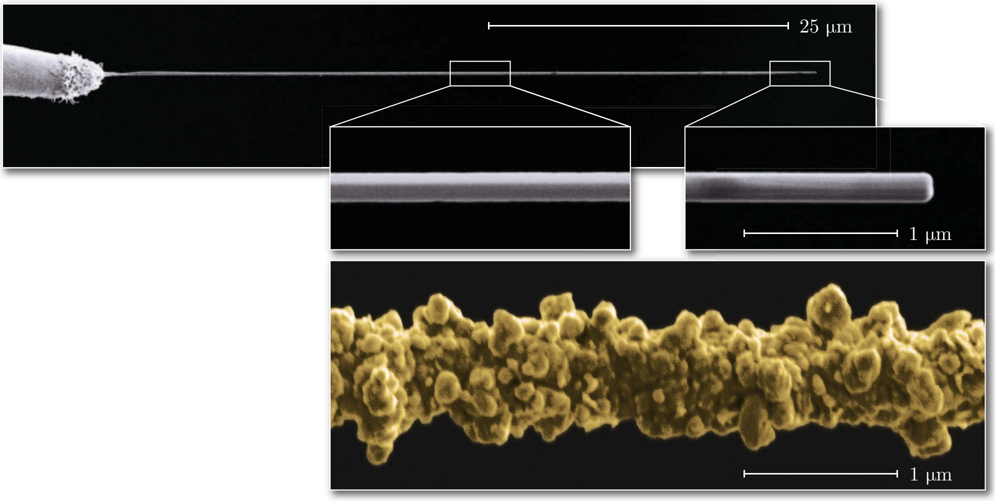

Figure 4.2: Images of a nanowire, obtained by scanning electron microscopy. The images in the insets show close-ups of the nanowire structure along the shaft and at the tip. For comparison, the detail of a gold-coated nanowire is shown on the same scale.

---

[1] NN-NCL from NaugaNeedles LLC (http://nauganeedles.com/)

4.2.1 Characteristics

The nanowires employed have a relatively wide range of specifications, summarized in Table 4.1. They range in size between 20 and 60 µm in length and between 50 and 200 nm in diameter. To push up the detection efficiency of their vibrational modes, which depends on the light scattered from their surface, a number of specimens was coated with about 50 nm of gold. Analysis of the nanowires' structure by scanning electron microscopy reveals an uneven coating with the gold collected in clusters around the crystalline cylinder, as illustrated in Fig. 4.2. Given the sub-wavelength dimensions of each nugget, however, this does not represent an impediment towards a more efficient scattering.

An estimate based on stoichiometric ratios gives a density of about 8960 kg m^{-3} for Ag_2Ga [128], projecting the mass of an uncoated nanowire to a few tens of picograms ($\approx 10^{-14}$ kg). The additional mass due to the gold coating is of a comparable magnitude, and the overall mass of a coated nanowire may end up ranging in the hundreds of picograms. As the nanowires are clamped on one extremity and free to oscillate at the other, the effective modal mass can be calculated using the Euler-Bernoully theory [129]. Almost 90 % of the total mass is accounted for by the first four modes, respectively participating by a factor of 61.31 %, 18.83 %, 6.47 %, and 3.31 %. The elastic modulus of the nanowires has been found to be on the order of 100 GPa [128].

The eigenfrequencies of the vibrational modes are calculated as

$$\omega_{\mathrm{m}} = \frac{\alpha^2}{l^2}\sqrt{\frac{YI}{\rho A}}, \tag{4.1}$$

where l is the length of the cylinder, A is the cross-sectional area, ρ is the density, Y is the elastic modulus, I is the areal moment, and α is a mode-dependent coefficient

Quantity	**Value**
Length	20–60 µm
Diameter	50–200 nm (coated: 90–500 nm)
Density	8960 kg m^{-3}
Mass	1–70 pg (coated: 4–150 pg)
Oscillation frequency	20–500 kHz (fundamental)
Stiffness	0.1–10 mN m^{-1} (fundamental)
Elastic modulus	$\approx$ 100 GPa
Damping rate	0.5–0.9 kHz (in air: $\approx$ 10 kHz)

Table 4.1: Typical characteristics of the Ag_2Ga nanowires used in the experiments.

which is respectively equal to 1.87510, 4.69409, 7.85476, 10.9955, etc., depending on the mode considered [130]. The areal moment for an object of circular cross section of radius r is $\pi r^4/4$. Ellipticity or general imperfections in the crystallization process induce, however, slight radial asymmetries in the nanowires. As a consequence, the eigenmodes of oscillation occur along two preferred directions in the plane orthogonal to the nanowire's axis, and the frequencies of modes of the same order exhibit a modest but measurable splitting. This quality, uncommon in rectangular beams and cantilevers with a single preferred direction of oscillation, can prove quite useful for mass sensing and stiffness spectroscopy [110]. The fundamental modes have frequencies typically in the 20 to 500 kHz range, depending on the aspect ratio of the nanowire. The stiffness of these oscillators is inferred to be in the range 0.1 or $1\,\mathrm{mN\,m^{-1}}$ [131].

4.2.2 Quality factor

The quality factor Q determines the capability of the system to store energy into the oscillations. It is defined as the ratio of the total energy divided by the energy lost over one cycle. Generally, the quality factor is strongly influenced by a variety of elements, such as thermoelastic and mechanical properties of the oscillator and its support, and the viscosity of the surrounding medium. For a mechanical oscillator where intrinsic mechanical damping and air viscosity are the main factors contributing to the dissipation, the quality factor Q satisfies the relation

$$Q^{-1} = Q_{\mathrm{m}}^{-1} + Q_{\mathrm{air}}^{-1}, \tag{4.2}$$

where $Q_{\mathrm{m}} := \omega_{\mathrm{m}}/\gamma_{\mathrm{m}}$ and $Q_{\mathrm{air}} := \omega_{\mathrm{m}}/\gamma_{\mathrm{air}}$ are the ratio of the oscillator's eigenfrequency and the damping rate due to the intrinsic mechanical losses or due to the air, respectively.

The contribution of air viscosity in ordinary atmospheric conditions is typically dominating for most high-quality resonators [132], saturating the quality factor to a value that can be estimated by

$$Q_{\mathrm{air}}^{(\mathrm{atm})} = \frac{2\alpha^2}{\mu_{\mathrm{air}} C_{\mathrm{d}} l^2} \sqrt{\rho A Y I}, \tag{4.3}$$

where μ_{air} is the dynamic viscosity of air and C_{d} is the drag coefficient, a function of the Reynolds number and of the oscillator's geometry. By transferring the oscillator into vacuum, the lower density of air molecules is such that they interact with the system without further collisions amongst each other. As more air is pumped out, background

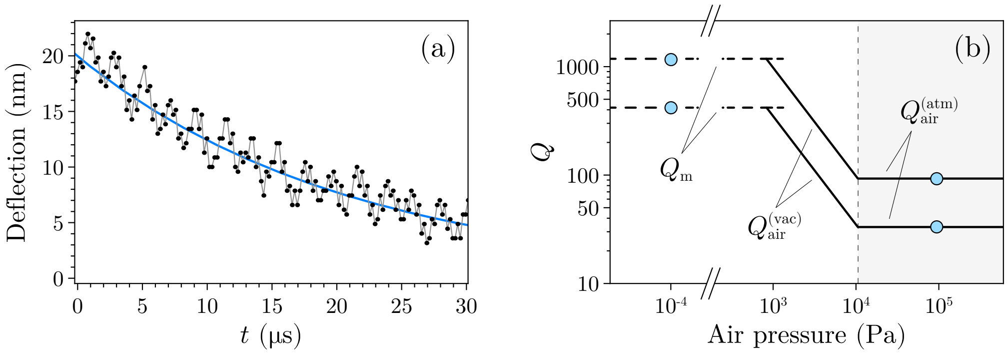

Figure 4.3: Dissipation properties of the nanowires. **(a)** Time-domain measurement of the relaxation rate of a nanowire in air. The nanowire (≈ 50 µm long, ≈ 300 nm thick) is subject to a thermally induced deflection until $t = 0$, at which point the amplitude of the deflection undergoes exponential decay to the original state. The high-frequency fluctuations on top of the decay represent oscillations at the mechanical frequency excited by thermal noise. For this specimen, the rate obtained by exponential fit of the moving average (solid blue line) is $(7.6 \pm 0.4)\,\mathrm{kHz}$. **(b)** Quality factor of two different oscillation modes in air and in vacuum conditions. The circles correspond to the quality factor obtained by dividing the first two eigenfrequencies of the nanowire, calculated according to Eq. 4.1, by the corresponding damping rates, empirically measured to be ≈ 10 kHz in air and ≈ 0.8 kHz in high vacuum for a nanowire with similar eigenfrequencies. The solid lines indicate the quality factor, dominated by air dissipation, which is expected by the model for a nanowire at room temperature ($T = 300\,\mathrm{K}$) with elastic modulus $Y = 85\,\mathrm{GPa}$, density $\rho = 8960\,\mathrm{kg\,m^{-3}}$, diameter $2r = 200\,\mathrm{nm}$, and length $l = 40\,\mathrm{\mu m}$. The molar mass used in the model in the high-pressure regime is $M_\mathrm{air} = 28.97 \times 10^{-3}\,\mathrm{kg\,mol^{-1}}$, and the air viscosity required in the high-pressure regime is $\mu_\mathrm{air} = 1.8 \times 10^{-5}\,\mathrm{Pa\,s}$. The drag coefficient C_d, estimated to be between 1 and 10 for a cylinder with Reynolds number around unity, was fitted to a value of 2.0. The transition between the regime of individual gas collisions and viscous dynamics is, for these parameters, around 10.5 kPa. The intrinsic mechanical dissipation takes over at pressures lower than 1 kPa.

gas collisions decrease and the quality factor becomes inversely proportional to the pressure P [133]:

$$Q_\mathrm{air}^\mathrm{(vac)} = \sqrt{\frac{\pi}{2}\frac{RT}{M_\mathrm{air}}}\frac{\alpha^2 r}{2l^2}\sqrt{\frac{\rho Y I}{A}}\frac{1}{P}, \tag{4.4}$$

where R is the universal gas constant, T the temperature, and M_air the molar mass of air. The quality factor cannot be increased arbitrarily, however. At some point further reduction of background gas collisions will have little or no effect, as other intrinsic damping attributes prevail. As these are often specific to the manufacturing process or other details not always easily accessible [101, 133], it is hard to predict what is the highest quality factor achievable by the apparatus without a direct measurement. The decay rates of the thermally excited oscillations of the nanowires in air, measured from the linewidth of the resonances on the spectrum analyser, was observed to be around 10 kHz due to the interaction with gas molecules (cf. Fig. 4.3). This corresponds to quality factors of up to 50 for the fundamental modes. Insertion of the nanowires in a vacuum chamber reduced the damping rates to less than 1 kHz, pushing the quality factors to 500 or more. When operating in vacuum, the damping rate of the nanowires was inferred from the time domain evolution of the oscillations to overcome the limit in resolution bandwidth of the spectrum analyser. The chamber was operated in high-vacuum conditions at pressures of 10^{-4} Pa or lower to avoid air having any role in the damping mechanism.

4.2.3 Scheme

All operations on the nanowires and the enhancement of their probing capabilities in the transient regime have been performed using a three-stage scheme: one part for the detection of the thermally driven modes, one part for the realization of feedback control, and one part for the analysis of the nanowires' response to an external signal. The simplified diagram of Fig. 4.4 shows how each different role is performed by a separate laser. The requirement for three independent sources comes primarily from the neces-

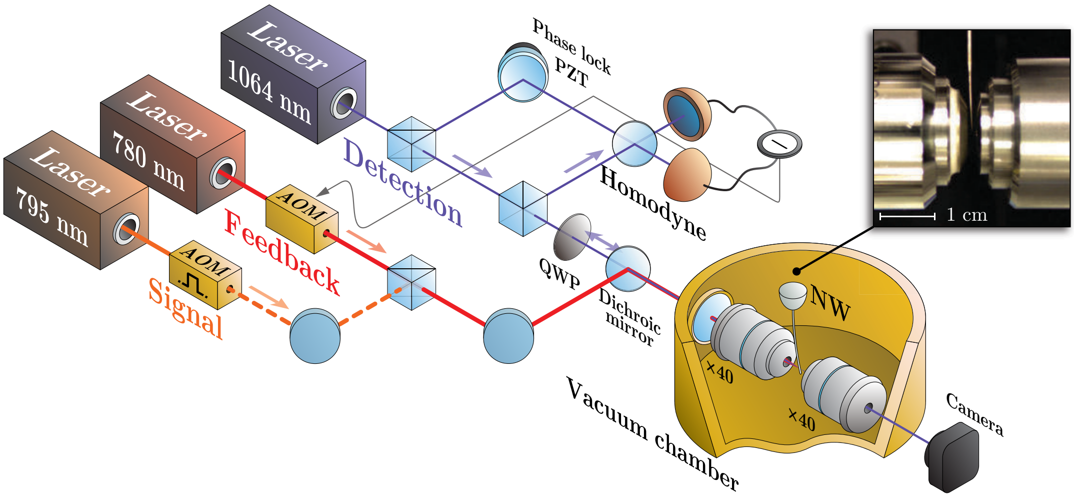

Figure 4.4: Comprehensive scheme of the experiment on the nanowire (NW). The three optical branches are used for the detection of the thermal motion of the nanowire (1064 nm), for the continuous or periodic feedback to suppress the thermal fluctuations (780 nm), and for the application of an impulsive signal during periods of feedback quiescence (795 nm). The inset shows a close-up photograph of the tungsten needle with the nanowire at its tip between the microscope objective lenses.

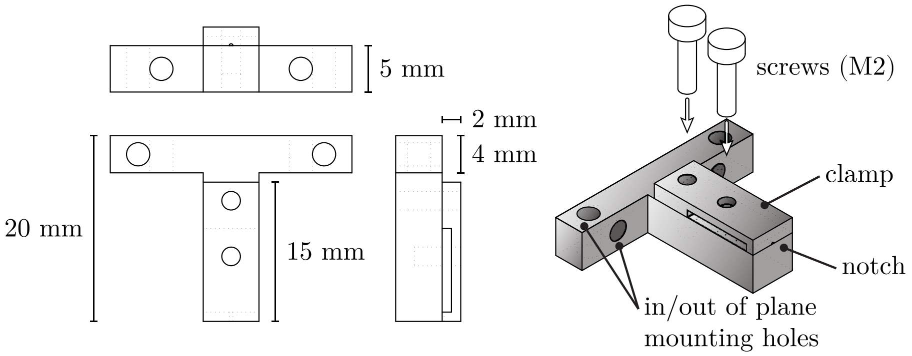

Figure 4.5: The mount used to clamp the nanowires to a positioning stage, in orthogonal projections showing the front, top, and side views and in isometric perspective. A screw is used to fix the top piece to the bottom. A second screw in the middle of the top piece is used to tighten the front end, where the tungsten needle is held in place thanks to a small notch.

sity of having the beams co-propagate without interference, and the wavelength of each laser is, in itself, only a secondary requirement—something largely demonstrated by the fact that the wavelengths of the detection laser and the feedback laser were swapped during the first round of investigations. The absorption and scattering properties of the nanowires are, of course, elements that need to be considered for an appropriate choice of the operating wavelengths. In the final setup, the detection branch is powered by a 1064 nm beam, while light around 780–795 nm is used for the actuation (for either feedback or simulation of a signal), largely because the nanowire under investigation displayed a stronger response in the near infrared and better resistance to high power at longer wavelengths. The vacuum chamber, where the nanowire and the two focusing microscope objective lenses are located, is maintained by an ion pump at pressures of 10^{-5}–10^{-4} Pa. A vacuum-compatible nano-positioning stage[2] is used to allow alignment within the enclosed chamber. The nanowire is clamped to the positioning stage by a custom-built mount especially designed for the purpose, capable of in-plane or out-of-plane orientation and compatible with most commercial stages (cf. Fig. 4.5).

For detection, many different schemes were trialled during the nanowire characterization phase, including the use of split photodiodes to measure differences of the diffracted shadow in the transmitted light, or observation of the effects of the nanowire's modulation of the optical field inside a cavity. Out of these, a detection method inspired by Doppler vibrometers proved to be the most practical and efficient, collecting information on the oscillation along the same direction as the optical axis by interference of a reference beam with the light scattered back by the nanowire. The presence

---

[2] ECS3030/HV from attocube systems AG (http://www.attocube.com/)

of phase-locked homodyne detection, as opposed to a single photodiode, renders the entire process more effective. In the feedback branch, control on the nanowire's motion is realized by an acousto-optic modulator (AOM) that varies the amplitude of the field and the consequent back-action on the oscillator. The AOM is driven in real time by a signal extracted from the detection scheme, after appropriate processing required to achieve the desired gain and phase for the feedback. The last stage uses a similar principle to also drive the nanowire, in this case with an arbitrary external signal independent of the state of the nanowire itself. The external signal comes in the form of a pulse modulated at frequencies close to the resonances of the mechanical oscillator. It is synchronized to arrive at specific times after the feedback is turned off, in order to study the nanowire's response in a transient regime before the full restoration of thermal fluctuations but without the suppression in susceptibility due to the feedback. All branches will be discussed more extensively in Chapters 5, 6, and 7, each specifically dedicated to the explanation of how detection, feedback, and signal-to-noise ratio enhancement come together in the context of the experiment.

Chapter 5

Detection

5.1 Scattering model

When dealing with objects of 100 nm in radius, effects at the sub-wavelength scale become a significant and inherent part of the system. In this regime radiation pressure is dominated by scattering forces. Therefore, appropriate modelling is required in order to gain an insight on how to make detection and general methods of interaction more optimal.

We follow Mie scattering theory for a sub-wavelength cylinder [134]. The solutions are expressed in terms of infinite series of the scattering coefficients $\{c_n\}_{n\in\mathbb{N}}$, whose value strongly depends on the geometry and refractive index of the object as well as the polarization and the angle of incidence of the field. Notably, any display of absorption is derived from a propagation of the imaginary part of the complex refractive index of the material. We limit our analysis to the case of light normally incident to the axis of the nanowire, with beam width W much larger than the cross-sectional dimensions,

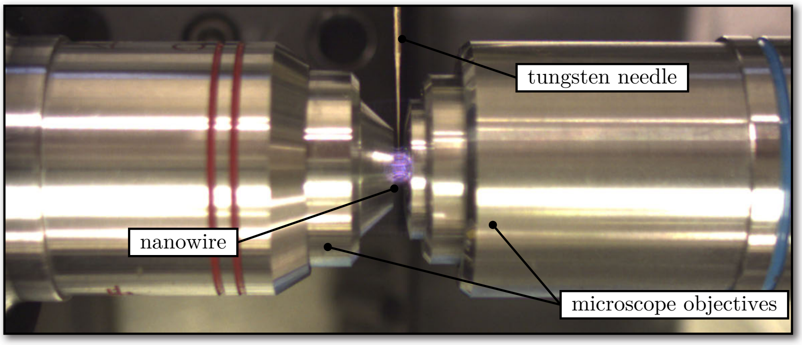

Figure 5.1: Scattering can induce some unexpected effects, such as a peculiar purple emission from the nanowire when illuminating it with infrared light. The direction of emission is orthogonal to the propagation axis of the beam, incoming from the left. The nanowire under inspection does not have a gold coating.

i.e. $W \gg r$ with r being the radius of the cylinder. The angular distribution of the scattered field is

$$E_{\text{sca}}(\phi) = \sqrt{\frac{2}{\pi\xi}} e^{i\left(\frac{3\pi}{4}+\xi\right)} T(\phi) E_{\text{in}}, \tag{5.1}$$

where ϕ is the polar angle, $\xi := 2\pi r/\lambda$ is a dimensionless ratio between the characteristic length of the object and the wavelength, and E_{in} is simply the input field. The dependence on the refractive index of the object is implicit in the transfer coefficient $T(\phi)$, which is determined by the scattering coefficients as

$$T(\phi) = c_0 + 2\sum_{n=1}^{+\infty} c_n \cos(n\,(\pi - \phi)). \tag{5.2}$$

The extinction, scattering, and absorption efficiencies, equivalent to the ratio between the effective cross section of each process and the cross-sectional area of the target, are also calculable from the scattering coefficients. They are

$$Q_{\text{ext}} = \frac{2}{\xi}\left(\text{Re}(c_0) + 2\sum_{n=1}^{+\infty} \text{Re}(c_n)\right), \tag{5.3}$$

$$Q_{\text{sca}} = \frac{2}{\xi}\left(|c_0|^2 + 2\sum_{n=1}^{+\infty} |c_n|^2\right), \tag{5.4}$$

$$Q_{\text{abs}} = Q_{\text{ext}} - Q_{\text{sca}}. \tag{5.5}$$

It should be specified that, despite their name, these *efficiencies* are not bound to unity in Mie scattering theory. As a matter of fact, in many examples the light scattered or absorbed is more than that geometrically incident on the object [134]. The efficiencies are needed to infer the amount of radiation pressure force contributing to each process [135]. Recalling the general relationship between force and power from Eq. 2.24, we have that the scattering and absorption components of radiation pressure force are respectively

$$F_{\text{sca}} = \frac{Q_{\text{sca}} P_{\text{in}}}{c}, \tag{5.6}$$

$$F_{\text{abs}} = \frac{Q_{\text{abs}} P_{\text{in}}}{c}, \tag{5.7}$$

in terms of the incident power P_{in}, which is calculated by integrating the intensity of the beam over the scattering cross section $(2r) \times (2W)$ [136]. The scattering coefficients are the only elements needed to calculate all of these quantities that are still unspecified. The reason lies in the fact that their definition differs depending on whether the polarization of the field is parallel or perpendicular to the cylinder's axis:

$$c_n = \begin{cases} \dfrac{J_n(\nu\xi)J_n'(\xi) - \nu J_n'(\nu\xi)J_n(\xi)}{J_n(\nu\xi)H_n^{1'}(\xi) - \nu J_n'(\nu\xi)H_n^1(\xi)} & \text{for parallel polarization,} \\[2ex] \dfrac{\nu J_n(\nu\xi)J_n'(\xi) - J_n'(\nu\xi)J_n(\xi)}{\nu J_n(\nu\xi)H_n^{1'}(\xi) - J_n'(\nu\xi)H_n^1(\xi)} & \text{for perpendicular polarization.} \end{cases} \tag{5.8}$$

Here, $\nu = n_{\mathrm{obj}}/n_0$ is the ratio between the refractive index of the cylindrical object, n_{obj}, and the one of the surrounding medium, n_0. The functions $\{J_n\}_{n\in\mathbb{N}}$ are the Bessel functions of the first kind and $\left\{H_n^1\right\}_{n\in\mathbb{N}}$ are the Hankel functions of the first kind. The prime indicates differentiation relative to the full argument of the relative function. The derivatives for both classes of functions can be easily computed as the halved difference of the involved functions with preceding and succeeding indices, e.g. $J_n'(x) = \left(J_{n-1}(x) - J_{n+1}(x)\right)/2$. For any other polarization the result are obtained by the appropriate linear combination of the different coefficients.

The results from this model are presented in Fig. 5.2 for a field with vertical polarization and in Fig. 5.3 for a field with horizontal polarization. Since the optical properties of $\mathrm{Ag_2Ga}$ are not very well known [135], all calculations have been performed for a gold-coated nanowire, under the assumption that the effects due to the presence of a different substance at the core could be ignored. Moreover, the image in Fig. 4.2 shows an uneven, irregular gold-coated nanowire surface which deviates from smooth cylindrical rod assumed by the model. These results are only meant for a qualitative analysis aimed at obtaining an order-of-magnitude estimate of the scattering forces and understanding the main directions of the scattered light.

The spatial distribution of the scattered field shows a predisposition for backward-scattering, though with quite a wide angle. This is particularly prominent for vertically polarized light, but it holds generally true in other cases as well. It should not be surprising, then, that the most effective procedure for optical detection uses light "reflected" back from the nanowire, although the potential for this (or any other) technique is limited by the aperture and light collecting ability of the setup. Alternatively, one could resort to the "transmission" line instead, looking at the information obtainable from the absence of light in the form the modulation of the diffracted shadow. Whilst less efficient, this method is not incompatible with the previous one and may be carried out concurrently. As we will see in more detail in the next section, the two detection methods actually address different modes, corresponding to oscillations along

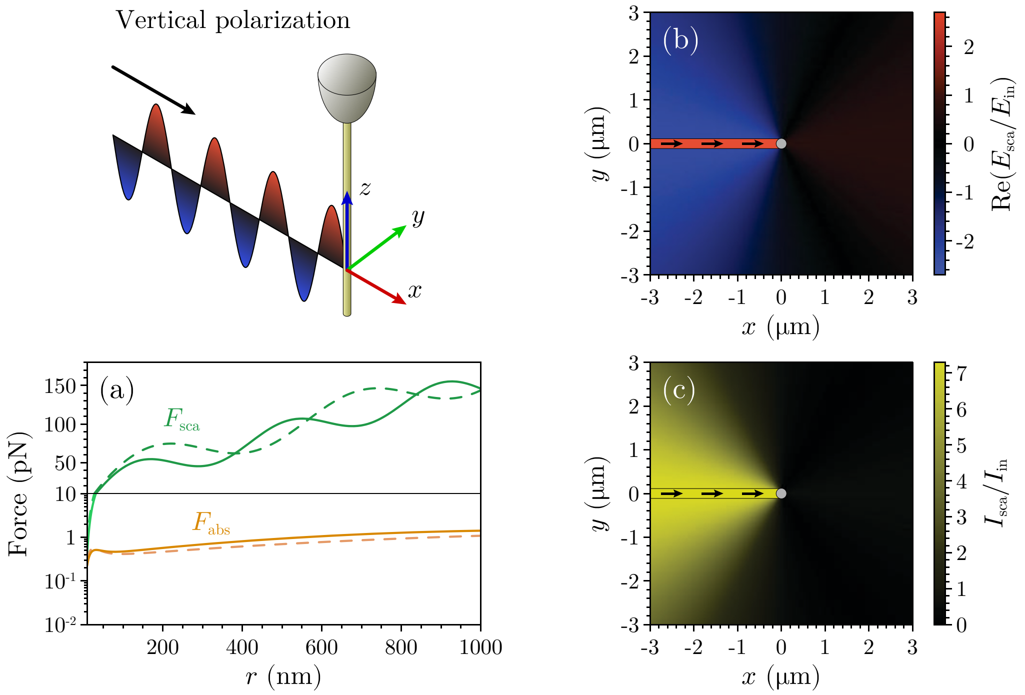

Figure 5.2: Scattering properties of a nanowire irradiated by a field with polarization parallel to the shaft. The nanowire is assumed to consist entirely of gold, with refractive index $n_{\text{obj}} = 0.2{+}4.8i$ ($0.2{+}7.0i$) for 780 nm (1064 nm) light. The refractive index of the medium, n_0, is taken to be 1 regardless of whether the nanowire is in air or in vacuum. **(a)** Forces due to scattering (green) and absorption (orange) as a function of the radius of the nanowire, calculated according to Eq. 5.6–5.7. The traces are plotted for a beam of width $W = 10\,\mu\text{m}$, power of 50 mW, and a wavelength of 780 nm (continuous) or 1064 nm (dashed). **(b–c)** Angular distribution of the scattered field and its intensity, as calculated from Eq. 5.1. The nanowire is placed at the origin and is assumed to have a radius of 120 nm. The incident light, of wavelength $\lambda = 780$ nm, is approaching from the negative x axis. Its colour is adjusted to the maximum value of the scale rather than normalized to 1 in order to reveal the polarization at a glance.

orthogonal directions.

Looking at the forces acting on the nanowire from Fig. 5.2a and Fig. 5.3a, we see that independently of wavelength or polarization the absorption forces are a couple of orders of magnitude smaller than the scattering forces. The model suggests fluctuating values of the forces depending on the radius of the nanowire (an effect less obvious for absorption forces due to the logarithmic scale). The positions and amplitudes of the local minima and maxima depend on the wavelength, creating situations in which the scattering force is, for example, stronger for 780 nm rather than 1064 nm. Therefore, depending on the geometry of the nanowire, one wavelength is more suitable for detection while the other is better for external control, as one applies a weaker back

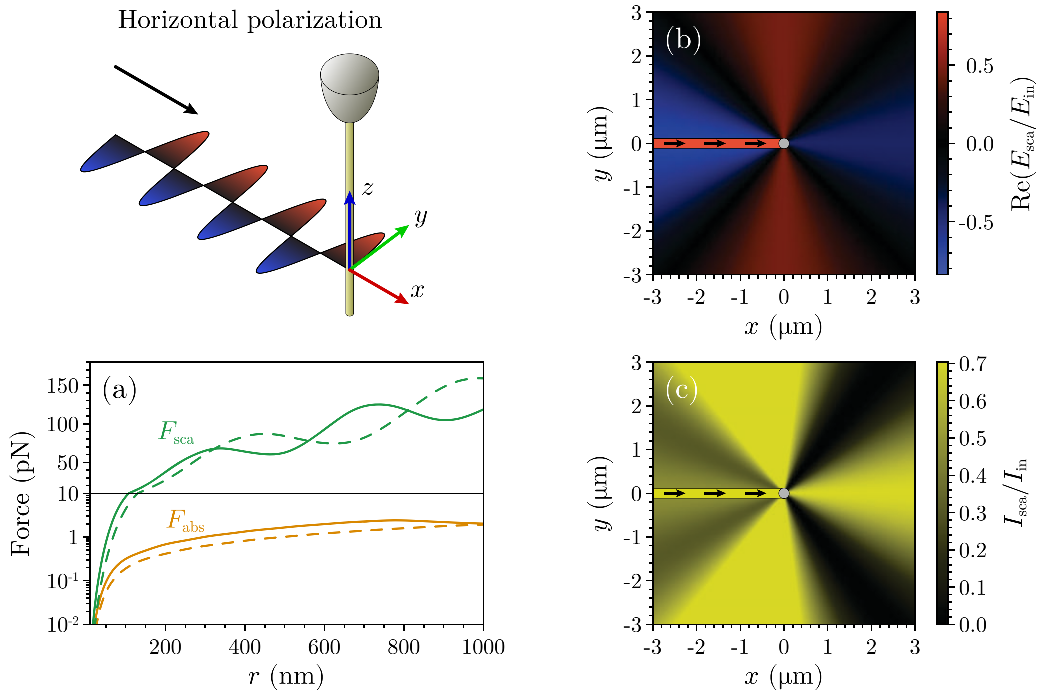

Figure 5.3: Scattering properties of a nanowire irradiated by a field with polarization normal to the shaft. The parameters used are the same as Fig. 5.2. **(a)** Forces due to scattering (green) and absorption (orange) as a function of the radius of the nanowire, for a wavelength of 780 nm (continuous) or 1064 nm (dashed). **(b–c)** Angular distribution of the scattered field and its intensity, for incident light of wavelength $\lambda = 780$ nm.

action and the other exerts stronger forces.

Even though absorption forces are relatively small, indirect effects due to photothermal absorption can have dramatic consequences. Any power higher than 100 mW induces permanent effects on the nanowire, which can be observed in the spectrum in the form of lasting resonance frequency shifts or more directly under microscopy as shortening, curling, and even complete obliteration. As a matter of fact, optically-induced thermal bending of the Au/Ag_2Ga bimorph nanowires generates a bolometric force which is crucial for the interaction, as we will see in Chap. 6.2. The bolometric forces observed are estimated to be about one hundred times stronger than the radiation pressure forces estimated by the model.

5.2 Free-space measurements

In deciding what detection method would be more suitable in relation to other sections of the experiment, priority was attributed to simplicity and practicality. These qualities, not necessarily exhibited by intra-cavity measurements, are common traits of detection methods performed in free space. Free-space measurements are more easily characterized and they require a less demanding implementation, with a comparatively straightforward alignment and no need for frequency locking schemes. Furthermore, the bandwidth of a detection technique in free space is in principle unlimited, rather than being restricted to frequencies within a cavity linewidth. When the option of feedback control is taken into account, the extended bandwidth is a particularly decisive feature that allows cooling of several modes simultaneously.

The general configuration for free-space measurements is illustrated in Fig. 5.4. Two microscope objective lenses (×40) are used to focus the beam onto the nanowire. The advantage of a small waist lies in the possibility of a more precise alignment of the beam onto specific sectors of the cylinder. The detection efficiency of the vibrational modes, for example, is increased by lining up the beam with the anti-nodes of the oscillation, where the amplitude is maximized. The actuation by bolometric forces, on the other hand, is increased when the beam is positioned about 10 µm away from the tip to enhance the thermal bending. Transmission of a collimated beam through the objective lens would achieve a waist of on the order of 10 µm. By using a converging beam, instead, the waist is reduced down to a little less than 1 µm. A camera (or a beam profiler) is located on transmission to capture the diffraction patterns of the nanowire, also confirming the beam waist by comparison with the size of the nanowire

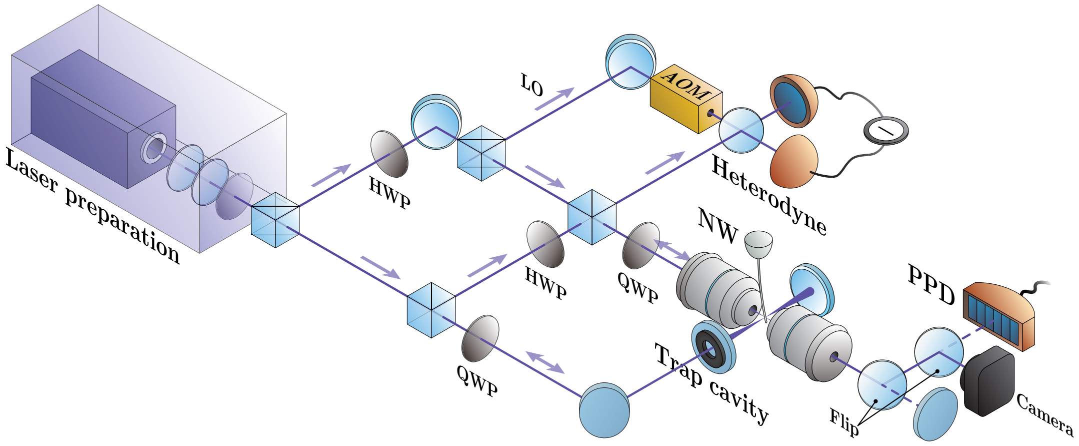

Figure 5.4: Detailed scheme of the detection branch. On reflection, the mechanical modes of the nanowire are detected by heterodyne interferometry with a local oscillator (LO). On transmission, a set of two flip mirrors allows a choice between an alignment mirror, a camera or beam profiler, and a pixel photodetector (PPD). The setup includes a trap cavity in the direction orthogonal to the microscope lenses.

itself. Two flip mirrors allow reorganization of the optical path to switch between the camera, a pixel photodetector (PPD), and a fixed flat mirror normal to the propagation of the beam. The main purpose of the flat mirror is to simulate the reflection from the nanowire in order to facilitate the alignment of the interferometric section. In addition, the same mirror was used to test the effects of radiation pressure force gradients from a single-pass standing wave [137], without any discernible results.

The main detection scheme is inspired by laser Doppler vibrometry [128, 131, 138, 139]. The beam incident on the nanowire is scattered back with a phase that depends on the position of the reflecting surface. As the nanowire oscillates, the reflection acquires a phase modulation at the mechanical frequency. The modulated reflection is then interfered with a reference beam (cf. Chap. 2.5.1) to obtain a real-time measurement of the phase and amplitude of the oscillation. The diagram in Fig. 5.4 reflects a scheme which is closer to conventional vibrometry than the one introduced in Fig. 4.4. Here, the first-order diffraction from an acousto-optic modulator (AOM) is used to shift the local oscillator to a reference carrier frequency (80 MHz in our case). This heterodyne-based detection, which centres the measurement around the shifted frequency, is useful to pick up low frequency modes that would otherwise be concealed under low-frequency background noise. However, since the mechanical frequencies involved in the experiment are at least 200 kHz or higher, the setup is ultimately converted to homodyne detection, using the same frequency for both the reflected beam and the reference local oscillator. This eliminates any averaging due to the beating which is distinctive of heterodyne, and up to a factor of two of improvement in the detection can be gained by phase-locking the two beams to ensure optimal interference over time. For the lock, we modulate the phase of the local oscillator by displacing a mirror along the path with a piezoelectric unit (PZT). Since the operating bandwidth of the piezoceramic does not exceed a few tens of kilohertz, the lock is ideal to account for low-frequency fluctuations (such as thermal drift of the optics) without interfering with the faster modulation due to the mechanical oscillation. Therefore, the read-out from the detectors, which doubles as the error signal, offers a direct measurement of the vibrational state of the nanowire.

An alternative setup for the detection of the nanowire's vibrations is realized on the transmitted light thanks to the pixel photodetector. As the nanowire oscillates, the lateral displacement causes one side of the beam to be subtly less bright than the other, and the intensity perceived by different pixels of the photodetector varies accordingly. The detection is refined by subtraction of the signals from two pixels [140],

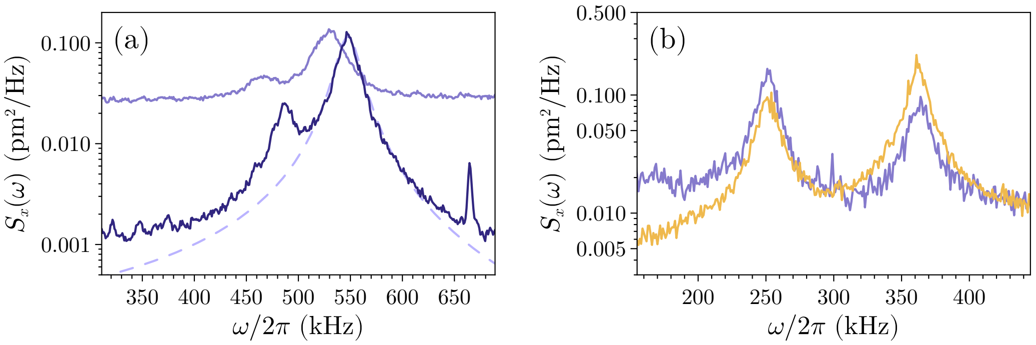

Figure 5.5: Spectra of the nanowires' thermal fluctuations. All traces have been recorded in atmospheric conditions. **(a)** Eigenmodes of a nanowire (≈ 60 µm long, ≈ 350 nm thick, gold-coated) obtained by interferometry on reflection, once with heterodyne (light) and once with homodyne (dark). Between the two measurements the nanowire may have been repositioned with a slightly different orientation, accounting for a small variation in the detection ratio of the two modes, and a permanent change was induced by the use of high power, slightly shifting both frequencies. The dashed trace follows the model of Eq. 5.9 at room temperature for an oscillator with parameters similar to the measured ones. **(b)** Comparison between the two different detection method: interferometry on reflection (violet) and intensity subtraction from different pixels on transmission (orange). The measurements were performed simultaneously, and the difference in ratio between the peaks is due to the fact that the two methods have preferential directions of detection. The nanowire is uncoated, ≈ 40 µm in length and ≈ 270 nm in diameter.

which increments the effect of the modulation due to the oscillation while at the same time eliminating the relatively stronger intensity background.

There is a fundamental difference between the two detection methods. The first, based on interferometry, measures the Doppler shift of the reflected beam and is therefore proportional to the oscillator's *velocity*. The second, dependent on intensity differences, is conditioned by the location of the nanowire and it produces a direct measurement of the oscillator's *position*. If one monitored the time evolution of the two signals, they would appear as similar sinusoids separated by a phase shift of $\pi/2$, modulo some normalization factor that would in any case depend on the different gains of each detection as well. In both situations, however, the power spectrum that would be displayed on a spectrum analyser would result proportional to the displacement spectrum

$$S_x(\omega) = |\chi_\mathrm{m}(\omega)|^2 \, S_F^{(\mathrm{th})}(\omega), \tag{5.9}$$

where x is the position of the oscillator, $\chi_\mathrm{m}(\omega) = \left[m\left(\omega_\mathrm{m}^2 - \omega^2 + i\gamma_\mathrm{m}\omega\right)\right]^{-1}$ its mechanical susceptibility (cf. Eq. 3.64), and $S_F^{(\mathrm{th})}(\omega) = 2m\gamma_\mathrm{m}k_\mathrm{B}T$ is the spectral density of the thermal Brownian forces, which is constant across all frequencies in the classical limit (cf. Eq. 3.30). Figure 5.5 shows some representative displacement spectra obtained using the two detection methods. The thermal forces drive the eigenmodes of the oscillation, which exhibit in both cases a split because of geometrical asymmetries. Each spectrum is originally recorded as a power spectrum and is subsequently converted to a displacement spectrum. The normalization is performed by comparing the integrated area with the total thermal energy anticipated by Eq. 5.9 at room temperature. The displacement spectra in Fig. 5.5a show the difference, after normalization, when homodyne rather than heterodyne interferometry is used in the main detection setup. The higher efficiency in detection, due to phase-locking of the homodyne but also to better visibility of the interference, appears in the power spectrum extracted directly from the spectrum analyser as a stronger signal above a comparable noise. It is only after the appropriate rescaling that both peaks appear to follow the same model of Eq. 5.5, and the bigger signal-to-noise ratio is revealed as a higher clearance from the background noise.

Another difference between the two detection schemes is that they address orthogonal directions, and spatially orthogonal modes of the same order are observed with complementary efficiency. This is due to the fact that the detection on reflection tracks oscillations in the direction parallel to the optical propagation, while the one on transmission reveals only oscillations which cross the beam transversally. This allows situations where a mode, if lined up exactly with one of these directions, could be completely invisible to one detection method and at the same time measured with maximum efficiency by the other. For example, if the nanowire has a 250 kHz mode aligned parallel to the beam and a 360 kHz mode normal to it, the interferometric detection would distinguish only the mode of lower frequency and the pixel photodetector would measure only the mode of higher frequency. If, on the other hand, the two modes are aligned at 45° with the beam, they will be measured with 50 % efficiency by both methods. This is almost the case in Fig. 5.5b, where only a slight deviation from the 45° orientation is already enough to account for an appreciable asymmetry in detection.

5.3 Intra-cavity interaction

The setup in Fig. 5.4 includes a linear cavity at 90° with the detection beam. This cavity was added during the development of the measurement scheme to explore additional characteristics of the nanowire and to see in particular how the intra-cavity field affects

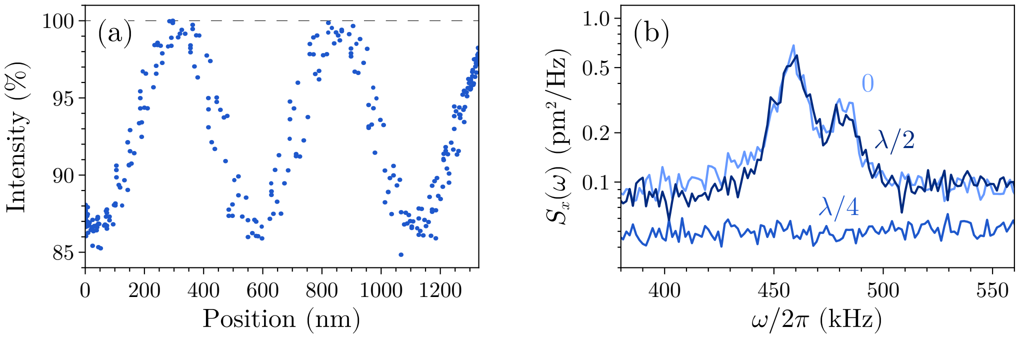

Figure 5.6: The output field of an optical cavity is influenced by the position of the nanowire within. The nanowire used is ≈ 30 µm long, ≈ 200 nm thick, gold-coated, and in air. **(a)** Variation of the intensity of the cavity's reflected field as a function of the nanowire's position. The intensity is scaled to the value at resonance when the nanowire is out of the cavity. **(b)** Detection of the nanowire's thermal fluctuations from the cavity output. When the nanowire is at an anti-node (lightest and darkest traces) the eigenmodes are detected thanks to the interaction with the cavity field. When the position is shifted to coincide with a node, no eigenmodes can be detected.

the oscillation.

The cavity is close to concentric in order to reduce the waist of the resonant modes. The end mirrors have both a radius of curvature of 2.5 cm, and the length of the cavity is about 4.7 cm. With a free spectral range exceeding 3 GHz, and a finesse measured at approximately 150, the cavity linewidth is estimated to be above 20 MHz, certainly wide enough to accommodate all of the detectable eigenmodes of the nanowire. The nanowire is positioned close to the middle of the TEM$_{00}$ mode, near the waist. This is achieved by moderately misaligning the cavity, so that higher-order modes such as TEM$_{10}$ and TEM$_{20}$ become partly resonant, and by looking at the eclipsing effect that the nanowire has on certain modes rather than others. In particular, the right location is reached when TEM$_{00}$ and TEM$_{20}$ are obscured the most and TEM$_{10}$ is unaffected. Once the nanowire is properly positioned within the cavity, the two microscope objective lenses are adjusted in order for the nanowire to be aligned for the detection beam as well.

The interaction between the nanowire and the intra-cavity field highly depends on the location of the mechanical oscillator [141], as illustrated in Fig. 5.6. When the nanowire's position is scanned across a range wider than the wavelength λ (1064 nm in Fig. 5.6a), the optical resonance is detected with varying intensity, periodic of $\lambda/2$, as the nanowire crosses the nodes and anti-nodes of the cavity field. This behaviour may initially remind of the sinusoidal response of the reflected and transmitted fields in a membrane-in-the-middle configuration [142, 143]. However, for a membrane the sinu-

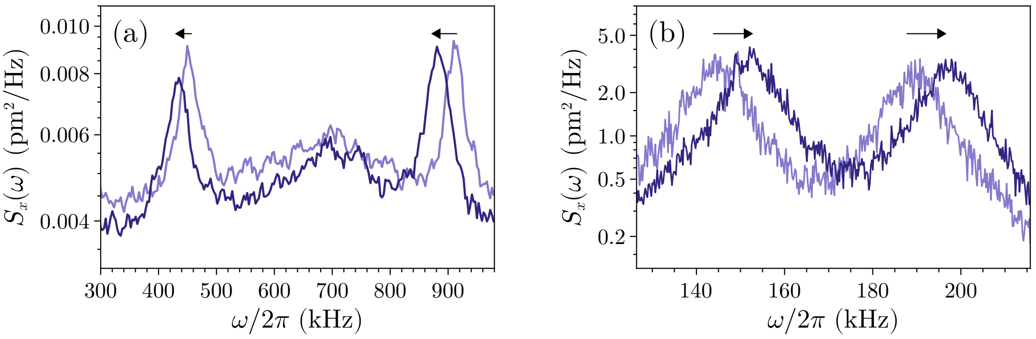

Figure 5.7: Two examples of frequency shifting of the nanowire's mechanical eigenmodes. The effect is not permanent and in both cases the new eigenmodes (dark traces) are restored to the original ones (light traces) simply by turning off the action of the external agent. All traces are recorded in atmospheric conditions. **(a)** Shifting due to the action of the intra-cavity field for two different order modes of the nanowire, which is ≈ 30 µm long, ≈ 180 nm thick, and gold-coated. **(b)** Shifting induced by the displacement from electric attraction. A voltage of 400 V is applied between the nanowire and an electrode close to it to induce the electric force. For voltages lower than 200 V no discernible shift could be observed. The nanowire is the same uncoated one used in Fig. 5.5b, although its modes have been permanently altered by optical damage.

soidal variation detected originates from the dependence of the cavity eigenfrequencies on the position, and not from the leaking of more or less photons from the cavity. In particular, a symmetric sinusoid is obtained only with a completely lossless membrane, whereas a lossy membrane introduces asymmetries in the periodic response. The case for a nanowire is quite different, since the relative difference in intensity is observed even when the cavity is scanned while the position is slowly changed, meaning that the response is not derived from a change in cavity eigenfrequency. Moreover, we know from Chap. 5.1 that considerable scattering losses introduced by the nanowire's geometry diffuse the field over a very wide angle. The field that interacts with the nanowire is not fully scattered away and lost, however, and the modulation introduced by the mechanical oscillations can be detected on the cavity output when the position coincides with an anti-node (Fig. 5.6b).

The most remarkable effect of the cavity field on the nanowire is a change of the mechanical resonances. Monitoring the thermal fluctuations on the detection line, a sudden shift of the eigenmodes of up to 30 kHz is observed when there is power circulating within the cavity (cf. Fig. 5.7a). The frequency shift is fully reversed as soon as no input is sent to the cavity, it is confidently repeatable, it does not depend on the cavity detuning, and its magnitude appears to be proportional to the order of the eigenmode. When the mechanical resonances are detected directly on the cavity field they appear to be already shifted, as would be expected. The origin of this effect is attributed to a fixed displacement induced by a constant force from the cavity field, which effectively alters the susceptibility and consequently modifies the resonance frequencies of the nanowire. To confirm this hypothesis is the fact that applying a fixed displacement by other external forces also has a similar effect. As an example, a high voltage difference was applied between the nanowire and an electrode in its vicinity to create an attractive electric force and therefore bend the nanowire towards the electrode, inspired by a technique for the characterization of field emission of SiC nanowires [144]. The result, shown in Fig. 5.7b, is once more a shift of a few kilohertz, although towards higher frequencies in this instance. The direction of the shift is likely due to the specific orientation of the nanowire. In Chap. 6.2 we will see how the evidence points towards an optomechanical interaction that relies on the nanowire's displacement from its natural state, which in the particular case of optical absorption forces occurs in a specific direction dictated by the asymmetries in the geometry and the bimorph structure.

Chapter 6

Feedback

6.1 The effects of active control

The use of active feedback control in optomechanics was proposed very early in the history of the field [145, 146]. As the systems became more and more refined, the opportunity for controlling the oscillations to achieve a desired state of the mechanics sparked a surge in interest that continues to this day. In particular, feedback control is extremely popular as an effective procedure to cool down the vibrational modes by actively counteracting the Brownian motion of the oscillator [147–150], reaching even temperatures that approach the quantum ground state of the macroscopic resonators [151–153].

Feedback control may also be utilized to suppress extra noise on the oscillator for applications in sensing. As we will see in more detail in Chap. 7.1, the specific conditions under which feedback induces a real measurement advantage have been more than once the subject of discussions [154, 155]. Notwithstanding, the active control of the oscillations can enhance the sensitivity by altering the response characteristics of an AFM cantilever [156] or by reducing the integration times required [157].

In this section we explore the effects of feedback on the oscillator, starting with a generic approach that analyses the general response of the system before focusing on the implementation of feedback cooling, also known as *cold damping.* We will also see how the feedback introduces artefacts in the measurement, and how this needs to be accounted for in order to understand what the physical state of the oscillator is precisely.

6.1.1 Modification of the oscillator's response

To understand how feedback control generally affects the position of the oscillator, we consider the driving forces separated into a random Brownian force F_{th}, which sustains the thermal fluctuations arising from the coupling with a thermal bath, and a force applied by the feedback, F_{fb}. Given the oscillator's susceptibility to be $\chi_{\mathrm{m}}(\omega) = \left[m\left(\omega_{\mathrm{m}}^2 - \omega^2 + i\gamma_{\mathrm{m}}\omega\right)\right]^{-1}$, we have, in the frequency domain,

$$x(\omega) = \chi_{\mathrm{m}}(\omega)\left(F_{\mathrm{th}}(\omega) + F_{\mathrm{fb}}(\omega)\right). \tag{6.1}$$

Similarly to the case of radiation pressure force (cf. Chap. 3.3.2), we can integrate the feedback force into the original dynamics to obtain an effective susceptibility [156,158]. To do so we consider a feedback force of the form $F_{\mathrm{fb}}(\omega) := K(\omega)x_{\mathrm{det}}(\omega)$, i.e. a force proportional to the detected position of the oscillator, x_{det}, with a generic transfer function $K(\omega)$. The detected position differs from the actual position because, in general, some noise is coupled into the measurement process. If this is taken into account, the generic feedback force in terms of the actual position is

$$F_{\mathrm{fb}}(\omega) = K(\omega)\left(x(\omega) + \delta x(\omega)\right), \tag{6.2}$$

where δx is the noise in the position measurement. After substituting in Eq. 6.1 and rearranging accordingly, we obtain

$$x(\omega) = \chi_{\mathrm{fb}}(\omega)\left(F_{\mathrm{th}}(\omega) + K(\omega)\delta x(\omega)\right), \tag{6.3}$$

where the effective susceptibility due to the feedback was defined as

$$\chi_{\mathrm{fb}}(\omega) := \frac{\chi_{\mathrm{m}}(\omega)}{1 - \chi_{\mathrm{m}}(\omega)K(\omega)}. \tag{6.4}$$

The position of the oscillator still responds to the thermal forces, but now with a susceptibility that is regulated by the feedback's transfer function. Additionally there is a residual force from the feedback, proportional to the measurement noise, which will be seen to have strong consequences towards the limits of active control. In our case, the signal used for the feedback is extracted from the interferometric detection and is therefore proportional to the velocity of the nanowire. As a consequence, the feedback force has viscous attributes that can be used to implement cold damping [145, 158], and it takes the form

$$F_{\mathrm{fb}}(t) = -\zeta_{\phi} m\gamma_{\mathrm{m}}\dot{x}_{\mathrm{det}}(t). \tag{6.5}$$

Here we express the strength of the interaction in units of the mass and the mechanical damping rate in order to isolate the dimensionless gain $\zeta_\phi := \zeta_0 e^{-i\phi}$, assumed to be complex to account for both the magnitude (ζ_0) and the phase (ϕ) of the feedback. Transforming to the frequency domain, we get that the associated transfer function is

$$K(\omega) = -i\zeta_\phi m\gamma_{\mathrm{m}}\omega, \tag{6.6}$$

and the feedback-dependent susceptibility is

$$\chi_{\mathrm{fb}}(\omega) = \left\{m\left[\omega_{\mathrm{m}}^2 - \omega^2 + \zeta_0\sin(\phi)\gamma_{\mathrm{m}}\omega + i\left(1 + \zeta_0\cos(\phi)\right)\gamma_{\mathrm{m}}\omega\right]\right\}^{-1}. \tag{6.7}$$

As would be expected, the original susceptibility is recovered in the case of $\zeta_0 = 0$, when the feedback is turned off. When $\phi = 0$ pure cold damping is achieved, whereas $\phi = \pi$ brings the system into parametric amplification. Any other phase introduces a frequency-dependent shift of the resonance, reminiscent of the effect due to a fixed displacement by the intra-cavity field presented in Chap. 5.3.

The spectrum of the oscillations obtained from Eq. 6.3 is described by

$$S_x(\omega) = \left|\chi_{\mathrm{fb}}(\omega)\right|^2 S_F^{(\mathrm{th})}(\omega) + \left|\chi_{\mathrm{fb}}(\omega)\right|^2 \left|K(\omega)\right|^2 S_{\delta x}(\omega), \tag{6.8}$$

where compared to Eq. 5.9 there is an additional term proportional to the background noise of the detection, $S_{\delta x}(\omega)$, and the original susceptibility is replaced by the effective one. It is important to distinguish, in the presence of feedback, between the spectrum of the *actual* oscillations described by Eq. 6.8 and the *measured* displacement spectrum, primarily because the feedback correlates the oscillator's position to the measurement noise. The correlations between x and δx are accounted by the inclusion of their cross spectral density in the measured displacement spectrum, which refers to $x_{\mathrm{det}} = x + \delta x$, as follows:

$$\begin{aligned} S_x^{(\mathrm{det})}(\omega) &= S_x(\omega) + S_{\delta x}(\omega) + 2S_{x\,\delta x}(\omega) \\ &= \left|\chi_{\mathrm{fb}}(\omega)\right|^2 S_F^{(\mathrm{th})}(\omega) + \Big(\left|\chi_{\mathrm{fb}}(\omega)\right|^2\left|K(\omega)\right|^2 + 1 + 2\,\mathrm{Re}(\chi_{\mathrm{fb}}(\omega)K(\omega))\Big)\, S_{\delta x}(\omega) \\ &= \left|\chi_{\mathrm{fb}}(\omega)\right|^2 S_F^{(\mathrm{th})}(\omega) + \frac{\left|\chi_{\mathrm{fb}}(\omega)\right|^2}{\left|\chi_{\mathrm{m}}(\omega)\right|^2} S_{\delta x}(\omega). \end{aligned} \tag{6.9}$$

Even though it does not correspond to the physical displacement of the oscillator, this spectral density is the only one that can be observed directly during an experiment. The spectral density of the actual displacement can only be inferred indirectly, despite

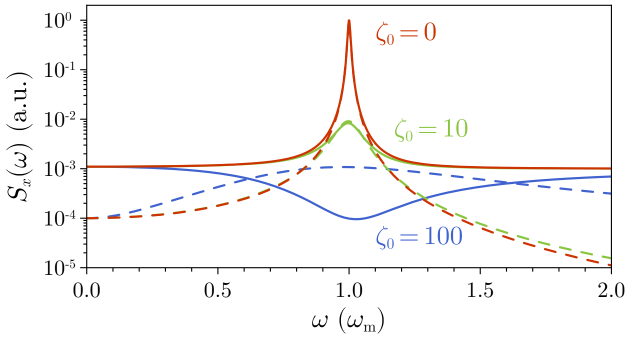

Figure 6.1: Indicative spectral densities of the actual (dashed line) and the measured (solid line) displacements, for an oscillator with quality factor $Q_{\mathrm{m}} = \omega_{\mathrm{m}}/\gamma_{\mathrm{m}} = 100$. The red traces correspond to the original spectra without feedback control. The green and blue traces correspond to cold damping with a gain of 10 and 100 respectively. In the latter case, squashing below the measurement noise is observed. All traces are normalized relative to the value of the actual displacement spectrum at resonance, and the measurement noise is assumed to be 1000 times smaller than the thermally driven fluctuations.

the central role that it plays in the calculation of a mode's temperature. Theoretical simulations showing the difference between the measured and the inherent displacement spectral densities, with and without active control, can be appreciated in Fig. 6.1.

The ratio in front of $S_{\delta x}(\omega)$ in Eq. 6.9 is responsible for a curious phenomenon: for high enough gain, the spectrum close to the mechanical frequency may be measured below the normal noise floor of the detection, similarly to how a squeezed state of light behaves relative to the vacuum noise. This occurrence is known as *squashing* [149, 158, 159], but unlike squeezing it does not seem to have practical applications on its own since it cannot be extracted from within the feedback loop [160]. A probe external to the feedback would measure the temperature of the oscillator to get higher as more squashing is introduced into the system. Even the inherent nature of squashing, whether it exists as a physical effect or it is just an artefact related to the measurement process, has been the object of debate without conclusive evidence. At any rate, squashing is mostly relevant to our case because it highlights how important it is to have a low noise floor in the measurement. It should be noted that the noise floor of a normalized spectrum (such as the ones seen in Fig. 5.5) is determined by the rescaling, and what truly matters in the raw power spectrum detected is the signal-to-noise ratio of the measurement, as would be expected in any other detection-based process.

6.1.2 Cold damping

Directing our attention to the case of purely negative feedback ($\phi = 0$ and $\zeta_\phi = \zeta > 0$), we can study the manifestation of cold damping in the system. In this regime, the effective susceptibility is simply

$$\chi_{\text{fb}}(\omega) = \left\{m\left[\omega_{\text{m}}^2 - \omega^2 + i\,(1+\zeta)\,\gamma_{\text{m}}\omega\right]\right\}^{-1}. \tag{6.10}$$

The resemblance with the original susceptibility is more pronounced, with the only difference being in the damping component changing from γ_{m} to $\gamma_{\text{fb}} = (1+\zeta)\,\gamma_{\text{m}}$.

The effecive temperature T_{eff} of a vibrational mode is related to the variance of the oscillations σ_x^2 by the equipartition theorem, which states that

$$\frac{1}{2}m\omega_{\text{m}}^2\sigma_x^2 = \frac{1}{2}k_{\text{B}}T_{\text{eff}}. \tag{6.11}$$

The variance can be calculated by integrating of the spectral density of the fluctuations. Because the theorem is relative to a physical process, the spectrum that needs to be considered is that from Eq. 6.8 relative to the actual displacement, not the measured one. The mode temperature is then

$$T_{\text{eff}} = \frac{m\omega_{\text{m}}^2}{k_{\text{B}}}\int_{-\infty}^{+\infty}\frac{d\omega}{2\pi}\,S_x(\omega). \tag{6.12}$$

If the spectrum features overlapping modes, the temperature of each mode can still be inferred by limiting the integration bounds around the resonance and by scaling the result proportionally to the integration area being neglected.

In the limit of small gain, the additional noise injected into the system by the feedback can be disregarded, allowing the displacement spectrum to be simply proportional to the spectrum of the thermal forces as $S_x(\omega) = |\chi_{\text{fb}}(\omega)|^2\,S_F^{(\text{th})}(\omega)$. This expression is analogous to Eq. 5.9, though with a response mediated by $\chi_{\text{fb}}(\omega)$ rather than $\chi_{\text{m}}(\omega)$. As we are working in a classical regime, the thermal noise is taken uniform across all frequencies, i.e. $S_F^{(\text{th})}(\omega) = 2m\gamma_{\text{m}}k_{\text{B}}T$. It should be remembered that here T represents the temperature of the thermal bath, equivalent to room temperature for a system in a non-cryogenic environment. Using the result that $\int\frac{d\omega}{2\pi}\;|\chi_{\text{fb}}(\omega)|^2 = \left(2m^2\gamma_{\text{fb}}\omega_{\text{m}}^2\right)^{-1}$, obtainable by applying Parseval's theorem to the inverse transform of a Lorentzian, we get that the temperature of the mode is

$$T_{\text{eff}} = \frac{T}{1+\zeta}. \tag{6.13}$$

Cooling is possible because the feedback force couples the resonator with an external system which is unrelated to the thermal bath. The coupling makes the mechanical resonator equivalent to an apparatus that has an effective damping $(1+\zeta)\,\gamma_{\text{m}}$ and that is subject to a bath at the effective temperature $T/\left(1+\zeta\right)$ [145, 158].

Since the new thermal equilibrium conditions scale with ζ, one would have to increase the feedback gain as much as possible to obtain a strong cooling factor. This, however, conflicts with the regime of small gain where Eq. 6.13 was derived, substantiating the need of a full treatment that does not neglect the detection noise. Substituting the full expression of $S_x(\omega)$ into Eq. 6.12, we have

$$T_{\text{eff}} = \frac{m\omega_{\text{m}}^2}{k_{\text{B}}}\left(\int_{-\infty}^{+\infty}\frac{d\omega}{2\pi}\,\left|\chi_{\text{fb}}(\omega)\right|^2 S_F^{(\text{th})}(\omega) + \zeta^2 m^2\gamma_{\text{m}}^2\int_{-\infty}^{+\infty}\frac{d\omega}{2\pi}\,\omega^2\left|\chi_{\text{fb}}(\omega)\right|^2 S_{\delta x}(\omega)\right). \tag{6.14}$$

With the assumption that both the thermal force spectrum and the detection noise are independent of frequency, and evaluating the integral of the second term on the right-hand once more thanks to Parseval's theorem as $\int\frac{d\omega}{2\pi}\,\omega^2\left|\chi_{\text{fb}}(\omega)\right|^2 = \left(2m^2\gamma_{\text{fb}}\right)^{-1}$, the mode temperature is

$$\begin{aligned} T_{\text{eff}} &= \frac{T}{1+\zeta} + \frac{\zeta^2}{1+\zeta}\frac{m\omega_{\text{m}}^2\gamma_{\text{m}}}{2k_{\text{B}}}S_{\delta x} \\ &= \frac{T}{1+\zeta}\left(1+\frac{\zeta^2}{2\eta_{\text{th}}}\right), \end{aligned} \tag{6.15}$$

where $\eta_{\text{th}} := k_{\text{B}}T/\left(m\omega_{\text{m}}^2\gamma_{\text{m}}S_{\delta x}\right)$ is the signal-to-noise ratio of the thermal fluctuations. This result shows that the feedback gain cannot be turned up indefinitely without consequences [149]. A higher value of ζ introduces more noise that becomes detrimental to the cold damping process, and increasing the gain beyond a certain point has only the effect of adding more incoherence into the system. The minimum temperature attainable depends, among other factors, on the measurement noise:

$$\begin{aligned} T_{\text{eff}}^{(\min)} &= T\frac{\sqrt{1+2\eta_{\text{th}}}-1}{\eta_{\text{th}}} \\ &\simeq T\sqrt{\frac{2m\omega_{\text{m}}^2\gamma_{\text{m}}S_{\delta x}}{k_{\text{B}}T}}. \end{aligned} \tag{6.16}$$

Here, the approximation is valid in the regime where the energy added to the mode by the measurement noise is not significantly larger than the oscillator's thermal energy, i.e. $m\omega_{\mathrm{m}}^2\gamma_{\mathrm{m}}S_{\delta x} \ll k_{\mathrm{B}}T$ or equivalently $\eta_{\mathrm{th}} \gg 1$. Cooling to extremely low temperatures is achieved only when the measurement noise is suppressed as much as possible. A higher quality factor $Q_{\mathrm{m}} := \omega_{\mathrm{m}}/\gamma_{\mathrm{m}}$ or a thermal bath at lower temperature, such as in cryogenic conditions, could also push the minimum temperature attainable by the feedback to lower limits. The gain at which the effective temperature corresponds to its minimum value corresponds to the turning point where the measured spectrum of Eq. 6.9 shifts from cold damping to squashing. Starting from low gain values, the effects of increasing ζ are observed on the spectrum as a suppression of the resonance peak until the point where the temperature is minimum and the resonance lies flat on the noise floor. Any higher gain pushes the spectrum close to resonance lower than the detection noise, indicating the presence of squashing. At the same time, however, the actual displacement spectrum experiences an overall broadening due to the prevailing effect of the injected noise, and the temperature of the mode increases.

6.2 Photothermal actuation

Regardless of what the trigger of the actuation induced by a laser on the nanowire is, be it radiation pressure or photothermal effects, it is the intensity of the laser that regulates the strength of the forces in play. The feedback is implemented by driving an acousto-optic modulator (AOM) with the signal obtained by the interferometric detection. The AOM modulates the amplitude of the field, in such a way that the reaction forces result proportional to the velocity of the oscillator and therefore exhibit dissipative attributes. The phase of the gain was initially controlled with the use of passive components along the feedback line. For this purpose, low- or high-pass filters were preferred to coaxial delay lines because they can generate similar phase shifts without introducing excessive dissipation. Eventually, however, the need for more precise phase control culminated in the use of an active phase-shifter module that allowed switching between cooling, heating, or pure frequency-shifting with full flexibility.

The feedback force acting on the nanowire is dominantly bolometric. The bolometric force is an indirect consequence of optical absorption, arising from the thermal stress and deformation due to the change in temperature. It is particularly substantial for bimorph structures [95, 161], a category that includes the gold-coated nanowires. Taking into account the reflectivity of the gold layer [162], the change in bulk tem-

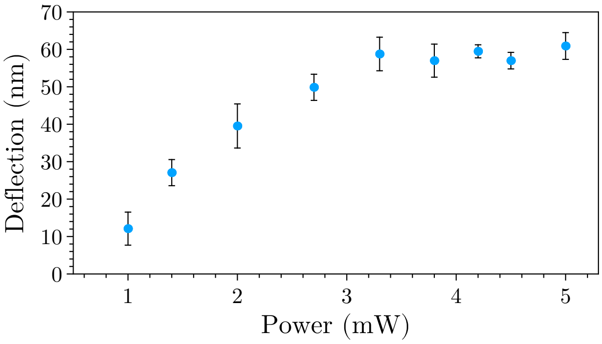

Figure 6.2: Thermally induced deflection of a nanowire as a function of the power of the feedback beam. The nanowire is the same as in Fig. 4.3a, with the data collected in atmospheric conditions. The deflection is measured by observing the change in the locked homodyne signal when the feedback beam is turned on. The amplitude is then calibrated by comparing it to the full size of the interference fringes observed during the scan of the homodyne phase, which corresponds to one wavelength.

perature in atmospheric conditions is estimated to be around 10 K for a modulated beam of 1 mW. In vacuum, where there is no air to facilitate the dissipation of thermal energy, the power required to achieve the same change in temperature is on the order of 100 µW. Such temperature increase is known to induce a thermal deflection of a few tens of nanometres on hybrid nanowires [163]. A direct measurement of how the power of the actuating beam affects the deflection is shown in Fig. 6.2. The error bars represent the standard deviation over sets of six successive measurements.

Thermal effects, including the bolometric force [164], are characterized by a finite response time which can sometimes be too slow for an appropriate control of the system. The actuation can be strongly affected by the delay due to a slow reaction, and the feedback force needs to be rectified by considering the convolution of the time derivative of the original signal with the nanowire's response function [94, 148]. Modelling an exponential response of characteristic time τ_{th}, the corrected feedback force is

$$F_{\text{fb}}(t) = -\zeta_\phi m \gamma_{\text{m}} \int_0^t dt' \, \ddot{x}_{\text{det}}(t') \left(1 - e^{-\frac{t-t'}{\tau_{\text{th}}}} \right), \tag{6.17}$$

implying a transfer function of the form

$$K(\omega) = -i \zeta_\phi m \gamma_{\text{m}} \frac{\omega}{1 + i\omega\tau_{\text{th}}}. \tag{6.18}$$

The new denominator in Eq 6.18 implicates a filter-like action that limits the bandwidth of the feedback to frequencies lower than $1/\tau_{\text{th}}$, reducing the overall effective-

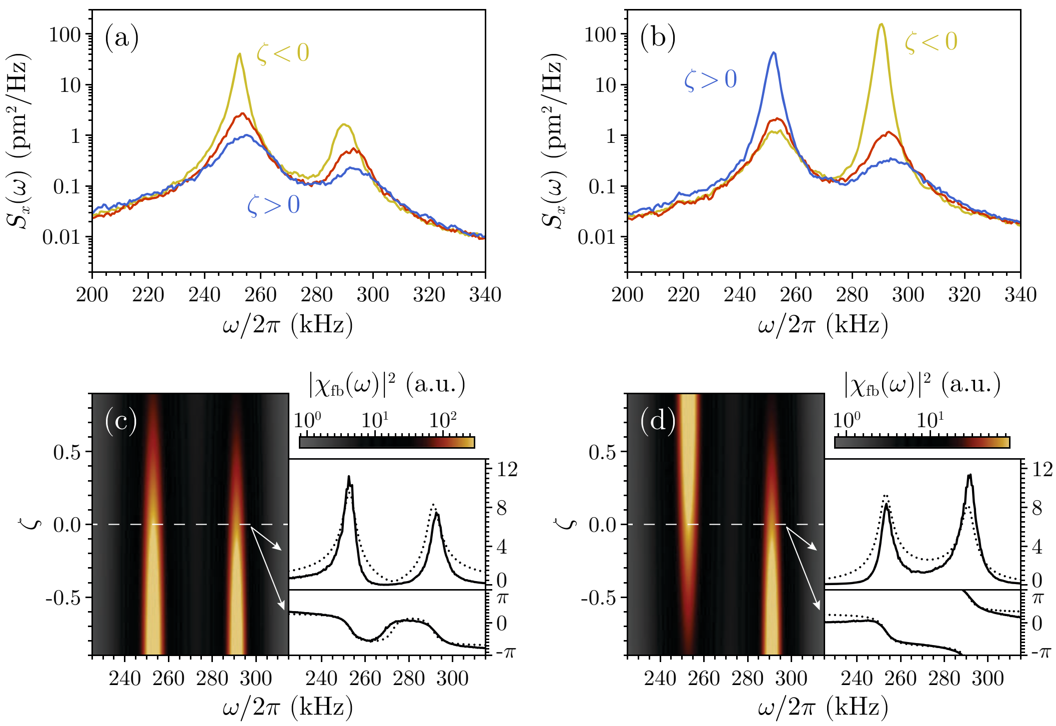

Figure 6.3: Response to feedback of a nanowire at different orientations. The nanowire is gold-coated, ≈ 50 µm in length and ≈ 300 nm in diameter, and it is always oriented at about 45° with the incident beam in order to detect the two spatially orthogonal modes together. **(a–b)** Displacement spectra in normal conditions (red) and when feedback is applied (blue for $\zeta > 0$, yellow for $\zeta < 0$). For one orientation (left), both modes are subject to cold damping when the gain is positive, and parametric amplification when the gain is negative. The other orientation (right), where the nanowire is rotated by 90°, sees the two modes alternatively damped or amplified in the presence of feedback. **(c–d)** Simulation of the nanowire's transfer function obtained by projecting the susceptibility $\chi_{\text{fb}}(\omega)$ of the two modes onto the detection axis. The density plot represents the combined transfer function as a function of gain ζ. The traces compare the experimental data obtained through a network analyser (solid lines) with the simulation (dotted lines) for both the magnitude (top) and phase (bottom) of the transfer function at $\zeta = 0$.

ness of the control. Fortunately, nanowires typically have much faster dynamics than macroscopic resonators, with characteristic times depending on radius r and thermal diffusivity D_{th} as $\tau_{\text{th}} \approx r^2/(4D_{\text{th}})$ [165]. Material properties and size strongly affect the thermal diffusivity, which can be almost two or three orders of magnitude smaller for nanoresonators compared to the bulk material [166, 167] due to phonon scattering overcoming the phonon-phonon coupling. Assuming an effective thermal diffusivity of approximately $10^{-6}\,\text{m}^2\,\text{s}^{-1}$, the characteristic time of the nanowire can be on the order of nanoseconds, substantially faster than the time scale of any eigenmode. The bolometric force may be employed reliably for feedback purposes, and Eq. 6.17 can be approximated to the expression considered in Chap. 6.1.1 without any inconvenience.

Unlike radiation pressure force, which always pushes the target in the direction of incidence of the beam, the bolometric force has a preferred axis which does not depend on the relative orientation of the nanowire and the beam. Being an indirect consequence of the absorption of optical energy, it is factors such as the specific geometry of the oscillator and its bimorph structure that determine the specific direction of the thermal deflection. The experimental proof for this comes from the mode-selective behaviour of the feedback: two spatially orthogonal modes have the same or the opposite response to the actuation depending on how they are aligned relative to the detection axis, as shown in Fig. 6.3. If the phase of the feedback is chosen to achieve cold damping of one mode, in one case the other mode will also be cooled down for the same phase. If the nanowire is rotated by 90°, the relative phase between the detected signal and the actuation will still be same for one mode, but opposite for the other. This occurs because the feedback-induced deflection does not depend on the orientation, whereas the measurement of the oscillations does.

6.3 Single- and multi-mode cooling of the nanowires

The cold damping technique is an appealing strategy for the suppression of the random thermal fluctuations in the mechanical system. If the issue of the measurement noise is addressed appropriately and the detection is sensitive enough to resolve the quantum fluctuations of the oscillator, the only limit to cold damping is technically set by the quantum zero-point energy of the oscillation [168]. Under these circumstances the bolometric force can be used, independently or in conjunction with radiation pressure force, to reduce the energy of the oscillator even towards its quantum ground state [169–171]. What happens may seem counterintuitive, as the mechanics are seemingly subject to "cooling by heating". However, it would be wrong to regard the oscillator as an autonomous system. The application of feedback stretches the extents of the system so that it encompasses an effective bath at lower temperature. This bath is strictly tied to the feedback loop, and the picture which considers only the energy being absorbed by the oscillator is incomplete. Examples of systems where photothermal forces have been used to cool down the vibrational modes, either by active control or passive self-cooling, include gold-coated microlevers [94,161], semiconductor membranes [172], and even graphene [173].

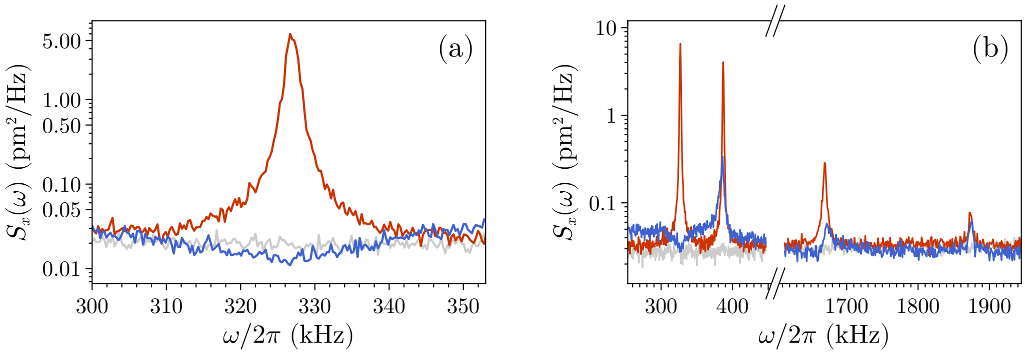

Figure 6.4: Displacement spectra of a nanowire subject to feedback cooling. The nanowire is ≈ 60 µm in length, ≈ 220 nm in diameter, gold-coated, and in vacuum. **(a)** Single-mode cooling. The amplitude of the thermal fluctuations (red) is suppressed down to the level of the background noise and beyond (blue), giving rise to squashing in the displacement spectrum. The grey trace indicates the detection noise in the absence of the nanowire. **(b)** Multi-mode cooling. The parameters of the feedback are optimized towards cooling of the mode with the lowest frequency, although in order to obtain cooling of the higher-order modes the phase of the feedback cannot be adjusted optimally and more measurement noise is injected into the system.

Examples of the spectral response of the nanowire when subject to cold damping are shown in Fig. 6.4. Feedback control can cool the nanowire's modes both individually and collectively. The practical limits of cold damping imposed by the measurement noise are reached with single-mode cooling, and for high gain squashing is observed (cf. Fig. 6.4a). For multi-mode cooling, besides the detection efficiency there are further limits set by the bandwidth of the feedback and more importantly the ability to control its phase across a wide spectrum of frequencies. The technical constraint to the bandwidth scales as the inverse of the characteristic response time $\tau_{\rm th}$, and is not found to be significant relative to the nanowire's modes. On the other hand, the feedback phase needs to be precisely tuned in order to achieve pure damping. Fine adjustments are only possible over a relatively small frequency range, and pushing more than one mode to the coldest temperature at the same time would only be feasible with the introduction of more advanced controls. Nevertheless, as Fig. 6.4b shows, the feedback implemented is capable of simultaneously cool modes spanning up to 2 MHz.

Figure 6.5 displays how cold damping of the vibrational modes performs as a function of the feedback gain. The results vary considerably depending on whether the nanowire is in ambient or in vacuum conditions. At atmospheric pressures, the additional dissipation due to the viscosity of the air molecules implies that more power is required to achieve the same levels of actuation obtained in vacuum. At low pressure

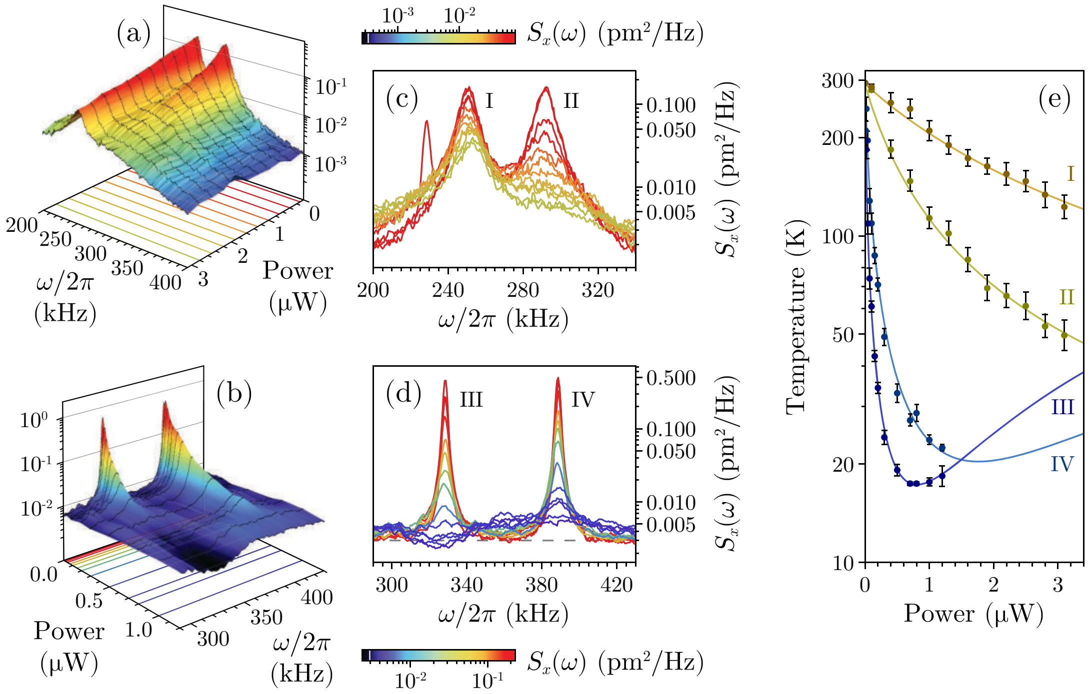

Figure 6.5: Cooling as a function of gain, which is controlled by the power of the feedback beam. The nanowires used correspond to the same as Fig. 6.3 for atmospheric conditions and the same as Fig. 6.4 under vacuum. **(a–b)** Spectrum of the thermal fluctuations for increasing power, in air (a) and in vacuum (b). The black mesh lines represent the individual traces, projected onto the bottom face with a colour corresponding to the peak value of the coldest mode. The detection noise level is indicated in the colour gradient scale by a grey line. **(c–d)** Front view of the spectra in (a–b), colour-coded according to the peak value of the coldest mode ("II" in air, "III" in vacuum). **(e)** The temperature of each mode, calculated according to Eq. 6.15. The error bars are estimated by propagating the uncertainty in the Lorentzian fit of the amplitude noise. The solid lines are theoretical fits assuming a linear relationship between the optical power of the feedback beam and the overall feedback gain. The resulting conversion factors between power and gain estimated for the four modes are 0.4 $\mu\mathrm{W}^{-1}$ (I), 1.6 $\mu\mathrm{W}^{-1}$ (II), 39.3 $\mu\mathrm{W}^{-1}$ (III), and 15.1 $\mu\mathrm{W}^{-1}$ (IV).

the quality factor of the oscillations is also much higher, rendering the entire procedure more effective. Starting from a room temperature of 293 K, the lowest single-mode temperature attained is (17.4 ± 0.2) K. In air it was only possible to cool down to (49 ± 5) K. It should be noted that, even under similar pressure conditions, different modes respond to feedback at different rates and one may be cooled more rapidly than the other. The degree of influence is determined by the spatial overlap of the modes with the direction of the bolometric actuation, which does not depend on the orientation relative to the feedback beam.

Typically a high gain, $\zeta \gg 1$, is needed to reach the lowest temperature. The electronic control of the gain, for example by variable amplifiers, risks introducing unnecessary noise and could contaminate the modulation. By varying the optical power of the actuating beam, instead, the regulation of the gain is transferred to the latest stages of the feedback loop, allowing more refined control over the system. This is the reason why the plots in Fig. 6.5 are expressed in function of the power of the feedback beam rather than the dimensionless gain parameter ζ. Naturally there is a limit to how much power can be delivered to the nanowire without damaging it, at which point other kinds of amplification become necessary. In vacuum, the power required for a productive actuation is low enough that the minimum possible temperature for a single mode is attainable well within the safety limits.

The results obtained are far from any regime where the oscillator would be expected to be near its quantum ground state. For a mechanical frequency of 300 kHz, the temperature needed to reach a phonon occupation number smaller than 1 is estimated to be around 20 mK, orders of magnitude away from the capability of our system. If the same experiment were to be repeated in cryogenic conditions, an extremely challenging initial temperature on the order of a mK would be required to observe the nanowire governed by its quantum fluctuations. Improvements in the detection process would also be very valuable, since a reduced measurement noise brings lower temperatures within the reach of the feedback. Similarly, other factors such as a higher mechanical quality factor can also help to lower the minimum bound of the temperatures achievable set by Eq. 6.16. At any rate, regardless of how close or far the nanowire is from its quantum state, feedback cooling provides a practical technique for quenching the thermal noise of the vibrations. This can provide a strategic advantage when the resonator is used to probe external signals, although an actual signal-to-noise ratio enhancement is only possible in the transient regime after the feedback is turned off and does not suppress the noise and the signal alike. The next chapter will focus on the exact conditions under which the sensor capabilities of the nanowires are improved.

Chapter 7

Sensitivity enhancement

7.1 Improving the signal-to-noise ratio using feedback

Whether or not a mechanical oscillator used as a measurement probe may benefit from the application of feedback cooling is a subject that requires careful examination. The reduction in thermal noise resulting from cold damping is not, in itself, an advantage towards the sensitivity of the system. The control does not distinguish between the noise and a possible external signal, and both are equally suppressed by the cooling process. It is the time scale of the measurement, instead, that takes advantage of the introduction of feedback control. In the steady-state dynamics of the oscillator, when the measurement integration time τ_{det} is much greater than the correlation time γ_{m}^{-1}, the probing resolution of the system scales as $\sqrt[4]{\gamma_{\mathrm{m}}\tau_{\mathrm{det}}}$ [121, 157]. This is quite inefficient, and in general long integration times might be required to reach a specific resolution. The feedback, however, has the effect of extending the narrow-band dynamics of the mechanical resonance onto a much larger bandwidth thanks to an effectively larger damping rate, meaning that a shorter time is needed to achieve the same resolution. The signal-to-noise ratio (SNR) is unaltered, but the measurement becomes faster by a factor equal to the ratio between the intrinsic and the effective damping rates, $\gamma_{\mathrm{eff}}/\gamma_{\mathrm{m}}$, which is proportional to the feedback gain.

It is interesting to note that there is no physical requirement for the implementation of stationary linear feedback, which could instead be simulated by appropriate data processing strategies [155]. In the case of force sensing, the entire feedback process may be reproduced by the application of an inverting module and a band-pass filter to the original measurement record. The inversion converts the displacement observed into a corresponding force by deconvolution of the dynamics from the oscillator's susceptibility, while the filter cuts off the noise which is far from the frequency band of interest to minimize the contamination of the results. This off-line virtual feedback is only an example of the possible estimation strategies, which also include other filtering techniques such as Kalman or Wiener filters [174]. A scheme using off-line data processing would only be limited by the bandwidth over which the thermal fluctuations overcome the overall detection noise, and could even be closer to optimal than schemes using real-time feedback thanks to the removal of any hardware constraints. Ultra-sensitive nanomechanical resonators are subject to increased measurement noise [175,176] which could change the parameters of the system and still entail the need for real-time tracking.

In a stationary regime, then, feedback cooling leads to a reduction in the integration time which in most cases can, however, be fully simulated and optimally integrated off-line by data processing and estimation techniques. But what if the signal to measure is brief or impulsive? In this case having the integration time span over the steady-state fluctuations would not make the system more sensitive, since the signal to be detected would be long gone. It has been suggested, however, that the actual SNR can be enhanced by feedback control when the oscillations are in the transient regime [154,158, 177], and once more feedback leads to an advantage in the sensitivity. Whether a similar or even better advantage can again be obtained by the relevant estimation strategies is not straightforward. Because of the non-stationary character of the oscillations it is not possible to extract the signal by a simple deconvolution as described before, and a more refined approach is necessary. The nanowire setup provided a good platform to test the SNR enhancement obtained in the transient regime [16], allowing the comparison of the sensitivity enhancement obtained by two off-line data processing techniques, which are presented in Chap. 7.2, with that obtained by physical feedback. The cooling scheme had to be specifically reorganized to be periodic, so that it would be turned on prior to the measurement and off during the measurement. The remaining part of this section outlines the experimental details of this *periodic quiescence* feedback technique.

7.1.1 Periodic quiescence feedback

The sensitivity advantage in the transient regime by real-time feedback is attained by regularly turning the cooling actuation on and off, according to the cyclic structure represented in Fig. 7.1. The periodic quiescence allows the nanowire to cycle between a state of overdamping and one of re-thermalization. Since the signal time τ_{sig} is assumed to be much shorter than the thermalization time γ_{m}^{-1}, which strictly depends on the intrinsic damping of the oscillations, the measurement of the signal is not significantly affected by the thermal noise until the new steady-state of the oscillations is reached. In vacuum conditions, where the intrinsic damping rate of the nanowires is $\gamma_\mathrm{m} \lesssim 1\,\mathrm{kHz}$, the integration times τ_det can last up to 1 ms. In particular, the linewidth of the nanowire used was measured to be roughly 0.8 kHz. The total duration of one cycle is set at 2 ms, although thanks to a faster temporal response of the nanowire to feedback (regulated by γ_eff^{-1}) it is generally possible to reach the cold-damped steady state more promptly than the thermalized state, and the total duration of the cycle could be optimized to be much shorter. The periodicity of the actuation is imposed by gating the feedback modulation rather than the full field amplitude of the feedback beam, so that the steady-state impact of the driving force is kept constant throughout the process.

To enact the incoherent force signal to be measured, a dedicated laser beam is sent to the nanowire in addition to the feedback and the detection beams. The wavelengths of the three lasers are all different to avoid any interference, although the signal's is close to the feedback's in order to achieve a similar influence. The amplitude of the signal beam is gated by an AOM to produce a 0.1 ms optical square pulse, modulated at the mechanical frequency ω_m, which is sent to the nanowire right after the feedback is

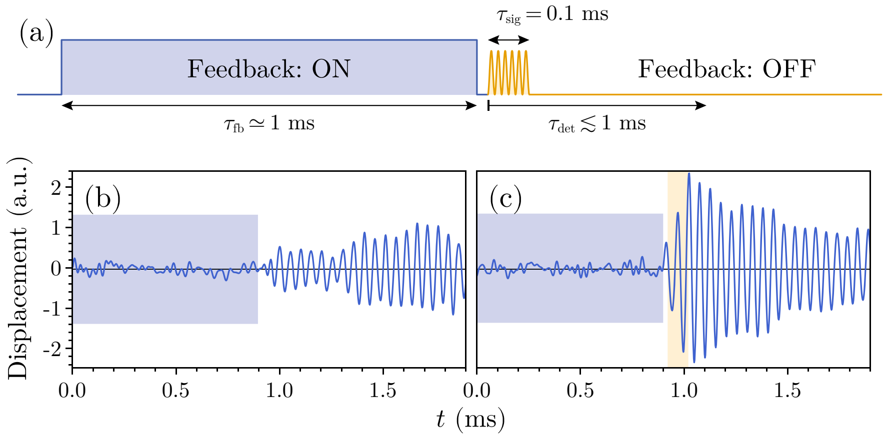

Figure 7.1: The cycle of periodic quiescence feedback. **(a)** Diagram of the cycle. During the first half of the cycle, feedback cooling is applied to increase the damping attributes of the nanowire. After about 1 ms, the control is turned off and the nanowire is allowed to re-thermalize. Before full thermalization, while the nanowire is in the transient regime, an optical pulse long 0.1 ms is sent to the oscillator to reproduce an external impulsive force. The integration of the measurement begins right after the feedback is turned off and can last up to 1 ms. **(b–c)** Examples of evolution of the oscillations during one cycle without (b) and with (d) the application of the external signal. The blue-shaded area represent the cooling interval, and the orange-shaded area stands for the duration of the impulsive drive. The traces have been frequency-filtered for clarity of illustration. The nanowire used is the same as that of Fig. 6.5.

turned off. After the impulsive force is introduced, the SNR is estimated by integrating the energy of the oscillator and comparing it to the thermal noise in the absence of the signal. A similar analysis is performed with the feedback turned permanently off to assess how much the SNR has been enhanced compared to normal conditions.

The diagram of the implementation of periodic quiescence feedback in Fig. 7.1 is followed by two examples of the time-domain evolution of the oscillations during one feedback cycle, once without and once with the external signal. The amplitude of the oscillations, subdued in the first half of the cycle by the feedback, is substantially amplified by the arrival of the incoherent force before it decays back to the steady-state size of the thermal fluctuations. The use of feedback before the arrival of the signal allows the amplification to stand out much more above the noise than it would in ordinary conditions, leading to the SNR enhancement. The full results are reported in Chap. 7.3 where the enhancement is compared with the one obtained using virtual estimation techniques.

7.2 Off-line processing

The problem of optimal estimation in the pursuit for better sensitivity is relevant to many fields of research, including optomechanics [154,178], atomic force microscopy [156], and gravity wave detection [179–181]. Given the assortment of systems under consideration, it is fair to assume that direct access to the inner dynamics in order to modify them by active control is not always allowed. When the physical implementation of feedback is challenging or altogether impossible, one can resort to off-line processing strategies of the data to replicate similar advantages in sensitivity [155]. This is also an option for the case when real-time feedback is possible, but it operates sub-optimally because of limiting conditions.

In this section we focus on two distinct filtering techniques for the enhancement of sensitivity in the transient regime: *virtual feedback*, which simulates the effects of physical feedback on the raw measurement record, and the *extended Kalman filter*, which uses a preliminary tracking of the oscillations to predict how the system would consequently evolve. Both schemes are applied to periodic cycles reminiscent of the one used for periodic quiescence feedback. Now, however, the temporal evolution of the oscillations is recorded without the presence of feedback control, letting only the signal interact periodically with the nanowire.

7.2.1 Virtual feedback

The dynamics of the oscillator are well known, and so is the response to the potential application of feedback. With this knowledge it is possible to estimate what the evolution of the oscillator would be at any specific point in time, even during the transient regime. Deviations from the expected behaviour can then be used to infer any external influence, such as the signal to be detected.

Because we are interested in the simulation of linear feedback, we consider the force in the time domain to be linearly dependent on the position's measurement record as

$$F_{\mathrm{fb}}(t) = \int_0^t dt' \; K(t,t')x(t'), \tag{7.1}$$

where $t = 0$ is taken to be the starting time of the feedback cycle and $K(t,t')$ is the kernel of the transformation applied by the feedback, which in steady-state conditions leads to the transfer function $K(\omega)$ considered in Chap. 6.1. The kernel is assumed to be of the form $K(t,t') \simeq K_0\Theta(\tau_{\mathrm{fb}} - t')\delta(t-t')$, where K_0 is proportional to the dimensionless feedback gain ζ, τ_{fb} is the length of the time interval where feedback is applied, $\Theta(t)$ is the Heaviside step function, and the presence of a Dirac delta function is justified by the fast characteristic time of the nanowires which allows the feedback to be considered instantaneous. The response at time t due to the state of the system at time t' is obtained by convolving the feedback kernel with the mechanical susceptibility

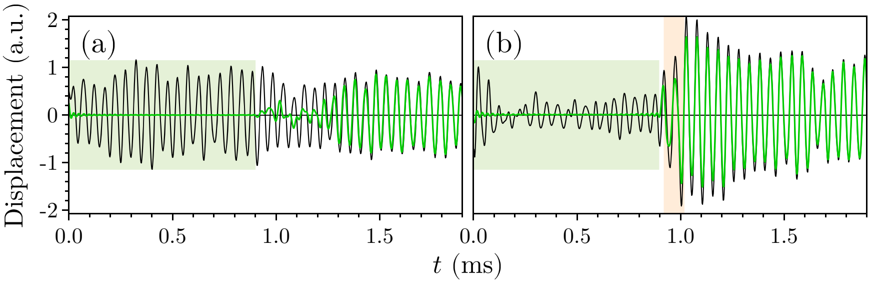

Figure 7.2: Simulation of the oscillator's dynamics with virtual feedback, without (a) and with (b) the application of an external signal to be detected. The black traces correspond to the experimental measurement record of the displacement. The green traces are obtained by applying the virtual feedback scheme during the first half of the cycle (green-shaded area). In this interval the oscillations are substantially reduced in amplitude, as if regular feedback were used. The orange-shaded area indicates the arrival of the external signal. As in Fig. 6.5, the traces have been filtered for illustration purposes.

of the oscillator,

$$H(t,t') := \int_{-\infty}^{+\infty} dt''\ K(t'',t')\chi_{\mathrm{m}}(t-t''). \tag{7.2}$$

This function can be used to simulate the feedback process, since it can be shown that the simulated displacement x_* satisfies the Fredholm equation of the second kind

$$x_*(t) - \int_{0}^{+\infty} dt'\ H(t,t')x_*(t') = x(t), \tag{7.3}$$

where x is the position measured in the absence of feedback [155]. Post-processing of x can therefore produce a record which simulates precisely what would have been measured if a real-time feedback scheme had been employed.

To solve Eq. 7.3, the full 2 ms length of a cycle is discretized into 1000 time steps of 2 µs. The response function H is then treated as a 1000×1000 matrix, $\mathbb{H}$, the measured position x and the simulated position x_* are respectively regarded as the input and the output vectors, $\mathbf{x}$ and $\mathbf{x}_*$, and the integration is carried out by the expansion of the matrix product. The solution for $\mathbf{x}_*$ is then found by numerically solving the approximated equation

$$\mathbf{x}_* = (\mathbb{I} - \mathbb{H})^{-1}\,\mathbf{x}, \tag{7.4}$$

where $\mathbb{I}$ is the identity matrix.

Figure 7.2 shows how post-processing changes the measurement record to simulate ideal periodic quiescence feedback. The numerical estimation from Eq. 7.4 is applied throughout the first half of the cycle, mimicking the cold damping effect of active control. In the second half the trace is allowed to converge back to the original fluctuation measured. The initial parameters of the simulation are estimated in the following way: first the gain is varied in order to maximize the SNR obtained using the parameters estimated from the raw data, then the values of the parameters are repeatedly adjusted in order to maximize the peak SNR. The final values used for the results in Chap. 7.3 are $\omega_{\mathrm{m}} = 2\pi \times 339.722\,\mathrm{kHz}$, $\gamma_{\mathrm{m}} = 2\pi \times 0.85\,\mathrm{kHz}$, $\tau_{\mathrm{fb}} = 0.896\,\mathrm{ms}$, and $K_0 = -1.6784 \cdot e^{-0.00004i}\,\mathrm{nN\,m^{-1}}$.

7.2.2 Extended Kalman filter

The Kalman filter is an optimal estimator algorithm which can be applied to linear systems to predict their evolution from their historical record [182–184]. Given a series of measurements affected by noise, the Kalman filter can be used to keep track of the underlying state by finding the statistically optimal estimate. The Kalman filter is optimal in the sense that it minimizes the mean square error of the estimated parameters. However, according to theory the best use of the measurements towards the estimation is achieved under the conditions that the noise entering the system is Gaussian and that the linear model faithfully reflects the full dynamics. For transition models, the extended Kalman filter (EKF) [185] represents the standard prediction technique to be used. The EKF is an adaptation of the Kalman filter to non-linear processes by linearization around the estimated state.

To implement the EKF scheme, the model requires knowledge of the natural oscillation frequency, the damping rate, the initial amplitude and velocity, the time interval, the process and measurement noise vectors, and the initial covariance estimates. The system's state is stored as a vector containing the oscillator's position x, the velocity $\dot{x}$, the damping ratio $\gamma_\mathrm{m}/\omega_\mathrm{m} = 1/Q_\mathrm{m}$, and the mechanical frequency ω_m. The algorithm also keeps track of a covariance matrix which describes the uncertainty in this state vector. At each time step of 2 µs the filter acts in two stages: "prediction" and "update". During the "prediction" stage the state of the system is propagated to the next step using the Runge-Kutta approximation (RK4), which determines the future value by adding to the present signal the weighted average of four increments (each given by the product of the time step interval with the derivative of the state vector). This method is used to estimate the evolution of the state for a short time into

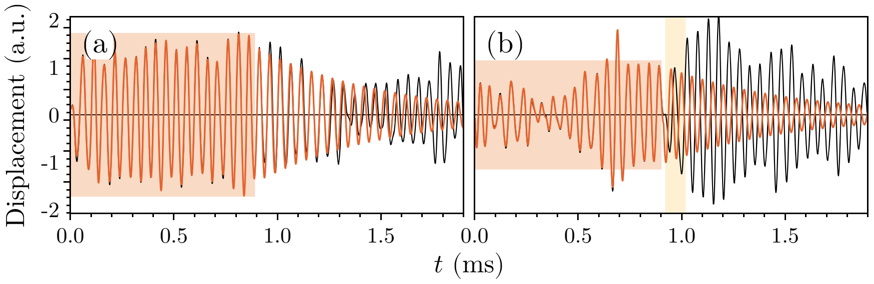

Figure 7.3: Prediction of the oscillator's dynamics by the extended Kalman filter algorithm, without (a) and with (b) the application of an external signal to be detected. The original measurement record of the displacement obtained experimentally is shown in black. The red traces correspond to the optimal estimate obtained by the EKF scheme. After tracking the original record for the first half of the cycle (red-shaded area), the algorithm stops updating and the state predicts normal decay at the thermal relaxation rate. The orange-shaded area indicates the arrival of the external signal. As in Fig. 6.5, the traces have been filtered for illustration purposes.

the future. In the "update" stage, the estimated evolution is refined using the actual measurement results together with the known measurement and process noise vectors. After comparing the prediction to the measured value, the estimated state vector is updated to reduce the difference between the two. The discrepancy is calculated according to the relative uncertainties, giving more weight to either the measurement or the estimation depending on which quantity has the lower uncertainty. After the two stages are complete, the estimated state vector is used as the initial state for the next time step. After about 1 ms, just before the optical pulse arrives, the "update" stage is switched off to let the EKF predict the subsequent evolution. The prediction is expected to be a reliable estimation of the phase-space trajectory of the oscillation, and the presence of an external stimulus can be deduced by looking at the deviations from the expected behaviour. The phase-space distance between the measured and predicted trajectories in the absence and in the presence of the impulsive force is used to evaluate the amplitudes of the signal and of the noise, respectively, which are then used to calculate the SNR.

As the virtual feedback scheme, the EKF requires precise definition of the parameters of the system. The initial values inferred from the raw data are iteratively adjusted across a very narrow parameter range in order to maximize the resulting SNR of the filtered trajectories. This procedure returned best results for the final values of $\omega_\mathrm{m} = 2\pi \times 339.9\,\mathrm{kHz}$ and $\gamma_\mathrm{m} = 2\pi \times 0.53\,\mathrm{kHz}$.

7.3 Comparison of the enhancement

The experimental data is collected as four sets of homodyne signals recorded at the rate of $25\,\mathrm{MS\,s^{-1}}$. Each set comprises a statistically significant number of traces for the nanowire's evolution with and without real-time feedback control, and in the presence or absence of the impulsive force. All traces are spectrally filtered to restrict the signal to a 40 kHz bandwidth around the mechanical frequency.

The outcomes for the SNR and the corresponding enhancement resulting from the various schemes are presented in Fig. 7.4. For physical feedback, the SNR is calculated by integrating the energy of the oscillations from the data with both feedback and impulsive force and dividing the result by the average integral of the energy from the data with feedback but without the application of the external signal. For the two filtering schemes a similar approach is applied to the data without feedback, although the SNR is evaluated by the phase-space distance between the observed and the pre-

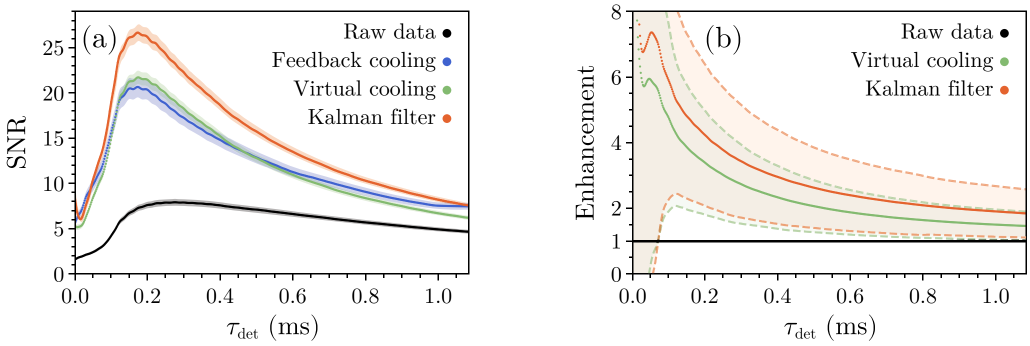

Figure 7.4: Signal-to-noise ratio enhancement for the schemes considered. **(a)** Measurement of the SNR of the impulsive force, without (black) and with (blue) feedback cooling. The SNRs for the two off-line processing strategies (virtual cooling in green, extended Kalman filter in red) are both calculated from the same data set without feedback. The shaded regions represent the standard error. **(b)** Enhancement in SNR of the two estimation techniques, calculated as the ratio of the SNR improved by the relative scheme with the SNR obtained from the raw data. The dashed lines indicate the standard deviation in the estimated enhancement.

dicted trajectories rather than the integral of the oscillator's energy. All the results are averaged over 150 traces, and the uncertainty is assigned according to the standard error (Fig. 7.4a) or the standard deviation (Fig. 7.4b).

For the specific schemes employed the SNR peaks after about 0.2 ms of integration time. For longer times the SNR degrades with a rate corresponding to the mechanical decay time as the thermalization of the oscillator starts to prevail. In this transient regime feedback cooling achieves a maximum SNR of about 20, more than double than the value obtained without feedback. In particular, physical cooling is shown to be roughly as effective as the virtual cooling, indicating near-optimal actuation of the nanowire. After about 0.4 ms, real-time feedback shows even a slightly higher improvement than its virtual counterpart. This is likely due to the fact that laser noise may affect the system's parameters within the time scale of the measurement, a factor that cannot be tracked by the filtering technique but would automatically be accounted for by active control. The extended Kalman filter algorithm outperforms all other strategies.

The ratio of the SNR from filtered and raw data gives the enhancement factor (Fig. 7.4b). This quantity, calculated on a trace-by-trace basis for the filtering techniques, cannot be similarly calculated in relation to physical feedback since the cooling action would need to be reverted, which is impossible. For this case, the enhancement might only be defined in terms of an average of the SNR over all traces without feedback, but this method does not allow an evaluation of the standard deviation and the

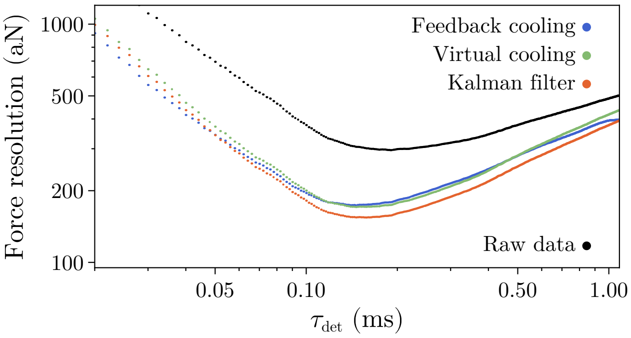

Figure 7.5: Force resolution as a function of integration time for raw, feedback, and filtered data, as processed from Eq. 7.7.

outcome may not be as reliable.

To calculate the force sensitivity of the system, we model a signal applying a monochromatic force of amplitude F and frequency $\omega_{\rm m}$ for the duration of an interval long $\tau_{\rm sig}$ which drives an oscillation

$$x(t) = \int_0^{\tau_{\rm sig}} dt'\ F \sin(\omega_{\rm m} t')\chi_{\rm m}(t-t'). \tag{7.5}$$

The uncertainty on x is obtained by looking at its variance over the duration of the measurement,

$$\sigma_x^2 = \frac{1}{\tau_{\rm det}} \int_0^{\tau_{\rm det}} dt\ \left| \int_0^{\tau_{\rm sig}} dt'\ F \sin(\omega_{\rm m} t')\chi_{\rm m}(t-t') \right|^2 . \tag{7.6}$$

Inverting this relation, we find that the smallest force detectable is

$$F = \sqrt{\frac{\tau_{\rm det}\sigma_x^2}{\int_0^{\tau_{\rm det}} dt\ \left| \int_0^{\tau_{\rm sig}} dt'\ \sin(\omega_{\rm m} t')\chi_{\rm m}(t-t') \right|^2}} . \tag{7.7}$$

The resolution attainable by the nanowire is shown in Fig. 7.5. The best sensitivity is achieved between 0.1 and 0.2 ms, in correspondence with the point of maximum SNR. A force as small as 200 aN can be resolved if any of the enhancement strategies is implemented, and as suggested before the extended Kalman filter delivers the best advantage.

Conclusions. The investigations based on optically induced thermal actuation demonstrate promising capabilities of the nanowires as sensitive force sensors. High resolution and fast force response are important qualities in bio-sensing applications where the dynamics can change rapidly and long integration times are not accessible.

The resolution in short transient regimes can be enhanced without foregoing any other trait if cold damping feedback is used, and the flexibility of the single-pass, low-power implementation is particularly relevant to biological samples that cannot be exposed to global refrigeration. The sensing performance can also be improved by the use of off-line processing techniques rather than active control of the nanowire. Estimation by filtering algorithms stand out as a viable alternative which removes the need for any feedback hardware while providing a similar or even better sensitivity advantage. A final verdict on which strategy is best, however, is only possible based on the specifics of the system. Incomplete knowledge of the probe's dynamics, untracked perturbation of the parameters, and insufficient computational power can all be factors that may favour real-time feedback over off-line processing. As an example, even a 0.1 % perturbation of the value of the natural frequency used as an input to the filter may significantly affect the SNR obtained. Such a change in frequency could easily occur through a change in the bulk temperature of the oscillator. From a more fundamental perspective, it should also be remembered that estimation strategies are based on a linear modelling of the system. While physical feedback is directly adapted to any non-linearities in the oscillation, it is not straightforward to retrieve a similar response from virtual feedback, and even the linearization of the extended Kalman filter scheme could fail when the non-linearity is too pronounced. Which technique results more convenient between physical feedback and off-line filtering techniques depends on whether the system is easily simulated and what kind of resources are available.

Part III

Towards optical levitation of a macroscopic mirror

This Part is devoted to a scheme for state-of-the-art metrological applications based on the optical levitation of a macroscopic mirror by the intra-cavity field of three optical resonators. Presenting the idea from its earliest formulation to the realization of a pilot experiment, the feasibility of the scheme is explored from both a conceptual and a practical point of view. Chapter 8 starts with a snapshot of the current scene in optical levitation, makes the case for measurements in suspended systems, and motivates the development of coherent levitation. It then continues with an explanation of how the optical spring effect can be used to obtain ideal isolation of the system and what other elements may obstruct its accomplishment. Chapter 9 enters into the technical details of the apparatus and describes the factors leading to the specific tripod configuration considered. In Chapter 10 we conclude with the preliminary results from the first trials and report on suggestions and priorities of potential upgrades based on what has been learned.

The research presented here has been featured in the following publication:

- [14] Guccione, G., Hosseini, M. et al., "Scattering-Free Optical Levitation of a Cavity Mirror", *Physical Review Letters* **111** 183001 (2013).

Upholding something can be a momentous task, as demonstrated by Atlas. According to Greek mythology, the Titan, brother of Prometheus and Menoetius, has to endure for all eternity the burden of the heavens upon his shoulders.

J. S. Sargent, *"Atlas and the Hesperides"*

Chapter 8

Conception and development of the scheme

8.1 The current scene in levitation

Levitation, the chance to defy the pull of gravity and hover free from tangible constraints, has held a place in mankind's aspirations for as long as historical records can confirm. Even today, with countless aircraft weaving trails through the skies and astronauts regularly experiencing weightlessness in a permanently occupied space station, the levitation of ground-based objects can still induce awe and inspiration in the general public. As with any other phenomenon, however, the interest on levitation would be quite short-lived if it had to depend merely on its wonder factor. The shift from novelty devices used to demonstrate physical principles to practical engineering tools with functional applications is nowadays being completed by more and more levitated systems. Levitated trains are a notable example [186], using the action at a distance from permanent electromagnets or superconducting circuits to guarantee fast, friction-less transportation. Other examples include contact-free manipulation of small particles by acoustic standing waves [187,188], and "levitation" of graphene using oxygen intercalation to lift and decouple the structure from a metal substrate [189].

Optical levitation dates back to the early 1970s, when micron-sized dielectric particles were trapped by radiation pressure force alone for the first time [190, 191]. The technique, now known as *optical tweezers* [192–194], exploits the high refractive index of the particle to deflect the beam and produce a back-action force that pushes the object towards the point of highest intensity, the focus. Since the first experiments the development of optical tweezers has been fuelled by continuous upgrades, which include single beam realization over diverse scales [195] and the broadening of the trapping range thanks to regenerative Bessel beams [47]. Advancements continue even to

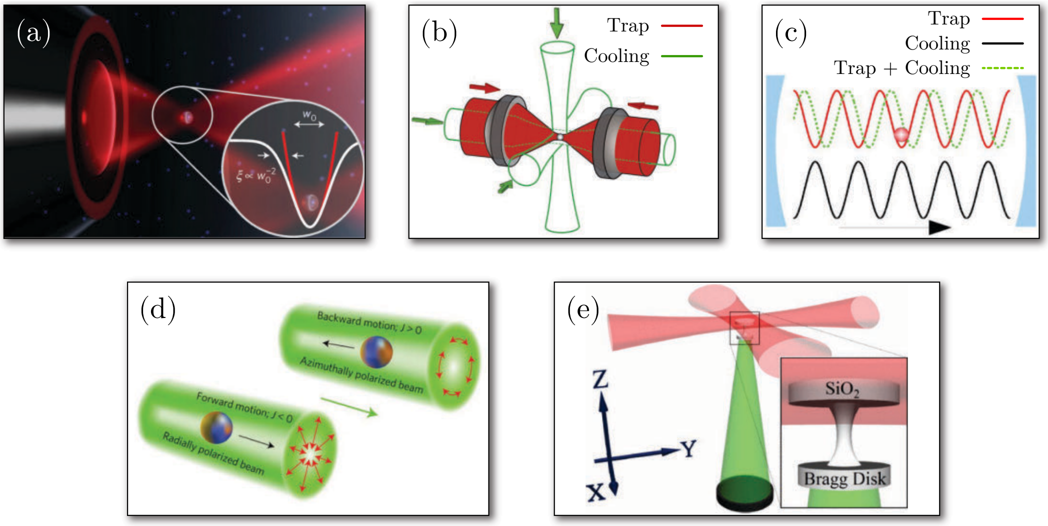

Figure 8.1: Only few of the many examples of optically levitated systems. **(a)** The principle of optical tweezers uses the intensity gradient to trap particles in the focus of the beam [199]. **(b)** Multiple optical tweezers along the three axes create an “optical molasses” that cools the centre-of-mass motion of the particle [152]. **(c)** Doubly resonant optical cavities can also create a trapping potential for tiny particles [200]. **(d)** In air, photophoretic forces allow manipulation of objects on a much bigger scale [198]. **(e)** A proposed system based on a cavity mirror attached to a silica disk which is suspended by two optical tweezers [97].

this date, for example with the establishment of robust techniques to deliver particles to high-vacuum environments [196]. Photophoresis can provide an alternative method of levitation for particles that are not required to be in vacuum conditions: the non-uniform heating of the air surrounding the particle causes the gas molecules to rebound off the surface with different velocities, producing a net force that can trap bodies several order of magnitude heavier compared to the particles lifted by radiation pressure force [197, 198]. A collection of representative systems based on optical levitation is shown in Fig. 8.1.

The success of optical levitation is largely attributable to the flexibility it provides in manipulating objects without direct contact [201, 202]. The technique is virtually suitable for anything ranging from single atoms to particles of a few micrometres in size, and has been successfully applied to manipulate DNA molecules [203] and colloidal systems [204, 205]. By transferring the orbital angular momentum of light onto the particle, it is possible to rotate and manoeuvre micro-machines [206] and micro-gyroscopes [207]. One could even think of using optical tweezers to operate a microscopic steam engine [208], evidence of the fact that only inventiveness poses a limit to the versatility of optically levitated systems.

Trapping in an optical potential makes particle's centre of mass behave like a harmonic oscillator. Thanks to the complete detachment from any mechanical support, which removes a direct coupling to a thermal reservoir, these suspended oscillators demonstrate ideal qualities for optomechanics experiments. In principle, in high vacuum the mechanical damping rate γ_{m} could be reduced almost indefinitely and the mechanical quality factor $Q_{\mathrm{m}} = \omega_{\mathrm{m}}/\gamma_{\mathrm{m}}$ of the centre-of-mass motion could become higher than 10^{12} [200] once it is decoupled from the internal degrees of freedom. A long coherence time and a high quality factor would make techniques like laser cooling, state transfer, and quantum superposition incredibly accessible [209].

Multiple approaches could be considered in connection to laser cooling. Doppler cooling along the optical axis can be achieved if the levitated particle enables resonance of whispering gallery modes around its perimeter [210]. A combination of three cooling beams encompassing all three spatial directions generates an "optical molasses", an expression derived from the viscous nature of the forces experienced by the levitated object. Any generic cooling technique can be applied to the principle of optical molasses, including modulation of the intensity of the trapping beam to realize active feedback damping rather than passive cooling [152, 153]. Alternatively, the principle of optical tweezers can be applied to suspend the object within an optical resonator, extending the possibility of passive Doppler cooling to any type of particle. With a doubly resonant arrangement, two optical fields can cooperate to simultaneously trap and cool the target [88, 211]. Sympathetic cooling by coupling of the levitated system with ultra-cold atoms has also been suggested to reach the quantum regime for macroscopic resonators with less demanding cavity requirements [212].

The absence of environmental noise makes levitated systems particularly useful platforms for metrological measurements. Force sensitivities down to a few $\mathrm{zN\,Hz^{-1/2}}$ have been accomplished by optically suspended nanoparticles [199], although feedback control is required to cancel the effect of thermal non-linearities that arise even at the lowest power in the absence of a thermal bath. Accurate measurements of temperature [213] and electric charge [214] are also possible, in the latter case with a resolution 10^{-5} smaller than the fundamental charge of the electron. A high-frequency gravitational wave detector based on optically trapped particles has also been proposed [215]. Levitated systems in general are particularly functional as accelerometers and gravimeters, and superconductive levitation of microspheres [216] or of magnetized macrospheres [217] has been suggested for long-term scanning of force gradients induced by surface gravity differentials.

Precision and sensitivity are critical for tests of fundamental physics. For instance, the extremely high resolution of levitated particles may be applied to the detection of short-range non-Newtonian forces or the characterization of Casimir interaction [218], and thanks to the availability of long integration times possible violations of the inverse-law of gravity may be expressly ruled out [219]. Oscillators that are completely decoupled from a thermal reservoir are more predisposed to anomalous dynamics which allow for example the study of non-equilibrium fluctuation theorems [220], important for chemical and biological processes based on irreversibility. The atypical susceptibility of levitated systems could in principle promote the achievement of strong coupling [221], also facilitating the observation of quantum dynamics. This leads to the inevitable appeal towards exotic operations such as matter-wave interferometry [222] and superposition of living organisms [223]. Other audacious proposals close the loop between fundamental physics and levitation by suggesting that repulsive quantum vacuum forces may be used to levitate an ultra-thin mirror [224].

Unavoidably, all the systems mentioned so far are affected by distinct limiting factors often tied to the levitation process itself. While certain noise processes may be monitored and counterbalanced by feedback control, such as classical laser amplitude noise in optical levitation, other effects may irreparably impair the measurements and hold back the sensitivity. Superconductive levitation suffers decoherence because of the generation of eddy currents, whereas optical tweezers are subject to scattering losses that become especially pronounced in cavity-enhanced systems. If the cavity is a pre-requisite for more refined sensitivity, a solution could be found by separating the trapping process from the measuring component. For example, two optical tweezers can be applied to a silica disk to trap it in the horizontal plane while balance in the vertical direction is obtained by the radiation pressure force on a cavity mirror attached to the disk [97] (cf. Fig. 8.1d). To completely eradicate scattering losses, however, a more extreme approach is necessary. The system that will be discussed in the following chapters, based on the fully coherent optical levitation of a cavity mirror [14], is designed to accomplish absolute detachment from the environment while preserving all of the information about the system. Using the resonantly amplified fields from three optical cavities in a tripod configuration, the weight of the common end mirror on top of the tripod can be cancelled by radiation pressure force. The trapping potential is provided by the optical spring effect, which induces restoring forces when the fields driving the cavities are blue-detuned with respect to resonance. Each "leg" of the tripod behaves like an extremely rigid spring, with the stiffness determined by the finesse of the corresponding cavity. Like levitated particles, the quality factor of the motional eigenfrequencies of the levitated mirror may grow to exceptionally high values in vacuum. Now, however, the read-out from all the cavities provides a complete picture of the state of the oscillator, making the system more robust and suitable for state-of-the-art applications.

8.2 Optical spring tripod

The idea of the optical tripod is founded around the radiation pressure of the intra-cavity fields of three Fabry–Pérot resonators, arranged in a vertical geometry as in Fig. 8.2. By letting the upper mirror act as the common end of the three cavities, the combined action of the radiation pressure forces provides a balancing force that can suspend the mass without the addition of any other support. To assist in the stability of the tripod the upper mirror is taken to be convex, so that its centre of mass lies level with the position of incidence of the cavity beams or below. Assuming the three cavities, labelled by the index $\nu \in \{1, 2, 3\}$, to be perfectly identical, and recalling the relationship between intra-cavity power and force from Eq. 3.58, one can derive that

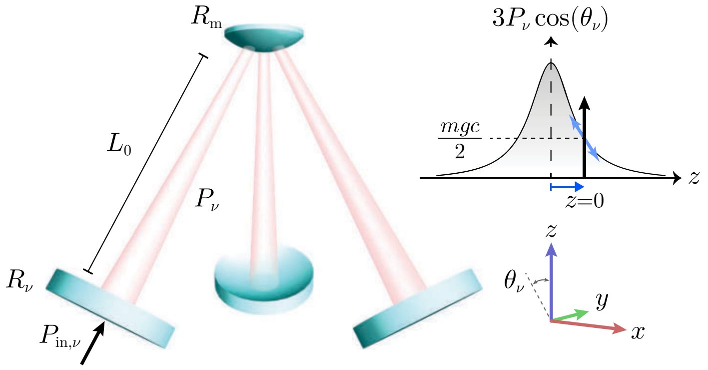

Figure 8.2: Concept diagram of the optical spring tripod. Three lower mirrors of radius of curvature R_ν and an upper mirror of radius of curvature R_m are aligned to form the three Fabry–Pérot cavities of length L_0 acting as the tripod legs. The coordinate system relative to the centre of mass of the upper mirror is shown in the bottom right, including the angle of the cavities from the vertical axis, θ_ν. The top right diagram is an outline of the cavity response as the upper mirror is displaced vertically. The input field (black arrow) is detuned so that the balancing condition is satisfied on the side of the resonance. When the mirror falls ($z < 0$), more power resonates inside the cavities to push it back, while the opposite happens when the mirror floats too high ($z > 0$). The derivative of the force, which is proportional to the power in the cavities, corresponds to the stiffness of the springs holding the mirror in place. The optical trap breaks if the mirror falls too far below resonance, where the spring becomes negative and the force turns anti-restoring.

the intra-cavity power P_ν required in each resonator to satisfy the balancing condition is

$$P_\nu^{(\mathrm{bal})} = \frac{1}{3\cos(\theta_\nu)}\frac{mgc}{2}, \tag{8.1}$$

where $g = 9.81\,\mathrm{m\,s^{-2}}$ is the surface gravitational acceleration, c is the speed of light, m is the mass of the mirror, and θ_ν is the cavity's angle from the vertical. Thanks to the resonant amplification of the cavities, the power available at the input of each leg of the tripod is used to lift a much heavier weight than otherwise possible. In addition, the coherent coupling with the cavities imprints the motion of the mirror directly onto the resonating modes without any added noise. Complete access to the state of the oscillator, unperturbed by scattering losses or mechanical supports, is paramount for applications based on detection efficiency, such as the measurement-based feedback seen in Chap. 6.

The equilibrium reached by the optical tripod would be short-lived if the forces had merely a balancing effect. To maintain the mirror floating on top of the cavity fields after a slight displacement, no matter how small, it is crucial to have the forces display restoring qualities. This can be realized by the optical spring effect, as blue-detuning of the input fields relative to the cavities' resonances generates a radiation pressure force gradient that confines the mirror to a specific region. Intuitively, detuning of the optical frequency to the side of the resonance ensures that if the mirror were to fall down, for example, the intra-cavity field would become more resonant and the mirror would be pushed back up by the stronger radiation pressure force. If the mirror moved too high, instead, the cavities would respond with a weaker force and the mirror would fall back to its original position. The angular aperture of the tripod projects this response to all three dimensions of space. Optical springs, occasionally employed to provide additional rigidity to weak mechanical springs [98, 137], are in this case involved for the full support of the mirror, which in the absence of mechanical attachments behaves like a free mass without an intrinsic frequency of oscillation. Because the trapping is entirely optical, appropriate tuning of the optical frequency and of the input power offers unprecedented flexibility on the system's parameters.

8.2.1 Stability potential

The stability of the mirror is best characterized by its potential energy $U(x, y, z)$, a function of the coordinates of the centre of mass oriented as in Fig. 8.2. A more generalized potential which also includes angles of rotation of the mirror is possible but unnecessary, since the symmetry of the spherical mirror is such that any small rotation around the centre of mass can be considered as a translation of the Cartesian coordinates. Should any torque instabilities arise, one can resort once more on the optical spring effect to reduce them and make the system more robust [225–227]. The potential is constructed by integrating the total force applied on the mirror $\mathbf{F}_{\text{tot}} = (F_x, F_y, F_z)$ over a path extending from the origin to the point $\mathbf{r} = (x, y, z)$:

$$U(x, y, z) := -\int_{\mathbf{0}}^{\mathbf{r}} d\mathbf{r}' \ \cdot \mathbf{F}_{\text{tot}}(\mathbf{r}'). \tag{8.2}$$

The path can be chosen arbitrarily as long as the forces are conservative. This is not strictly the case for the radiation pressure force once the finite response time of the cavity is taken into account, which introduces a viscous element to the dynamical back-action. The present analysis will presently ignore this fact and assume an undamped system subject to fully conservative forces in order to obtain an uncomplicated picture of the stability. The premises allowing such assumption will be justified in Chap. 8.2.3 with the introduction of dual cavity fields. With complete freedom of choice for the path of integration, the calculation can be simplified to the sum of three integrals along directions parallel to the axes:

$$U(x, y, z) = -\int_0^x dx'\ F_x(x', 0, 0) - \int_0^y dy'\ F_y(x, y', 0) - \int_0^z dz'\ F_z(x, y, z'). \tag{8.3}$$

The total force results from the combination of the gravitational weight of the mirror with the forces from the three cavities, $\mathbf{F}_\nu$:

$$\mathbf{F}_{\text{tot}}(x, y, z) = \begin{pmatrix} F_x(x, y, z) \\ F_y(x, y, z) \\ F_z(x, y, z) \end{pmatrix} = \begin{pmatrix} 0 \\ 0 \\ -mg \end{pmatrix} + \sum_\nu \mathbf{F}_\nu(x, y, z). \tag{8.4}$$

The action of each cavity is proportional to the power and aligned with the optical axes as

$$\mathbf{F}_\nu(x, y, z) = \frac{2P_\nu(x, y, z)}{c} \begin{pmatrix} -\cos(\varphi_\nu)\sin(\theta_\nu) \\ -\sin(\varphi_\nu)\sin(\theta_\nu) \\ \cos(\theta_\nu) \end{pmatrix}, \tag{8.5}$$

where the resonators' orientation is specified by the polar angle φ_ν, respectively 0, $2\pi/3$, or $-2\pi/3$, and the azimuthal angle θ_ν, identical for all three cavities. Since the upper mirror is shared by the three resonators, the three optical axes join at the former's centre of curvature. The angular aperture of the tripod is therefore $\theta_\nu \simeq \arcsin(d_\nu/R_\mathrm{m})$, where d_ν is the distance of the beam's spot from the origin and R_m the radius of curvature of the upper mirror. The general form of the intra-cavity power P_ν, recalled from Eq. 2.41, is

$$P_\nu(x,y,z) = \frac{\mathcal{T}_\nu}{1+\frac{4\mathcal{F}_\nu^2}{\pi^2}\sin^2(\phi_\nu(x,y,z)/2)}\frac{\mathcal{F}_\nu^2}{\pi^2}P_{\mathrm{in},\nu}, \tag{8.6}$$

where ϕ_ν is the round-trip phase shift of the cavity, $\mathcal{F}_\nu$ is the finesse, $\mathcal{T}_\nu$ is the transmissivity of the bottom mirror, and $P_{\mathrm{in},\nu}$ is the input power. The round-trip phase shift is concomitantly determined by how the detuning of the optical frequency Δ_ν compares to the free spectral range[1] ω_FSR and by how the length of the cavity compares to the half-wavelength $\lambda/2$:

$$\begin{aligned}\phi_\nu(x,y,z) &= 2\pi\left(\frac{\Delta_\nu}{\omega_\mathrm{FSR}}+\frac{\delta L_\nu(x,y,z)}{\lambda/2}\right)\\ &= \tau\left(\Delta_\nu + G_0\delta L_\nu(x,y,z)\right).\end{aligned} \tag{8.7}$$

Here, $\delta L_\nu(x,y,z) := L_\nu(x,y,z) - L_0$ is the difference between the cavity length when the mirror is displaced and the cavity length at rest, which is assumed to be a multiple number of $\lambda/2$. In the last line, Eq. 8.7 has been rearranged to reveal its connection with the cavity lifetime τ and with the optomechanical coupling constant G_0, which is equal to $2\omega_\mathrm{FSR}/\lambda$ for a Fabry–Pérot cavity. It should be noted that Eq. 8.6 is equivalent to the apparently simpler form of Eq. 2.60, with the only difference that the latter is obtained in a regime of small detunings while the former preserves the full periodicity over different free spectral ranges. The simpler expression is however convenient to determine the detuning required to satisfy the balancing condition of Eq. 8.1,

$$\Delta_\nu^{(\mathrm{bal})} = \pm\sqrt{\frac{3\cos(\theta_\nu)P_{\mathrm{in},\nu}\cdot 2\kappa_\nu/\tau}{mgc/2} - \kappa_\nu^2}, \tag{8.8}$$

where $\kappa_\nu = \mathcal{T}_\nu/\left(2\tau\right)$ is the linewidth of the cavity under the assumption that the upper mirror is fully reflective and the field only leaks out from the input mirror.

---

[1] Technically, the free spectral range depends on the length of the corresponding cavity and should also be indexed by ν. Here, however, ω_FSR and the related τ and G_0 are calculated at the origin where

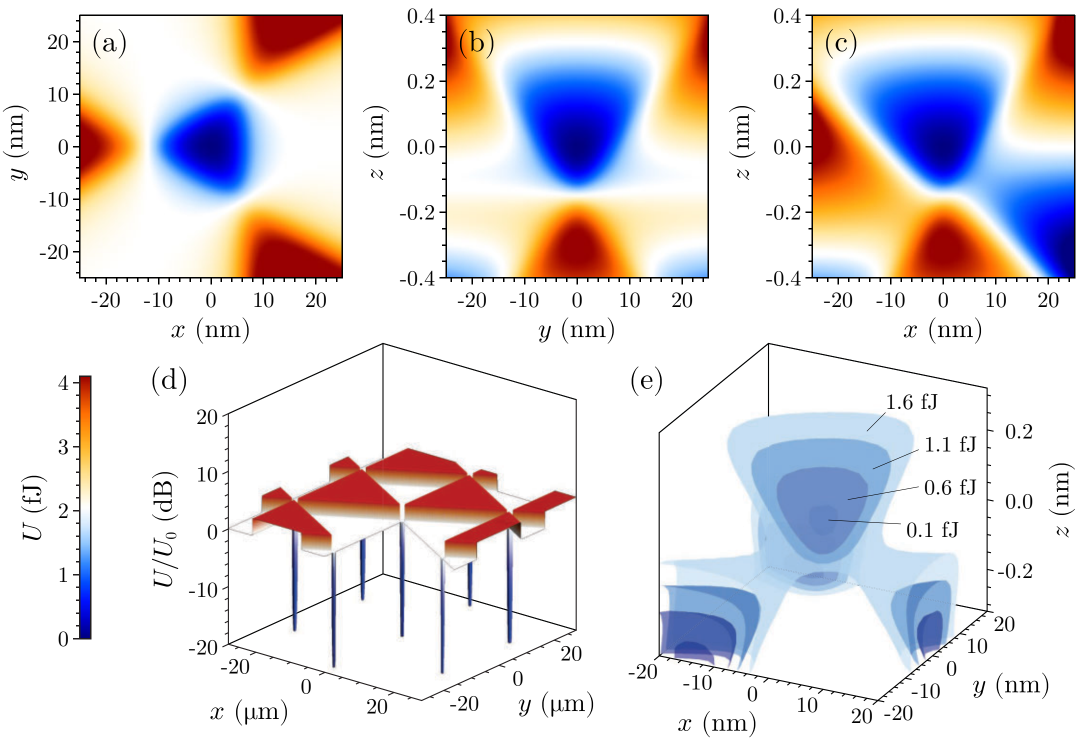

Figure 8.3: Potential energy of the tripod's upper mirror. **(a–c)** Planar cross sections of $U(x, y, z)$ passing through the origin, revealing a tight-confinement region. **(d)** Horizontal cut of the triangular lattice of trapping nodes, each similar to the one at the origin. The energy axis is expressed in a dB scale relative to the value of the potential just outside of the trapping region, $U_0 = 2\,\text{fJ}$. **(e)** Isopotential surfaces showing the confinement of the mirror in space. The mirror is trapped as long as its energy does not exceed $\approx 1\,\text{fJ}$. The parameters used are: $m = 1\,\text{mg}$, $\lambda = 1064\,\text{nm}$, $L_0 \approx 185\,\text{mm}$ rounded to the closest multiple of $\lambda/2$, $\mathcal{F}_\nu \approx 3100$ with the upper mirror fully reflective and the lower mirrors 99.8 % reflective, $\omega_{\text{FSR}} \approx 2\pi \times 810\,\text{kHz}$, $\kappa_\nu \approx 2\pi \times 130\,\text{kHz}$, $\Delta_\nu \approx 2\pi \times 230\,\text{kHz}$, $P_{\text{in},\nu} = 1\,\text{W}$.

From the calculation of the potential energy it emerges that the tripod configuration traps the upper mirror in a site whose dimensions depend on the tripod's aperture and the finesse of the cavities. The parameter regime used for the estimation shown in Fig. 8.3 displays a trap stretching approximately 20 nm horizontally and 0.3 nm vertically, for $\mathcal{F}_\nu \approx 3100$ and $\theta_\nu \approx 1.4°$ for all three cavities. The large discrepancy in size between the horizontal and the vertical directions is largely due to the narrow angular aperture chosen, which makes the three cavities close to vertical in order to maximise the component of radiation pressure force acting against gravity. The finesse is selected as a compromise between the size of the trap and the power required for levitation. A high finesse would allow an easier fulfilment of the balancing condition

---

the three cavities are taken to have equal length L_0.

with less input power, but at the same time the Lorentzian envelope of the cavity resonance would be narrower and the upper mirror would perceive the positive stiffness over a smaller domain. The mass of the mirror is 1 mg, which demands at least 1.5 kW of combined intra-cavity power to achieve levitation. The finesse considered is high enough that 1 W of input power per cavity would suffice to have enough circulating power even with detunings on the order of the linewidth.

A particularly remarkable feature is the recurrence of trapping sites at each free spectral range of the cavities, effectively creating a three-dimensional lattice of tight-confinement nodes (cf. Fig. 8.3d). The small dimensions of a each node should not be concerning, as they are simply determined by the extent of the cavities' resonance compared to the full free spectral range. Trapping within a stability node is equivalent to locking the cavity at or near resonance, a task that is regularly achieved with incredible precision. Despite the fact that the system should be self-stabilized once trapped, active feedback may nevertheless be opportune to ensure the simultaneous lock of the three cavities.

8.2.2 Stiffness and oscillations

Under the confining influence of the stability potential, the mirror's centre of mass is maintained close to the origin by the restoring action of the radiation. The stiffness of the three-dimensional optical spring, which depends on the direction of the displacement, is described by a second-order tensor [228] obtained as the Jacobian of the force from Eq. 8.4. The components of the stiffness tensor are, for $i, j \in \{x, y, z\}$,

$$\mathbb{K}_{ij}(x, y, z) = -\partial_i F_j(x, y, z). \tag{8.9}$$

The preferred directions of oscillation are inferred by diagonalizing $\mathbb{K}$. This task is automatically settled at the origin, where the dynamics is reduced to motion along the original basis of Cartesian coordinates for small vertical displacements. Specifically, the eigenvalues of the stiffness tensor at the origin (obtained in the regime of small

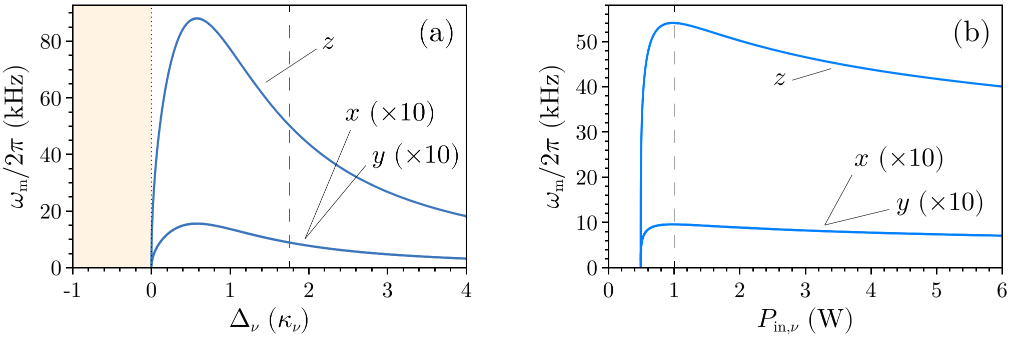

Figure 8.4: The mirror's centre of mass eigenfrequencies, for the same parameters used in Fig. 8.3, as a function of detuning (a) and input power (b) of the three cavities. The frequencies of oscillation along the x and the y axes overlap because of symmetry. Also, they are both magnified by a factor of 10 to increase their visibility relative to the frequency of oscillation in the vertical direction. The shaded area in (a) represents the region of instability, while the dashed line indicates the detuning required to satisfy the balancing condition. In (b) the balancing condition is always satisfied, and the dashed line corresponds simply to the input power used in (a).

detunings) are

$$\mathbb{K}_{xx}(0,0,0) = \sum_\nu \frac{8G_0 P_{\mathrm{in},\nu}}{c\tau} \frac{\kappa_\nu \Delta_\nu}{(\kappa_\nu^2 + \Delta_\nu^2)^2} \cos^2(\varphi_\nu) \sin^2(\theta_\nu), \tag{8.10}$$

$$\mathbb{K}_{yy}(0,0,0) = \sum_\nu \frac{8G_0 P_{\mathrm{in},\nu}}{c\tau} \frac{\kappa_\nu \Delta_\nu}{(\kappa_\nu^2 + \Delta_\nu^2)^2} \sin^2(\varphi_\nu) \sin^2(\theta_\nu), \tag{8.11}$$

$$\mathbb{K}_{zz}(0,0,0) = \sum_\nu \frac{8G_0 P_{\mathrm{in},\nu}}{c\tau} \frac{\kappa_\nu \Delta_\nu}{(\kappa_\nu^2 + \Delta_\nu^2)^2} \cos^2(\theta_\nu), \tag{8.12}$$

each consistent with the static limit of the optical spring of Eq. 3.70.

The optically induced frequencies of oscillation, proportional to the square root of the stiffness, are directly inferred from the eigenvalues of $\mathbb{K}$:

$$\omega_{\mathrm{os},i} = \sqrt{\mathbb{K}_{ii}(0,0,0)/m}. \tag{8.13}$$

The results, based on the same parameter used for the modelling of the stability potential, are illustrated in Fig. 8.4. Because of horizontal symmetry at the centre of the trapping region, the frequencies in the x and y directions perfectly coincide, with an estimated value of about 900 Hz at balance and up to 1.5 kHz when dynamically displaced within the stability node. The oscillations in the vertical direction are much stiffer, with a frequency of approximately 50 kHz at balance and peaking at more than 80 kHz when displaced.

The traces in Fig. 8.4a shows how the eigenfrequencies vary as a function of the detuning of the cavities when the input power of each cavity is 1 W. Even if the intra-cavity power is adequate for levitation, at zero or negative detunings there is no restoring force to steadily support the mirror. Only for positive detunings the eigenfrequencies adopt real values, effectively following the slope of the Lorentzian. The balancing condition in this case is satisfied when $\Delta_\nu \approx 1.75\,\kappa_\nu \approx 230\,\mathrm{kHz}$ (cf. Eq. 8.8).

Traces similar in behaviour but at the same time with very different characteristics are obtained when the power is increased while the detuning is adjusted to maintain the balancing condition in the same position, as in Fig. 8.4b. As it would be expected no eigenfrequencies are possible when the input power is below a threshold of $\frac{1}{3\cos(\theta_\nu)}\frac{mgc}{2} \times \frac{2\mathcal{F}_\nu}{\pi}$, which corresponds to the minimum power necessary to achieve levitation at resonance. As soon as the threshold is passed, the injection of higher input power has the effect of pushing the balancing detuning further away from resonance, now however with a much less pronounced asymptotic drop to zero. For high (but reasonable) input power, the optical spring frequencies may almost be treated as constants.

8.2.3 Dual-beam configuration

It is well known, especially in the gravitational wave community [228], that single-cavity configurations with a suspended mirror introduce tilt instabilities. The triple-cavity configuration of the optical tripod, however, combines the optical springs from three independent fields to create a fully stable system. Yet this is not enough: the self-locking that originates from the restoring effect of the radiation pressure force gradient is tainted by the occurrence of anti-damping and parametric amplification of the oscillations due to the delayed response of the cavities [80].

As the tripod's upper mirror does not have any mechanical supports acting as dissipative sinks, a remedy to the problem needs to be found in the interaction with the optical field. In particular, one can resort to the same optical spring effect which introduces the dynamical instability in the first place, since detuning the field to the other side of the resonance induces a damping, anti-restoring force instead. The three blue-detuned beams creating the trap can therefore be combined with another set of red-detuned beams to make the system robust against parametric amplification and favour lasting stability. The newly introduced fields need not be comparable in intensity to the trapping ones. Because the dispersive and the dissipative attributes of the optical spring scale differently as a function of detuning (cf. Fig. 3.4), it is possible to use low-power damping beams with a different detuning than the trapping ones to introduce a dissipation capable of stabilizing the system without introducing substantial changes to the stiffness.

To implement the dual-beam configuration, rather than doubling the number of cavities to six it is certainly more convenient to let the original three cavities be doubly resonant [89]. When considering this option it should be remembered that, unless orthogonal polarizations are used, the injection of two different fields into the same cavity results into interference that will cause part of the intra-cavity power to beat. The beating consequently extends to the force experienced by the mirror, and the levitation dynamics may be affected beyond control. The mechanical response of the system, however, is more or less receptive to the interference depending on the time scale of the beating. The susceptibility of the upper mirror is particularly prominent only at frequencies close to the motional eigenfrequency ω_{os}, which for the optical tripod is fully determined by the optical spring. The bandwidth of the susceptibility is determined by the magnitude of the damping rate, $|\gamma_{\mathrm{m}}|$. Even though we are trying to ultimately minimize the (anti-)damping, we may for now assume it to be finite but smaller than the frequency of oscillation, i.e. $|\gamma_{\mathrm{m}}| \lesssim \omega_{\mathrm{os}}$. The mirror's motion is not driven by the beating when the beat frequency is many multiples of $|\gamma_{\mathrm{m}}|$ higher than ω_{os}, when only a time-averaged effect is perceived. Since the beat frequency is determined by the relative detuning between the two fields, the complications emerging from the interference can thus be neglected if the two input beams are detuned sufficiently apart from each other. Whether this condition is naturally satisfied or not, it is always possible to take advantage of the periodicity of the cavity's resonance and detune the two beams to independent free spectral ranges. As the beat frequency is up-shifted by one or more free spectral ranges, orders of magnitude higher than the peak in susceptibility, the mirror's dynamics become clear from any undesired effects. Numerical support to these claims is offered in Appendix C. Under these circumstances the optical springs can be added together as if the two intra-cavity fields acted independently and without reciprocal interference.

The damping component of the optical spring is manifest only in the full dynamical expression of Eq. 3.70, in which case the optical spring is a function of the spectral frequency ω. The generalized eigenvalue of the stiffness tensor at the origin is, in the vertical direction,

$$\mathbb{K}_{zz}(\omega) = \sum_{\nu} \frac{8G_0 P_{\mathrm{in},\nu}}{c\tau} \frac{\kappa_\nu \Delta_\nu}{(\kappa_\nu^2 + \Delta_\nu^2)^2} \left[1 - \frac{\omega}{\kappa_\nu^2 + \Delta_\nu^2} (\omega - 2i\kappa_\nu)\right]^{-1} \cos^2(\theta_\nu). \tag{8.14}$$

The frequency of the oscillations and the corresponding damping depend, respectively, on the real and the imaginary part as

$$\omega_{\mathrm{m},z}(\omega) = \sqrt{\frac{\mathrm{Re}(\mathbb{K}_{zz}(\omega))}{m}}, \tag{8.15}$$

$$\gamma_{\mathrm{m},z}(\omega) = -\frac{\mathrm{Im}(\mathbb{K}_{zz}(\omega))}{m\omega}. \tag{8.16}$$

In ordinary optomechanical systems, the frequency dependence of the optically induced parameters is typically convolved with the mechanical susceptibility of the oscillator. For high mechanical quality factors the peak in susceptibility at the intrinsic mechanical frequency can be approximated as a delta function, implying that only the component at the natural frequency of the oscillator is relevant in the optical spring.

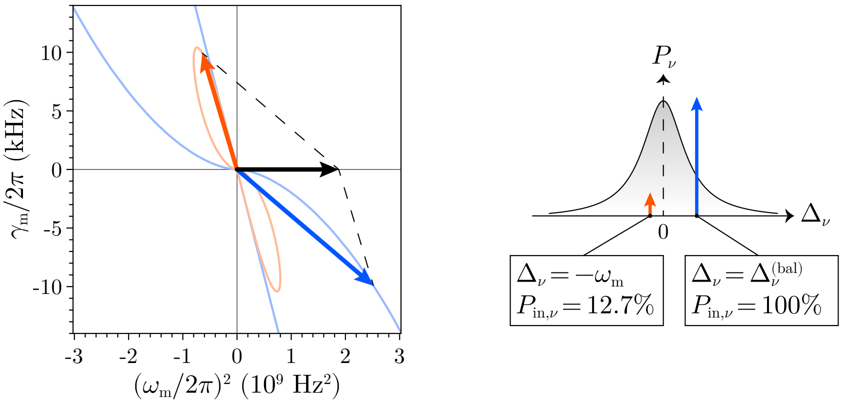

Figure 8.5: The dual-beam configuration combines two optical springs to change the damping of the system. The two optical springs can be represented in the complex plane, where the horizontal axis is the square of the oscillation frequency and the vertical axis is the optical damping. In this representation they can be combined as any two vectors as long as beams' relative detuning is large compared to the dynamics of the mirror. The curves trace the course of the optical spring of Eq. 8.15–8.16 as a function of detuning. The arrows point to the values of the optical spring of the blue-shifted trapping beam (in blue) and of the red-shifted damping beam (in red), which combine to a strictly real and positive optical spring (in black). The trapping beam in each cavity has an input power of 1 W and is detuned to satisfy the balancing condition as in Eq. 8.8. The damping beam has a negative detuning equivalent to the oscillation frequency, and the input power is adjusted to 12.7 % of the power of the trapping beam in order to make the overall damping component vanish.

Since the optomechanical system under analysis behaves like a free mass, however, this line of reasoning cannot be directly applied. The frequency of the oscillations is directly determined by the optical spring, which itself depends on the spectral frequency considered, and without a well-defined resonance there might not be a well-defined solution. The argument results into a recurrence relation for the frequency of the oscillations,

$$\omega_{\mathrm{m},z}[n+1] = \sqrt{\frac{\mathrm{Re}(\mathbb{K}_{zz}(\omega_{\mathrm{m},z}[n]))}{m}}, \tag{8.17}$$

with seed value $\omega_{\mathrm{m},z}[0] = 0$. Numerical estimates suggest that in the regime of small and medium finesses, where we operate, the recursion settles very rapidly after the first few iterations. For cavities with very high finesse the recursion fails to converge to a single solution, suggesting that the dynamical stability may additionally depend on the spatial extent of the tight-confinement.

With the same choice of parameters used to calculate the static stability (cf. Fig. 8.3), we have that the single-beam optical spring of the trapping beam converges, at balance, to $\omega_{\mathrm{m},z} = 2\pi \times 50.1\,\mathrm{kHz}$ and $\gamma_{\mathrm{m},z} = -2\pi \times 9.9\,\mathrm{kHz}$. The second optical spring from the damping beam is tuned to have equal but positive damping $\gamma_{\mathrm{m},z}$ when detuned by $-\omega_{\mathrm{m},z}$. The two optical springs cooperate as shown in Fig. 8.5 to cancel any optical dissipation effects. The modest anti-restoring component of the damping beam also combines to the stiffness of the original trapping beam, but because the power and the detuning have been tailored specifically to minimize this drawback the net stiffness is still largely positive. The radiation pressure force is thus purely restoring and conservative. The oscillation frequency modelled for the combined dual-beam configuration is $\omega_{\mathrm{m},z} = 2\pi \times 43.3\,\mathrm{kHz}$. Similar corrections occur at the same time on the horizontal directions, where the effects of the damping beam rescale as those of the trapping beam because they have equal projections onto the x and y axes. The frequency of the oscillations in the horizontal plane adjusts from 0.89 kHz to 0.77 kHz.

8.3 Practical considerations

The path to coherent optical levitation and full isolation from the environment is not clear of obstacles. Before realizing a successful decoupling from the initial support, for example, the small scale of the participating forces may be burdened by the presence of Van der Waals interactions. During levitation the energy of the mirror is subject to continuous random fluctuations stemming from laser noise and collisions with residual gas particles in low pressure conditions. Even when the mirror is successfully suspended over long periods of time, the high intensities involved could be enough to overwhelm the system, which is devoid of any dissipation methods apart from blackbody radiation and interaction with the optical field. In this section we perform order-of-magnitude estimations for the major points of concern that could prevent the functional operation of the system.

8.3.1 Van der Waals interactions

Van der Waals forces are weak, attractive electric forces arising between neutral molecules. They originate from the interaction of the electric dipoles induced by asymmetries in the charge distribution, and decay extremely rapidly as a function of distance between the molecules [229]. These forces will occur between the mirror and the platform supporting it before levitation, and it is important to check that their magnitude is not significant compared to the weight of the mirror.

Considering the separation between the mirror and its launching platform to be much smaller compared to the extent of either object, we can treat the two as semi-infinite media at a relative distance d from each other. This assumption is good for a worst-case estimate, since the strength of the interaction is only reduced when accounting for a finite thickness. The Van der Waals interaction energy density per unit area is expressed by

$$U_{\mathrm{VdW}}(d) = -\frac{A_{\mathrm{Ham}}(d)}{12\pi d^2}, \tag{8.18}$$

where A_{Ham} is the Hamaker coefficient, a function of the materials and of the distance, which determines the strength of the interaction. The dependance of A_{Ham} on d is relevant only in situations where the finite speed of the electromagnetic interaction is of importance, and it is not unusual to consider the Hamaker coefficient constant for small distances [229]. The Van der Waals force per unit area is obtained by differentiating the energy density:

$$F_{\mathrm{VdW}}(d) = \frac{A}{6\pi d^3}. \tag{8.19}$$

For the mirror, assumed to be an HR-coated silica substrate, the Hamaker coefficient in vacuum is 65 zJ [230]. For the support, which is expected to consist of aluminium or another metal, the coefficient is estimated around ≈ 200 zJ. The Hamaker coefficient between the two materials is evaluated as the geometric mean of the coefficients of each material acting on itself [231]. The result for the case considered is $A_{\mathrm{Ham}} \approx 114\,\mathrm{zJ}$. Assuming a contacting surface of $4\,\mathrm{mm}^2$ and an average distance of $1\,\mu\mathrm{m}$ caused by the roughness of the support, the Van der Waals interaction is estimated to be approximately $24\,\mathrm{nN}$, more than 400 times smaller than the weight of a 1-mg mirror.

8.3.2 Background gas collisions

Without other major elements of interaction, individual collisions with gas molecules become the most significant source of dissipation for the levitated mirror. These background collisions increase or decrease the energy of the mirror depending on its size and, more importantly, the pressure conditions of the gas.

In normal pressure conditions, such as in an atmospheric environment, the gas surrounding the mirror is in the *continuous* regime and responds to the laws of classical fluid dynamics. A full expression for the collision rate is hard to obtain in this case, and any approximation might not reflect the full dynamics of the mirror because of flow separation and turbulence caused by the high aspect ratio of the disk [232]. Under high vacuum, instead, the pressure is low enough that the mean free path of the gas molecules is much larger than the size of the mirror. In this regime of *free molecular flow* the difference in momentum exchange between the front and the back of the mirror produces a drag force which, assuming elastic collisions between the mirror and the gas molecules, is characterized by a damping rate [233]

$$\gamma_{\mathrm{m}} = \frac{2\rho_{\mathrm{g}} v_{\mathrm{g}} \Sigma}{m}, \tag{8.20}$$

where ρ_{g} is the density of the gas, v_{g} is the velocity of the molecules, m is the mirror's mass, and Σ is the surface acting as the collisional cross section. The velocities of the gas molecules follow the Maxwell–Boltzmann distribution,

$$f_{\mathrm{B}}(v_{\mathrm{g}}) = \left(\frac{m_{\mathrm{g}}}{2\pi k_{\mathrm{B}} T}\right)^{\frac{3}{2}} 4\pi v_{\mathrm{g}}^2\, e^{-\frac{m_{\mathrm{g}} v_{\mathrm{g}}^2}{2k_{\mathrm{B}}T}}, \tag{8.21}$$

where m_{g} is the molecule's mass and T is the temperature of the gas. The mean velocity of the gas in any one direction is $\langle v_{\mathrm{g}} \rangle = \sqrt{\frac{8k_{\mathrm{B}}T}{\pi m_{\mathrm{g}}}}$, which is around $460\,\mathrm{m\,s^{-1}}$ for air at room temperature. In these conditions, at a vacuum pressure of $10^{-3}\,\mathrm{Pa}$ the damping rate for a mirror 3 mm in diameter is on the order of $10^{-4}\,\mathrm{Hz}$. This suggests a quality factor higher than 10^9 for the 50-kHz mode of oscillation in the vertical direction, which is limited only by the vacuum pressure when other sources of dissipation such as possible optical damping are ignored.

The overall collision rate can be evaluated by the total number of gas molecules hitting the surface of the mirror per unit time. Assuming the mirror to be a flat disk of surface Σ, whose velocity within the confinement trap for realistic oscillation parameters is much slower than the velocity of the gas molecules, we have that the collision rate is

$$\mathcal{R} = 2 n_{\mathrm{g}} v_{\mathrm{g}} \Sigma, \tag{8.22}$$

where $n_{\mathrm{g}} = \rho_{\mathrm{g}}/m_{\mathrm{g}}$ is the number density of the gas. To determine the energy transferred to the mirror by the gas, we integrate the kinetic energy exchanged at each collision over the distribution of velocities to obtain the energy rate

$$\eta_{\mathrm{m}} = \int_{0}^{+\infty} dv_{\mathrm{g}}\, f_{\mathrm{B}}(v_{\mathrm{g}}) \mathcal{R}(v_{\mathrm{g}}) \frac{2 m_{\mathrm{g}}^2 v_{\mathrm{g}}^2}{m}, \tag{8.23}$$

which evaluates at $\approx 2 \times 10^{-8}\,\mathrm{J\,s^{-1}}$. Taking into account the dissipation calculated from Eq. 8.20, the energy acquired by the mirror from background gas collisions amounts to $E_{\mathrm{m}} = \eta_{\mathrm{m}}/\gamma_{\mathrm{m}} \approx 10^{-20}\,\mathrm{J}$, five orders of magnitude smaller than the trapping potential created by the optical spring.

8.3.3 Laser noise

Noise in the laser intensity transfers to the mirror via radiation pressure, inducing fluctuations in the optical spring that can foment anti-damping and parametric heating of the system. Following a method based on the application of perturbation theory to optically trapped atoms, which can be extended to any kind of oscillator within an optical trap, we aim to determine the lifetime of the mirror's trap given a certain degree of intensity noise [234, 235].

The average transition rate $\mathcal{R}_{n\to m}$ from the state $|n\rangle$ to the state $|m\rangle$ of the oscillator depends on the elements of the interaction matrix $\langle m|\delta\hat{V}|n\rangle$, where $\delta\hat{V}$ is the first-order perturbation of the potential term in the system's Hamiltonian. The perturbation depends on the fractional fluctuations of the trap's frequency, ϵ, which are time-dependent and determined by the intensity noise. Specifically, the harmonic frequency ω_{m} modifies as $\omega_{\mathrm{m}}^2 \to \omega_{\mathrm{m}}^2 (1 + \epsilon(t))$, where $\epsilon(t) := \frac{I(t)-\langle I\rangle}{\langle I\rangle}$ and $I(t)$ is the laser's intensity with time average $\langle I\rangle$. As the harmonic oscillator's potential is quadratic, the only non-vanishing rates $\mathcal{R}_{n\to m}$ correspond to second-harmonic transitions where the phonon number jumps in pairs, specifically

$$\mathcal{R}_{n\to n\pm 2} = \frac{\pi\omega_{\mathrm{m}}^2}{16} S_\epsilon(2\omega_{\mathrm{m}})\,(n+1\pm 1)\,(n\pm 1)\,, \tag{8.24}$$

where $S_\epsilon(\omega) = \langle|\epsilon(\omega)|^2\rangle$ is the power spectrum of the fractional noise. It can be shown that the average energy E of the oscillator increases exponentially over time, at a rate

$$\gamma_I = \frac{\langle\dot{E}\rangle}{\langle E\rangle} = \frac{\sum_n p_n 2\hbar\omega_{\mathrm{m}}\,(\mathcal{R}_{n\to n+2} - \mathcal{R}_{n\to n-2})}{\sum_n p_n \hbar\omega_{\mathrm{m}}\,(n+1/2)}, \tag{8.25}$$

where p_n is the average probability of the oscillator being in the state $|n\rangle$. Expanding using Eq. 8.24, the heating rate becomes

$$\gamma_I = \frac{\pi\omega_{\mathrm{m}}^2}{2} S_\epsilon(2\omega_{\mathrm{m}}). \tag{8.26}$$

This result, which could also be calculated classically [234], relates the e-folding time of the oscillator, γ_I^{-1}, to the spectrum of the intensity noise at the double harmonic of the trap, $S_\epsilon(2\omega_{\mathrm{m}})$.

In order for the e-folding time of the levitating mirror's parametric processes to be longer than 10 s, for example, the laser needs to satisfy $\sqrt{S_\epsilon(2\omega_{\mathrm{m}})} \lesssim 2\times 10^{-6}\,\mathrm{Hz}^{-1/2}$ for a mode at 50 kHz. If we assume that the majority of the noise is evenly distributed across a bandwidth of 300 kHz, the corresponding fractional intensity fluctuations ϵ is required to be on the order of 10^{-3} or less. Even lasers that are not shot-noise limited can satisfy this requirement with a clearance of at least a couple orders of magnitude.

8.3.4 Black-body radiation

For levitated particles, the recoil experienced from absorption or emission of black-body radiation can represent a source of heating and decoherence [200,236]. Even when the state of the oscillator is predominantly classical, the role of black-body radiation processes is undeniably important especially when the power involved is high. In vacuum, with no means of mechanical dissipation, the only way for the levitated object to dissipate the excess energy absorbed over time is through radiative emission [237].

For the levitating mirror, the absorption of even a fraction of the incident power could represent a significant change in the system's conditions. Having a macroscopic thickness h much greater than the optical wavelength, the mirror responds to the Stefan–Boltzmann law according to which the power radiated is proportional to the surface area and the fourth power of the temperature:

$$P_{\mathrm{rad}} = \varepsilon_{\mathrm{bb}} \sigma_{\mathrm{SB}} \left(T^4 - T_0^4\right) \Sigma, \tag{8.27}$$

where $\varepsilon_{\mathrm{bb}}$ is the black-body emissivity of the mirror, σ_{SB} is the Stefan–Boltzmann constant, Σ is the emitting area, and T and T_0 are the mirror's temperatures with and without the incident power, respectively. The field leaking from the cavity through the coating is absorbed in the substrate with exponential decay before being transmitted through:

$$P_{\mathrm{abs}} = \left(1 - e^{-\alpha h}\right) \mathcal{T}_{\mathrm{m}} P_{\mathrm{cav}}, \tag{8.28}$$

where α is the absorption coefficient of the substrate, $\mathcal{T}_{\mathrm{m}}$ the transmissivity of the coating, and P_{cav} is the power in the cavity. After balancing the two equations, the raise in temperature of a cylindrical silica substrate ($\epsilon_{\mathrm{bb}} \approx 0.8$, $\alpha \approx 10^{-2}\,\mathrm{cm}^{-1}$, diameter of 3 mm and thickness of 50 µm) at room temperature conditions is about 1 K when the cavity has enough power for levitation and about 0.1 % of it is transmitted through the coating. The change in temperature expected is far from reaching the melting point of silica, but it is significant enough that there is a potential for less drastic consequences to be manifest, such as thermal expansion or excitation of the mirror's drum modes. It should be noted that, due to the time-independent nature of the radiation, the net work done by the black-body emission on the mirror over one oscillation is zero.

Chapter 9

Experimental design

9.1 Specifications of the mirrors

The model developed in Chap. 8 suggests that a macroscopic mirror can indeed be successfully decoupled from the environment and be supported entirely by the optical field of three cavities. A better idea of what “macro” exactly means in this context is obtained by considering the mass employed in all simulations, 1 mg. This mass, a million times bigger than the average human cell (≈ 1 ng), is characteristic of granular substances. It is about twenty times larger than the mass of a single grain of fine salt (≈ 0.06 mg), but still smaller than the typical mass of a grain of sand (10–50 mg). Assuming the convex substrate to be made of fused silica, which has a density of $2203\,\mathrm{kg\,m^{-3}}$, a mass of 1 mg prescribes the dimensions of the mirror to range between 2 to 3 mm in diameter and 30 to 70 µm in thickness, similar to a shrunk down contact lens.

The thickness anticipated is small enough that the mirror is a simple spherical cap with no cylindrical base. The convex shape, which was chosen so that the three beams would hit the mirror higher than the height of its centre of mass, provides several other unanticipated benefits that go beyond the improvement of the mirror’s stability. The convex-concave cavity configuration places the waists of the beams outside of the optical resonators. By having a virtual waist the intensity is prevented from being at its highest at any physical point. Also, compared to a concave mirror of similar dimensions, a convex mirror is much lighter and the power requirement for levitation is lower. The choice of the mirror’s radius of curvature (RoC) reflects a balance between two contrasting demands. A large RoC (i.e. a less pronounced curvature) is perfect for having the three cavities as close to vertical as possible. This allows most of the radiation pressure force to contribute towards levitation, but at the same time there is a limit to how close the lower mirrors can be placed. Given a certain distance between

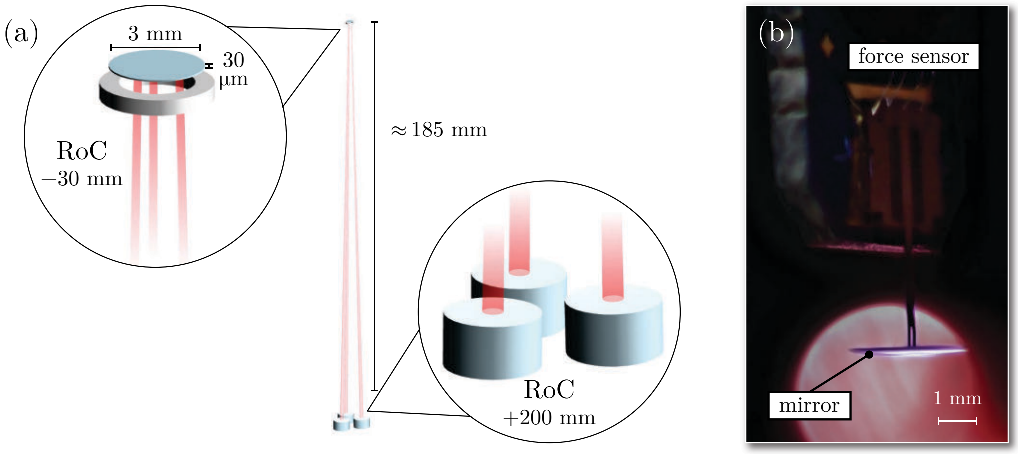

Figure 9.1: The actual specifications provide a different image of the tripod than the concept diagram of Fig. 8.2. **(a)** Realistic diagram of the optical tripod, with dimensions to scale. The metal ring on the top part provides the initial support for the mirror. **(b)** Close-up picture of one of the 3-mm mirrors, from the side. The exhibited mirror is directly attached to a force sensor in order to measure its mass. The original photograph has been modified to reduce the noise and enhance the contrast with the background.

the input mirrors, a small RoC (i.e. a more pronounced curvature) for the upper mirror allows the cavities to be much shorter, increasing the linewidth and thus allowing the spatial dimensions of the trap to be extended without having to decrease the finesse. However, when the cavities are shorter the aperture of the tripod gets larger and the vertical component of the combined radiation pressure force becomes smaller. Feasible radii of curvature for the upper mirror are around 20–35 mm. The illustration in Fig. 9.1 shows a scale diagram of the tripod for a mirror which is 3 mm in diameter, 30 µm thick, and with a radius of curvature of −30 mm (the negative sign indicates that it is convex). These dimensions, taken as a benchmark for the experimental implementation, lead to a distance of roughly 10 mm between the centres of the beams at the bottom of the cavities. For lower mirrors with RoC of 200 mm, the cavities are optically stable when their length is between 170 mm and 200 mm. The length of 185 mm is chosen in the middle of this range to let the spot size on the upper mirror be at its largest and reduce the risk of laser-induced damage. The virtual waists are always close to the centre of curvature of the lower mirrors, around 15 mm above the upper mirror. All three beams virtually coincide at the centre of curvature of the upper mirror, acting as the centre of the tripod which has an aperture of ≈ 1.4°.

With an expected spot size of 100 µm in radius and about 0.5 kW of circulating power in each cavity, a few considerations on optical damage are inevitable. The laser-

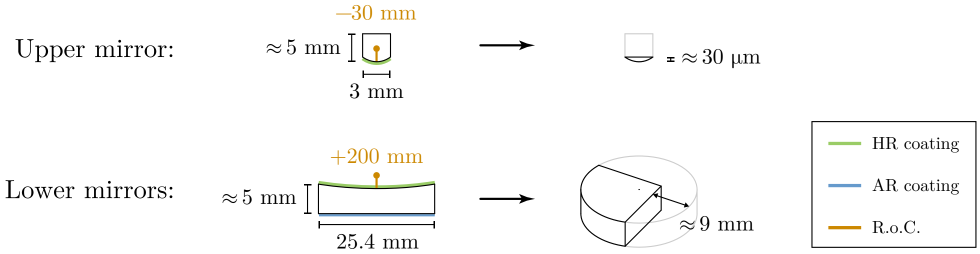

Figure 9.2: The cavity mirrors required special adjustments in order to be ready for the tripod. The upper mirror, originally about 5 mm thick, was lapped to a spherical cap of thickness of ≈ 30 µm. The lower mirrors, with high-reflective coating on the concave side and anti-reflective coating on the flat side, had to be sliced so that their centres could be placed closer.

induced damage threshold (LIDT) of the mirror's coating is required to be at least a few times higher than the intensity of 1.6 MW cm^{-2}. This figure may be too high for conventional high-reflectivity mirrors where the coating is obtained by electron beam or ion-assisted vapour deposition [238]. Modern ion-beam sputtering coating techniques, on the other hand, have evolved to the point where these and even more ambitious requirements are easily met[1], with certified LIDTs higher than 1 GW cm^{-2}. The striking difference between the different techniques lies in the density of the coatings obtained. Coatings obtained by vapour deposition are characteristically more porous and less dense than ion-beam sputtered coatings. The pores are usually filled up with water, making the coating more sensitive to temperature and humidity conditions while also increasing absorption losses. The higher density obtained with ion-beam sputtering produces extremely uniform and lossless coatings, also allowing greater variations in refractive index which is essential for high-end Bragg mirrors. At the same time, however, the greater adhesion induces extremely high stresses on the substrates. The surface tension which is usually supported by regular substrates might be excessive for the thin mirrors involved, and there is a high risk of shattering during or after the coating process.

The mirror employed in the preliminary stage of the experiment (cf. Fig. 9.1b) consists of a small fused silica lens substrate[2], 3 mm in diameter, with a surface roughness of 10 nm, and coated by vapour deposition to a reflectivity of 99.9 %. The original mirror is lapped[3] in order to reduce the thickness to 30 µm (with an upper uncertainty of almost 100 %). The lapping process may have slightly reduced the diameter depending

---

[1] from personal communications with D. Samuels, from Advanced Thin Films Inc. (http://advancedthinfilms.com/)

[2] custom order from FOCtek Photonics Inc. (http://www.foctek.net/)

[3] lapping by Photon LaserOptik GmbH (http://www.photon-laseroptik.de/)

on the final thickness due to the aspect ratio of the spherical cap. The reflectivity is selected to favour impedance matching over a capacity for higher finesse. The lower mirrors are more conventional high-reflective mirrors[4], sliced as in Fig. 9.2 to allow close positioning. They are coated on the concave side to a reflectivity of 99.9 % by ion-beam sputtering, and they also feature an anti-reflective coating on the flat surface to prevent the creation of intra-substrate etalon modes.

It should be emphasized that an upper mirror coated by vapour deposition is a moderate gamble, more vulnerable to thermal effects and optical damage. One solution for future iterations might be to manufacture the mirror out of a harder substrate that can better tolerate the high stresses induced by ion-beam sputtering. Diamond is a possible choice, with a tensile strength between 2 and 5 times that of fused silica. It is also a much stiffer material, meaning that the excitation of the vibrational drum modes would be curbed. On the other hand, diamond is denser and the mass to be supported by the radiation pressure force is heavier. Unless power is not the limiting factor, this issue may outweigh the advantages.

9.2 Assembling the tripod

Putting together the tripod involves forming three separate cavities in a vertical configuration, with a common end mirror which is not clamped to any form of physical support. This singular undertaking may seem like an extension of the ordinary alignment of a Fabry–Pérot resonator. Yet it is important to employ special measures and equipment to prevent complications and ensure attention to the smallest details in the apparatus.

Proceeding with a top-to-bottom approach, it is immediately clear that the upper mirror requires a stand during the initial alignment. This task is assigned to a small aluminium ring[5] which is designed specifically to minimize the effect of Van der Waals interactions. The ring, which is 3.5 mm in diameter, is cut to have a circular hole 2.5 mm wide in the centre so that most of the mirror's surface is exposed. The top part of the ring features a containing wall along the outer edge which is 60 µm thick and 450 µm tall. The vertical thickness of the inner part, where the mirror sits, varies sinusoidally along the circumference between 0 and 150 µm. This is done in order to have three rounded maxima acting as minimalistic contact points.

---

[4] L-12173 from LASEROPTIK GmbH (http://www.laseroptik.de/)

[5] sincere gratitude to J. Janousek for fabricating the ring

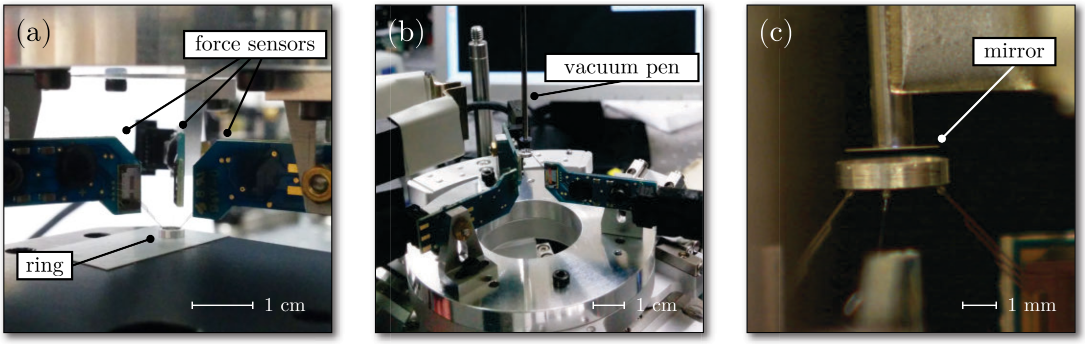

Figure 9.3: Different steps in the preparation of the stage for the upper mirror. **(a)** Attaching the supporting ring to the tips of the three force sensors. **(b)** Holding the mirror with the vacuum pick-up pen during positioning. **(c)** Close-up of the mirror held by the vacuum pick-up pen just before releasing it onto the ring.

The holding ring is in its turn supported by a set of three force sensors[6], each with a sensitivity range of ±1000 µN and a resolution of about $16\,\mathrm{nN\,Hz^{-1/2}}$. The probing cantilevers are oriented laterally relative to the full body of the sensors to allow measurement of perpendicular forces. This attribute is particularly important for the arrangement, since the sensors exhibit photosensitivity to 1064 nm light which results in the read-out of negative forces (i.e. in the downward direction). By having the probes off-axis, the intra-cavity path is free from obstacles and the readings from the sensors are clear from any optical interference. The ring was fixed on top of the force sensors with a specific procedure (cf. Fig. 9.3a). First, the ring was positioned upside down onto a flat platform that could be rotated around its in-plane axes and elevated with a vertical micro-positioning stage. Then the force sensors, mounted onto a different platform, were also flipped upside down and placed just above the ring. By monitoring the force while raising the ring, it was possible to determine the precise moment when one of the sensors made contact. The ring would then be lowered and its orientation adjusted to bring its bottom side parallel to the plane determined by the three tips of the sensors. The procedure was iterated several times until the force measured by the three sensors upon contact was exactly the same. At this point epoxy resin was applied to the tips of the sensors, which were then brought to contact with the ring one last time until the resin fully hardened.

The platform where the three force sensors are installed is part of a closed-loop nano-positioning stage[7] with six degrees of freedom (three for translations and three

---

[6] FT-S1000-LAT from FemtoTools AG (http://www.femtotools.com/)
[7] SmarPod 110.45-S from SmarAct GmbH (http://www.smaract.com/)

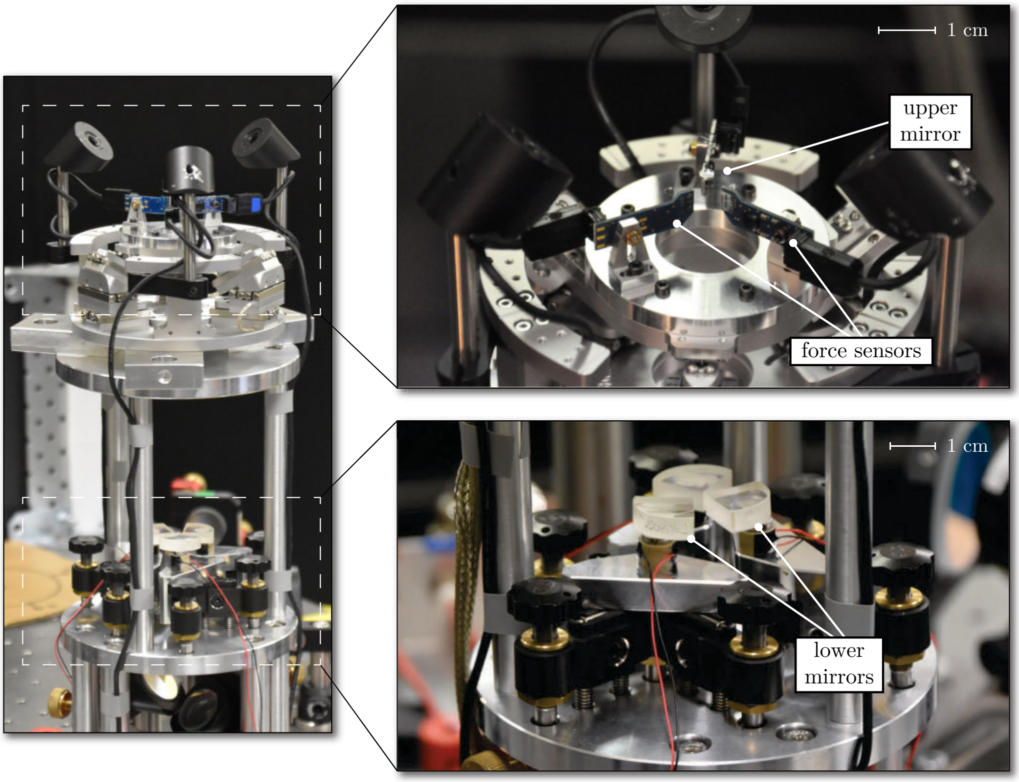

Figure 9.4: The cavity tripod, with in situ close-ups of the upper and lower mirrors.

for rotations). The stage includes a wide central opening for the intra-cavity fields to go through. The manoeuvrability of the stage allowed precise positioning of the mirror inside the ring, an operation performed with the assistance of a vacuum pick-up pen[8] (cf. Fig. 9.3b–c). The exact dimensions and location of the mirror were inferred by observing the vibrations induced by the vacuum pump of the pick-up system onto the force sensors when the mirror was brought close to the containing walls of the ring. Upon reaching the exact centre, the pump was turned off and the mirror was released onto its support. The comparison of the force sensors' records before and after releasing the mirror provide an estimate of the mirror's mass, (0.9 ± 0.1) mg, which is close to the target value. The stage was subsequently employed to align the upper portion to the midpoint of the tripod.

The nano-positioning stage serves as the top part of an aluminium frame that houses the rest of the tripod[9]. The lowest section of this frame provides enough space for the optics used to deflect the input beams vertically. The middle contains the lower mirrors

---

[8] PELCO 520-1-220 from Ted Pella Inc. (http://www.tedpella.com/)

[9] special thanks to P. McNamara and N. Devlin for fabricating the frame, designing the adaptive masks for the lower mirrors, and contributing to the manufacturing from its earliest developments

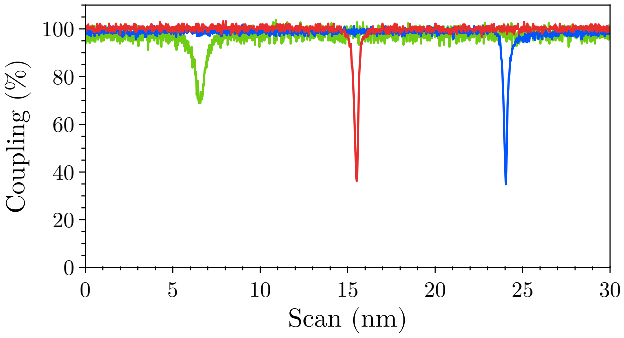

Figure 9.5: Simultaneous alignment of the three cavities of the tripod. The traces correspond to the reflected signals detected from each cavity, normalized by the respective input power to obtain the coupling. The cavity peaks are obtained by scanning the length of each cavity over time.

of the cavities, together with their alignment mounts and the piezoelectric actuators. The alignment mounts are directly embedded into the aluminium disk for improved stability, and they are complemented by adaptive masks that permit a quick removal of the mirrors. The actuators consist of 6-mm thick piezoceramic rings[10]. Each actuator is pre-loaded to increase its spring constant and consequently its bandwidth [239]. The pre-loading is performed by having a flat-head screw go through the inner hole of the piezoceramic into the adaptive mask. A gap within the mask allows the placement of a rubber O-ring and a tightening nut onto the tip of the screw. The sliced mirrors forming the bottom halves of the cavities are glued directly onto the flat top of the screws. A snapshot of the full tripod can be found in Fig. 9.4. At this stage the experiment is not yet performed in vacuum, and the apparatus is protected by an acrylic box[11] from unwanted air flows and dust particles.

The three input beams are mode-matched separately to better suit the corresponding cavities. They are obtained from the same source using three polarizing beam splitters, which are also used to independently control the power in each branch. The source laser can be switched between two options: a 1-W Nd:YAG laser[12] at 1064 nm, used for alignment purposes, and a 20-W fibre-amplified laser[13] at 1050 nm, used for regular high-power operations. A mode-cleaner cavity after the two different lasers acts as a filtering node to guarantee the same output mode regardless of the source selected.

---

[10] HPCh150/10x5/6 from Piezomechanik GmbH (http://www.piezomechanik.com/)

[11] E. Slatyer is to be thanked for laser-cutting the entire box, complete with windows for alignment access and beam propagation

[12] Mephisto 1200NE from Innolight GmbH (http://www.innolight.de/)

[13] YAR-20K-LP-SF from IPG Photonics (http://www.ipgphotonics.com/), seeded by a Rock Source from NP Photonics, Inc. (http://www.npphotonics.com/)

Cavity	Coupling	Finesse	Half-linewidth
Red	$(65 \pm 2)\,\%$	1600 ± 90	$(176 \pm 4)\,\mathrm{kHz}$
Blue	$(68 \pm 2)\,\%$	1700 ± 100	$(171 \pm 3)\,\mathrm{kHz}$
Green	$(35 \pm 1)\,\%$	850 ± 50	$(440 \pm 10)\,\mathrm{kHz}$

Table 9.1: Properties of the three cavities of the tripod. The errors on coupling and half-linewidth are calculated directly from the measured data. For finesse, the major contribution to the error comes from the uncertainty in the linearity of the scan.

Its finesse is around 350, and the coupling achieved for either laser is above 90 %.

The specifications of the three cavities of the tripod display marginal differences. This is unavoidable, even despite the fact that mirrors from the same coating batch and with a nearly identical distance from the top were used. The green, red, and blue traces in Fig. 9.5 show the response of each cavity while their length is linearly scanned with the piezo-actuators, allowing the measurement of their properties as reported in Table 9.1. The apparent capping in the visible coupling is possibly due to the fact that having different coatings for the upper and the lower mirrors contributed to an appreciable impedance mismatch. Also, all three input beams are imperceptibly clipped just before entering the cavities. It is possible that the slight deviation from a perfect TEM_{00} mode contributes to the limited coupling. The finesse of the cavity corresponding to the green trace is noticeably smaller than the other two. This suggests additional intra-cavity losses that would also account for the coupling being even lower.

Chapter 10

Preliminary observations

10.1 Lock of a single cavity

As in any other high-power system, the thermal effects arising during regular operations of the cavities are expected to play a significant role. This is especially the case for the upper mirror used in the preliminary setup of the experiment, which is coated by vapour deposition and is therefore subject to increased absorption losses. A qualitative characterization of the thermal response of the system is possible by actively locking one of the cavities on resonance.

A first sign of the thermal influence of the circulating light is observed in the instability of the lock itself. The intensity detected at the output of the cavity appears to be steady for a few seconds before starting to decrease slowly, to the point where the error signal becomes too small and the lock fails to hold abruptly. The time scale of the effect is measured more accurately by tracking the evolution of the force sensors' records, as shown in Fig. 10.1. While the lock is immediate, the reaction of the system is not. The force sensors register a new signal with a finite response time which is on the order of 3 s. This is very far from the time scale of radiation pressure force, which occurs at the speed of light. False measurements due to the photosensitivity of the sensors can equally be excluded as they would also be much faster. When the lock holds for long enough the signal can be observed to saturate at a new steady-state level, which is proportional to the power applied. Another indication of the thermal nature of the effect is the fact that energy is stored into the system, and when the lock is suddenly interrupted the signal decays to its original value with the same time constant. An accurate measurement of the characteristic exponential time of this effect is arduous due to the concurrent decrease in intensity of the circulating field. The maximum shift obtained even at high power is roughly 2 µN, which is lower than the weight of the mirror (≈ 9 µN) but still within the same order of magnitude.

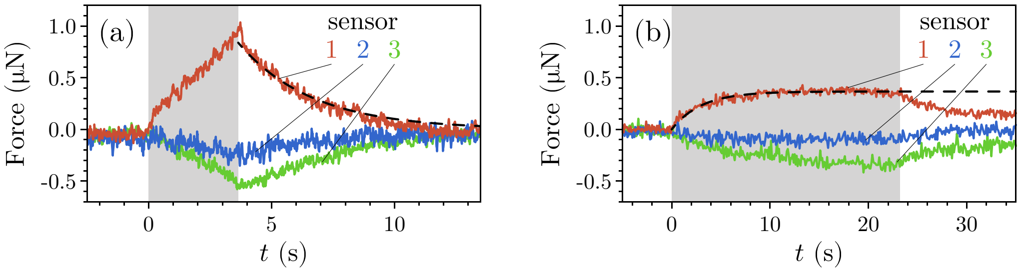

Figure 10.1: Upon locking of a single cavity, the force sensors reveal a slowly charging signal. The two plots correspond to higher (a) and lower (b) power. The shaded region indicates the period of time during which the cavity lock was active. The measurements from the three separate sensors, represented by differently coloured traces, are taken at a resolution of 100 Hz. For comparison, an exponential model with characteristic time of 3.0 s is also plotted (dashed black lines).

The different signs and amplitudes of the forces detected hint to a redistribution of the weight of the mirror onto its support. Some of the possible causes may be thermal expansion, softening, or deformation. The radius of curvature of the upper mirror is also a dynamic quantity, and as the temperature gradient applies local changes it is possible that the mode structure of the cavity follows accordingly until the lock breaks down. This behaviour has been observed in high-power interferometers, such as LIGO [83], and there is a risk of it escalating into parametric excitations of the acoustic modes of the mirror. Aside from the destabilization of the lock, however, there are no obvious indications of self-sustained resonances or instabilities. Another possible cause, also reported by the LIGO community, is thermoelastic noise on the coating. The power absorbed might be greater than expected due to the additional dissipation introduced by friction between different layers of the coating [240, 241]. Scanning of the other cavities during the lock to observe how their modes reacted did not lead to any conclusive evidence on whether the effect was localized to the bright spot of the locked cavity or whether it extended to the rest of the mirror.

In the remainder analysis, locking is replaced by scanning of the cavity length to observe the evolution of the system under high power conditions. Due to the different time scales involved, it is generally harder to observe the slow thermal drift on the force sensors in those conditions. As the optical traces carry a greater amount of information, thanks to the larger bandwidth of the photodetectors, we will mostly refer to the signals detected from the optical output of the cavities and look at either the reflected or the transmitted field.

10.2 Self-feedback

The thermal response of the cavity may induce a reciprocal dependence between optical power and position of the mirror which conforms to the same model presented in Chap. 3 for radiation pressure force. In both cases, the power is responsible for a cavity length variation which translates into a shift of the resonance condition, with consequences reverberating back to the circulating power. The main difference lies in the nature of the interaction, which may occur on a different time scale and may even be inverted in sign. Radiation pressure force is instantaneous and it invariably pushes on the mirror, therefore leading to an increase in cavity length. Thermal effects, instead, have a finite characteristic time due to the transfer of the heat within the substrate, and higher power might cause the cavity to be shorter rather than longer, as is the case for thermal expansion of the mirror. With the appropriate corrections, the effects of the interaction will still be manifest as of self-feedback in the form of bistability and dynamical back-action (cf. Chap. 3.2 and 3.3).

This self-regulating behaviour is observed in the cavities by slowly scanning their length with the piezo-actuators attached to the lower mirrors, which is equivalent to sweeping the resonance condition relative to the fixed frequency of the input field. At high power the resonance condition additionally changes due to the response of the upper mirror. This produces an asymmetric response [242, 243], as the cavity displays self-locking or anti-locking behaviour depending on whether the change in resonance occurs in the same or in the opposite direction of the scan. The observations indicate that the self-locking mechanism triggers when the cavity becomes longer (i.e. the lower mirror goes down), which is the opposite of what would be expected from the pushing action of radiation pressure force on the upper mirror. This is a clear sign of the dominant role played by thermal forces in the system.

Figure 10.2 shows the appearance of bistability in the system [244]. When the cavity becomes longer (i.e. from red to blue detuning) the resonance condition is dragged for a long way as the scan pursues forth. Conversely, when the cavity is shortened (i.e. blue to red detuning) the resonance condition suddenly jumps to a state already past in the scan. This behaviour can be simulated by adapting the model of Chap. 3.2 to have the correct sign for the interaction and to account for the time evolution of the resonance condition. Specifically, the scan of the cavity frequency accounts for a linear dependence of the round-trip phase shift on time, while the change in resonance induced by the thermal effect is determined by the exponential rate at which power is

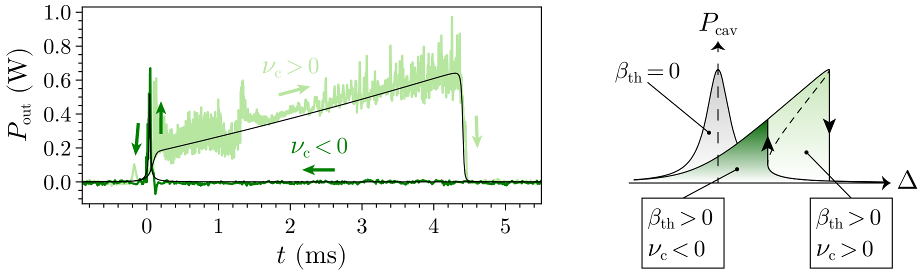

Figure 10.2: Bistability of one of the tripod cavities. The experimental traces show the output power of the cavity when scanned at exactly the same speed but in opposite directions (dark green when the scan makes the cavity shorter, light green when it makes the cavity longer). Both traces correspond to data collected from the reflected field, averaged and inverted for a more intuitive comparison with the diagram on the right. The two black traces represent the simulated evolution based on the model described in the main text, using identical parameters but opposite scan speed. The diagram on the right gives an intuitive picture of the hysteretic behaviour as a function of detuning (cf. Fig. 3.3).

absorbed [243]. Thus, the round-trip phase shift ϕ evolves as

$$\phi(t) = \phi_0\,(1 + \nu_c t)\,[1 + \beta_{\rm th}(P_{\rm cav} * h)(t)]\,, \tag{10.1}$$

where ϕ_0 is the phase at the start of the scan, $\nu_c = \dot{\omega}_c/\omega_c$ is the fractional rate of change in frequency determined by the speed of the scan (either positive or negative), $\beta_{\rm th}$ is a constant proportional to the strength of the interaction (negative in our case), and $h(t) = e^{-t/\tau_{\rm th}}/\tau_{\rm th}$ is the first-order impulse response of the system with time constant $\tau_{\rm th}$. The cavity solution of Eq. 2.48 becomes a functional equation for $P_{\rm cav}$, which can be numerically solved to yield the simulated results.

Thermally induced bistability provides an explanation to only part of the full dynamics unfolding at high power. The traces shown in Fig. 10.2 are averaged to display the evolution of the mean cavity power. They seem to show that the cavity follows the scan almost evenly along the distorted Lorentzian profile, while in fact the upper mirror oscillates persistently back and forth across resonance. This is another by-product of the optomechanical interaction, and it is visible on the optical output as a comb-like response during the scan in either direction, as shown by the raw traces of Fig. 10.3. The optical comb for this cavity is actually characterized by two separate frequencies. The signature of the oscillations is also detected by the force sensors attached to the support of the mirror. In this case however only a time-averaged measurement is possible, because the bandwidth of the force sensors is limited to 10 kHz and they cannot resolve the full oscillations.

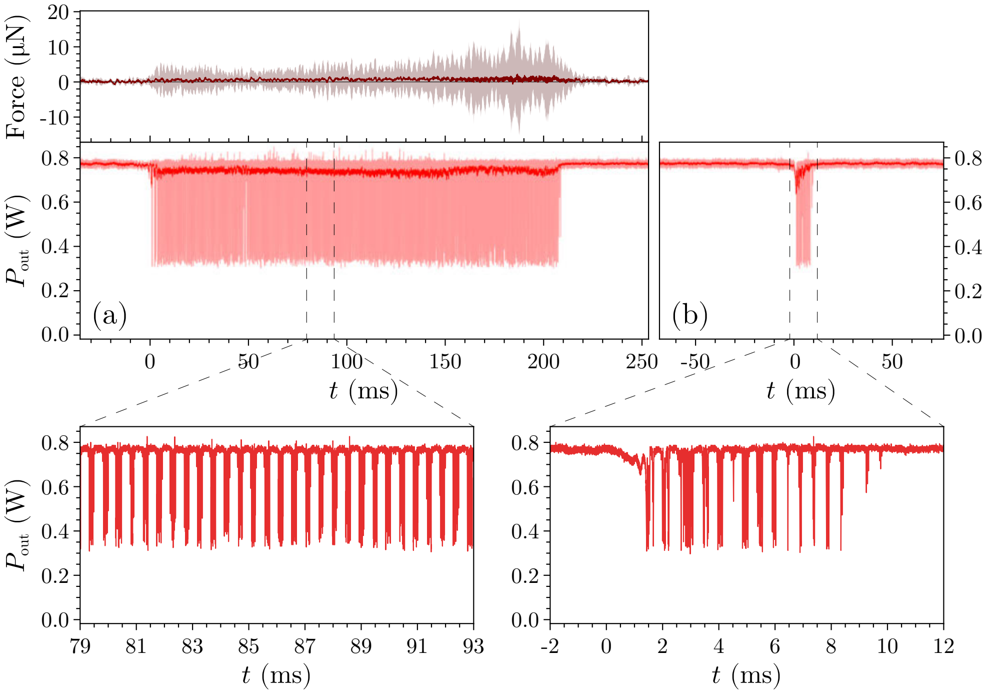

Figure 10.3: Comparison of the output of one of the cavities during self-locking (a) and anti-locking (b). The optical output is taken from the reflection of the cavity. The main plots show the full record together with the moving average, taken over 0.4 ms, to show the mean power level in the cavity over time. Extracts of the raw traces are shown in detail in the two insets. The plot at the top shows the signal from one of the force sensors, recorded in parallel to the self-locked trace at a resolution of 10 kHz. The shaded region corresponds to the standard deviation of the points sampled over 1 ms, bringing the effective.

The two frequencies of the comb can be seen in more detail in Fig. 10.4. A high-frequency oscillation, measured at (25 480 ± 50) Hz, quickly crosses the full width of the resonance. At the same time, a much slower oscillation at (2100 ± 50) Hz collects multiple repetitions of the resonance into clusters due to its larger amplitude.

The self-locking shown in Fig. 10.4 presents a striking difference from that of Fig. 10.3, despite the two traces being collected at exactly the same power and scan speed. In fact, especially at high powers, the self-locking regime of this cavity would sometimes last for much longer. Throughout this occasional extension of the lock, the low-frequency clustering disappears and the optical output is subject to regular, uniform spiking. Additionally, there are no vibrations detected on the force sensors, while the mean value of the force becomes more and more displaced as further energy is absorbed due to the increased duration of the lock. Even though this behaviour occurs more frequently at higher circulating power, it still occurs occasionally even when the

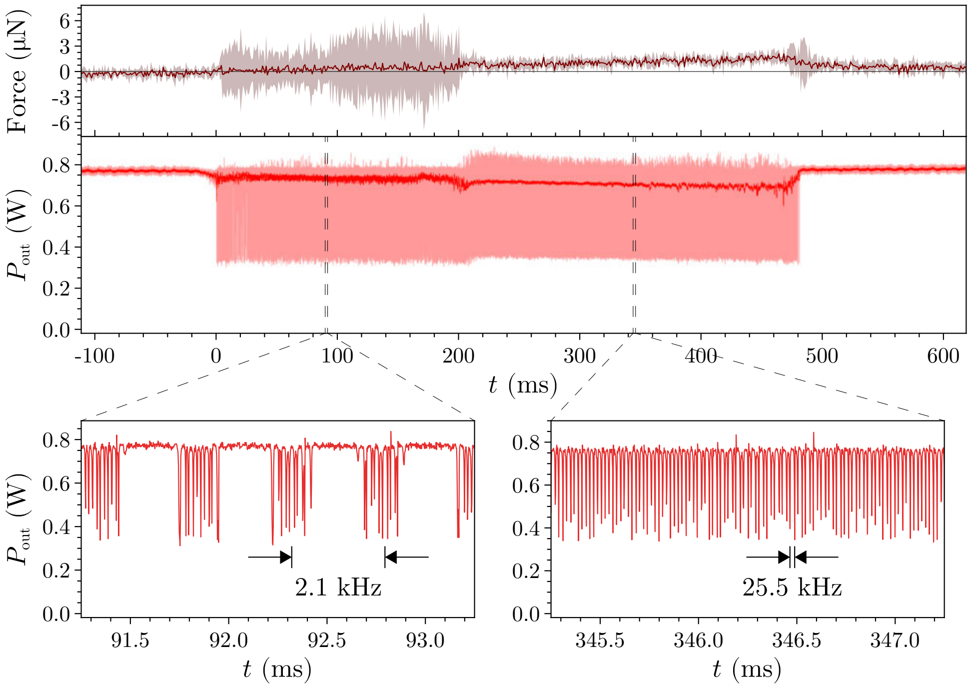

Figure 10.4: Self-locking of the same cavity as Fig. 10.3, now manifesting an extended duration where the low-frequency oscillations are absent. Power and scan speed are the same as the previous case.

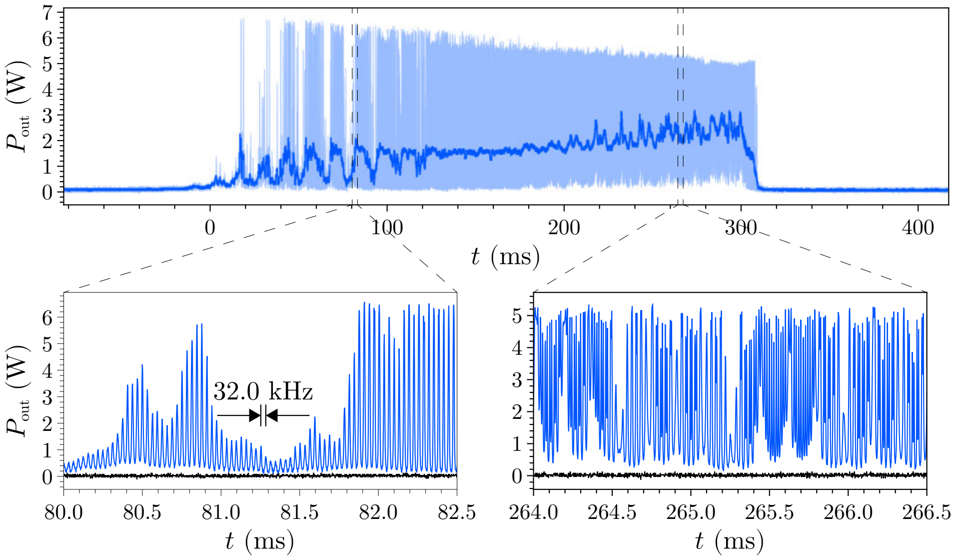

Figure 10.5: Self-locking of the second cavity. The traces represent the optical output obtained on transmission from the cavity. The optical comb is more regular than the other cavity, and it is possible to observe the oscillations decrease in amplitude as the average power increases. The black traces in the insets illustrate the level of the dark noise for comparison.

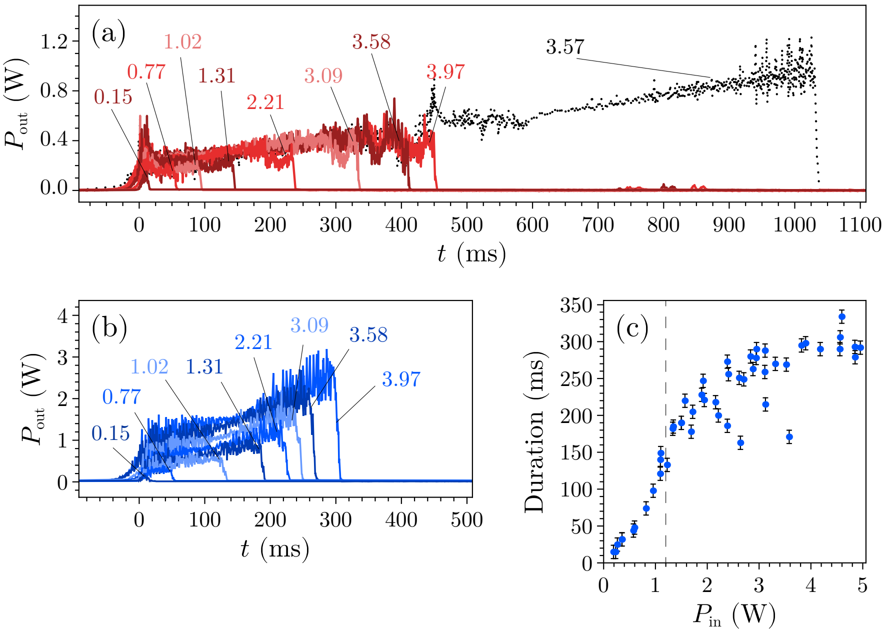

Figure 10.6: The duration of the self-locking regime depends on the power used. **(a)** Transmission output of the first cavity (averaged over 1 ms) for different levels of input power. Each trace is labelled by the value of the corresponding input power in watts. The dotted black trace presents a representative case of the extended self-lock that occurs stochastically. For all traces the length of the cavity is scanned at a speed of $80\,\text{nm}\,\text{s}^{-1}$. **(b)** Same as (a), but for the second cavity. The time scale is kept the same for comparison, although since the piezo-actuator is different the scan speed is half as fast, at $40\,\text{nm}\,\text{s}^{-1}$. **(c)** Duration of the self-lock of the second cavity as a function of input power. The dashed line indicates a rough threshold for the change in trend described in the main text.

input power is varied by a factor of four or more.

The comb-like response is also observed in the other cavities, however without the occurrence of two frequencies together. The cavity of similar coupling and finesse as the one of Fig. 10.3–10.4 displays self-sustained oscillations with a frequency of $(32\,010 \pm 50)$ Hz. As long as the power is enough to support them, they always manifest as a clean comb and no regular clustering is observed.

The duration of the self-locking regime for the two cavities is compared in Fig. 10.6. One trace corresponding to the first cavity's extended self-lock is also provided representatively at the highest power. Although not explicitly shown, the extension also occurs sporadically at lower power, generally doubling the extent of the self-lock. The second cavity is more consistent in its response. Looking at Fig. 10.6b it can be observed that, at high input power, the mean circulating power increases more sharply during the last stages of the self-lock. The phenomenon seems to be correlated to a shorter duration of the lock than the one that would be projected from the traces at low input power. This fact is also evident from Fig. 10.6c, where the linear trend of the first points is curbed after a threshold of approximately 1.2 W of input power. In terms of oscillations, the threshold power corresponds to the point where the optical output transitions from disordered to regular spiking. Similar trends are observed on the first cavity, however it is impossible to reproduce a similar plot due to the stochastic occurrence of the extension. Because of reduced coupling and lower finesse, the third cavity presents only disordered low-frequency oscillations at 1470 Hz and does not self-lock as substantially as the other two.

10.3 Interaction between the cavities

The non-linearities demonstrated by the cavities raise the question of what really happens to the upper mirror's dynamics at high power. More evidence can be gathered by looking at the combined effects of two cavities scanned at the same time.

By driving one cavity at high power while using the other as a probe at very low

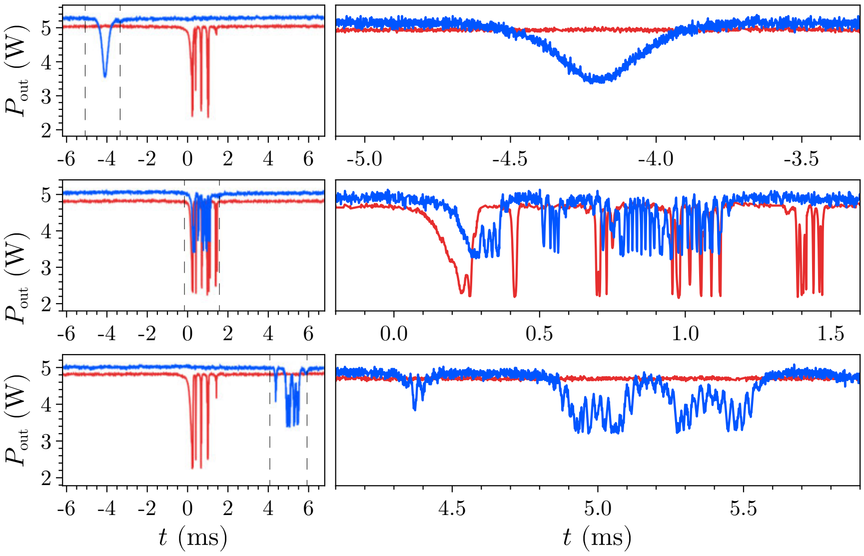

Figure 10.7: Optical output of two cavities, one pumped at high power (red) and one used to probe the effects on the mirror. The top, middle, and bottom plots correspond to the situations where the probe resonance occurs before, during, or after the resonance driven at high power. The panels on the right-hand side focus on the areas enclosed by the dashed lines on the left-hand side. Both outputs are detected from the reflected field of the corresponding cavity. The vertical scale of the probe is magnified by a factor of 10 to facilitate the comparison. The scan speed is approximately 4 µm s^{-1}.

power it is possible to see if the effects of the former are widespread to the entire mirror. By independently changing the offset of the two scans, the probing resonance can be observed before, during, and after the self-lock of the other cavity (cf. Fig. 10.7). When the probe temporally precedes the driven cavity, no exceptional response is discerned and the resonance presents a clean Lorentzian profile. When the two resonances overlap, the stirring caused by the absorption of high power is detected on the probe cavity as well, indicating that the impact spreads to the full substrate. The oscillations on the probe persist even after the conclusion of the high power drive, although inevitably they have a smaller amplitude that decays as the two resonances get further apart. The decay rate is measured at approximately 50 Hz, and the optical resonance of the probe returns to be a regular Lorentzian after about 20–30 ms. The decaying oscillations after the end of the optical drive can also be noticed on the force sensor traces, such as the one of Fig. 10.3.

When the two cavities are pumped at high power at the same time, they influence

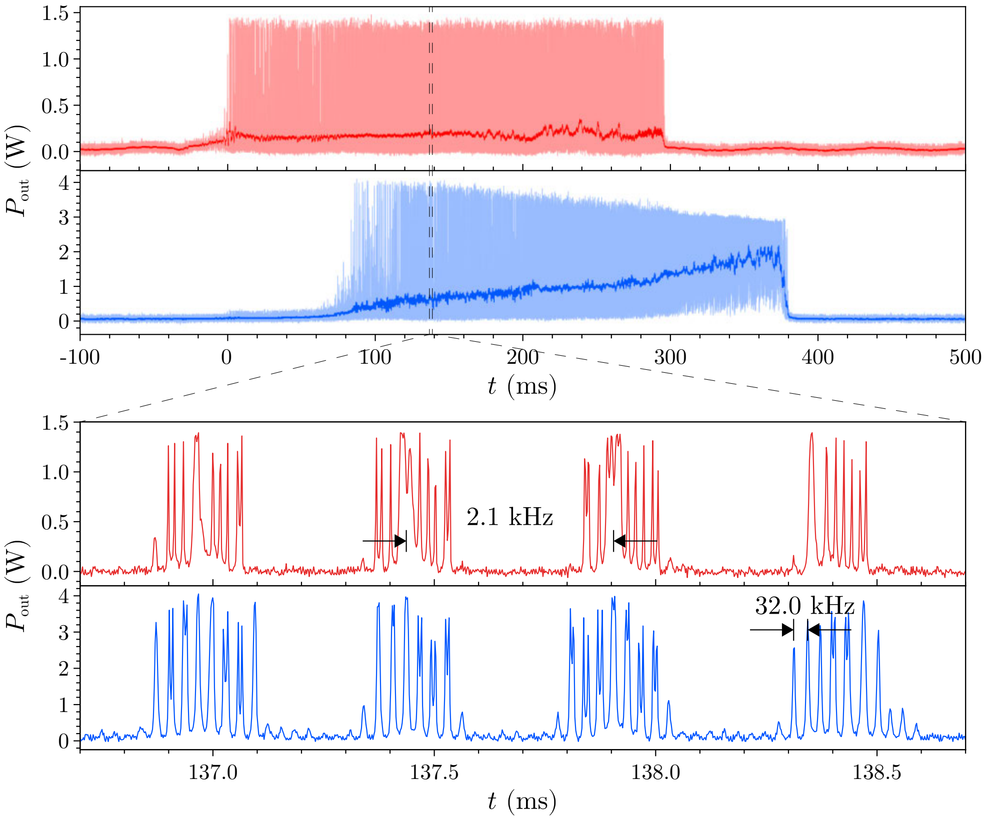

Figure 10.8: Self-locking of the two cavities in the dual pump configuration. The top corresponds to the optical output of each cavity detected on transmission. The bottom demonstrates the synchronized clustering of the two optical combs in detail.

each other in a very specific way. On the whole, the two self-locking regimes have a tendency of triggering one another. Also, as can be seen in Fig. 10.8, the dominant frequency characteristic of each cavity spills to the other one. This effect occurs on the first cavity, where the high-frequency comb in each cluster strays from the semi-regular oscillations at 25.5 kHz and is contaminated by a 32.0 kHz component. It is even more obvious on the second cavity, which on its own would not display any clustering at 2.1 kHz whereas now it synchronizes to the low frequency of the first cavity.

Both high- and low-level correlations point to the fact that the two cavities interact through the oscillations of the upper mirror of the tripod. Ideally this interaction would only occur through the optical spring effect of the radiation pressure force, but if thermal forces are capable of exhibiting analogous attributes it may be possible to reach similar regimes of stability.

10.4 Discussion

From what has been witnessed on the current setup, one thing is clear: the intracavity field has a strong impact on the resonance conditions. The oscillations of the upper mirror excited by the optical field culminate into a spiked response where the resonance is crossed numerous times. Each individual peak is much narrower than the Lorentzian profile that would emerge in normal conditions. This is a sign that the oscillations are much faster than the scan, a fact which is also confirmed by the occasional appearance of ring-down self-interference on the output field (as can be inferred for example in Fig. 10.4, where the power level of the reflected field rises even higher than the input power). The two high frequencies characteristic of the cavities with consistent self-locking (25.5 kHz and 32.0 kHz) are compatible with the order of magnitude expected from the optical spring effect, but no further evidence could be collected at this stage in favour of this hypothesis. One of the cavities also oscillates at a lower frequency (2.1 kHz) with much larger amplitude, several times wider than the cavity linewidth. These fluctuations are also picked up by the force sensors and extend to the full substrate, indicating that they probably correspond to the excitation of a drum mode of the mirror. Regardless of their origin, the optically driven oscillations decay with a time constant of 20 ms.

The appearance of self-sustained oscillations together with bistability is characteristic of systems where different types of non-linearities coexist. They have been observed in whispering gallery mode resonators in relation to competing heat transport mechanisms [245] and in suspended-mirror Fabry–Pérot cavities subject to both radiation pressure and photothermal forces [246]. The clash between different non-linearities operating at separate time scales induces cyclic transitions between the multiple stable solutions, especially when the strength of the two interactions is comparable [58]. While radiation pressure would increase the cavity length by pushing on the mirror, the photothermal effect would act in the opposite direction by slowly expanding the substrate, for example. Their interplay leads to periodic excitations of the optical intensity, provided that either effect is strong enough to shift the cavity resonance by at least one linewidth. The stationary stability of the system is lost through one or more Hopf bifurcations that can burst into chaotic spiking when the mechanical quality factor of the oscillations is high enough [247]. A similar chaotic response has been recently reported in microtoroid optomechanical resonators [248], demonstrating the interest for chaos-driven devices with the capacity of interfacing between different systems for secure communication.

Conclusions. The stable optical levitation of a macroscopic mirror is, in principle, possible. The proposed scheme, consisting of an optical tripod relying on radiation pressure forces and the optical spring effect, could serve as an ideal platform for applications that are extremely sensitive to environmental noise. In the current experimental configuration, the influence of radiation pressure force was observed in combination with the impact of thermal effects. Similar effects in other systems have been observed before, suggesting that it could be possible to operate the system in a different regime where chaos could be observed. Whether new operational regimes are considered or not, it is necessary to achieve a much larger degree of control over the cavities in order to achieve stable suspension of the mirror on the optical field alone. The concurrence of multiple effects limits the general understanding of the full dynamics, and a reduction in thermal absorption is indispensable for the successful levitation of the mirror. It should be remembered that the present configuration is only a prototype and there is a lot of room for improvement. The coating of the upper mirror, for example, should be obtained by ion-beam sputtering (or equivalent) to minimize the absorption of intracavity power. The substrate of the mirror would then need to be more resistant in order to withstand the higher stresses induced by the denser coating. Diamond, thanks to its mechanical strength and low optical absorption, presents a viable option for this optical component. Additional enhancements to the apparatus require operations in a vacuum environment and a dual-beam configuration to prevent the parametric amplification of the oscillations from driving the cavities into unstable regimes. Should the combined upgrades not be enough to suppress the thermal effects and restrain the competition with radiation pressure, one can always resort to tailored stabilization protocols based, for example, on dual-mode thermal stabilization and self-locking [249].

Part IV

Extensions of optomechanical theory

This final Part consists of additional theoretical research performed in parallel to the experimental investigations presented so far. Even though the topics covered by each chapter are not directly related, they share the common interest of developing new techniques and applications aim at broadening the scope of optomechanics. Chapter 11 explores the possibility of adapting the stability potential arising from the optical spring effect to better suit specific tasks. Chapter 12 explains how the reciprocal interaction between mechanical systems and light can be used to generate squeezed states of light. The squeezing obtained by optomechanical systems is then shown to display very specific spectral qualities that are attractive to the gravitational wave community and could be used to obtained an advantage in interferometric measurements.

The research presented here has been featured in the following publications:

- [96] Slatyer, H. J., Guccione, G. et al., "Synthesis of optical spring potentials in optomechanical systems", *Journal of Physics B* **49** 125401 (2016);
- [17] Guccione, G., Slatyer, H. J. et al., "Squeezing quadrature rotation in the acoustic band via optomechanics", *Journal of Physics B* **49** 065401 (2016).

The fourth and last son of Iapetus acknowledged by Greek mythology is Epimetheus, whose actions led to the opening of Pandora's box. The name of the Titan name is a reflection of his twin brother's, Prometheus: it translates to "afterthought", a meaning appropriate for this conclusive part.

G. Bonasone, *"Epimeteo apre il vaso di Pandora da cui escono le virtù"*

Chapter 11

Synthesis of optical spring potentials in optomechanical systems

11.1 The advantage of engineered potentials

Most metrological applications of optomechanical systems rely on the accurate sensing of the oscillator's position [250]. The measurement of acceleration, gravity, magnetic fields, and many other physical quantities is regulated by the susceptibility of the mechanical system, which converts any action perceived by the oscillator into a displacement that can be monitored precisely by the optical field. The susceptibility of optically trapped systems is determined by the trapping potential applied by the optical field. The performance of these optomechanical systems can then be improved if the potential, or equivalently the force function, is tailored around an optimal use of the system's resources towards the intended task.

In the case of optical tweezers, the optical potential experienced by the trapped particles can be tuned by shaping the transverse mode of the laser used for suspension [201], or by using an optical cavity [200] to modify the longitudinal mode of the light. Other schemes subject to a strong influence of the optical spring effect can also benefit from engineering of the trapping potential, in this case entrusted to the spectral properties of the field rather than the spatial distribution of its intensity. Even though precise control is possible, the range of possible optical spring parameters is fixed by the finesse of the cavity. Applications based on the use of high-finesse cavities are typically characterized by very stiff optical springs, which may not always be the desired outcome. If one wants to sense the position of an optically trapped mirror to measure a force, for example, then a large mechanical response is required in order to maximise the signal. Ideally, one would desire an optical spring of lower stiffness, while still being able to use a high-finesse cavity to maintain the full interferometric sensitivity of the position read-out. The use of polychromatic light has been suggested before to synthesise complex optical force or potential profiles in cavity-based optomechanical systems [251]. In general, control over the spectral attributes of the cavity's input field can be used to approximate customised force functions that modify the oscillator's response to enhance its sensing capacities.

In this chapter, we specifically analyse how the light source needs to be manipulated in order to create elaborate force profiles to be adapted for a specific requirement of a system [96]. In particular we develop an analytical theory based on continuous power spectral densities of the optical field. Because these continuous spectral distributions are hard to produce experimentally, we continue the analysis by investigating how they can be approximated by appropriate frequency comb inputs. Finally, we apply the formalism developed to the measurement of relative variations of gravitational acceleration with the levitating mirror proposed in Chap. 8.

11.2 Interaction of multiple optical springs

We want to modify the response of an optomechanical system by modifying the effective optical forces acting in the system. The aim is to achieve this result by modifying only the spectral properties of the input field, without having to modify any other aspect of the system, such as the cavity finesse or the intrinsic susceptibility of the oscillator. In particular, we consider an extension of the optical spring effect in the case of a multi-mode input to the cavity.

Recall, from Chap. 3.3, the expressions for the radiation pressure force,

$$F_{\mathrm{rp}}(x,\delta) = \frac{4P_{\mathrm{in}}}{c\kappa\tau}\frac{\kappa^2}{\kappa^2+(\delta+G_0x)^2}, \tag{11.1}$$

and the corresponding optical spring,

$$k_{\mathrm{os}}(x,\delta) = \frac{8G_0P_{\mathrm{in}}}{c\tau}\frac{\kappa\,(\delta+G_0x)}{\left[\kappa^2+(\delta+G_0x)^2\right]^2}, \tag{11.2}$$

as a function of the oscillator's position, x, and of the detuning of the input field relative to the closest cavity resonance, δ. Here, G_0 is the optomechanical coupling constant, P_{in} is the power of the input beam, and τ and κ are the cavity's round-trip time and half-linewidth. These expressions were derived assuming a typical optomechanical cavity with a single-mode input of fixed detuning $\delta = \Delta_0$, and they are not valid for the multi-mode input that we need to consider. This is because the optical force of a multi-mode input, resulting from the interference of two or more different fields injected into the cavity, does not correspond to the linear sum of the forces that would be obtained with each input separately. A similar situation was encountered in Chap. 8.2.3, where a dual-mode input was considered to allow the radiation pressure to be restoring without introducing anti-damping into the system. The solution in that case was found by taking advantage of the periodicity of the cavity's response and opportunely detuning one of the fields by a full free spectral range, ω_{FSR}. By doing so, the beating would occur on a very fast time scale and the oscillator would perceive only an averaged effect. If the mechanical frequency of the oscillator, ω_{m}, happened to be comparable to ω_{FSR}, then the procedure would need to be modified by allowing the relative detuning between the two modes to be some multiple of ω_{FSR} in order to make the beating faster than the dynamics of the oscillator. The claim that a fast beating component of the optical force can be neglected from the oscillator's point of view is numerically justified in Appendix C for a realistic case.

The same argument can be extended to a multi-mode input with more than two frequencies. Suppose a frequency comb input with constant spacing ϵ between the modes. We may identify an integer N such that $N\epsilon \gg \omega_{\mathrm{m}}$. Beating between modes separated by $N\epsilon$ does not drive the oscillator. For any two modes separated by less than $N\epsilon$, one can apply the method outlined above to up-shift the relative detuning by some multiple of the free spectral range. The process can be iterated over all modes in the comb so that each free spectral range only carries modes that are spectrally separated by more than $N\epsilon$. Formally, the nth peak of the comb is shifted by (n modulo N) multiples of ω_{FSR}, so that a total of N free spectral ranges are employed. Each free spectral range, then, hosts a number of modes equal to the total number of modes of the comb divided by N. This technique ensures that every pair of modes beats at a frequency much higher than ω_{m} and therefore that no interference effect drives the oscillator, provided that $\omega_{\mathrm{FSR}} \gg \omega_{\mathrm{m}}$. Again, if the frequency of oscillation is comparable to the free spectral range, it is simply necessary to shift each mode by a higher multiple of ω_{FSR}. We assume such preparation technique to be implicitly applied to the input if necessary, in order to expect the superposition principle to hold given *any* multi-mode frequency comb input. The average effective optical force experienced by the mirror can then be approximated by the sum of the forces due to each individual mode.

Importantly, this method only holds for an input that has a discrete distribution of modes. It is not applicable to an input that has a broad, continuous spectral distribution, since in this case it would be necessary to shift a “continuum” of frequencies. From a practical point of view, however, we will see that this is not an obstacle and that the class of frequency comb input fields is sufficient for the approximation of a generic potential. In the next section we continue the analysis in terms of a continuous input, mostly to have the possibility of developing a formal treatment in terms of integrals rather than sums. Then we will see what considerations are necessary to approximate the continuous power spectrum with a discrete frequency comb, for which the superposition principle can be assumed to hold for the optical forces and the associated optical springs.

11.3 Approximation of an arbitrary force function

Suppose we desire the optical forces to reproduce a theoretical force $F_{\text{th}}(x)$, which is some function of the mirror's position x. The aim is to find a power spectral distribution (PSD) for the input laser, $p(\delta)$, that will produce an overall radiation pressure force $F_{\text{rp}}^{(\text{tot})}(x)$ as close to $F_{\text{th}}(x)$ as possible.

Under the assumption that no interference effects occur between the different frequency components of the input field, we have that the total optical force due to the input $p(\delta)$ is

$$\begin{aligned} F_{\text{rp}}^{(\text{tot})}(x) &= \int_{-\infty}^{+\infty} d\delta \; F_{\text{rp}}(x,\delta)p(\delta) \\ &= \int_{-\infty}^{+\infty} d\delta \; F_0(\delta + G_0 x)p(\delta) \\ &= (F_0 * p)(-G_0 x), \end{aligned} \tag{11.3}$$

where $F_0(\delta) := F_{\text{rp}}(0,\delta)$ is the force obtained from a single-mode input when the mirror is in its rest position, and $F_0 * p$ is its convolution with the PSD. The idea is then to choose $p(\delta)$ to have the function $(F_0 * p)(-G_0 x)$ coincide with $F_{\text{th}}(x)$. For convenience, the convolution can be rewritten in the equivalent form

$$F_{\text{rp}}^{(\text{tot})}(x) = (F_0/\beta * \beta p)(\delta)|_{\delta=-G_0 x}\,, \tag{11.4}$$

where $\beta := \int_{-\infty}^{+\infty} d\delta \; F_0(\delta)$. By doing so, we can view the action of the cavity as a combination of a smoothing by the normalized Lorentzian F_0/β, a rescaling of the input field by β, and a change of variable $\delta \rightarrow x = -\delta/G_0$. The smoothing action has a role analogous to that of a Gaussian blur, levelling out any feature finer than the linewidth of the cavity while preserving larger features. With this we identify one of the constraints of the approximation method: the fidelity of the approximation of the theoretical force function by the optical forces depends on the finesse of the cavity. Any theoretical force function whose features are larger than the cavity linewidth can be reliably approximated. For this reason we limit the analysis to the reproduction of functions that are not affected significantly by the smoothing, i.e. F_{th} satisfying the condition

$$F_{\text{th}}(-\delta/G_0) \approx (F_0/\beta * F_{\text{th}}|_{x=-\delta/G_0})(\delta). \tag{11.5}$$

With this assumption, the approximation of an arbitrary force function by the optical forces is satisfied by the choice

$$p(\delta) = F_{\text{th}}(-\delta/G_0)/\beta, \tag{11.6}$$

for which we have

$$\begin{aligned} F_{\text{rp}}^{(\text{tot})}(x) &= (F_0/\beta * F_{\text{th}}|_{x=-\delta/G_0})(\delta)\Big|_{\delta=-G_0 x} \\ &\approx F_{\text{th}}(-\delta/G_0)|_{\delta=-G_0 x} \\ &= F_{\text{th}}(x), \end{aligned} \tag{11.7}$$

as desired. Choosing the input according to Eq. 11.6 will cause the mirror to experience an optical force which is modelled around the required theoretical force profile.

This result hinges on the linear superposition of the optical forces, as indicated by the integration in Eq. 11.3. Such superposition is only possible in the lack of interference effects between different frequency components of the input field. For an input with a continuous PSD this assumption is very speculative. However, it is feasible in the case of a discrete frequency comb, as discussed in the last section. To confirm the validity of the result we need to prove its compatibility when the continuous PSD $p(\delta)$ is replaced by a frequency comb of discrete modes of spacing ϵ. Applying a rectangular approximation to Eq. 11.3, we have

$$\begin{aligned}F_{\mathrm{rp}}^{(\mathrm{tot})}(x) &= \int d\delta\, F_{\mathrm{rp}}(x,\delta)p(\delta) \\ &\approx \sum_n \epsilon\, F_{\mathrm{rp}}(x,n\epsilon)p(n\epsilon).\end{aligned} \tag{11.8}$$

Then, if the PSD is chosen according to Eq. 11.6, the optical force resulting from the action of the cavity on the mirror is given by

$$F_{\mathrm{rp}}^{(\mathrm{tot})}(x) = \sum_n F_{\mathrm{rp}}(x,n\epsilon)\cdot F_{\mathrm{th}}(-n\epsilon/G_0)\epsilon/\beta. \tag{11.9}$$

The right-hand side corresponds to the force obtained by a frequency comb input such that the component detuned by $n\epsilon$ has power $F_{\mathrm{th}}(-n\epsilon/G_0)\epsilon/\beta$, assuming that interference effects are removed by appropriate shifting of each mode.

The required frequency comb could be generated in several ways. For many types of force functions, the modulation of a normal single-mode input might be enough to induce sidebands to the central frequency acting as the different components of the comb. The strength of each component is determined by the strength of the modulation. Potential asymmetries required in the comb may be enforced with a combination of amplitude and phase modulation. As the size of the comb would be determined by the maximum modulation frequency allowed, it could be possible to use a sequence of modulations to allow the generation of wider combs, at the expense of simplicity and flexibility. Alternatively, the different modes of the comb might be generated by commercial multi-channel laser systems, which are capable of independently tuning the frequency of each channel by up to a few tens of terahertz.

In summary, the optomechanical system can be engineered to let the oscillator experience any theoretical force function $F_{\mathrm{th}}(x)$, as long as the profile of such function does not involve features finer than the linewidth of the cavity. The arbitrary force profile is resolved by an approximation which is mediated by the optical forces, $F_{\mathrm{rp}}^{(\mathrm{tot})}(x)$, and which is determined by the appropriate choice for the spectral distribution of the input. The realization of this technique relies on the absence of interference effects. These can be suppressed by separating the frequency components of the input to separate free spectral ranges of the cavity to let the oscillator experience only the average effect of the beating. For inputs with a continuous spectral density, $F_{\mathrm{rp}}^{(\mathrm{tot})}(x)$ can itself be approximated by an equivalent frequency comb input to allow the required separation of the modes.

11.4 Engineering the sensitivity of a gravimeter

In this section we apply the method developed earlier to the specific case of an optomechanical gravimeter. In particular, we see how to engineer the potential of the levitating mirror proposed in Chap. 8 in order to obtain better measurements of the variations in gravitational acceleration, g. The levitating mirror is a particularly illustrative example, since its motional stiffness is fully determined by the optical spring. The ability to arbitrarily engineer the optical spring is therefore especially relevant for this system. Nevertheless, the technique would be equally applicable to oscillators where the optical spring only modifies the intrinsic attributes that already exist in the system.

The equilibrium position of the levitating mirror depends on its weight. Assuming the mass m to be constant, then the weight can only change if g varies. By monitoring the equilibrium position, which is directly determined by the weight, one can estimate local variations in the gravitational acceleration. The goal is to demonstrate how adapting the force function to this specific task can bring an advantage. Because this application is intended primarily for illustrative purposes, sources of noise that could affect the measurement, such as laser intensity fluctuations, will be ignored. Also, the original tripod of cavities intended for levitation will be simplified to a configuration with a single vertical cavity configuration in order to have a single degree of freedom, x, for both the optical propagation and the motion in the vertical direction.

The sensitivity of the system can be increased by letting the same variation in weight produce a larger variation in position. This is achieved with a softer spring constant for the mirror. Because the spring constant is determined by the gradient of the force function, the aim is to have a profile with a slope as gentle as possible. While considering which force function is better suited for the role, we need to ensure that the balancing condition for levitation holds. Only forces that can support the weight of the mirror should be taken into account. For this purpose we build the analysis around two directly related thresholds which set a reference for the comparison of different profiles. The first threshold is $f_0 := mg$, which is the force corresponding to the weight of the mirror and sets the equilibrium point of the system. In terms of optical field, this threshold corresponds to an intra-cavity power $p_0 := cf_0/2$ (cf. Eq. 3.58). The second threshold is given by the maximum optical force applied to the mirror, set to be equal to $1.5\, f_0$ in order to compare different profiles at equal optical trap depth. The trap width, on the other hand, is unconstrained and depends on the specific profile considered.

A gentler slope can be obtained directly by reducing the finesse of the cavity, thus avoiding the need of a multi-mode input or of an engineered potential. However, this approach has the downside that a lower finesse also corresponds to lower power in the cavity at resonance. More input power would then be required to meet the trap depth requirement obtained in the case of higher finesse. Intuitively, as the slope is reduced to soften the stiffness, it is clear geometrically that to maintain the same threshold of $1.5\, f_0$ the integral of the force function needs to increase, regardless of its shape. For a given trap depth, there is a limit to how much reduction in stiffness is possible without an increase in input power. Availability and other technical impediments, such as optical damage, determine how much improvement in sensitivity can be obtained by simply lowering the finesse. Another determining factor is given by the precision in the measurement of the displacement allowed by the cavity. The total phase shift accumulated by the field on reflection with the moving mirror scales with the finesse of the cavity. Reducing the finesse, therefore, sacrifices the high-precision interferometric read-out that would otherwise be allowed by a cavity with higher finesse. By using a multi-mode input, one can recreate a gentler slope without having to renounce to finesse and measurement quality. At the same time, the multi-mode input can be used to optimize the trade-off between stiffness and input power by ensuring the efficient use of the available power where it is most needed.

The force profiles expected from single- and multi-mode inputs are shown in Fig. 11.1. The single-mode input is considered in application to two cavities of different finesses for comparison.As explained before, the low-finesse cavity allows a softer spring but it also requires more input power in order to meet the required trap threshold. For multi-mode inputs, the continuous PSD of an ideal ramp function and its approximation with a plausible discrete frequency comb are shown. The ideal force function is designed to extend further in the blue-detuned region in order to have the trap depth requirement be satisfied by the approximated functions. A ramping profile is chosen to adapt to the particular task considered. The ramp has a gentle slope on the blue-detuned side of the resonance, where the mirror is trapped. Thus, in the region around the equilibrium point, it achieves even a softer spring than the one obtained by the low-finesse cavity with a single-mode input. The ramp drops off immediately outside of the trapping region, minimizing the input power needed. Thanks to this, both the continuous and the discrete approximations of the ideal force function lead to a significant reduction in stiffness, without the same power requirements of the low-finesse cavity. The specific inputs of Fig. 11.1b–c correspond to a total power of $3.75 \times 10^{-3}\ p_0$ for the continuous

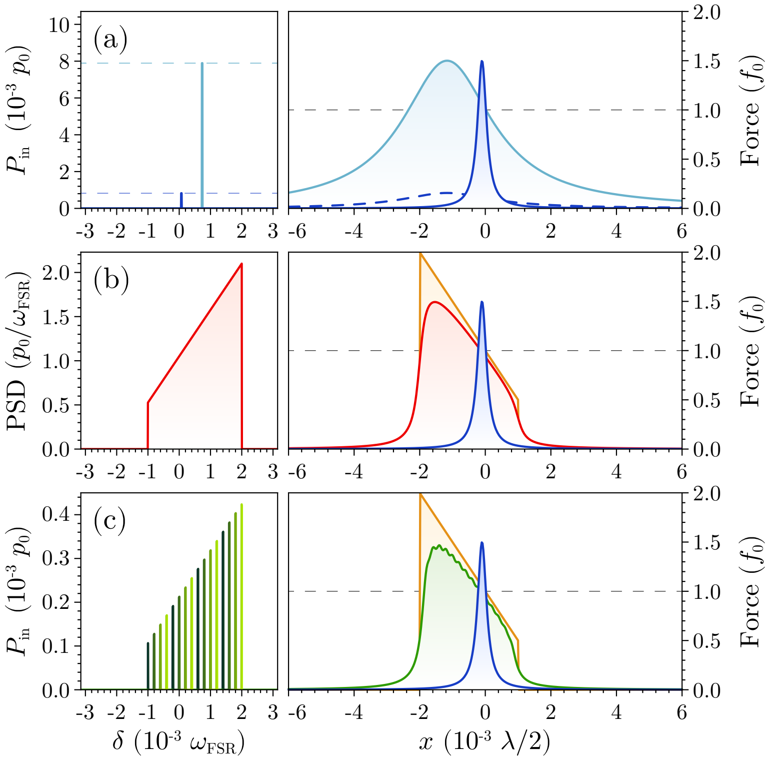

Figure 11.1: Different choices of input field (left panels) with the corresponding force functions (right panels). The axes are scaled in terms of the power required for levitation p_0, the weight of the mirror f_0, the free spectral range of the cavity $\omega_{\rm FSR}$, and the optical wavelength λ. **(a)** Single-mode inputs induce a force function which follows the typical Lorentzian profile of the cavity. Two cavities with a high finesse of 3000 (dark blue) and a low finesse of 300 (light blue) are considered. The input fields are blue-detuned to let the equilibrium condition correspond to the position $x = 0$. In the case of low finesse, more input power is needed to maintain the same trap depth. If the same power as the high-finesse case were used (dashed blue trace), the maximum force would be noticeably lower than the force required to support the weight of the mirror, f_0 (indicated by the dashed line for convenience). **(b)** Multi-mode input with a continuous PSD can approximate the desired force function, in this case represented by a ramp (yellow). The ramp is adjusted to have the approximated force function (red) satisfy the trap depth requirement of $1.5\,f_0$. The approximation is obtained in the case of the high-finesse cavity, whose response is also shown for comparison (blue). **(c)** Multi-mode input given by a discrete frequency comb. The comb is adapted to approximate the continuous PSD of (b). The desired function (yellow) and the normal cavity response to a single frequency (blue) are also shown for comparison. Each frequency component of the input is plotted modulo $\omega_{\rm FSR}$, with each free spectral range depicted with a different shade of green. In this representative case the spacing ϵ is chosen so that $4\,\epsilon \gg \omega_{\rm m}$. Therefore, only four different free spectral ranges need to be considered to avoid interference effects.

PSD input and of $4.2 \times 10^{-3}\ p_0$ for the frequency comb input, in both cases lower than the input power of $8 \times 10^{-3}\ p_0$ needed for the low-finesse cavity of Fig. 11.1a. Another

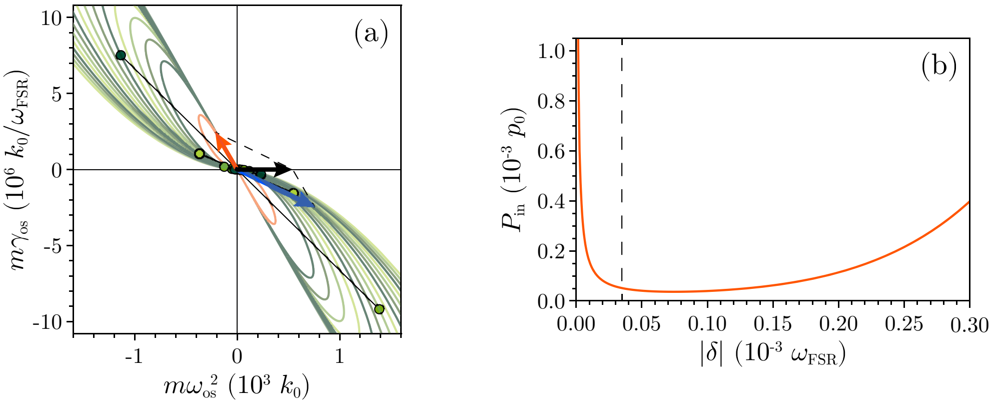

Figure 11.2: Stabilisation of the optical spring resulting from the frequency comb input of Fig. 11.1c. **(a)** Representation of the real and imaginary parts of the optical spring, corresponding to the optical stiffness and the optical damping introduced by the cavity. The axes are scaled in terms of $k_0 := 2f_0/\lambda$, where f_0 is the mirror's weight and λ is the optical wavelength. The parametric curves correspond to the effect of each separate mode parametrized as a function of detuning $\delta \in (-\infty, +\infty)$. The individual springs obtained at $x = 0$ for each mode are indicated by circles on the parametrized curves. Different shades of green correspond to modes shifted to different free spectral ranges. The blue arrow represents the total optical spring resulting from the superposition of the comb modes. The red arrow represents the spring obtained from the red-detuned field used to cancel the effects of anti-damping. The black arrow corresponds to the final optical spring. **(b)** Power needed for the red-detuned field to cancel the anti-damping effects as a function of its (negative) detuning δ. A dashed line indicates the detuning (and corresponding power) used in (a). Depending on detuning and power, the resulting stiffness of the total spring may be different.

advantage of the customised potential is that it can make the trap wider, resulting in greater robustness against large displacements.

It should be remembered that, due to the finite response time of the cavity, the optical force obtained from a blue-detuned input is restoring but also anti-damping. In the case of a multi-mode input, the character of the optical force is determined by the contribution of each frequency component. The plots in Fig. 11.2 are obtained considering the full dynamical expression of the optical spring, which in the case of a single input is (cf. Eq. 3.70):

$$k_{\mathrm{os}}(\omega) = \frac{8G_0P_{\mathrm{in}}}{c\tau}\,\frac{\kappa\,(\delta+G_0x)}{\left[\kappa^2+(\delta+G_0x)^2\right]^2}\left[1-\frac{\omega}{\kappa^2+(\delta+G_0x)^2}\,(\omega-2i\kappa)\right]^{-1}. \qquad (11.10)$$

The real part of $k_{\mathrm{os}}(\omega)$ determines the optical stiffness and thus the frequency of oscillation within the trap, $\omega_{\mathrm{os}} := \sqrt{\mathrm{Re}(k_{\mathrm{os}})/m}$. The imaginary part gives the optical damping, $\gamma_{\mathrm{os}} := \mathrm{Im}(k_{\mathrm{os}})/\,(m\omega)$. In Chap. 8.2.3 we saw how the anti-damping can be

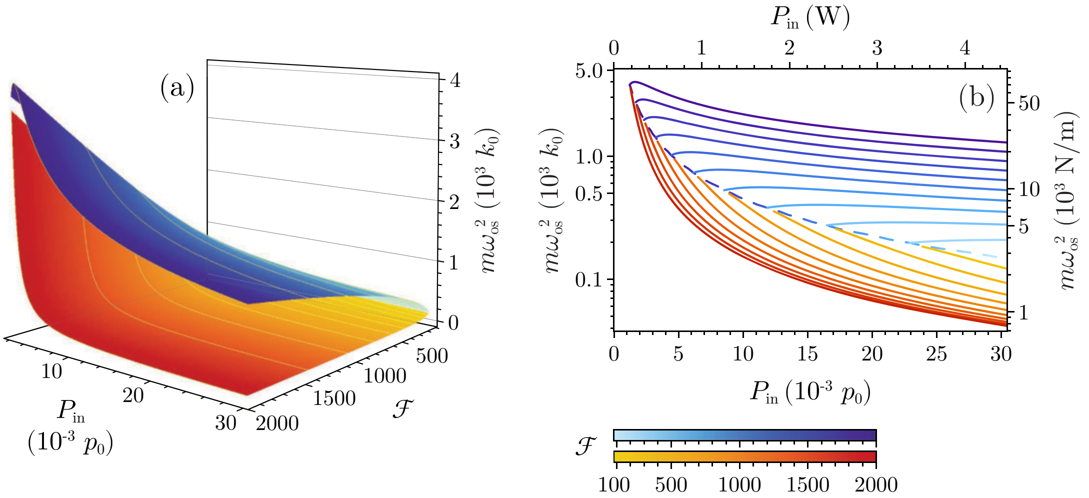

Figure 11.3: Comparison of the optical stiffness obtained with single- and a multi-mode inputs. The axes are scaled in terms of the constants p_0 and k_0 introduced before. Physical scaling in SI units is also given, corresponding to $\lambda = 1064\,\text{nm}$, $\omega_{\rm FSR} = 2\pi \times 750\,\text{MHz}$, and $m = 1\,\text{mg}$. **(a)** Full comparison as a function of input power $P_{\rm in}$ and cavity finesse $\mathcal{F}$. The blue surface is the spring constant obtained from a single-mode input. The red surface is the minimum spring constant achievable when a multi-mode continuous ramp input is used instead. **(b)** Cross sections of the full comparison for different values of finesse. The starting point of each curve corresponds to the lowest power satisfying the trap depth requirement at a specific finesse, i.e. such that the cavity power is at least $1.5\,p_0$ and the corresponding force is at least $1.5\,f_0$. The locus of such points is shown as a dashed line. A further increase in power shifts the balancing point f_0 along the profile of the Lorentzian force function, yielding different optical stiffness. Each point on a red curve corresponds to the lowest stiffness achievable, which is obtained when the maximum cavity power is kept constant at $1.5\,p_0$ to satisfy the trap depth requirement while the additional power available is used to make the ramp wider.

neutralized by the introduction of an additional red-detuned field [89]. A similar argument applies in this case, where a separate beam can be appropriately tuned to induce an optical spring with positive damping (red arrow) that cancels the anti-damping effects of the combined optical springs from the multi-mode input (blue arrow). Only few modes contribute towards the optical spring at any given position of the mirror. As the mirror moves, different modes start contributing more as they become resonant. The total optical spring then oscillates between different values, with more or less anti-damping to be cancelled. A worst case scenario can then be considered to balance the system. Even in this case, the addition of such a damping beam does not limit the ability to engineer the desired force function. The power assigned to this additional beam can be lower than any individual mode of the comb, as shown in Fig. 11.2b.

The performance of single- and multi-mode inputs is compared in Fig. 11.3, which shows the optical stiffness obtained in both cases as a function of power and finesse. The multi-mode input used in this case is the continuous, ramping PSD of Fig. 11.1b, primarily because it allows for a simpler mathematical formulation. A more physical multi-mode input returning comparable results can always be obtained in the limit of very fine spacing of the approximating comb. For both types of inputs, no spring value is reported when the combination of input power and finesse does not generate enough cavity power to satisfy the trap depth requirement. Focusing on the single-mode input (blue), we can see that the trend of the optical stiffness follows the gradient of the Lorentzian force function when the power is increased while the finesse is kept constant. This is because the increasing power pushes the balancing condition down along the familiar Lorentzian profile. Lower stiffness values are obtained close to the base of the Lorentzian, which is accessible only at high input power. Note that in general the slope of the Lorentzian is also gentle close to resonance, but these points can not be taken into account as they do not satisfy the necessary trap depth. A higher finesse corresponds to a steeper profile, and therefore a generally higher stiffness value. This tendency can be inverted when a multi-mode input is considered. Thanks to the additional freedom provided by the ramping profile, when more power is available in the cavity it can be used towards the intended task of softening the optical stiffness instead of having it push the equilibrium condition further down along the profile. By fixing the maximum of the force function to $1.5\, f_0$, which correspond to a maximum cavity power of $1.5\, p_0$, the additional power can be used to increase the width of the ramp and thus allow a softer spring. The trap does not become deeper, but it becomes wider. This method allows significantly reduced spring constants compared to the ones obtained with a single-frequency input. Moreover, as finesse is increased the quality of the approximation becomes only better.

Conclusions. The spectral properties of the input of an optomechanical cavity can be tailored to produce arbitrary potentials or force functions for optically trapped objects. The engineered potential can be used to improve the performance of the system for a certain task. The approximation of a desired force function is conditional on the absence of features finer than the cavity linewidth. Given the practical difficulty of handling inputs with continuous power spectral densities, it was also shown how these can be approximated by discrete frequency combs. The protocol was finally applied to a simplified version of the levitating mirror scheme to show that even a relatively simple class of force functions can lead to a significant enhancement in performance. Given its simplicity and generality, this technique could conceivably be used in a wide variety of optomechanical systems as a simple way to improve performance.

Chapter 12

Squeezing quadrature rotation in the acoustic band via optomechanics

12.1 The role of squeezing in interferometric measurements

The precision of optical measurements is intrinsically limited by the field's noise. Even ideal laser sources cannot escape a minimum level of uncertainty, as Heisenberg's principle manifests in the form of fundamental quantum fluctuations of the light's degrees of freedom, such as its amplitude and phase. Shot noise, which is the error in the photon-counting process, is a by-product of these fluctuations [26]. The impact of shot noise is reduced when the number of photons is large, i.e. when high laser power is used. This might not always be practical: there could be a limit to the resources available, or the system might require low power to avoid damage, or it could also be the case that additional sources of noise are introduced at high power. A typical example of this is found in optomechanics, where the modulation of the mechanical oscillator translates the increased power into additional radiation pressure noise.

Interferometric measurements at the quantum level can be strongly affected by both photon-counting and radiation pressure noise. To understand how, it should first be understood how these systems usually operate (cf. Fig. 12.1). The arms of the interferometers are typically phase-locked in order to achieve complete constructive interference on one of the ports, the input port, and complete destructive interference on the other port, the output or "dark" port. When a perturbation moves the test masses of the interferometer, the dark port detects the signal. The signal-to-noise ratio of the measurement generally improves when the power used in the interferometer is high, as

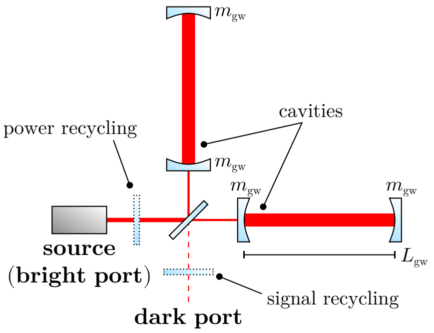

Figure 12.1: Diagram of the interferometer considered in this chapter: a Michelson interferometer with Fabry–Pérot cavities in the two arms. In gravitational-wave detectors, additional mirrors are used at the input and the output of the interferometer to meet the power requirements of the detection. The test masses are indicated by m_{gw}, while L_{gw} corresponds to the length of the interferometer's arms.

the photon-counting error becomes small compared to the signal. At the same time, however, the measurement becomes contaminated by the fundamental fluctuations of the test masses driven by radiation pressure force. The two effects become particularly relevant when optical cavities are introduced in the interferometer's arms to effectively increase the optical path and enhance its sensitivity. As a consequence of the cavities' resonance, the photon-counting noise is suppressed due to the higher circulating power and starts to prevail only at high frequencies. Radiation pressure, on the other hand, introduces a much greater noise at low frequencies, within the operation bandwidth of the cavities. The trade-off between photon-counting noise and radiation pressure noise determines the *standard quantum limit* (SQL) of the measurement [252, 253]. The influence of the SQL on the sensitivity spectrum depends on the power used to drive the interferometer, as the two noise sources combine differently to determine the band of minimum uncertainty.

Despite its fundamental origin, the SQL does not represent an ultimate limit to the measurement's capacity. It can be beaten if one resorts to modified states of light where the fluctuations are balanced differently between different quadratures, i.e. squeezed states of light as those introduced in Chap. 2.3.5. Gravitational-wave interferometers, whose measurements are already bound only by the SQL over the detection's band of interest, have already used squeezing to push their sensitivity even beyond [36, 254]. Squeezed light is applied to the dark port of the interferometers, where the conventional vacuum state is replaced by a state with reduced noise in one quadrature. In the case of phase-squeezed light the effect is similar to that obtained by using high power. However, the improvement in signal-to-noise ratio is obtained because of the reduction in noise rather than an increase in signal strength. Unfortunately phase-squeezed states also suffer from a larger uncertainty on the amplitude quadrature. The additional noise is fed into the system through radiation pressure on the test masses. Then, in complete analogy to high-power operations, the sensitivity is deteriorated at low frequencies and improved only at high frequencies. The outcome is completely reversed when amplitude-squeezed light is used instead. In this case the interferometer is subject to less radiation pressure noise but more photon-counting noise, and the sensitivity is bound by the same SQL obtained when operating at low power.

The low-frequency region of the sensitivity spectrum is usually dominated by alternative sources of technical noise that burrow the effects of anti-squeezing of the amplitude quadrature, thus making the use of phase-squeezed light unconditionally advantageous. The measurements of the next generation of gravitational-wave detectors, however, will reach such a level of refinement that the role of radiation pressure noise at low frequencies will also be significant. In order to extend the enhancement to the full spectrum, one requires frequency-dependent squeezing to address the dominant sources of noise separately [31, 255, 256]. A broadband enhancement is accomplished with light squeezed on the amplitude quadrature at low frequencies to suppress radiation pressure noise, and squeezed on the phase quadrature at high frequencies to reduce the photon-counting noise.

The dispersive properties of a filter cavity can achieve the desired quadrature rotation from a conventional squeezed source, provided that the bandwidth of the cavity matches that of the interferometer [255, 257–259]. This technique has already been implemented with proof-of-principle demonstrations [30, 31]. However, technical impediments such as decoherence and degradation can impact the overall effectiveness [260], and, in order to reach the storage time required to match the bandwidth of gravitational-wave detectors, the length of the resonator would be required between a few tens of meters and the entire length of the arms of the interferometer [261]. Optomechanically induced transparency [10] has the capacity of implementing dispersion over a narrow bandwidth and also qualifies as a possible candidate for the achievement of frequency-dependent squeezing [262, 263]. The same principle has inspired other proposals, such as the inclusion of a feedback-controlled unstable optomechanical system within the signal-recycling cavities of the interferometer [264].

Squeezed light can also be generated via the optomechanical interaction [65, 66, 265, 266]. Thanks to the dispersive nature of the mechanical resonance, optomechanical squeezing also displays frequency-dependent properties that could offer a strategic advantage over other techniques. This would project optomechanical squeezing beyond the recent proof-of-principle demonstrations [8, 9, 267] and demonstrate its value as a metrological asset.

In this chapter we explore how the optomechanical interaction correlates different quadratures of the optical field, and how this can be used to squeeze the noise ellipse of the output state of light. After characterizing the noise spectrum to find a suitable parameter regime, we use a simple model of the sensitivity of gravitational-wave detectors to determine the effects that optomechanical squeezing can have on interferometric measurements [17].

12.2 Optomechanical squeezing

In an optomechanical system, the movement of the mirror induced by the *intensity* of light is converted onto the field as a modulation of its *phase*. This conversion occurs also at the noise level, meaning that the field's amplitude fluctuations can be turned into phase fluctuations, and vice versa. With the appropriate superposition of the correlated fluctuations, one quadrature of the optical field can experience smaller fluctuations than the vacuum state, therefore transforming the output of the optomechanical system into a squeezed state.

12.2.1 Cross-correlations in the optical quadratures

To see how the cross-correlations between different optical quadratures emerge through the optomechanical interaction, consider the equations of motion of a generic optomechanical system derived in Chap. 3.1.4:

$$\delta\dot{\hat{a}}(t) = (-\kappa + i\Delta)\,\delta\hat{a}(t) + iG_\alpha\delta\hat{x}(t) + \sqrt{2\kappa}\delta\hat{a}_{\mathrm{in}}(t), \tag{12.1}$$

$$\delta\dot{\hat{x}}(t) = \delta\hat{p}(t)/m, \tag{12.2}$$

$$\delta\dot{\hat{p}}(t) = -m\omega_{\mathrm{m}}^2\delta\hat{x}(t) - \gamma_{\mathrm{m}}\delta\hat{p}(t) + \delta\hat{F}_{\mathrm{rp}}(t) + \delta\hat{F}_{\mathrm{th}}(t). \tag{12.3}$$

The degrees of freedom for the optical field are given by the quantum fluctuations of its ladder operators, $\delta\hat{a}$ and $\delta\hat{a}^\dagger$. The mechanical degrees of freedom, $\delta\hat{x}$ and $\delta\hat{p}$, correspond to the quantum fluctuations of the oscillator's position and momentum respectively. The equations include the quantum fluctuations of the radiation pressure force, $\delta\hat{F}_{\mathrm{rp}} := \hbar\big(G_\alpha^*\delta\hat{a} + G_\alpha\delta\hat{a}^\dagger\big)$. The other force term, $\delta\hat{F}_{\mathrm{th}}$, represents the stochastic forces originating from the thermal bath of the mechanical oscillator, with power spectrum $S_F^{(\mathrm{th})}(\omega) = m\gamma_\mathrm{m}\hbar\omega \coth\left(\frac{\hbar\omega}{2k_\mathrm{B}T}\right)$. The operator $\delta\hat{a}_\mathrm{in}$ stands for the fluctuations of the input field driving the cavity. The parameters κ and Δ characterize the half-linewidth and the effective detuning of the cavity. The mirror's mass, natural oscillation frequency, and mechanical damping rate are expressed by m, ω_m, and γ_m, respectively. The quantity $G_\alpha := G_0\alpha_\mathrm{s}$ is the product of the optomechanical coupling constant, which depends on the wavelength λ and on the cavity's free spectral range ω_FSR as $G_0 = 2\omega_\mathrm{FSR}/\lambda$, and the steady-state amplitude of the optical field, which depends on the input amplitude α_in as $\alpha_\mathrm{s} = \sqrt{2\kappa}\alpha_\mathrm{in}/\left(\kappa - i\Delta\right)$.

We will be looking at the spectral response of the optomechanical degrees of freedom, as we did in Chap. 3.3.2 when the optical spring effect was derived. Expanding the inter-dependence of $\delta\hat{x}$ and $\delta\hat{a}$ in Eq. 3.62–3.63, we obtain the frequency-domain expressions

$$\delta\hat{a}(\omega) = \frac{\chi_\mathrm{eff}(\omega)}{\chi_\mathrm{m}(\omega)}\sqrt{2\kappa}\mathcal{A}_-(\omega)\left[\delta\hat{a}_\mathrm{in}(\omega) + iG_\alpha\chi_\mathrm{m}(\omega)\left(\mathcal{A}_+(\omega)\delta\hat{F}_\mathrm{rp}^{(\mathrm{in})}(\omega) + \frac{\delta\hat{F}_\mathrm{th}(\omega)}{\sqrt{2\kappa}}\right)\right], \tag{12.4}$$

$$\delta\hat{x}(\omega) = \chi_\mathrm{eff}(\omega)\left(\delta\hat{F}_\mathrm{sh}(\omega) + \delta\hat{F}_\mathrm{th}(\omega)\right). \tag{12.5}$$

Here we are using the definitions of the two Airy functions, $\mathcal{A}_\pm(\omega) := \left[\kappa \pm i\left(\Delta \pm \omega\right)\right]^{-1}$, of the original mechanical susceptibility, $\chi_\mathrm{m}(\omega) := \left[m\left(\omega_\mathrm{m}^2 - \omega^2 + i\gamma_\mathrm{m}\omega\right)\right]^{-1}$, and of the effective susceptibility, $\chi_\mathrm{eff}(\omega) := \left[\chi_\mathrm{m}(\omega)^{-1} - i\hbar\left|G_\alpha\right|^2\left(\mathcal{A}_-(\omega) - \mathcal{A}_+(\omega)\right)\right]^{-1}$. The term $\delta\hat{F}_\mathrm{rp}^{(\mathrm{in})} := \hbar\big(G_\alpha^*\delta\hat{a}_\mathrm{in} + G_\alpha\delta\hat{a}_\mathrm{in}^\dagger\big)$ corresponds to the radiation pressure force of the input field, while $\delta\hat{F}_\mathrm{sh}(\omega) := \sqrt{2\kappa}\left(\hbar G_\alpha^*\mathcal{A}_-(\omega)\delta\hat{a}_\mathrm{in}(\omega) + \hbar G_\alpha\mathcal{A}_+(\omega)\delta\hat{a}_\mathrm{in}^\dagger(\omega)\right)$ is the frequency-dependent force due to the response of the cavity to shot noise (cf. Eq. 3.67).

The dynamical back-action on the optical degrees of freedom cannot be accessed directly from within the cavity. We need to consider the output field, which responds to the input-output relation $\delta\hat{a}_\mathrm{out} = -\delta\hat{a}_\mathrm{in} + \sqrt{2\kappa}\,\delta\hat{a}$ (cf. Eq. 2.56). Using Eq. 12.4, we can solve for $\delta\hat{a}_{\text{out}}$ (and its conjugate) in terms of $\delta\hat{a}_{\text{in}}$, $\delta\hat{a}^\dagger_{\text{in}}$, and $\delta\hat{F}_{\text{th}}$ to obtain

$$\begin{aligned}
\delta\hat{a}_{\text{out}}(\omega) = {} & \left(-1 + 2\kappa\mathcal{A}_-(\omega)\frac{\chi_{\text{eff}}(\omega)}{\chi_{\text{m}}(\omega)} + 2i\kappa\hbar\left|G_\alpha\right|^2\mathcal{A}_-(\omega)\mathcal{A}_+(\omega)\chi_{\text{eff}}(\omega)\right)\delta\hat{a}_{\text{in}}(\omega) \\
& + \left(2i\kappa\hbar G_\alpha^2\mathcal{A}_-(\omega)\mathcal{A}_+(\omega)\chi_{\text{eff}}(\omega)\right)\delta\hat{a}^\dagger_{\text{in}}(\omega) \\
& + \left(i\sqrt{2\kappa}G_\alpha\mathcal{A}_-(\omega)\chi_{\text{eff}}(\omega)\right)\delta\hat{F}_{\text{th}}(\omega), \qquad (12.6) \\
\delta\hat{a}^\dagger_{\text{out}}(\omega) = {} & \left(-1 + 2\kappa\mathcal{A}_+(\omega)\frac{\chi_{\text{eff}}(\omega)}{\chi_{\text{m}}(\omega)} - 2i\kappa\hbar\left|G_\alpha\right|^2\mathcal{A}_-(\omega)\mathcal{A}_+(\omega)\chi_{\text{eff}}(\omega)\right)\delta\hat{a}^\dagger_{\text{in}}(\omega) \\
& + \left(-2i\kappa\hbar {G^*_\alpha}^2\mathcal{A}_-(\omega)\mathcal{A}_+(\omega)\chi_{\text{eff}}(\omega)\right)\delta\hat{a}_{\text{in}}(\omega) \\
& + \left(-i\sqrt{2\kappa}G^*_\alpha\mathcal{A}_+(\omega)\chi_{\text{eff}}(\omega)\right)\delta\hat{F}_{\text{th}}(\omega). \qquad (12.7)
\end{aligned}$$

The property $[\delta\hat{a}_{\text{out}}(\omega)]^\dagger = \delta\hat{a}^\dagger_{\text{out}}(-\omega)$ can be useful for the derivation of the conjugate equation, in particular if one recalls that the Airy functions satisfy $[\mathcal{A}_\mp(\omega)]^* = \mathcal{A}_\pm(-\omega)$ and the mechanical susceptibility satisfies $[\chi_{\text{m}}(\omega)]^* = \chi_{\text{m}}(-\omega)$ (and similarly for χ_{eff}). In both equations it can be seen how the output variables depend not only on the corresponding input variable, but on its conjugate as well. These cross-correlations are what allows the exchange of uncertainty between different quadratures. They depend on the susceptibility of the moving mirror, and in particular they become stronger at frequencies closer to the mechanical resonance. The presence of $\delta\hat{F}_{\text{th}}$ testifies how the optomechanical interaction also couples the thermal fluctuations of the mirror to the optical field. When the optomechanical interaction is turned off ($G_\alpha = 0$), both cross-correlations and thermal noise disappear and the equations turn into the familiar cavity equations, as expected. It should be noted that squeezing can be generated by the similar cross-correlations arising from dissipative (as opposed to dispersive) coupling [268, 269]. However, dissipative optomechanics typically has weaker coupling strengths and its contribution will not be considered for the following analysis.

To proceed further, and infer the uncertainty on different quadratures of the output field, we need to know more information about the system's inputs. We assume the system to be in the limit of fast thermal correlation times and the stochastic thermal forces acting on the mirror to be stochastic, therefore implying a frequency-domain correlation function $\langle\delta\hat{F}_{\text{th}}(\omega)\delta\hat{F}_{\text{th}}(\omega')\rangle = 2\pi\delta(\omega+\omega')S_F^{(\text{th})}(\omega)$ [57, 270]. For the optical input, we know that for a general thermal state the correlation functions are $\langle\delta\hat{a}^\dagger_{\text{in}}(\omega)\delta\hat{a}_{\text{in}}(\omega')\rangle = 2\pi\delta(\omega+\omega')n_{\text{o}}^{(\text{th})}$, $\langle\delta\hat{a}_{\text{in}}(\omega)\delta\hat{a}^\dagger_{\text{in}}(\omega')\rangle = 2\pi\delta(\omega+\omega')\big(n_{\text{o}}^{(\text{th})}+1\big)$, and $\langle\delta\hat{a}_{\text{in}}(\omega)\delta\hat{a}_{\text{in}}(\omega')\rangle = \langle\delta\hat{a}^\dagger_{\text{in}}(\omega)\delta\hat{a}^\dagger_{\text{in}}(\omega')\rangle = 0$. The non-vanishing correlations and the associated uncertainty increase with the mean thermal occupation number of the photons, $n_{\mathrm{o}}^{\mathrm{th}}$. Since we are interested in beating the fundamental quantum noise, for simplicity we will assume the input state to be a canonical coherent state, which has the same uncertainty as the vacuum state and satisfies $n_{\mathrm{o}}^{(\mathrm{th})} = 0$. The input field has therefore only one non-vanishing expectation value, $\langle \delta\hat{a}_{\mathrm{in}}(\omega)\delta\hat{a}_{\mathrm{in}}^{\dagger}(\omega')\rangle$. The same does not apply to the output field, where the variables result correlated by the optomechanical interaction. We can calculate all the output correlations by first using the explicit dependence of $\delta\hat{a}_{\mathrm{out}}$ and $\delta\hat{a}_{\mathrm{out}}^{\dagger}$ on the input variables, then expanding the known non-vanishing correlations, and finally using the sifting property of the Dirac delta function together with the properties of the complex conjugates of the Airy functions and the susceptibilities. The results are

$$\langle \delta\hat{a}_{\mathrm{out}}(\omega)\delta\hat{a}_{\mathrm{out}}^{\dagger}(\omega')\rangle = \Big(|C_1(\omega)|^2 + |C_3(\omega)|^2\, S_F^{(\mathrm{th})}(\omega)\Big)\, 2\pi\delta(\omega+\omega'), \tag{12.8}$$

$$\langle \delta\hat{a}_{\mathrm{out}}^{\dagger}(\omega)\delta\hat{a}_{\mathrm{out}}(\omega')\rangle = \Big(|C_2(\omega)|^2 + |C_4(\omega)|^2\, S_F^{(\mathrm{th})}(\omega)\Big)\, 2\pi\delta(\omega+\omega'), \tag{12.9}$$

$$\langle \delta\hat{a}_{\mathrm{out}}(\omega)\delta\hat{a}_{\mathrm{out}}(\omega')\rangle = \Big(C_1(\omega)C_2(\omega)^* + C_3(\omega)C_4(\omega)^* S_F^{(\mathrm{th})}(\omega)\Big)\, 2\pi\delta(\omega+\omega'), \tag{12.10}$$

$$\langle \delta\hat{a}_{\mathrm{out}}^{\dagger}(\omega)\delta\hat{a}_{\mathrm{out}}^{\dagger}(\omega')\rangle = \Big(C_2(\omega)C_1(\omega)^* + C_4(\omega)C_3(\omega)^* S_F^{(\mathrm{th})}(\omega)\Big)\, 2\pi\delta(\omega+\omega'), \tag{12.11}$$

where the four coefficients introduced are defined as

$$C_1(\omega) := -1 + 2\kappa\mathcal{A}_-(\omega)\chi_{\mathrm{eff}}(\omega)/\chi_{\mathrm{m}}(\omega) + 2i\kappa\hbar\,|G_\alpha|^2\,\mathcal{A}_-(\omega)\mathcal{A}_+(\omega)\chi_{\mathrm{eff}}(\omega), \tag{12.12}$$

$$C_2(\omega) := -2i\kappa\hbar {G_\alpha^*}^2\mathcal{A}_-(\omega)\mathcal{A}_+(\omega)\chi_{\mathrm{eff}}(\omega), \tag{12.13}$$

$$C_3(\omega) := +i\sqrt{2\kappa}G_\alpha\mathcal{A}_-(\omega)\chi_{\mathrm{eff}}(\omega), \tag{12.14}$$

$$C_4(\omega) := -i\sqrt{2\kappa}G_\alpha^*\mathcal{A}_+(\omega)\chi_{\mathrm{eff}}(\omega). \tag{12.15}$$

Note that $[C_3(\omega)]^* = C_4(-\omega)$, and that only $C_1(\omega)$ would be non-vanishing in the absence of optomechanical interaction.

We are now ready to deduce the uncertainty for the quadratures of the output field. Define the generic quadrature parametrized by the angle θ,

$$\hat{X}_\theta^{(\mathrm{out})} := e^{-i\theta}\delta\hat{a}_{\mathrm{out}} + e^{+i\theta}\delta\hat{a}_{\mathrm{out}}^{\dagger}. \tag{12.16}$$

In particular, we identify the amplitude quadrature $\hat{X}$ and the phase quadrature $\hat{Y}$ as those corresponding to the angles $\theta = 0$ and $\theta = \pi/2$, respectively:

$$\hat{X} := \hat{X}_0^{(\mathrm{out})} = \delta\hat{a}_{\mathrm{out}} + \delta\hat{a}_{\mathrm{out}}^{\dagger}, \tag{12.17}$$

$$\hat{Y} := \hat{X}_{\pi/2}^{(\mathrm{out})} = -i\left(\delta\hat{a}_{\mathrm{out}} - \delta\hat{a}_{\mathrm{out}}^{\dagger}\right). \tag{12.18}$$

Their correlation functions are obtained directly in terms of Eq. 12.8–12.11. For the self-correlations, we have

$$\begin{aligned}\langle\hat{X}(\omega)\hat{X}(\omega')\rangle &= \langle\delta\hat{a}_{\mathrm{out}}(\omega)\delta\hat{a}_{\mathrm{out}}^{\dagger}(\omega')\rangle + \langle\delta\hat{a}_{\mathrm{out}}^{\dagger}(\omega)\delta\hat{a}_{\mathrm{out}}(\omega')\rangle \\ &\quad + \langle\delta\hat{a}_{\mathrm{out}}(\omega)\delta\hat{a}_{\mathrm{out}}(\omega')\rangle + \langle\delta\hat{a}_{\mathrm{out}}^{\dagger}(\omega)\delta\hat{a}_{\mathrm{out}}^{\dagger}(\omega')\rangle \\ &= \Big(\left|C_1(\omega) + C_2(\omega)\right|^2 + \left|C_3(\omega) + C_4(\omega)\right|^2 S_F^{(\mathrm{th})}(\omega)\Big)\, 2\pi\delta(\omega+\omega'),\end{aligned} \tag{12.19}$$

$$\begin{aligned}\langle\hat{Y}(\omega)\hat{Y}(\omega')\rangle &= \langle\delta\hat{a}_{\mathrm{out}}(\omega)\delta\hat{a}_{\mathrm{out}}^{\dagger}(\omega')\rangle + \langle\delta\hat{a}_{\mathrm{out}}^{\dagger}(\omega)\delta\hat{a}_{\mathrm{out}}(\omega')\rangle \\ &\quad - \langle\delta\hat{a}_{\mathrm{out}}(\omega)\delta\hat{a}_{\mathrm{out}}(\omega')\rangle - \langle\delta\hat{a}_{\mathrm{out}}^{\dagger}(\omega)\delta\hat{a}_{\mathrm{out}}^{\dagger}(\omega')\rangle \\ &= \Big(\left|C_1(\omega) - C_2(\omega)\right|^2 + \left|C_3(\omega) - C_4(\omega)\right|^2 S_F^{(\mathrm{th})}(\omega)\Big)\, 2\pi\delta(\omega+\omega'),\end{aligned} \tag{12.20}$$

while for the cross-correlation we find

$$\begin{aligned}\frac{\langle\hat{X}(\omega)\hat{Y}(\omega')\rangle + \langle\hat{Y}(\omega)\hat{X}(\omega')\rangle}{2} &= -i\langle\delta\hat{a}_{\mathrm{out}}(\omega)\delta\hat{a}_{\mathrm{out}}(\omega')\rangle + i\langle\delta\hat{a}_{\mathrm{out}}^{\dagger}(\omega)\delta\hat{a}_{\mathrm{out}}^{\dagger}(\omega')\rangle \\ &= \Big[2\,\mathrm{Im}\left(C_1(\omega)C_2(\omega)^*\right) \\ &\qquad 2\,\mathrm{Im}\left(C_3(\omega)C_4(\omega)^*\right)S_F^{(\mathrm{th})}(\omega)\Big]\, 2\pi\delta(\omega+\omega').\end{aligned} \tag{12.21}$$

By using the amplitude and phase quadratures as reference, we can write the parametrized quadrature as $\hat{X}_\theta^{(\mathrm{out})} = \cos(\theta)\hat{X} + \sin(\theta)\hat{Y}$. It is then possible to use Eq. 12.19–12.21 as the building blocks for the generic correlation function, so that

$$\begin{aligned}\langle\hat{X}_\theta^{(\mathrm{out})}(\omega)\hat{X}_\theta^{(\mathrm{out})}(\omega')\rangle &= \cos^2(\theta)\langle\hat{X}(\omega)\hat{X}(\omega')\rangle + \sin^2(\theta)\langle\hat{Y}(\omega)\hat{Y}(\omega')\rangle \\ &\quad + 2\cos(\theta)\sin(\theta)\frac{\langle\hat{X}(\omega)\hat{Y}(\omega')\rangle + \langle\hat{Y}(\omega)\hat{X}(\omega')\rangle}{2}.\end{aligned} \tag{12.22}$$

12.2.2 Frequency-dependent spectrum

The noise ellipse of the output field is uniquely determined by the symmetrized power spectral density of $\hat{X}_\theta^{(\mathrm{out})}$ [271], defined as

$$S_\theta(\omega) := \int \frac{d\omega'}{2\pi} \, \langle \{ \hat{X}_\theta(\omega) \hat{X}_\theta(\omega') \} \rangle. \tag{12.23}$$

The symmetrizing action, indicated by the curly brackets (cf. Eq. 2.10), extracts the information available from the system with a classical measurement [20]. Similarly to the generic correlation function, the parametric spectral density can be reformulated in terms of the amplitude and phase quadratures:

$$\begin{aligned} S_\theta(\omega) &= \cos^2(\theta) S_X(\omega) + \sin^2(\theta) S_Y(\omega) + 2\sin(\theta)\cos(\theta) S_{XY}(\omega) \\ &= \frac{S_X(\omega) + S_Y(\omega)}{2} + \cos(2\theta) \frac{S_X(\omega) - S_Y(\omega)}{2} + \sin(2\theta) S_{XY}(\omega). \end{aligned} \tag{12.24}$$

Here, $S_X(\omega)$, $S_Y(\omega)$, and $S_{XY}(\omega)$ are respectively the spectral densities of the amplitude quadrature, of the phase quadrature, and of the cross-correlations between the two. In their fully expanded form, they are given by

$$\begin{aligned} S_X(\omega) = \frac{1}{2} \Bigg[& \left| -1 + 2\kappa \mathcal{A}_-(\omega) \frac{\chi_{\mathrm{eff}}(\omega)}{\chi_{\mathrm{m}}(\omega)} + 2i\kappa\hbar \left(|G_\alpha|^2 - G_\alpha^{*\,2} \right) \mathcal{A}_-(\omega) \mathcal{A}_+(\omega) \chi_{\mathrm{eff}}(\omega) \right|^2 \\ & + \left| -1 + 2\kappa \mathcal{A}_+(\omega) \frac{\chi_{\mathrm{eff}}(\omega)}{\chi_{\mathrm{m}}(\omega)} - 2i\kappa\hbar \left(|G_\alpha|^2 - G_\alpha^2 \right) \mathcal{A}_-(\omega) \mathcal{A}_+(\omega) \chi_{\mathrm{eff}}(\omega) \right|^2 \Bigg] \\ & + 2\kappa \left| G_\alpha \mathcal{A}_-(\omega) - G_\alpha^* \mathcal{A}_+(\omega) \right|^2 \left| \chi_{\mathrm{eff}}(\omega) \right|^2 S_F^{(\mathrm{th})}(\omega), \end{aligned} \tag{12.25}$$

$$\begin{aligned} S_Y(\omega) = \frac{1}{2} \Bigg[& \left| -1 + 2\kappa \mathcal{A}_-(\omega) \frac{\chi_{\mathrm{eff}}(\omega)}{\chi_{\mathrm{m}}(\omega)} + 2i\kappa\hbar \left(|G_\alpha|^2 + G_\alpha^{*\,2} \right) \mathcal{A}_-(\omega) \mathcal{A}_+(\omega) \chi_{\mathrm{eff}}(\omega) \right|^2 \\ & + \left| -1 + 2\kappa \mathcal{A}_+(\omega) \frac{\chi_{\mathrm{eff}}(\omega)}{\chi_{\mathrm{m}}(\omega)} - 2i\kappa\hbar \left(|G_\alpha|^2 + G_\alpha^2 \right) \mathcal{A}_-(\omega) \mathcal{A}_+(\omega) \chi_{\mathrm{eff}}(\omega) \right|^2 \Bigg] \\ & + 2\kappa \left| G_\alpha \mathcal{A}_-(\omega) + G_\alpha^* \mathcal{A}_+(\omega) \right|^2 \left| \chi_{\mathrm{eff}}(\omega) \right|^2 S_F^{(\mathrm{th})}(\omega), \end{aligned} \tag{12.26}$$

$$\begin{aligned} S_{XY}(\omega) = 4\kappa \Big[\Big(& - \mathrm{Re}\left(\hbar G_\alpha^2 \right) \mathrm{Re}\left(\mathcal{A}_-(\omega) \mathcal{A}_+(\omega) \chi_{\mathrm{eff}}(\omega) \right) \\ & + 2\kappa \, \mathrm{Re}\left(\hbar G_\alpha^2 \mathcal{A}_-(\omega) \mathcal{A}_+(\omega)^* \right) \mathrm{Re}\left(\mathcal{A}_-(\omega)^* / \chi_{\mathrm{m}}(\omega) \right) \left| \chi_{\mathrm{eff}}(\omega) \right|^2 \\ & - 2\kappa \, \hbar \left| G_\alpha \right|^2 \mathrm{Im}\left(\hbar G_\alpha^2 \right) \left| \mathcal{A}_-(\omega) \mathcal{A}_+(\omega) \chi_{\mathrm{eff}}(\omega) \right|^2 \Big) \\ & - \mathrm{Im}\left(G_\alpha^2 \mathcal{A}_-(\omega) \mathcal{A}_+(\omega)^* \right) \left| \chi_{\mathrm{eff}}(\omega) \right|^2 S_F^{(\mathrm{th})}(\omega) \Big]. \end{aligned} \tag{12.27}$$

The frequency-dependence of each spectral density is non-trivial. Thanks to the parametric expression of Eq. 12.24, however, it is easy to identify the quadrature angle that minimizes the spectrum at any given frequency:

$$\theta_{\mathrm{min}} = \frac{\pi}{2} + \frac{1}{2}\arctan\left(\frac{2S_{XY}(\omega)}{S_X(\omega) - S_Y(\omega)}\right). \tag{12.28}$$

In practice, unless the interferometer's output is extracted with a variational readout [255], only one quadrature angle should be considered for the entire spectrum. The minimized spectrum $S_{\mathrm{min}}(\omega) := S_\theta(\omega)|_{\theta=\theta_{\mathrm{min}}(\omega)}$ offers nevertheless a comprehensive picture of optomechanical squeezing that helps in the full characterization of the results.

With all the key elements in place we can now examine how optomechanical squeezing performs under a specific parameter regime. In particular, we consider the system's specifications required for a rotation of the squeezed quadrature over the acoustic frequency bandwidth, where the ground-based interferometers operate to detect gravitational waves. Even though the optomechanical interaction would be stronger with a more intense intra-cavity field, the cavity is assumed to have only medium finesse and thus a relatively short lifetime. Because of this premise we know that any observed frequency-dependence emerges because of the optomechanical dispersion rather than the filtering action of the cavity. In addition, in order to allow a realistic comparison with a traditional squeezing source, all parameters are tuned to cap the squeeze factor to a maximum of 10 dB, a tenth of the original noise level. It should also be noted that the mechanical oscillator does not need to be close to its quantum ground state for optomechanical squeezing to be observed. The only requirement is to have the radiation pressure interaction comparable in strength to the thermal noise imparted on the oscillator. The spectrum of the thermal forces can be approximated to $S_F^{(\mathrm{th})}(\omega) = 2m\gamma_{\mathrm{m}}k_{\mathrm{B}}T$ for a classical oscillator. A mechanical oscillator with a very high mechanical quality factor $Q_{\mathrm{m}} := \omega_{\mathrm{m}}/\gamma_{\mathrm{m}}$ is therefore less susceptible to the thermal noise. Between two mechanical oscillators experiencing the same level of radiation pressure force, the higher suppression in the optical noise is produced by the one with larger Q_{m}. A worse quality factor can be compensated by lowering the temperature T, since ultimately it is the ratio T/Q_{m} that determines how much squeezing can be extracted from the system. Even though extremely high quality factors have been reported at room temperature [104, 272] it is nevertheless appealing to refrigerate the mechanical oscillator at very low temperature so that all other requirements can be relaxed.

We consider a moving mirror with mass $m = 0.5\,\mathrm{kg}$, natural oscillation frequency

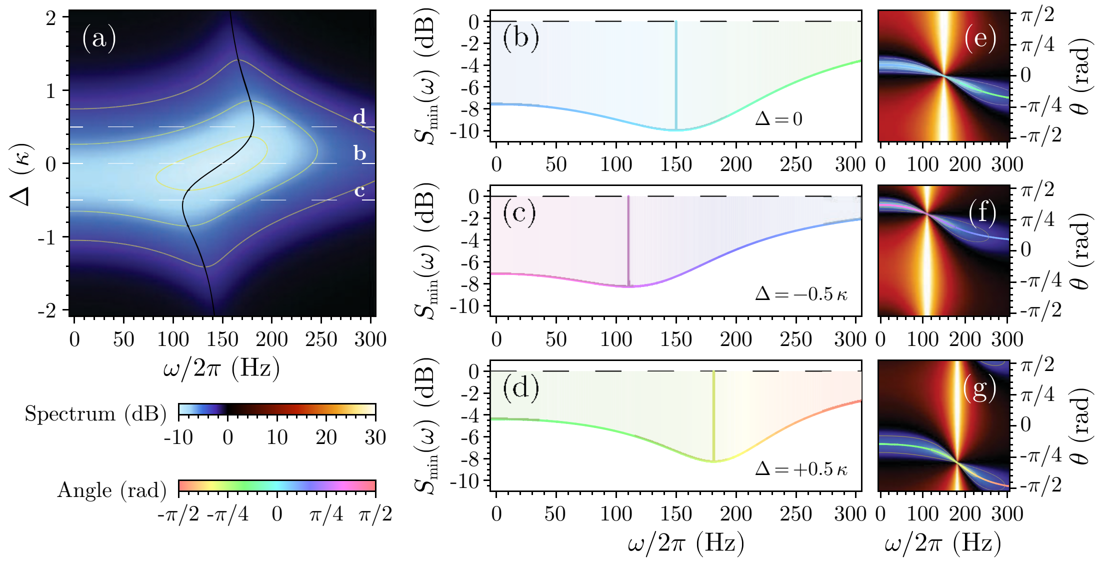

Figure 12.2: Characterization of the spectral density of the output field noise. **(a)** Minimized spectrum $S_{\text{min}}(\omega)$ as a function of detuning Δ (vertical axis). The black line crossing the spectrum corresponds to the effective frequency of the oscillator, ω_{eff}, which changes for different detunings because of the optical spring effect. The yellow mesh lines enclose the regions squeezed by 3, 6 and 9 dB. The dashed lines indicate the detunings chosen for the plots in the figure. **(b–d)** Frequency-dependence of optomechanical squeezing for detunings $\Delta = 0$ (b), $\Delta = -0.5\kappa$ (c), and $\Delta = +0.5\kappa$ (d). For each detuning the optimal spectrum $S_{\text{min}}(\omega)$ is shown, coloured according to the quadrature angle that minimizes the noise spectrum. The noise level of a conventional vacuum state is indicated by a dashed line. **(e–g)** Normalized spectral density $S_\theta(\omega)$ as a function of the quadrature angle θ (vertical axis). Both squeezing (blue) and anti-squeezing (red) are shown. As in the first plot, the mesh lines enclose the regions squeezed by 3, 6 and 9 dB. The line in the centre of the squeezed region follows the angle that minimizes the spectrum, $\theta_{\text{min}}(\omega)$.

$\omega_{\text{m}} = 2\pi \times 150\,\text{Hz}$, and quality factor $Q_{\text{m}} = 5 \times 10^6$, cooled to a challenging but realistic cryogenic temperature of $T = 3\,\text{mK}$. The cavity is tuned to be resonant for an optical wavelength $\lambda = 2\pi c/\omega_{\text{o}} = 1064\,\text{nm}$, with free spectral range $\omega_{\text{FSR}} = 2\pi \times 1\,\text{GHz}$ and half-linewidth $\kappa = 2\pi \times 0.5\,\text{MHz}$. The input power $P_{\text{in}} = \hbar\omega_{\text{o}}\,|\alpha_{\text{in}}|^2 = 20\,\text{W}$ is set to conform to the operational requirement of the new generation of gravitational-wave interferometers. The reduced optomechanical coupling, which depends on the zero-point fluctuations $x_{\text{ZPF}} = \sqrt{\hbar/(2m\omega_{\text{m}})}$, is equal to $g_0 = G_0 x_{\text{ZPF}} = 2\pi \times 0.63\,\text{mHz}$ for this set of parameters. The system defined by this selection of parameters attains frequency-dependent squeezing over a band of a few hundred hertz, as shown in Fig. 12.2. This is what is required for a comparison with traditional fixed-quadrature squeezing in connection with gravitational-wave interferometers, which usually reach their best sensitivity at around 100 Hz. The strongest dispersion occurs in proximity of the effective mechanical frequency, $\omega_{\text{eff}} := 1/\sqrt{m\chi_{\text{eff}}(\omega_{\text{m}})}$, which acts as the focal point for the light-mirror dynamics. The spectrum culminates into a distinctive peak-like feature at ω_{eff}, as this is a point of inversion for the frequency response of the system where squeezing and anti-squeezing converge together. This feature is shown as a black line in Fig. 12.2a, varying with detuning according to the optical spring effect. At this frequency the spectrum can at best match the original noise, although realistically one should expect fluctuations in the locking mechanism to introduce additional anti-squeezing noise. This can be inferred from Fig. 12.2e–g, where both squeezing and anti-squeezing are shown to be more strongly concentrated around the inversion node. The width of the narrow band where no noise reduction is obtained is inversely proportional to the quality factor of the oscillator. Even a quality factor of 50, five orders of magnitude smaller than the one considered, would not extend this effect over a linewidth larger than 1 Hz. Moreover, the possibility of changing the detuning allows control over what part of the spectrum would be most influenced.

Limiting the observations to a region of 3 dB of squeezing around the dispersive feature, one can see that at $\Delta = 0$ (Fig. 12.2b and 12.2e) the squeezed angle varies from about $\pi/12$ at low frequencies to about $-\pi/6$ at 300 Hz, achieving an overall rotation of $\pi/4$. A slightly larger quadrature rotation is obtained at a detuning $\Delta = -0.5\,\kappa$ (Fig. 12.2c and 12.2f) or $\Delta = +0.5\,\kappa$ (Fig. 12.2d and 12.2g). A full $\pi/2$ rotation is obtained only at much higher frequencies, but it should also be considered that far from ω_{eff} the interaction is not strong enough to correlate the noise of different quadratures and the squeezing is much more diluted. Increasing the detuning also has the effect of reaching a rotation asymptotically close to $\pi/2$, but again the reduction in noise becomes negligible and there is no advantage for $|\Delta| \gtrsim 1.5\,\kappa$.

12.3 Sensitivity enhancement in gravitational-wave detectors

The sensitivity of a gravitational-wave interferometer is determined by how well one can infer its *strain*, or the variation in optical path between opposite ends of the interferometer's arms divided by the total length of the interferometer. The strain sensitivity required to detect gravitational waves from potential astrophysical sources is estimated to be about one part in 10^{21} or 10^{22}. For large scale interferometers this corresponds to a displacement sensitivity of $\approx 10^{-18}$ m, about one-thousandth of the radius of a proton, over a total path of a few kilometres. Considering the

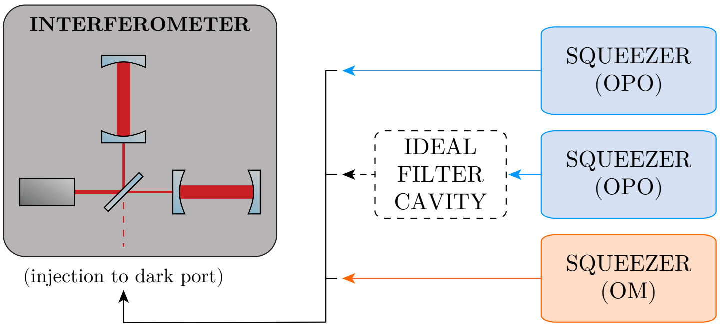

Figure 12.3: Schematic of the injection scheme for improving the sensitivity of the interferometer. The vacuum state normally present at the dark port is replaced by a squeezed state. The squeezing can be directly extracted from an optical parametric oscillator (OPO), in which case the noise reduction is bound to the same quadrature at all frequencies. Alternatively, the squeezing could be filtered through an ideal cavity that achieves the necessary quadrature rotation. The squeezing obtained from an optomechanical system naturally displays the frequency-dependent properties obtained from a filter cavity.

extreme resolution required for such a measurement, it should not be surprising that the sensitivity of gravitational-wave interferometers is limited by the quantum fluctuations of the light used for the observations. We will see in this section that a judicious modification of the interferometer's input state, as shown in the diagram of Fig. 12.3, can bring the sensitivity even beyond this limit.

The standard quantum limit (SQL) is an expression of the uncertainty principle, and it arises as a consequence of photon-counting noise and radiation pressure noise [255]. The minimum uncertainty in strain sensitivity allowed by the SQL is

$$h_{\mathrm{SQL}}(\omega) = \sqrt{\frac{8\hbar}{m_{\mathrm{gw}} L_{\mathrm{gw}}^2 \omega^2}}, \tag{12.29}$$

where m_{gw} is the mass of the test mirrors and L_{gw} is the length of the arm cavities. Accordingly, the strain noise spectral density due to the SQL is $S_{\mathrm{SQL}} = h_{\mathrm{SQL}}(\omega)^2$. Both noise sources are mediated by the arm cavities, and thus their spectral density is related to the transfer function

$$K(\omega) := \frac{2\kappa_{\mathrm{gw}}^4}{\omega^2 \left(\kappa_{\mathrm{gw}}^2 + \omega^2\right)} \frac{P_{\mathrm{gw}}}{P_{\mathrm{SQL}}}, \tag{12.30}$$

where κ_{gw} is the half-linewidth of the arm cavities of the interferometer, P_{gw} is the operating power measured at the beam splitter, and P_{SQL} is a reference power necessary to reach the SQL at $\omega = \kappa_{\mathrm{gw}}$, defined in terms of the optical frequency ω_{o} as

$$P_{\mathrm{SQL}} := \frac{m_{\mathrm{gw}} L_{\mathrm{gw}}^2 \kappa_{\mathrm{gw}}^4}{4\omega_{\mathrm{o}}}. \tag{12.31}$$

In particular, since the signal-to-noise ratio is better on resonance, the spectral density of the photon-counting shot noise results inversely proportional to the cavities' response:

$$S_{\mathrm{sh}}(\omega) = \frac{1}{2} K(\omega)^{-1} S_{\mathrm{SQL}}(\omega). \tag{12.32}$$

On the contrary, the contribution of radiation pressure force on the test masses is increased when more power circulates within the cavities, and the spectral density of the radiation pressure noise is directly proportional to the cavities' response:

$$S_{\mathrm{rp}}(\omega) = \frac{1}{2} K(\omega) S_{\mathrm{SQL}}(\omega). \tag{12.33}$$

The noise spectrum of a quantum-limited interferometer is obtained by summing the two together:

$$S_{\mathrm{gw}}(\omega) := S_{\mathrm{rp}}(\omega) + S_{\mathrm{sh}}(\omega) = \frac{1}{2} \left(K(\omega) + K(\omega)^{-1} \right) S_{\mathrm{SQL}}(\omega). \tag{12.34}$$

The sensitivity for inspiralling astrophysical sources of gravitational waves is calculated as the square root of the noise spectrum weighted by the frequency [255], i.e. $\sqrt{\omega\, S_{\mathrm{gw}}(\omega)}$. Because we are interested in relative enhancements we can normalize all sensitivities by the value of the SQL obtained when operating at P_{SQL}. For this reason, all the traces considered in the following analysis will represent the ratio between the corresponding sensitivity and $\sqrt{\kappa_{\mathrm{gw}}\, S_{\mathrm{SQL}}(\kappa_{\mathrm{gw}})}$. Also, we will use the parameters of the last generation of the advanced LIGO interferometer: $m_{\mathrm{gw}} = 40\,\mathrm{kg}$, $L_{\mathrm{gw}} = 4\,\mathrm{km}$, $\kappa_{\mathrm{gw}} = 2\pi \times 100\,\mathrm{Hz}$. The plots in Fig. 12.4a illustrate how the different noise sources combine into the typical interferometer noise spectrum. By definition of P_{SQL}, the best sensitivity of an interferometer exercising at this power is achieved at $\omega = \kappa_{\mathrm{gw}}$. When the operating power is lower (i.e. $P_{\mathrm{gw}} < P_{\mathrm{SQL}}$) the resulting sensitivity is degraded at high frequencies, as photon-counting noise has a stronger impact on the signal, while it is improved at low frequencies, where the contribution of radiation pressure noise is lower. As a consequence, the band of minimum noise is effectively moved towards lower frequencies. The opposite effect occurs when the power is higher (i.e. $P_{\mathrm{gw}} > P_{\mathrm{SQL}}$), in which case the band of best sensitivity is shifted towards higher frequencies. The minima obtained

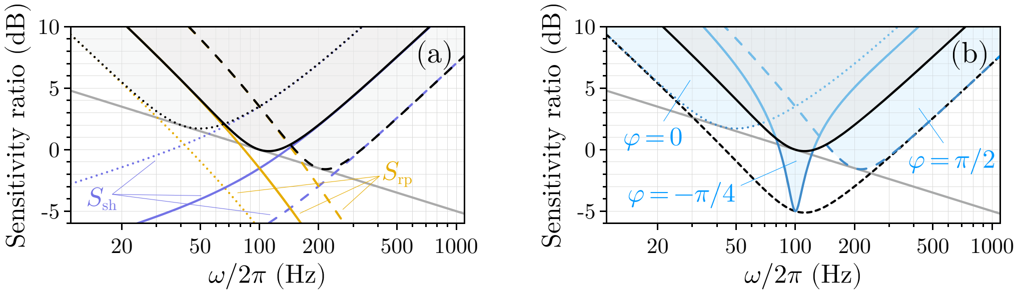

Figure 12.4: Sensitivity spectra of an interferometer as the one shown in Fig. 12.1. The standard quantum limit is indicated by a straight grey line. **(a)** The typical sensitivity spectrum (black) is obtained as the combination of radiation pressure noise (yellow) and photon-counting shot noise (violet). The sensitivity is shown for an interferometer operating at $P_{\mathrm{gw}} = P_{\mathrm{SQL}}$ (solid lines), $P_{\mathrm{gw}} = 0.1\,P_{\mathrm{SQL}}$ (dotted lines), and $P_{\mathrm{gw}} = 10\,P_{\mathrm{SQL}}$ (dashed lines). **(b)** Sensitivity spectra of the same interferometer, operating at $P_{\mathrm{gw}} = P_{\mathrm{SQL}}$, when squeezed light is injected to the dark port. The squeezing factor is assumed to be constant at 10 dB over the entire spectrum. The three representative cases shown correspond to amplitude squeezing (dotted blue), phase squeezing (dashed blue), and hybrid quadrature squeezing (solid blue). The conventional sensitivity (solid black) is also shown for comparison. The dashed black line indicates the sensitivity attainable if the squeezing propagated through an ideal filter cavity, with variable squeezed quadrature $\varphi(\omega) = \theta_{\mathrm{gw}}(\omega)$ rotating from amplitude at low frequencies to phase at high frequencies.

as power is varied determine a straight line in the logarithmic scale which corresponds to the best sensitivity allowed by the SQL, $\sqrt{\omega\, S_{\mathrm{SQL}}(\omega)}$.

Refined readings are possible with the injection of squeezed light, which pushes the capabilities of the interferometer beyond the SQL [256]. By replacing the vacuum state at the dark port of the interferometer with a squeezed state of light, the detection spectrum is modified to

$$\overline{S}_{\mathrm{gw}}(\omega) = \left[\cosh(2r) - \cos\left(2\left(\theta_{\mathrm{gw}}(\omega) - \varphi\right)\right)\sinh(2r)\right] S_{\mathrm{gw}}(\omega), \tag{12.35}$$

where $\theta_{\mathrm{gw}}(\omega) := -\arctan(K(\omega)^{-1})$ is the phase rotation imposed by the arm cavities [255], r is the squeezing factor, and φ is the angle of the squeezed quadrature (cf. Eq. 2.33). It is straightforward to see that this spectrum is minimized for frequency-dependent squeezing satisfying $\varphi(\omega) = \theta_{\mathrm{gw}}(\omega)$, as shown by the dashed black trace in Fig. 12.4b. This frequency dependence could be obtained by letting the squeezed light generated by a conventional optical parametric oscillator (OPO) propagate through a filter cavity before the injection [30,31]. However, the ideal rotation would be achieved only by a filter cavity with exactly the same characteristics as the cavities in the interferometer's arms. This task is quite impractical for gravitational-wave detectors, which extend for several kilometres in length and therefore demand an extremely narrow cavity linewidth [273]. The other traces in Fig. 12.4b show the impact of fixed quadrature squeezing. The sensitivity obtained by using phase-squeezed light ($\varphi = \pi/2$) is identical to the one obtained when the same interferometer operates without squeezing but at increased power. In both cases the signal-to-noise ratio of the measurement is improved, with the difference that the application of high power increments the size of the signal while the use of phase squeezing reduces the photon-counting noise. At low frequency, the stronger noise is justified by a stronger radiation pressure in the case of high power, and by the presence of anti-squeezing in the amplitude quadrature in the case of squeezing. A very similar argument applies when comparing the injection of amplitude squeezing ($\varphi = 0$) with the use of lower power, with the roles of radiation pressure and photon-counting noise reversed. The injection of hybrid quadrature squeezing ($-\pi/2 < \varphi < 0$) does not have an equivalent counterpart in terms of power. In this case the noise reduction pushes the sensitivity beyond the SQL in a narrow band around $\kappa_{\rm gw}$. At the same time the anti-squeezing noise spreads between the phase and amplitude quadratures, inducing a slightly higher uncertainty at low and high frequency.

The frequency-dependent characteristics required to obtain a broadband enhancement in sensitivity arise naturally in optomechanically generated squeezing. The dispersion obtained through the interaction with the mechanical resonator rotates the squeezed quadrature over the spectrum, similarly to how a filter cavity rotates its input. The centre of the rotation is determined by the mechanical frequency, which is a more flexible variable than the linewidth of a filter cavity and can more easily target the acoustic frequency band. However, as was shown in Fig. 12.2, the optomechanical dispersion does not complete a full $\pi/2$ rotation over the frequency band of interest. Nevertheless, the frequency dependence achieved may nevertheless be enough to compensate for $\theta_{\rm gw}(\omega)$ over a section of the measurement band wider than the one covered by fixed quadrature squeezing. Moreover, in the optomechanical system the squeezing factor also varies across the spectrum. This seemingly undesirable property may be used to one's advantage if the system is adjusted to have less interaction, and thus reduced anti-squeezing, around frequencies where the squeezed quadrature does not match $\theta_{\rm gw}(\omega)$. The system can therefore be prepared to provide high squeezing in a region with reduced quadrature rotation (for example, from 0 to $-\pi/4$) and no change from the conventional sensitivity elsewhere. The performance of the optomechanical system is illustrated in Fig. 12.5, which compares on a case-by-case basis the sensitivity

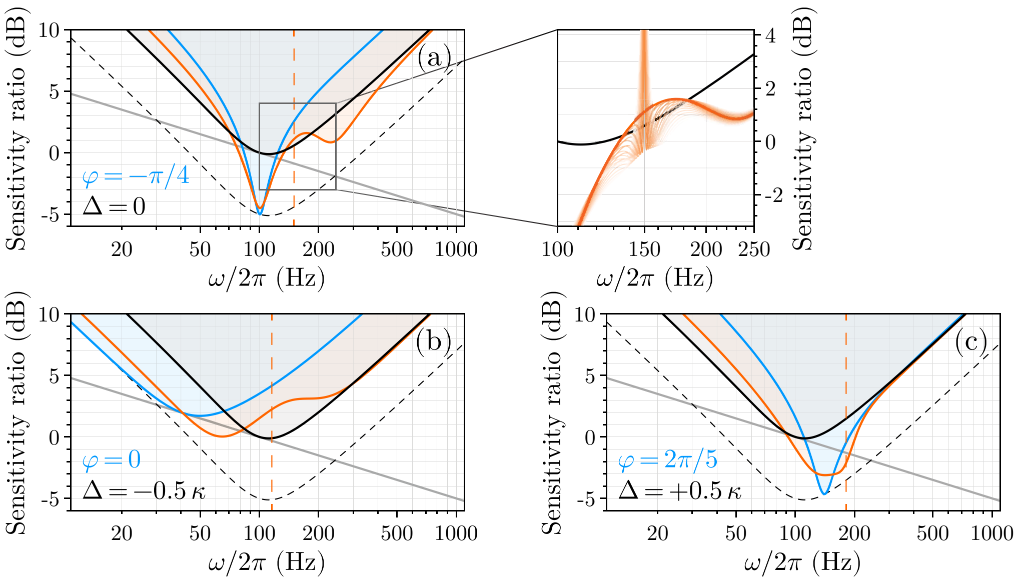

Figure 12.5: Comparison of the sensitivity of an interferometer subject to squeezing injection at the dark port, as suggested by the scheme in Fig. 12.3. The comparison includes the case of fixed-quadrature squeezing from a typical OPO source (blue), squeezing propagated through an ideal filter cavity (dashed black), and frequency-dependent optomechanical squeezing (orange). The parameters used for the optomechanical system are the same used to obtain the spectra of Fig. 12.2. The plots consider different detuning configurations for the optomechanical cavity, specifically $\Delta = 0$ (a), $\Delta = -0.5\,\kappa$ (b), and $\Delta = +0.5\,\kappa$ (c). In all cases, the optomechanical squeezing is capped to have a highest noise reduction of 10 dB. The fixed-quadrature squeezing is considered to have a similar noise reduction of 10 dB, but across the entire spectrum. The inset shows how the characteristic feature of the optomechanical spectrum at $\omega = \omega_{\text{eff}}$ affects the sensitivity. Starting from the initial trace corresponding to $\theta_{\text{min}}(\omega)$, subsequent traces (light orange to white) are obtained by accounting for a total deviation of up to 6 % of a radian in intervals of 0.3 %. A similar behaviour should be expected in the other two plots, where the position of the effective mechanical frequency is indicated by a dashed orange line.

obtained with fixed-quadrature squeezing to that obtained with frequency-dependent squeezing examined in the previous section. When the optomechanical cavity is not detuned (Fig. 12.2a, $\Delta = 0$), optomechanical squeezing performs generally better than hybrid quadrature squeezing. The sensitivity advantage is particularly noticeable at frequencies higher than 100 Hz, where most of the quadrature rotation takes place. The difference between the two traces gets as high as 5.5 dB, after which point the interaction becomes progressively weaker and the sensitivity of the optomechanically enhanced system converges to that of a conventional interferometer. The situation is similar when the optomechanical cavity has a negative detuning (Fig. 12.2b, $\Delta = -0.5\,\kappa$). Compared with pure amplitude squeezing, optomechanical squeezing achieves noise reduction in the lower end of the spectrum while avoiding the additional noise introduced by anti-squeezing on the phase quadrature at high frequencies. A positive detuning (Fig. 12.2c, $\Delta = +0.5\,\kappa$) can result in a broad sensitivity enhancement in the region between 100 Hz and 200 Hz without having to sacrifice too much sensitivity at lower frequencies, as opposed to the fixed-quadrature squeezing that does not neutralize the anti-squeezing in the wrong quadrature. It should be remembered that the spectrum of the optomechanical squeezing presents a characteristic feature at the effective mechanical frequency. Close to this frequency, any deviation from the optimal quadrature risks introducing undesired noise into the system. The effects of imprecisions in the locking system of up to 6 % of a radian are shown in the inset of Fig. 12.2a. When the locked quadrature differs from $\theta_{\min}(\omega)$, the sensitivity around the resonance is slightly improved before a spike of overwhelming noise takes over. The hint of better sensitivity is possible because the rotation achieved by the optomechanical system is not ideal, and a slight deviation may better approximate the desired rotation in a very small region of the spectrum. This advantage is certainly negligible compared to the high level of uncertainty introduced by the adjacent spike in anti-squeezing. As the angle gets closer to optimal the effect is imposed onto an increasingly narrower region, until it is completely cancelled when $\varphi = \theta_{\min}(\omega)$. It should also be considered that such a distinctive feature may only be a product of the specific detection method used for the measurement. A novel detection technique, called *synodyne detection*, has been suggested to replace the conventional homodyne detection method used for traditional squeezing in order to reveal the complex nature of optomechanical squeezing and thus take full advantage of its frequency-dependent nature [34].

Conclusions. The frequency-dependent properties of optomechanical squeezing lead to interesting applications in gravitational-wave detectors. Optomechanical squeezing presents an elegant alternative to filter cavities by achieving squeezed quadrature rotation over the spectrum in order to address different sources of noise at different frequencies. Comparing the sensitivity obtained with optomechanical squeezing with the one obtained using a traditional source, the former can obtain a relative enhancement of up to 5.5 dB when both methods are capped to a maximum noise reduction of 10 dB. The use of optomechanical squeezing is not without shortcomings. The parameter regime considered is realistic, but it requires state-of-the-art technology for a successful implementation. On top of this, an extremely high precision in homodyne quadrature locking is required to avoid excessive measurement noise close to the frequency of the mechanical resonator. The high flexibility allowed by the detuning of the optomechanical cavity can however be used to shift this noise to different frequencies, for example affected by other unavoidable sources of background noise, or where a measurement would not be expected for other reasons. Alternatively, the whole detection process could be tailored to fully account for the optomechanical back-action. Another issue is given by the fact that the squeezed quadrature rotation obtained by the optomechanical system under analysis does not cover the full range of quadratures that would be needed for an ideal broadband suppression of noise. The imperfect rotation is compensated by a weakening of the interaction that prevents the fluctuations of the anti-squeezed quadrature to impose additional noise. It should also be remembered that the technical feasibility of a cavity-induced rotation at 100 Hz has yet to be demonstrated, while it is already plausible for a high-quality mechanical oscillator to have a resonant frequency in that frequency band. Overall, the extensive efforts placed by the gravitational-wave community in the suppression of all sources of noise should pose a strong foundation for the experimental demonstration of the injection of squeezing obtained via optomechanics.

Conclusions and outlook

The field of optomechanics is currently projected on a very exciting path, as the field matures from its developing stages into a fully independent discipline. Thanks to entirely new levels of refinement of the optical feedback forces involved in the optomechanical interaction, the creation of non-classical states of motion is becoming increasingly accessible. Among the variety of platforms in development for quantum applications, optomechanical systems are uniquely qualified to bridge the gap between heterogeneous structures. Photon-phonon interaction; entanglement with coherent states, single atoms, or Bose-Einstein condensates; operating ranges from a few hertz to the gigahertz domain; possibility of interaction with optical or microwave fields. These are only some of the resources that make optomechanical systems exceptional interfacing devices.

For metrological applications, the expectations for the following years will also be higher than ever, as quantum optomechanics paves the way for measurements of unprecedented accuracy. Proposals to reach and beat the standard quantum limit for advanced displacement sensitivity are central to the future development of the field, and both experimental and theoretical efforts are highly focused towards this direction.

Optomechanical systems will also serve as a remarkable resource for fundamental investigations, as they have the potential to answer many of the open questions in physics. Can a quantum state be manifested at a macroscopic scale? How does decoherence evolve? What is the role of gravity in quantum systems? The answers might be very close or very far in time, and they might lead to dead ends or to even more interesting questions. Nevertheless, it is highly possible that optomechanical systems will often feature as a meaningful point of discussion for these topics in the coming years.

Overall, the wide range of possibilities is evolving in a direction where sensitivity and noise suppression are decisive traits. This is the case for levitated systems, which target complete detachment from the environment to avoid the coupling of thermal fluctuations into the measurement. Another example is given by gravitational-wave interferometers, among the most sensitive devices ever built, which will be more optomechanically sensitive with future advancements as low-frequency thermal noise is reduced and the measurement becomes limited by radiation pressure noise. Kilometre-sized interferometers, milligram-scale mirrors, and nanomechanical oscillators are only a few representative cases of the wide range of possible configurations in optomechanics. In this thesis we have seen a diversity of approaches applied to these systems to push their sensitivity: filtering techniques, full optical trapping and optical spring manipulation, and enhancement by injection of optomechanical squeezing. Summaries and possible future directions for each of the schemes considered are offered below.

Feedback with nanowires

In Part II we explored the effects of feedback on nanomechanical oscillators. The feedback, based on homodyne detection, was used to suppress the thermal noise and lead to enhanced sensitivity of impulsive forces during the transient dynamics of the oscillators. Due to the linear, classical nature of the system, it was also shown that similar enhancements could be produced off-line with post-processing filtering techniques.

There are several opportunities for the extension of this research. One option would be to consider conversion from measurement-based to fully coherent feedback [274,275], in order to avoid the limits imposed by the detection noise and achieve stronger cooling. This could also allow the study of the performance of filtering techniques in the quantum regime. Further studies could also follow a different course and explore whether an array of synchronized nanowires could be used to form a network of oscillators for applications as a memory [276].

Levitation of a cavity mirror

The optical levitation scheme envisioned in Part III, based on the optical springs from three separate cavities, has the potential to achieve unparalleled isolation from environmental noise. The optical self-feedback mechanism observed is only a first step towards a fully operating system, and many practical barriers need to be overcome for pure levitation of the mirror. Among these, the reduction of thermal effects on the coating and the stabilization of the optical spring should be given the highest priority.

The levitating mirror would undoubtedly constitute an ideal platform for sensitive applications in metrology or fundamental physics. Without the scattering characteristic of other optical levitation schemes, the accuracy for position readings reached by the cavity tripod can reach extremely high levels. The sensitivity of this optically trapped mirror could be enhanced even further by engineering the optical potential using the technique proposed in Part IV.

Novel protocols

The extreme flexibility of optomechanical systems is a key property for the evolution of diverse techniques. The two techniques developed in Part IV serve as an example of this. The first involved the demonstration that custom force profiles can be synthesized in optically trapped systems by changing the frequency components of the input to the optomechanical cavity. The second showed how the sensitivity of interferometers at the limit of their resolution can be increased even further with the back-action evasion provided by optomechanically squeezed light.

These protocols were developed around the idea that optomechanics can be used to gain a sensitivity advantage. Indeed, the breadth of optomechanics extends well beyond this specific function. Trying to predict what other applications could be found for each procedure would however require some degree of speculation. For example, arbitrary potentials may result particularly useful for optical manipulation, while the frequency-dependent properties of optomechanical squeezing could be required for the creation of novel forms of entangled states. Only time will be able to tell what new paths will be followed by the field in the end.

End matter

Appendix

A Hamiltonian tools

A.1 Reference frame transformations

The evolution of the state is not attached to the reference frame chosen for its description. When moving to a different reference, the Hamiltonian needs to be transformed appropriately to preserve the dynamics in the new frame. Considering the unitary transformation operated by $\hat{U}$, the state $|\psi\rangle$ is described in the new reference frame by

$$|\psi'\rangle := \hat{U}|\psi\rangle. \tag{36}$$

Requesting the evolution of $|\tilde{\psi}\rangle$ to be also determined by Schrödinger's equation (cf. Eq. 2.11), we can see how the transformation affects the Hamiltonian of the old coordinate system:

$$\begin{aligned}
i\hbar\frac{\partial}{\partial t}|\psi'\rangle &= i\hbar\frac{\partial}{\partial t}\left(\hat{U}|\psi\rangle\right) \\
&= i\hbar\left[\hat{U}\left(\frac{\partial}{\partial t}|\psi\rangle\right) + \left(\frac{\partial\hat{U}}{\partial t}\right)|\psi\rangle\right] \\
&= \hat{U}\hat{\mathcal{H}}|\psi\rangle + i\hbar\frac{\partial\hat{U}}{\partial t}|\psi\rangle \\
&= \hat{U}\hat{\mathcal{H}}\hat{U}^\dagger\hat{U}|\psi\rangle + i\hbar\frac{\partial\hat{U}}{\partial t}\hat{U}^\dagger\hat{U}|\psi\rangle \\
&= \left(\hat{U}\hat{\mathcal{H}}\hat{U}^\dagger + i\hbar\frac{\partial\hat{U}}{\partial t}\hat{U}^\dagger\right)|\psi'\rangle.
\end{aligned} \tag{37}$$

The expression for the Hamiltonian in the new frame is, therefore,

$$\hat{\mathcal{H}}' := \hat{U}\hat{\mathcal{H}}\hat{U}^\dagger + i\hbar\frac{\partial\hat{U}}{\partial t}\hat{U}^\dagger. \tag{38}$$

A.2 Equations of motion

Working in the Heisenberg picture, we need to convert the time evolution described by Schrödinger's equation into a time evolution of the operators acting on the state. That is, instead of letting the state $|\psi\rangle$ evolve in time like in the Schrödinger picture, we let the operators be a function of time. This does not affect the expectation value:

$$\langle\hat{\mathcal{O}}\rangle_t = \langle\psi(t)|\hat{\mathcal{O}}|\psi(t)\rangle\Big|_{\mathrm{S}} = \langle\psi|\hat{\mathcal{O}}(t)|\psi\rangle\Big|_{\mathrm{H}}. \tag{39}$$

Define $\hat{U}(t)$ to be the time-evolution operator, so that its application on the state at some initial time results in the state at a later time t:

$$\hat{U}(t)|\psi\rangle := |\psi(t)\rangle. \tag{40}$$

From Schrödinger's equation it follows that

$$\begin{aligned}\frac{\partial}{\partial t}\hat{U}(t)|\psi\rangle &= \frac{1}{i\hbar}\hat{\mathcal{H}}|\psi(t)\rangle \\ &= \frac{1}{i\hbar}\hat{\mathcal{H}}\hat{U}(t)|\psi\rangle.\end{aligned} \tag{41}$$

Since the equality holds no matter what the state $|\psi\rangle$ is, the above can be considered a differential equation for $\hat{U}(t)$. For a time-independent Hamiltonian, the solution, satisfying the commutation relation $\big[\hat{U}(t), \hat{\mathcal{H}}\big] = 0$, is

$$\hat{U}(t) = e^{-\frac{i}{\hbar}\hat{\mathcal{H}}t}. \tag{42}$$

We can now transfer the evolution from the state to the observable. From Eq. 39 we obtain that the observable in the Heisenberg picture is

$$\hat{\mathcal{O}}(t)\Big|_{\mathrm{H}} = \hat{U}^\dagger(t)\hat{\mathcal{O}}\hat{U}(t) \tag{43}$$

and evolves according to

$$\begin{aligned}\frac{d\hat{\mathcal{O}}(t)}{dt}\bigg|_{\mathrm{H}} &= \frac{\partial \hat{U}^\dagger(t)}{\partial t}\hat{\mathcal{O}}(t)\hat{U}(t) + \hat{U}^\dagger(t)\frac{\partial\hat{\mathcal{O}}(t)}{\partial t}\hat{U}(t) + \hat{U}^\dagger(t)\hat{\mathcal{O}}(t)\frac{\partial\hat{U}(t)}{\partial t} \\ &= \frac{i}{\hbar}\hat{\mathcal{H}}\hat{U}^\dagger(t)\hat{\mathcal{O}}(t)\hat{U}(t) + \hat{U}^\dagger(t)\frac{\partial\hat{\mathcal{O}}(t)}{\partial t}\hat{U}(t) - \frac{i}{\hbar}\hat{U}^\dagger(t)\hat{\mathcal{O}}(t)\hat{\mathcal{H}}\hat{U}(t) \\ &= \frac{i}{\hbar}\hat{U}^\dagger(t)\left(\hat{\mathcal{H}}\hat{\mathcal{O}}(t) - \hat{\mathcal{O}}(t)\hat{\mathcal{H}}\right)\hat{U}(t) + \hat{U}^\dagger(t)\frac{\partial\hat{\mathcal{O}}(t)}{\partial t}\hat{U}(t) \\ &= \frac{i}{\hbar}\big[\hat{\mathcal{H}}, \hat{\mathcal{O}}(t)\big]\bigg|_{\mathrm{H}} + \frac{\partial\hat{\mathcal{O}}(t)}{\partial t}\bigg|_{\mathrm{H}}.\end{aligned} \tag{44}$$

In general, if in the Schrödinger picture the observable does not have an explicit dependence on time, the equation of motion in the Heisenberg picture can simply be taken as

$$\dot{\hat{\mathcal{O}}}(t) = \frac{i}{\hbar}\big[\hat{\mathcal{H}}, \hat{\mathcal{O}}(t)\big]. \tag{45}$$

B Quantum harmonic oscillator

The quantum harmonic oscillator is described by the Hamiltonian

$$\hat{\mathcal{H}} = \frac{\hat{p}^2}{2m} + \frac{1}{2} m\omega_{\mathrm{m}}^2 \hat{x}^2, \tag{46}$$

where m is the oscillator's effective mass, ω_{m} the resonant frequency, and $\hat{x}$ and $\hat{p}$ are conjugate Hermitian operators representing the observables of position and momentum of the oscillator. They respond to the canonical commutation relation

$$\big[\hat{x}, \hat{p}\big] = i\hbar, \tag{47}$$

from which follows Heisenberg's uncertainty principle:

$$\Delta x \, \Delta p \geq \frac{\hbar}{2}. \tag{48}$$

The eigenvalues of $\hat{\mathcal{H}}$ represent the possible energy levels of the system, and the corresponding eigenstates form a complete basis for a generic state. To obtain the solution to the eigenvalue problem

$$\hat{\mathcal{H}} |\psi\rangle = E |\psi\rangle \tag{49}$$

we consider the coordinate representation, specified by the eigenstates of the position operator, $|x\rangle$; in this framework, the state is represented by a function of the coordinates $\psi(x) := \langle x|\psi\rangle$ and the momentum operator acts on the state as its derivative, $\hat{p} \to -i\hbar\partial_x$. The problem is then reduced to the differential equation

$$-\frac{\hbar^2}{2m} \psi''(x) = \left(E - \frac{1}{2} m\omega_{\mathrm{m}} x^2\right) \psi(x). \tag{50}$$

Because the Hamiltonian is Hermitian, we expect the solutions of the differential equation to form a basis of orthogonal, real states. These are given by the normalized eigenfunctions [21]

$$\psi_n(x) = \frac{1}{\sqrt{2^n n!}} \left(\frac{m\omega_{\mathrm{m}}}{\pi\hbar}\right)^{1/4} e^{-\frac{m\omega_{\mathrm{m}}}{2\hbar} x^2} H_n\Big(\sqrt{\frac{m\omega_{\mathrm{m}}}{\hbar}} x\Big), \tag{51}$$

which are indexed by an integer n and are implicitly dependent on the Hermite polynomials defined by $H_n(x) := (-1)^n e^{x^2} \frac{d^n}{dx^n}(e^{-x^2})$. The eigenvalues for each $\psi_n(x)$ are given by the discrete energy levels

$$E_n = \hbar\omega_{\mathrm{m}}\left(n + \frac{1}{2}\right). \tag{52}$$

In bra-ket notation the eigenstates of the Hamiltonian are generally denoted by $|n\rangle$. A notable feature of the eigenstates is that their energy levels are equally spaced by $\hbar\omega_{\mathrm{m}}$, indicating the quantum of energy of the harmonic oscillator. The ground state is the eigenstate state with the lowest possible energy, $E_0 = \hbar\omega_{\mathrm{m}}/2$.

The original observables can be used to define new non-Hermitian operators

$$\hat{b} = \frac{1}{\sqrt{2\hbar m\omega_{\mathrm{m}}}}\left(m\omega_{\mathrm{m}}\hat{x} + i\hat{p}\right), \tag{53}$$

$$\hat{b}^{\dagger} = \frac{1}{\sqrt{2\hbar m\omega_{\mathrm{m}}}}\left(m\omega_{\mathrm{m}}\hat{x} - i\hat{p}\right). \tag{54}$$

The normalization is chosen to imply a unitary commutation relation:

$$\begin{aligned}\left[\hat{b}, \hat{b}^{\dagger}\right] &= \frac{1}{2\hbar m\omega_{\mathrm{m}}}\left[m\omega_{\mathrm{m}}\hat{x} + i\hat{p}, m\omega_{\mathrm{m}}\hat{x} - i\hat{p}\right] \\ &= \frac{1}{2\hbar m\omega_{\mathrm{m}}}\left(-im\omega_{\mathrm{m}}\left[\hat{x}, \hat{p}\right] + im\omega_{\mathrm{m}}\left[\hat{p}, \hat{x}\right]\right) \\ &= \frac{-i}{\hbar}\left[\hat{x}, \hat{p}\right] \\ &= 1. \end{aligned} \tag{55}$$

From $\hat{b}$ and $\hat{b}^{\dagger}$ we can define a new Hermitian operator, $\hat{b}^{\dagger}\hat{b}$. Expanding the product,

$$\begin{aligned}\hat{b}^{\dagger}\hat{b} &= \frac{\left(m\omega_{\mathrm{m}}\hat{x} - i\hat{p}\right)\left(m\omega_{\mathrm{m}}\hat{x} + i\hat{p}\right)}{2\hbar m\omega_{\mathrm{m}}} \\ &= \frac{m^2\omega_{\mathrm{m}}^2\hat{x}^2 + \hat{p}^2 + im\omega_{\mathrm{m}}\left[\hat{x}, \hat{p}\right]}{2\hbar m\omega_{\mathrm{m}}} \\ &= \frac{1}{\hbar\omega_{\mathrm{m}}}\left(\frac{1}{2}m\omega_{\mathrm{m}}^2\hat{x}^2 + \frac{\hat{p}^2}{2m} - \frac{\hbar\omega_{\mathrm{m}}}{2}\right) \\ &= \frac{1}{\hbar\omega_{\mathrm{m}}}\left(\hat{\mathcal{H}} - \frac{\hbar\omega_{\mathrm{m}}}{2}\right), \end{aligned} \tag{56}$$

we can then rewrite the Hamiltonian as

$$\hat{\mathcal{H}} = \hbar\omega_{\mathrm{m}}\left(\hat{b}^{\dagger}\hat{b} + \frac{1}{2}\right). \tag{57}$$

A quick comparison with Eq. 52 reveals that $\hat{b}^{\dagger}\hat{b}$ can be interpreted as a *number operator* acting on eigenstates of the Hamiltonian to return the number of quanta of that state:

$$\hat{b}^\dagger \hat{b}|n\rangle = n|n\rangle. \tag{58}$$

The quanta indicated by n may correspond to the quanta of energy, as $|n\rangle$ is an eigenstate of the Hamiltonian, but it is more common to refer to them as *phonons*, quanta of oscillation of the mechanical motion behaving like quasi-particles with energy $\hbar\omega_\mathrm{m}$.

To better understand the role of $\hat{b}$ and $\hat{b}^\dagger$, we notice that their action on one of the eigenstates, $|n\rangle$, returns a state which is still an eigenstate, albeit for a different eigenvalue:

$$\begin{aligned}
\hat{b}^\dagger \hat{b} \cdot \hat{b}|n\rangle &= \left(\hat{b} \cdot \hat{b}^\dagger \hat{b} - \left[\hat{b}, \hat{b}^\dagger \hat{b}\right]\right)|n\rangle \\
&= \hat{b}\left(\hat{b}^\dagger \hat{b} - \left[\hat{b}, \hat{b}^\dagger\right]\right)|n\rangle \\
&= (n-1) \cdot \hat{b}|n\rangle, \qquad (59) \\
\hat{b}^\dagger \hat{b} \cdot \hat{b}^\dagger|n\rangle &= \dots \\
&= (n+1) \cdot \hat{b}^\dagger|n\rangle. \qquad (60)
\end{aligned}$$

Thus, $\hat{b}|n\rangle$ is proportional to $|n-1\rangle$ and $\hat{b}^\dagger|n\rangle$ is proportional to $|n+1\rangle$. For this reason $\hat{b}$ and $\hat{b}^\dagger$ are known as the *ladder operators* of the quantum harmonic oscillator: their action changes the state to one with lower or higher energy, and their repeated application brings the total energy level of the system arbitrarily up or down along set of discrete energy levels. In terms of phonons, $\hat{b}$ acts as if it destroys one such excitation, whereas $\hat{b}$ has the effect of creating one; this justifies their alternative name as, respectively, *annihilation* and *creation* operators. Using the appropriate normalization, all the eigenstates can be obtained starting from the ground state $|0\rangle$ by successive applications of the creation operator:

$$|n\rangle = \frac{1}{\sqrt{n!}}\hat{b}^n|0\rangle. \tag{61}$$

Considering the inverse relations of Eq. 53 and 54 to obtain the original observables in terms of the creation and annihilation operators,

$$\hat{x} = \sqrt{\frac{\hbar}{2m\omega_\mathrm{m}}}\left(\hat{b} + \hat{b}^\dagger\right), \tag{62}$$

$$\hat{p} = i\sqrt{\frac{\hbar m\omega_\mathrm{m}}{2}}\left(\hat{b} - \hat{b}^\dagger\right), \tag{63}$$

we can directly calculate the amplitude of the fluctuations of the harmonic oscillator in the ground state, or *zero-point fluctuations*:

$$\begin{aligned} x_{\mathrm{ZPF}} &:= \sqrt{\langle 0|\hat{x}^2|0\rangle} \\ &= \sqrt{\langle 0|\frac{\hbar}{2m\omega_{\mathrm{m}}}\left(\hat{b}^2+(\hat{b}^\dagger)^2+2\hat{b}^\dagger\hat{b}+1\right)|0\rangle} \\ &= \sqrt{\frac{\hbar}{2m\omega_{\mathrm{m}}}}. \end{aligned} \tag{64}$$

C Numerical estimates for dual-beam interference

We are interested in quantifying the effects that the beating of two input fields has on the oscillations of the cavity mirror in an optomechanical setup, in particular in relation to the problem of suspending the mirror on the radiation pressure force of a vertical cavity. Here m will denote the mass of the mirror, g the gravitational acceleration, c the speed of light, ω_{m} the frequency of the oscillation, and ω_{d} the dual beam's separation in optical frequency.

Consider a worst-case scenario where the two input fields have identical strength and the total power is modulated between perfect destructive and constructive interference. With the assumption that each input beam, independently, produces enough resonating power to support the weight of the mirror, $mgc/2$, we have that the beating of the two inputs produces a time-dependent intra-cavity power,

$$P(t) = mgc\cos^2(\omega_{\mathrm{d}}t), \tag{65}$$

which leads to the radiation pressure force

$$F(t) = \frac{2P(t)}{c} = 2mg\cos^2(\omega_{\mathrm{d}}t), \tag{66}$$

also a function of time.

The equation of motion for the position of the mirror along the vertical optical axis, z, includes the gravitational force, the restoring force of the harmonic oscillator, and the radiation pressure force of Eq. 66:

$$m\ddot{z}(t) = -mg - m\omega_{\mathrm{m}}^2 z(t) + 2mg\cos^2(\omega_{\mathrm{d}}t). \tag{67}$$

We will assume now that the beating is much faster than the mechanical oscillations of the mirror. If this condition is not naturally satisfied, it can always be imposed by detuning one of the two input beams to a separate free spectral range (FSR). This operation, which changes nothing from the cavity's perspective, shifts the beating to much higher frequencies. The amplitude of the fast oscillations due to the interference is obtained by the solution of Eq. 67 in the limit $\omega_{\mathrm{d}} \gg \omega_{\mathrm{m}}$,

$$z(t) = -\frac{g}{4\omega_{\mathrm{d}}^2}\cos(2\omega_{\mathrm{d}}t), \tag{68}$$

obtained first by moving into the frequency domain, then applying the limit, and then transforming back to the time domain. The oscillations can be made arbitrarily small by choosing the detuning between the two fields, ω_{d}, to be large enough. Choosing the relative detuning to be on the order of the FSR of a cavity approximately 20 cm long, i.e. $\omega_{\mathrm{d}} \approx 2\pi \times 750\,\mathrm{MHz}$, the off-resonance oscillations induced by the beating have amplitude on the order of 10^{-9} Å. These oscillations are therefore even smaller than the zero-point fluctuations, $z_{\mathrm{ZPF}} = \sqrt{\hbar/(2m\omega_{\mathrm{m}})}$, which is on the order of 10^{-8} Å for a mirror of mass $m = 1\,\mathrm{mg}$ and harmonic frequency $\omega_{\mathrm{m}} = 2\pi \times 1\,\mathrm{MHz}$.

The effect on the mechanics is minimal, but this might not be enough. The oscillations driven at $2\omega_{\mathrm{d}}$ risk to coherently interact with the cavity field and lead to resonant redistribution of the optical modes. The induced oscillations, functioning as a source of frequency modulation, create sidebands that resonate at frequencies $2\omega_{\mathrm{d}}$ away, and it is important to check that these sidebands have negligible effect on the system especially when the relative detuning has a value close to the FSR. Assuming the cavity to be at resonance when the mirror is at the centre of the oscillation, the dynamics of cavity field α are described by the differential equation (cf. Eq. 3.27)

$$\dot{\alpha}(t) = \left(-\kappa + iG_0 z(t)\right)\alpha(t) + \sqrt{2\kappa}\alpha_{\mathrm{in}}, \tag{69}$$

where G_0 is the optomechanical coupling constant, equivalent to the ratio between the FSR and the half-wavelength, and α_{in} is the amplitude of the input field. Transforming to the frequency domain, we get

$$(\kappa + i\omega)\,\alpha(\omega) + i\frac{\pi G_0 g}{4\omega_{\mathrm{d}}^2}\left(\alpha(\omega - 2\omega_{\mathrm{d}}) + \alpha(\omega + 2\omega_{\mathrm{d}})\right) = \sqrt{2\kappa}\alpha_{\mathrm{in}}(\omega). \tag{70}$$

The input field on the right-hand side splits between three separate terms on the left-hand side representing the carrier of the cavity field and two sidebands at $2\omega_{\mathrm{d}}$ induced by the modulation. The amplitude of the sidebands scales as the inverse of the beat frequency by a factor of $\pi G_0 g/\left(4\kappa\omega_{\mathrm{d}}^2\right)$ relative to the carrier. For a wavelength of 1064 nm, finesse of 1000, and beat frequency once more on the order of the FSR, the sidebands are estimated at less than 1 part per billion of the main resonance.

References

1. Nichols, E. E. and Hull, G. F., "A Preliminary Communication on the Pressure of Heat and Light Radiation", *Physical Review* **13**, 5 307–320 (1901).
   CITED ON PAGE 5
2. Nichols, E. E. and Hull, G. F., "The Pressure Due to Radiation (Second Paper)", *Physical Review* **17**, 1 26–50 (1903).
   CITED ON PAGE 5
3. Musen, P., "The Influence of the Solar Radiation Pressure on the Motion of an Artificial Satellite", *Journal of Geophysical Research* **65**, 5 1391–1396 (1960).
   CITED ON PAGE 5
4. Tsuda, Y., Mori, O., Funase, R. et al., "Achievement of IKAROS — Japanese deep space solar sail demonstration mission", *Acta Austronautica* **82** 183–188 (2013).
   CITED ON PAGE 5
5. Braginsky, V. B. and Manukin, A. B., "Ponderomotive effects of electromagnetic radiation", *Journal of Experimental and Theoretical Physics* **25**, 4 653–655 (1967).
   CITED ON PAGE 5
6. Braginsky, V. B., Manukin, A. B., and Tikhonov, M. Y., "Investigation of dissipative ponderomotive effects of electromagnetic radiation", *Journal of Experimental and Theoretical Physics* **31**, 5 829–830 (1970).
   CITED ON PAGES 5 AND 63
7. Teufel, J. D., Donner, T., Li, D. et al., "Sideband cooling of micromechanical motion to the quantum ground state", *Nature* **475** 359–363 (2011).
   CITED ON PAGES 5, 60, AND 69
8. Brooks, D. W. C., Botter, T., Schreppler, S. et al., "Non-classical light generated by quantum-noise-driven cavity optomechanics", *Nature* **488** 476–480 (2012).
   CITED ON PAGES 5, 61, AND 182
9. Safavi-Naeini, A. H., Gröblacher, S., Hill, J. T. et al., "Squeezed light from a silicon micromechanical resonator", *Nature* **500** 185–189 (2013).
   CITED ON PAGES 5, 61, AND 182
10. Weis, S., Rivière, R., Deléglise, S. et al., "Optomechanically induced transparency", *Science* **330**, 6010 1520–1523 (2010).
    CITED ON PAGES 5 AND 181
11. Safavi-Naeini, A. H., Mayer Alegre, T. P., Chan, J. et al., "Electromagnetically induced transparency and slow light with optomechanics", *Nature* **472** 69–73 (2011).
    CITED ON PAGE 5

12. Adler, S. L. and Bassi, A., "Is Quantum Theory Exact?", *Science* **325**, 5938 275–276 (2009).
CITED ON PAGE 6

13. Bassi, A., Lochan, K., Satin, S. et al., "Models of wave-function collapse, underlying theories, and experimental tests", *Reviews of Modern Physics* **85**, 2 471–527 (2013).
CITED ON PAGE 6

14. Guccione, G., Hosseini, M., Adlong, S. et al., "Scattering-Free Optical Levitation of a Cavity Mirror", *Physical Review Letters* **111**, 183001 (2013).
CITED ON PAGES 6, 69, 122, AND 126

15. Gan, C. C., Savage, C. M., and Scully, S., "Optomechanical tests of a Schrödinger-Newton equation for gravitational quantum mechanics", *Physical Review D* **93**, 124049 (2016).
CITED ON PAGE 6

16. Hosseini, M., Guccione, G., Slatyer, H. J. et al., "Multimode laser cooling and ultra-high sensitivity force sensing with nanowires", *Nature Communications* **5**, 4663 (2014).
CITED ON PAGES 7, 72, AND 110

17. Guccione, G., Slatyer, H. J., Carvalho, A. R. R. et al., "Squeezing quadrature rotation in the acoustic band via optomechanics", *Journal of Physics B* **49**, 065401 (2016).
CITED ON PAGES 7, 164, AND 182

18. Mohr, P. J., Taylor, B. N., and Newell, D. B., "CODATA Recommended Values of the Fundamental Physical Constants: 2010", *Journal of Physical and Chemical Reference Data* **41**, 043109 (2012).
CITED ON PAGE 10

19. Stade, E., Fourier Analysis, Wiley-Interscience (2005).
CITED ON PAGE 10

20. Clerk, A. A., Devoret, M. H., Girvin, S. M. et al., "Introduction to quantum noise, measurement, and amplification", *Reviews of Modern Physics* **82**, 2 1155–1208 (2010).
CITED ON PAGES 13 AND 187

21. Griffiths, D. J., Introduction to Quantum Mechanics, Prentice Hall (1995).
CITED ON PAGES 13 AND 207

22. Griffiths, D. J., Introduction to Electrodynamics, Pearson, 4th edition (2013).
CITED ON PAGES 15 AND 17

23. Scully, M. O. and Zubairy, M. S., Quantum Optics, Cambridge University Press (1997).
CITED ON PAGES 15, 16, 18, AND 19

24. Rothman, T. and Boughn, S., "The Lorentz force and the radiation pressure of light", *American Journal of Physics* **77**, 2 122–127 (2009).
CITED ON PAGE 17

25. Webster, S. A., Oxborrow, M., and Gill, P., “Subhertz-linewidth NdYAG laser.pdf”, *Optics Letters* **29**, 13 1497–1499 (2004).
CITED ON PAGE 18

26. Yuen, H. P. and Chan, V. W. S., “Noise in homodyne and heterodyne detection”, *Optics Letters* **8**, 3 177–179 (1983).
CITED ON PAGES 20 AND 179

27. Bachor, H.-A. and Ralph, T. C., A Guide to Experiments in Quantum Optics, Wiley-VCH, 2nd edition (2004).
CITED ON PAGES 21, 22, 39, AND 41

28. Ferraro, A., Olivares, S., and Paris, M. G. A., “Gaussian states in continuous variable quantum information”, *arXiv* **0503237** (2005).
CITED ON PAGE 22

29. Vahlbruch, H., Mehmet, M., Danzmann, K. et al., “Detection of 15 dB Squeezed States of Light and their Application for the Absolute Calibration of Photoelectric Quantum Efficiency”, *Physical Review Letters* **117**, 110801 (2016).
CITED ON PAGE 22

30. Oelker, E., Isogai, T., Miller, J. et al., “Audio-Band Frequency-Dependent Squeezing for Gravitational-Wave Detectors”, *Physical Review Letters* **116**, 041102 (2016).
CITED ON PAGES 22, 181, AND 193

31. Chelkowski, S., Vahlbruch, H., Hage, B. et al., “Experimental characterization of frequency-dependent squeezed light”, *Physical Review A* **71**, 013806 (2005).
CITED ON PAGES 22, 181, AND 193

32. Brieussel, A., Shen, Y., Campbell, G. T. et al., “Squeezed light from a diamond-turned monolithic cavity”, *Optics Express* **24**, 4 (2016).
CITED ON PAGE 22

33. Shen, Y., Assad, S. M., Grosse, N. B. et al., “Nonlinear Entanglement and its Application to Generating Cat States”, *Physical Review Letters* **114**, 100403 (2015).
CITED ON PAGE 22

34. Buchmann, L. F., Schreppler, S., Kohler, J. et al., “Complex Squeezing and Force Measurement Beyond the Standard Quantum Limit”, *Physical Review Letters* **117**, 030801 (2016).
CITED ON PAGES 22 AND 196

35. Furusawa, A., Sørensen, J. L., Braunstein, S. L. et al., “Unconditional Quantum Teleportation”, *Science* **282**, 5389 706–709 (1998).
CITED ON PAGE 22

36. Aasi, J., Abadie, J., Abbott, B. P. et al., “Enhanced sensitivity of the LIGO gravitational wave detector by using squeezed states of light”, *Nature Photonics* **7** 613–619 (2013).
CITED ON PAGES 22 AND 180

37. Kronwald, A., Marquardt, F., and Clerk, A. A., “Dissipative optomechanical squeezing of light”, *New Journal of Physics* **16**, 063058 (2014).
CITED ON PAGE 22

38. Siegman, A. E., Lasers, University Science Books (1986).
CITED ON PAGES 22, 33, 35, AND 37

39. Matsko, A. B. and Ilchenko, V. S., "Optical Resonators With Whispering-Gallery Modes – Part I: Basics", *Journal of Selected Topics in Quantum Electronics* **12**, 1 3–14 (2006).
CITED ON PAGE 23

40. Ilchenko, V. S. and Matsko, A. B., "Optical Resonators With Whispering-Gallery Modes – Part II: Applications", *Journal of Selected Topics in Quantum Electronics* **12**, 1 15–32 (2006).
CITED ON PAGE 23

41. Weber, H., "The Fresnel equations for lossy dielectrics and conservation of energy", *Journal of Modern Optics* **61**, 15 1219–1224 (2014).
CITED ON PAGE 23

42. Poirson, J., Bretenaker, F., Vallet, M. et al., "Analytical and experimental study of ringing effects in a Fabry–Perot cavity. Application to the measurement of high finesses", *Journal of the Optical Society of America B* **14**, 11 2811–2817 (1997).
CITED ON PAGE 30

43. Saleh, B. E. A. and Teich, M. C., Fundamentals of Photonics, Wiley-Interscience (1991).
CITED ON PAGE 33

44. Tapley, B. D., Bettadpur, S., Ries, J. C. et al., "GRACE Measurements of Mass Variability in the Earth System", *Science* **305**, 5683 503–505 (2004).
CITED ON PAGE 36

45. Abbott, B. P., Abbott, R., Adhikari, R. X. et al., "Observation of a kilogram-scale oscillator near its quantum ground state", *New Journal of Physics* **11**, 07 073032 (2009).
CITED ON PAGE 36

46. Ma, X.-S., Herbst, T., Scheidl, T. et al., "Quantum teleportation over 143 kilometres using active feed-forward", *Nature* **489** 269–273 (2012).
CITED ON PAGE 36

47. Garcés-Chávez, V., McGloin, D., Melville, H. et al., "Simultaneous micromanipulation in multiple planes using a self-reconstructing light beam", *Nature* **419** 147–147 (2002).
CITED ON PAGES 37 AND 123

48. Hauck, R., Kortz, H. P., and Weber, H., "Misalignment sensitivity of optical resonators", *Applied Optics* **19**, 4 598–601 (1980).
CITED ON PAGE 39

49. Zeilinger, A., "General properties of lossless beam splitters in interferometry", *American Journal of Physics* **49**, 9 882–883 (1981).
CITED ON PAGES 39 AND 40

50. Dorf, R. C. and Bishop, R. H., Modern Control Systems, Pearson, 11th edition (2007).
CITED ON PAGE 41

51. Pound, R. V., "Electronic Frequency Stabilization of Microwave Oscillators", *Review of Scientific Instruments* **17**, 11 490–505 (1946).
CITED ON PAGE 44

52. Drever, R. W. P., Hall, J. L., Kowalski, F. V. et al., "Laser Phase and Frequency Stabilization Using an Optical Resonator", *Applied Physics B* **31** 97–105 (1983).
CITED ON PAGE 44

53. Black, E. D., "An introduction to Pound-Drever-Hall laser frequency stabilization", *American Journal of Physics* **69**, 1 (2001).
CITED ON PAGES 45 AND 46

54. Sparkes, B. M., "Storage and Manipulation of Optical Information Using Gradient Echo Memory in Warm Vapours and Cold Ensembles", Ph.D. thesis, The Australian National University (2013).
CITED ON PAGE 48

55. Armstrong, S., "Experiments in Quantum Optics: Scalable Entangled States and Quantum Computation with Cluster States", Ph.D. thesis, The Australian National University (2014).
CITED ON PAGE 48

56. Gardiner, C. W. and Collett, M. J., "Input and output in damped quantum systems: Quantum stochastic differential equations and the master equation", *Physical Review A* **31**, 6 3761–3774 (1985).
CITED ON PAGES 51 AND 52

57. Gardiner, C. W. and Zoller, P., Quantum Noise: A Handbook of Markovian and Non-Markovian Quantum Stochastic Methods with Applications to Quantum Optics, Springer, 2nd edition (2004).
CITED ON PAGES 53, 55, AND 184

58. Marino, F., De Rosa, M., and Marin, F., "Canard orbits in Fabry-Perot cavities induced by radiation pressure and photothermal effects", *Physical Review E* **73**, 026217 (2006).
CITED ON PAGES 54 AND 161

59. Schliesser, A., Arcizet, O., Rivière, R. et al., "Resolved-sideband cooling and position measurement of a micromechanical oscillator close to the Heisenberg uncertainty limit", *Nature Physics* **5** 509–514 (2009).
CITED ON PAGES 59 AND 69

60. Palomaki, T. A., Harlow, J. W., Teufel, J. D. et al., "Coherent state transfer between itinerant microwave fields and a mechanical oscillator", *Nature* **495** 210–214 (2013).
CITED ON PAGE 60

61. Singh, S., Wright, E. M., and Meystre, P., "Quantum-state transfer between a Bose-Einstein condensate and an optomechanical mirror", *Physical Review A* **86**, 021801 (2012).
CITED ON PAGE 60

62. Andrews, R. W., Peterson, R. W., Purdy, T. P. et al., "Bidirectional and efficient conversion between microwave and optical light", *Nature Physics* **10** 321–326

(2014).
CITED ON PAGE 60

63. Chan, J., Mayer Alegre, T. P., Safavi-Naeini, A. H. et al., “Laser cooling of a nanomechanical oscillator into its quantum ground state”, *Nature* **478** 89–92 (2011).
CITED ON PAGES 60 AND 69

64. Heidmann, A., Horowicz, R. J., Reynaud, S. et al., “Observation of Quantum Noise Reduction on Twin Laser Beams”, *Physical Review Letters* **59**, 22 2555–2557 (1987).
CITED ON PAGE 61

65. Fabre, C., Pinard, M., Bourzeix, S. et al., “Quantum-noise reduction using a cavity with a movable mirror”, *Physical Review A* **49**, 2 (1994).
CITED ON PAGES 61 AND 181

66. Mancini, S. and Tombesi, P., “Quantum noise reduction by radiation pressure”, *Physical Review A* **49**, 5 (1994).
CITED ON PAGES 61 AND 181

67. Vitali, D., Gigan, S., Ferreira, A. et al., “Optomechanical Entanglement between a Movable Mirror and a Cavity Field”, *Physical Review Letters* **98**, 030405 (2007).
CITED ON PAGE 61

68. Paternostro, M., Vitali, D., Gigan, S. et al., “Creating and Probing Multipartite Macroscopic Entanglement with Light”, *Physical Review Letters* **99**, 250401 (2007).
CITED ON PAGE 61

69. Hofer, S. G., Wieczorek, W., Aspelmeyer, M. et al., “Quantum entanglement and teleportation in pulsed cavity optomechanics”, *Physical Review A* **84**, 052327 (2011).
CITED ON PAGE 61

70. Agrawal, G. P. and Carmichael, H. J., “Optical bistability through nonlinear dispersion and absorption”, *Physical Review A* **19**, 5 (1979).
CITED ON PAGE 63

71. Savage, C. M. and Carmichael, H. J., “Single-Atom Optical Bistability”, *Journal of Quantum Electronics* **24**, 8 1495–1498 (1988).
CITED ON PAGE 63

72. Qiang, Z., Sheng-Chang, L., Xiao-Ping, Z. et al., “Controllable optical bistability of Bose Einstein condensate in an optical cavity with Kerr medium”, *Chinese Physics B* **21**, 093702 (2012).
CITED ON PAGE 63

73. Dorsel, A., McCullen, J. D., Meystre, P. et al., “Optical Bistability and Mirror Confinement Induced by Radiation Pressure”, *Physical Review Letters* **51**, 17 (1983).
CITED ON PAGE 63

74. Meystre, P., Wright, E. M., McCullen, J. D. et al., "Theory of radiation-pressure-driven interferometers", *Journal of the Optical Society of America B* **2**, 11 (1985).
CITED ON PAGE 63

75. Aspelmeyer, M., Kippenberg, T. J., and Marquardt, F., "Cavity optomechanics", *Reviews of Modern Physics* **86**, 4 1391–1452 (2014).
CITED ON PAGE 63

76. Sheard, B. S., Gray, M. B., Mow-Lowry, C. M. et al., "Observation and characterization of an optical spring", *Physical Review A* **69**, 051801 (2004).
CITED ON PAGE 64

77. Khalili, F. Y., "Frequency-dependent rigidity in large-scale interferometric gravitational-wave detectors", *Physics Letters A* **288** 251–256 (2001).
CITED ON PAGE 65

78. Zhao, C., Ju, L., Degallaix, J. et al., "Parametric Instabilities and Their Control in Advanced Interferometer Gravitational-Wave Detectors", *Physical Review Letters* **94**, 121102 (2005).
CITED ON PAGE 69

79. Arcizet, O., Cohadon, P.-F., Briant, T. et al., "Radiation-pressure cooling and optomechanical instability of a micromirror", *Nature* **444** 71–74 (2006).
CITED ON PAGE 69

80. Corbitt, T. R., Ottaway, D., Innerhofer, E. et al., "Measurement of radiation-pressure-induced optomechanical dynamics in a suspended Fabry-Perot cavity", *Physical Review A* **74**, 02 021802 (2006).
CITED ON PAGES 69 AND 134

81. Massel, F., Heikkilä, T. T., Pirkkalainen, J.-M. et al., "Microwave amplification with nanomechanical resonators", *Nature* **480** 351–354 (2011).
CITED ON PAGE 69

82. Buters, F. M., Eerkens, H. J., Heeck, K. et al., "Large parametric amplification in an optomechanical system", *Physica Scripta* **T165**, 014003 (2015).
CITED ON PAGE 69

83. Evans, M., Gras, S., Fritschel, P. et al., "Observation of Parametric Instability in Advanced LIGO", *Physical Review Letters* **114**, 161102 (2015).
CITED ON PAGES 69 AND 152

84. Braginsky, V. B. and Vyatchanin, S. P., "Low quantum noise tranquilizer for Fabry-Perot interferometer", *Physics Letters A* **293** 228–234 (2002).
CITED ON PAGE 69

85. Gigan, S., Böhm, H. R., Paternostro, M. et al., "Self-cooling of a micromirror by radiation pressure", *Nature* **444** 67–70 (2006).
CITED ON PAGE 69

86. Schliesser, A., Del'Haye, P., Nooshi, N. et al., "Radiation Pressure Cooling of a Micromechanical Oscillator Using Dynamical Backaction", *Physical Review Letters* **97**, 243905 (2006).
CITED ON PAGE 69

87. Marquardt, F., Chen, J. P., Clerk, A. A. et al., “Quantum Theory of Cavity-Assisted Sideband Cooling of Mechanical Motion”, *Physical Review Letters* **99**, 093902 (2007).
CITED ON PAGE 69

88. Kiesel, N., Blaser, F., Delić, U. et al., “Cavity cooling of an optically levitated submicron particle”, *Proceedings of the National Academy of Sciences* **110**, 35 14180–14185 (2013).
CITED ON PAGES 69 AND 125

89. Corbitt, T. R., Chen, Y., Innerhofer, E. et al., “An all-optical trap for a gram-scale mirror”, *Physical Review Letters* **98**, 150802 (2007).
CITED ON PAGES 69, 135, AND 175

90. Wilson-Rae, I., Nooshi, N., Zwerger, W. et al., “Theory of Ground State Cooling of a Mechanical Oscillator Using Dynamical Backaction”, *Physical Review Letters* **99**, 093901 (2007).
CITED ON PAGE 69

91. Gröblacher, S., Hertzberg, J. B., Vanner, M. R. et al., “Demonstration of an ultracold microoptomechanical oscillator in a cryogenic cavity”, *Nature Physics* **5** 485–488 (2009).
CITED ON PAGE 69

92. Park, Y.-S. and Wang, H., “Resolved-sideband and cryogenic cooling of an optomechanical resonator”, *Nature Physics* **5** 489–493 (2009).
CITED ON PAGE 69

93. Peterson, R. W., Purdy, T. P., Kampel, N. S. et al., “Laser Cooling of a Micromechanical Membrane to the Quantum Backaction Limit”, *Physical Review Letters* **116**, 063601 (2016).
CITED ON PAGE 69

94. Metzger, C. and Karrai, K., “Cavity cooling of a microlever”, *Nature* **432** 1002–1005 (2004).
CITED ON PAGES 69, 102, AND 104

95. Metzger, C., Ludwig, M., Neuenhahn, C. et al., “Self-Induced Oscillations in an Optomechanical System Driven by Bolometric Backaction”, *Physical Review Letters* **101**, 133903 (2008).
CITED ON PAGES 69 AND 101

96. Slatyer, H. J., Guccione, G., Cho, Y.-W. et al., “Synthesis of optical spring potentials in optomechanical systems”, *Journal of Physics B* **49**, 125401 (2016).
CITED ON PAGES 69, 164, AND 166

97. Singh, S., Phelps, G. A., Goldbaum, D. S. et al., “All-Optical Optomechanics: An Optical Spring Mirror”, *Physical Review Letters* **105**, 213602 (2010).
CITED ON PAGES 69, 124, AND 126

98. Chang, D. E., Ni, K.-K., Painter, O. et al., “Ultrahigh-Q mechanical oscillators through optical trapping”, *New Journal of Physics* **14**, 045002 (2012).
CITED ON PAGES 69 AND 128

99. Korth, W. Z., Miao, H., Corbitt, T. R. et al., "Suppression of quantum-radiation-pressure noise in an optical spring", *Physical Review A* **88**, 033805 (2013).
CITED ON PAGE 69

100. Page, M. A., Ma, Y., Zhao, C. et al., "Towards thermal noise free optomechanics", *arXiv* **1602.03621** (2016).
CITED ON PAGE 69

101. Imboden, M. and Mohanty, P., "Dissipation in nanoelectromechanical systems", *Physics Reports* **534** 89–146 (2014).
CITED ON PAGES 73 AND 78

102. Hossein-Zadeh, M. and Vahala, K. J., "Free ultra-high-Q microtoroid: a tool for designing photonic devices", *Optics Express* **15**, 1 166–175 (2007).
CITED ON PAGE 73

103. Anetsberger, G., Rivière, R., Schliesser, A. et al., "Ultralow-dissipation optomechanical resonators on a chip", *Nature Photonics* **2** 627 (2008).
CITED ON PAGE 73

104. Reinhardt, C., Müller, T., Bourassa, A. et al., "Ultralow-Noise SiN Trampoline Resonators for Sensing and Optomechanics", *Physical Review X* **6**, 021001 (2016).
CITED ON PAGES 73 AND 188

105. Ekinci, K. L. and Roukes, M. L., "Nanoelectromechanical systems", *Review of Scientific Instruments* **76**, 061101 (2005).
CITED ON PAGE 73

106. Ilic, B., Craighead, H. G., Krylov, S. et al., "Attogram detection using nanoelectromechanical oscillators", *Journal of Applied Physics* **95**, 7 (2004).
CITED ON PAGE 73

107. Burg, T. P., Godin, M., Knudsen, S. M. et al., "Weighing of biomolecules, single cells and single nanoparticles in fluid", *Nature* **446** 1066–1069 (2007).
CITED ON PAGES 73 AND 74

108. Naik, A. K., Hanay, M. S., Hiebert, W. K. et al., "Towards single-molecule nanomechanical mass spectrometry", *Nature Nanotechnology* **4** 445–450 (2009).
CITED ON PAGES 73 AND 74

109. Li, M., Myers, E. B., Tang, H. X. et al., "Nanoelectromechanical resonator arrays for ultrafast, gas-phase chromatographic chemical analysis", *Nano Letters* **10** 3899–3903 (2010).
CITED ON PAGES 73 AND 74

110. Gil-Santos, E., Ramos, D., Martínez, J. et al., "Nanomechanical mass sensing and stiffness spectrometry based on two-dimensional vibrations of resonant nanowires", *Nature Nanotechnology* **5** 641–645 (2010).
CITED ON PAGES 73 AND 77

111. Liu, F., Alaie, S., Leseman, Z. C. et al., "Sub-pg mass sensing and measurement with an optomechanical oscillator", *Optics Express* **21**, 17 19555–19567 (2013).
CITED ON PAGE 73

112. Jensen, K., Kim, K., and Zettl, A., "An atomic-resolution nanomechanical mass sensor", *Nature Nanotechnology* **3** 533–537 (2008).
CITED ON PAGES 73 AND 74

113. Chaste, J., Eichler, A., Moser, J. et al., "A nanomechanical mass sensor with yoctogram resolution", *Nature Nanotechnology* **7** 301–304 (2012).
CITED ON PAGES 73 AND 74

114. Mamin, H. J. and Rugar, D., "Sub-attonewton force detection at millikelvin temperatures", *Applied Physics Letters* **79**, 20 (2001).
CITED ON PAGE 73

115. Binnig, G., Quate, C. F., and Gerber, C., "Atomic Force Microscope", *Physical Review Letters* **56**, 9 930–933 (1986).
CITED ON PAGE 73

116. Albrecht, T. R., Grütter, P., Horne, D. et al., "Frequency modulation detection using highQ cantilevers for enhanced force microscope sensitivity", *Journal of Applied Physics* **69**, 2 (1991).
CITED ON PAGE 74

117. Jourdan, G., Torricelli, G., Chevrier, J. et al., "Tuning the effective coupling of an AFM lever to a thermal bath", *Nanotechnology* **18**, 475502 (2007).
CITED ON PAGE 74

118. Liu, C.-H., Barzilai, A. M., Reynolds, J. K. et al., "Characterization of a High-Sensitivity Micromachined Tunneling Accelerometer with Micro-g Resolution", *Journal of Microeletromechanical Systems* **7**, 2 235–244 (1998).
CITED ON PAGE 74

119. Krause, A. G., Winger, M., Blasius, T. D. et al., "A high-resolution microchip optomechanical accelerometer", *Nature Photonics* **6** 769–772 (2012).
CITED ON PAGE 74

120. Cleland, A. N. and Roukes, M. L., "A nanometre-scale mechanical electrometer", *Nature* **392** 160–162 (1998).
CITED ON PAGE 74

121. Rugar, D., Budaklan, R., Mamin, H. J. et al., "Single spin detection by magnetic resonance force microscopy", *Nature* **430** 329–332 (2004).
CITED ON PAGES 74 AND 109

122. Gao, P. and Cai, Y., "Label-free detection of the aptamer binding on protein patterns using Kelvin probe force microscopy (KPFM)", *Analytical and Bioanalytical Chemistry* **394**, 1 207–214 (2009).
CITED ON PAGES 74 AND 75

123. Dong, M., Husale, S., and Sahin, O., "Determination of protein structural flexibility by microsecond force spectroscopy", *Nature Nanotechnology* **4** 514–517 (2009).
CITED ON PAGE 74

124. Yazdanpanah, M. M., Hosseini, M., Pabba, S. et al., "Micro-wilhelmy and related liquid property measurements using constant-diameter nanoneedle-tipped atomic

force microscope probes", *Langmuir* **24**, 23 13753–13764 (2008).
CITED ON PAGES 74 AND 75

125. Dobrokhotov, V. V., Yazdanpanah, M. M., Pabba, S. et al., "Visual force sensing with flexible nanowire buckling springs", *Nanotechnology* **19**, 035502 (2008).
CITED ON PAGES 74 AND 75

126. Yazdanpanah, M. M., Harfenist, S. A., Safir, A. et al., "Selective self-assembly at room temperature of individual freestanding Ag2Ga alloy nanoneedles", *Journal of Applied Physics* **98**, 07 073510 (2005).
CITED ON PAGE 75

127. Zhao, M., Gu, X., Lowther, S. E. et al., "Subsurface characterization of carbon nanotubes in polymer composites via quantitative electric force microscopy", *Nanotechnology* **21**, 225702 (2010).
CITED ON PAGE 75

128. Biedermann, L. B., Tung, R. C., Raman, A. et al., "Characterization of silver-gallium nanowires for force and mass sensing applications", *Nanotechnology* **21**, 30 305701 (2010).
CITED ON PAGES 76 AND 89

129. Blevins, R. D., Formulas for natural frequency and mode shape, Krieger Publishing Company (1979).
CITED ON PAGE 76

130. Butt, H.-J. and Jaschke, M., "Calculation of thermal noise in atomic force microscopy", *Nanotechnology* **6**, 1 1–7 (1995).
CITED ON PAGE 77

131. Kiracofe, D. R., Yazdanpanah, M. M., and Raman, A., "Mass and stiffness calibration of nanowires using thermally driven vibration", *Nanotechnology* **22**, 29 295504 (2011).
CITED ON PAGES 77 AND 89

132. Chen, C., Ma, M., Zhe Liu, J. et al., "Viscous damping of nanobeam resonators: Humidity, thermal noise, and a paddling effect", *Journal of Applied Physics* **110**, 034320 (2011).
CITED ON PAGE 77

133. Newell, W. E., "Miniaturization of Tuning Forks", *Science* **161**, 3848 1320–1326 (1968).
CITED ON PAGE 78

134. Bohren, C. F. and Huffman, D. R., Absorption and Scattering of Light by Small Particles, Wiley-VCH (2008).
CITED ON PAGES 83 AND 84

135. Biedermann, L. B., "Vibrational Spectra of Nanowires Measured Using Laser Doppler Vibrometry and STM Studies of Epitaxial Graphene", Technical report, Sandia National Laboratories (2009).
CITED ON PAGES 84 AND 85

136. Svoboda, K. and Block, S. M., "Optical trapping of metallic Rayleigh particles", *Optics Letters* **19**, 13 930–932 (1994).
CITED ON PAGE 84

137. Ni, K.-K., Norte, R., Wilson, D. J. et al., "Enhancement of Mechanical Q Factors by Optical Trapping", *Physical Review Letters* **108**, 214302 (2012).
CITED ON PAGES 89 AND 128

138. Sutton, C. M., "Accelerometer Calibration by Dynamic Position Measurement Using Heterodyne Laser Interferometry", *Metrologia* **27** 133–138 (1990).
CITED ON PAGE 89

139. Portolés, J. F., Cumpson, P. J., Hedley, J. et al., "Accurate velocity measurements of AFM-cantilever vibrations by Doppler interferometry", *Journal of Experimental Nanoscience* **1**, 1 51–62 (2006).
CITED ON PAGE 89

140. Sanii, B. and Ashby, P. D., "High Sensitivity Deflection Detection of Nanowires", *Physical Review Letters* **104**, 147203 (2010).
CITED ON PAGE 89

141. Favero, I., Stapfner, S., Paulitschke, P. et al., "Fluctuating nanomechanical systems in a high finesse optical microcavity", *Optics Express* **17**, 15 12813–12820 (2009).
CITED ON PAGE 92

142. Jayich, A. M., Sankey, J. C., Zwickl, B. M. et al., "Dispersive optomechanics: a membrane inside a cavity", *New Journal of Physics* **10**, 095008 (2008).
CITED ON PAGE 92

143. Wilson, D. J., Regal, C. A., Papp, S. B. et al., "Cavity Optomechanics with Stoichiometric SiN Films", *Physical Review Letters* **103**, 207204 (2009).
CITED ON PAGE 92

144. Perisanu, S., Ayari, A., Purcell, S. T. et al., "Electro-mechanics of Resonating Nanotubes and Nanowires in the Field Emission Environment", *International Journal of Nanotechnology* **7** 702 (2010).
CITED ON PAGE 94

145. Mancini, S., Vitali, D., and Tombesi, P., "Optomechanical Cooling of a Macroscopic Oscillator by Homodyne Feedback", *Physical Review Letters* **80**, 4 688–691 (1998).
CITED ON PAGES 95, 96, AND 100

146. Cohadon, P.-F., Heidmann, A., and Pinard, M., "Cooling of a Mirror by Radiation Pressure", *Physical Review Letters* **83**, 16 3174–3177 (1999).
CITED ON PAGE 95

147. Hopkins, A., Jacobs, K., Habib, S. et al., "Feedback cooling of a nanomechanical resonator", *Physical Review B* **68**, 235328 (2003).
CITED ON PAGE 95

148. Kleckner, D. and Bouwmeester, D., "Sub-kelvin optical cooling of a micromechanical resonator", *Nature* **444** 75–78 (2006).
CITED ON PAGES 95 AND 102

149. Poggio, M., Degen, C. L., Mamin, H. J. et al., “Feedback Cooling of a Cantilever’s Fundamental Mode below 5 mK”, *Physical Review Letters* **99**, 017201 (2007).
CITED ON PAGES 95, 98, AND 100

150. Corbitt, T. R., Wipf, C., Bodiya, T. P. et al., “Optical Dilution and Feedback Cooling of a Gram-Scale Oscillator to 6.9 mK”, *Physical Review Letters* **99**, 160801 (2007).
CITED ON PAGE 95

151. Arcizet, O., Cohadon, P.-F., Briant, T. et al., “High-sensitivity optical monitoring of a micromechanical resonator with a quantum-limited optomechanical sensor”, *Physical Review Letters* **97**, 13 133601 (2006).
CITED ON PAGE 95

152. Li, T., Kheifets, S., and Raizen, M. G., “Millikelvin cooling of an optically trapped microsphere in vacuum”, *Nature Physics* **7** 527–530 (2011).
CITED ON PAGES 95, 124, AND 125

153. Gieseler, J., Deutsch, B., Quidant, R. et al., “Subkelvin Parametric Feedback Cooling of a Laser-Trapped Nanoparticle”, *Physical Review Letters* **109**, 103603 (2012).
CITED ON PAGES 95 AND 125

154. Vitali, D., Mancini, S., and Tombesi, P., “Optomechanical scheme for the detection of weak impulsive forces”, *Physical Review A* **64**, 051401 (2001).
CITED ON PAGES 95, 110, AND 112

155. Harris, G. I., McAuslan, D. L., Stace, T. M. et al., “Minimum Requirements for Feedback Enhanced Force Sensing”, *Physical Review Letters* **111**, 103603 (2013).
CITED ON PAGES 95, 109, 112, AND 114

156. Mertz, J., Marti, O., and Mlynek, J., “Regulation of a microcantilever response by force feedback”, *Applied Physics Letters* **62**, 19 2344–2346 (1993).
CITED ON PAGES 95, 96, AND 112

157. Gavartin, E., Verlot, P., and Kippenberg, T. J., “A hybrid on-chip optomechanical transducer for ultrasensitive force measurements”, *Nature Nanotechnology* **7** 509–514 (2012).
CITED ON PAGES 95 AND 109

158. Pinard, M., Cohadon, P.-F., Briant, T. et al., “Full mechanical characterization of a cold damped mirror”, *Physical Review A* **63**, 01 013808 (2000).
CITED ON PAGES 96, 98, 100, AND 110

159. Buchler, B. C., Gray, M. B., Shaddock, D. A. et al., “Suppression of classic and quantum radiation pressure noise by electro-optic feedback”, *Optics Letters* **24**, 4 259–261 (1999).
CITED ON PAGE 98

160. Wiseman, H. M., “Squashed states of light: theory and applications to quantum spectroscopy”, *Journal of Optics B* **1** 459–463 (1999).
CITED ON PAGE 98

161. Fu, H., Liu, C., Liu, Y. et al., “Selective photothermal self-excitation of mechanical modes of a micro-cantilever for force microscopy”, *Applied Physics Letters* **99**, 173501 (2011).
CITED ON PAGES 101 AND 104

162. Oloomi, S. A. A., Saboonchi, A., and Sedaghat, A., “Effects of thin film thickness on emittance, reflectance and transmittance of nano scale multilayers”, *International Journal of the Physical Sciences* **5**, 5 465–469 (2010).
CITED ON PAGE 101

163. Ikuno, T., Honda, S., Yasuda, T. et al., “Thermally driven nanomechanical deflection of hybrid nanowires”, *Applied Physics Letters* **87**, 21 213104 (2005).
CITED ON PAGE 102

164. Hossein-Zadeh, M. and Vahala, K. J., “An Optomechanical Oscillator on a Silicon Chip”, *Journal of Selected Topics in Quantum Electronics* **16**, 1 276–287 (2010).
CITED ON PAGE 102

165. Anderson, R. R. and Parrish, J. A., “Selective Photothermolysis: Precise Microsurgery by Selective Absorption of Pulsed Radiation”, *Science* **220**, 4596 524–527 (1983).
CITED ON PAGE 103

166. Pradhan, N. R., “Thermal conductivity of nanowires, nanotubes and polymer-nanotube composites”, Ph.D. thesis, Worcester Polytechnic Institute (2010).
CITED ON PAGE 103

167. Dhara, S., Solanki, H. S., Ravikumar, A. P. et al., “Tunable thermal conductivity in defect engineered nanowires at low temperatures”, *Physical Review B* **84**, 121307(R) (2011).
CITED ON PAGE 103

168. Courty, J.-M., Heidmann, A., and Pinard, M., “Quantum limits of cold damping with optomechanical coupling”, *European Physical Journal D* **17**, 3 399–408 (2001).
CITED ON PAGE 104

169. Pinard, M. and Dantan, A., “Quantum limits of photothermal and radiation pressure cooling of a movable mirror”, *New Journal of Physics* **10**, 095012 (2008).
CITED ON PAGE 104

170. Restrepo, J., Gabelli, J., Ciuti, C. et al., “Classical and quantum theory of photothermal cavity cooling of a mechanical oscillator”, *Comptes Rendus Physique* **12** 860–870 (2011).
CITED ON PAGE 104

171. Abdi, M., Bahrampour, A. R., and Vitali, D., “Quantum optomechanics of a multimode system coupled via a photothermal and a radiation pressure force”, *Physical Review A* **86**, 043803 (2012).
CITED ON PAGE 104

172. Usami, K., Naesby, A., Bagci, T. et al., “Optical cavity cooling of mechanical modes of a semiconductor nanomembrane”, *Nature Physics* **8** 168–172 (2012).
CITED ON PAGE 104

173. Barton, R. A., Storch, I. R., Adiga, V. P. et al., “Photothermal Self-Oscillation and Laser Cooling of Graphene Optomechanical Systems”, *Nano Letters* **12** 4681–4686 (2012).
CITED ON PAGE 104

174. Vinante, A., Bonaldi, M., Marin, F. et al., “Dissipative feedback does not improve the optimal resolution of incoherent force detection”, *Nature Nanotechnology* **8** 470 (2013).
CITED ON PAGE 110

175. Gavartin, E., Verlot, P., and Kippenberg, T. J., “Reply to ’Dissipative feedback does not improve the optimal resolution of incoherent force detection”’, *Nature Nanotechnology* **8** 692 (2013).
CITED ON PAGE 110

176. Gavartin, E., Verlot, P., and Kippenberg, T. J., “Stabilization of a linear nanomechanical oscillator to its thermodynamic limit”, *Nature Communications* **4**, 2860 (2013).
CITED ON PAGE 110

177. Vitali, D., Mancini, S., Ribichini, L. et al., “Mirror quiescence and high-sensitivity position measurements with feedback”, *Physical Review A* **65**, 063803 (2002).
CITED ON PAGE 110

178. Wieczorek, W., Hofer, S. G., Hoelscher-Obermaier, J. et al., “Optimal State Estimation for Cavity Optomechanical Systems”, *Physical Review Letters* **114**, 223601 (2015).
CITED ON PAGE 112

179. Oide, K., Hirakawa, H., and Fujimoto, M.-K., “Search for gravitational radiation from the Crab pulsar”, *Physical Review D* **20**, 10 2480 (1979).
CITED ON PAGE 112

180. Astone, P., Bonifazi, P., and Pallottino, G. V., “Fast estimation of the variance of a narrowband process”, *Review of Scientific Instruments* **61**, 12 3899–3903 (1990).
CITED ON PAGE 112

181. Finn, L. S. and Mukherjee, S., “Data conditioning for gravitational wave detectors: A Kalman filter for regressing suspension violin modes”, *Physical Review D* **63**, 062004 (2001).
CITED ON PAGE 112

182. Kalman, R. E., “A New Approach to Linear Filtering and Prediction Problems”, *Journal of Basic Engineering* **82**, 1 35–45 (1960).
CITED ON PAGE 114

183. Sorenson, H. W., “Least-squares estimation: from Gauss to Kalman”, *Spectrum* **7**, 7 63–68 (1970).
CITED ON PAGE 114

184. Maybeck, P. S., Stochastic models, estimation, and control, Academic Press (1982).
CITED ON PAGE 114

185. Iplikci, S., "Runge–Kutta model-based adaptive predictive control mechanism for non-linear processes", *Transactions of the Institute of Measurement and Control* **35**, 2 166–180 (2012).
CITED ON PAGE 115

186. Jayawant, B. V., "Electromagnetic suspension and levitation", *Reports on Progress in Physics* **44**, 4 411–477 (1981).
CITED ON PAGE 123

187. Ochiai, Y., Hoshi, T., and Rekimoto, J., "Three-Dimensional Mid-Air Acoustic Manipulation by Ultrasonic Phased Arrays", *PLOS ONE* **9**, 5 (2014).
CITED ON PAGE 123

188. Andrade, M. A. B., Pérez, N., and Adamowski, J. C., "Particle manipulation by a non-resonant acoustic levitator", *Applied Physics Letters* **106**, 014101 (2015).
CITED ON PAGE 123

189. Larciprete, R., Ulstrup, S., Lacovig, P. et al., "Oxygen Switching of the Epitaxial Graphene-Metal Interaction", *ACS Nano* **6**, 11 9551–9558 (2012).
CITED ON PAGE 123

190. Ashkin, A., "Acceleration and Trapping of Particles by Radiation Pressure", *Physical Review Letters* **24**, 4 156–159 (1970).
CITED ON PAGE 123

191. Ashkin, A. and Dziedzic, J. M., "Optical Levitation by Radiation Pressure", *Applied Physics Letters* **19**, 283 (1971).
CITED ON PAGE 123

192. Ashkin, A., "History of Optical Trapping and Manipulation of Small-Neutral Particle, Atoms, and Molecules", *Journal of Selected Topics in Quantum Electronics* **6**, 6 841–856 (2000).
CITED ON PAGE 123

193. Neuman, K. C. and Block, S. M., "Optical trapping", *Review of Scientific Instruments* **75**, 9 2787–2809 (2004).
CITED ON PAGE 123

194. Moffitt, J. R., Chemla, Y. R., Smith, S. B. et al., "Recent advances in optical tweezers", *Annual Review of Biochemistry* **77** 205–228 (2008).
CITED ON PAGE 123

195. Ashkin, A., Dziedzic, J. M., Bjorkholm, J. E. et al., "Observation of a single-beam gradient force optical trap for dielectric particles", *Optics Letters* **11**, 5 288–290 (1986).
CITED ON PAGE 123

196. Mestres, P., Berthelot, J., Spasenović, M. et al., "Cooling and manipulation of a levitated nanoparticle with an optical fiber trap", *Applied Physics Letters* **107**, 151102 (2015).
CITED ON PAGE 124

197. Shvedov, V. G., Rode, A. V., Izdebskaya, Y. V. et al., "Giant Optical Manipulation", *Physical Review Letters* **105**, 118103 (2010).
CITED ON PAGE 124

198. Shvedov, V. G., Davoyan, A. R., Hnatovsky, C. et al., “A long-range polarization-controlled optical tractor beam”, *Nature Photonics* **8** 846–850 (2014).
CITED ON PAGE 124

199. Gieseler, J., Novotny, L., and Quidant, R., “Thermal nonlinearities in a nanomechanical oscillator”, *Nature Physics* **9** 806–810 (2013).
CITED ON PAGES 124 AND 125

200. Chang, D. E., Regal, C. A., Papp, S. B. et al., “Cavity opto-mechanics using an optically levitated nanosphere”, *Proceedings of the National Academy of Sciences* **107**, 3 1005–1010 (2010).
CITED ON PAGES 124, 125, 141, AND 165

201. Dholakia, K. and Čižmár, T., “Shaping the future of manipulation”, *Nature Photonics* **5** 335–342 (2011).
CITED ON PAGES 124 AND 165

202. Maragò, O. M., Jones, P. H., Gucciardi, P. G. et al., “Optical trapping and manipulation of nanostructures”, *Nature Nanotechnology* **8**, 11 807–819 (2013).
CITED ON PAGE 124

203. Smith, S. B., Cui, Y., and Bustamante, C., “Overstretching B-DNA: The elastic response of individual double-stranded and single-stranded DNA molecules”, *Science* **271**, 5250 795–799 (1996).
CITED ON PAGE 124

204. Larsen, A. E. and Grier, D. G., “Like-Charge Attraction in Metastable Colloidal Crystallites”, *Nature* **385** 230–233 (1997).
CITED ON PAGE 124

205. Crocker, J. C., Matteo, J. A., Dinsmore, A. D. et al., “Entropic Attraction and Repulsion in Binary Colloids Probed with a Line Optical Tweezer”, *Physical Review Letters* **82**, 21 (1999).
CITED ON PAGE 124

206. Friese, M. E. J., Rubinsztein-Dunlop, H., Gold, J. et al., “Optically driven micromachine elements”, *Applied Physics Letters* **78**, 4 547–549 (2001).
CITED ON PAGE 124

207. Arita, Y., Mazilu, M., and Dholakia, K., “Laser-induced rotation and cooling of a trapped microgyroscope in vacuum”, *Nature Communications* **4**, 2374 (2013).
CITED ON PAGE 124

208. Quinto-Su, P. A., “A microscopic steam engine implemented in an optical tweezer”, *Nature Communications* **5**, 5889 (2014).
CITED ON PAGE 124

209. Neukirch, L. P. and Vamivakas, A. N., “Nano-optomechanics with optically levitated nanoparticles”, *Contemporary Physics* **56**, 1 48–62 (2015).
CITED ON PAGE 125

210. Barker, P. F., “Doppler Cooling a Microsphere”, *Physical Review Letters* **105**, 073002 (2010).
CITED ON PAGE 125

211. Pender, G. A. T., Barker, P. F., Marquardt, F. et al., “Optomechanical cooling of levitated spheres with doubly resonant fields”, *Physical Review A* **85**, 021802 (2012).
CITED ON PAGE 125

212. Ranjit, G., Montoya, C., and Geraci, A. A., “Cold atoms as a coolant for levitated optomechanical systems”, *Physical Review A* **91**, 013416 (2015).
CITED ON PAGE 125

213. Millen, J., Deesuwan, T., Barker, P. F. et al., “Nanoscale temperature measurements using non-equilibrium Brownian dynamics of a levitated nanosphere”, *Nature Nanotechnology* **9** 425–429 (2014).
CITED ON PAGE 125

214. Moore, D. C., Rider, A. D., and Gratta, G., “Search for Millicharged Particles Using Optically Levitated Microspheres”, *Physical Review Letters* **113**, 251801 (2014).
CITED ON PAGE 125

215. Arvanitaki, A. and Geraci, A. A., “Detecting High-Frequency Gravitational Waves with Optically Levitated Sensors”, *Physical Review Letters* **110**, 071105 (2013).
CITED ON PAGE 125

216. Crossley, D., Hinderer, J., and Riccardi, U., “The measurement of surface gravity”, *Reports on Progress in Physics* **76**, 046101 (2013).
CITED ON PAGE 125

217. Cirio, M., Brennen, G. K., and Twamley, J., “Quantum Magnetomechanics: Ultrahigh-Q-Levitated Mechanical Oscillators”, *Physical Review Letters* **109**, 147206 (2012).
CITED ON PAGE 125

218. Geraci, A. A., Papp, S. B., and Kitching, J., “Short-Range Force Detection Using Optically Cooled Levitated Microspheres”, *Physical Review Letters* **105**, 101101 (2010).
CITED ON PAGE 126

219. Ranjit, G., Atherton, D. P., Stutz, J. H. et al., “Attonewton force detection using microspheres in a dual-beam optical trap in high vacuum”, *Physical Review A* **91**, 051805(R) (2015).
CITED ON PAGE 126

220. Gieseler, J., Quidant, R., Dellago, C. et al., “Dynamic relaxation of a levitated nanoparticle from a non-equilibrium steady state”, *Nature Nanotechnology* **9** 358–364 (2014).
CITED ON PAGE 126

221. Monteiro, T. S., Millen, J., Pender, G. A. T. et al., “Dynamics of levitated nanospheres: towards the strong coupling regime”, *New Journal of Physics* **15**, 015001 (2013).
CITED ON PAGE 126

222. Bateman, J., Nimmrichter, S., Hornberger, K. et al., “Near-field interferometry of a free-falling nanoparticle from a point-like source”, *Nature Communications*

5, 4788 (2014).
CITED ON PAGE 126

223. Romero-Isart, O., Juan, M. L., Quidant, R. et al., “Toward quantum superposition of living organisms”, *New Journal of Physics* **12**, 033015 (2010).
CITED ON PAGE 126

224. Leonhardt, U. and Philbin, T. G., “Quantum levitation by left-handed metamaterials”, *New Journal of Physics* **9**, 254 (2007).
CITED ON PAGE 126

225. Matsumoto, N., Michimura, Y., Aso, Y. et al., “Optically trapped mirror for reaching the standard quantum limit”, *Optics Express* **22**, 11 12915–12923 (2014).
CITED ON PAGE 129

226. Perreca, A., Lough, J., Kelley, D. B. et al., “Multidimensional optical trapping of a mirror”, *Physical Review D* **89**, 122002 (2014).
CITED ON PAGE 129

227. Enomoto, Y., Nagano, K., Nakano, M. et al., “Observation of reduction of radiation-pressure-induced rotational anti-spring effect on a 23 mg mirror in a Fabry–Perot cavity”, *Classical and Quantum Gravity* **33**, 145002 (2016).
CITED ON PAGE 129

228. Sidles, J. A. and Sigg, D., “Optical torques in suspended Fabry-Perot interferometers”, *Physics Letters A* **354** 167–172 (2006).
CITED ON PAGES 132 AND 134

229. Parsegian, V. A., Van der Waals Forces, Cambridge University Press (2006).
CITED ON PAGE 138

230. Bergström, L., “Hamaker constants of inorganic materials”, *Advances in Colloid and Interface Science* **70** 125–169 (1997).
CITED ON PAGE 138

231. Owens, N. F. and Richmond, P., “Hamaker Constants and Combining Rules”, *Journal of the Chemical Society, Faraday Transactions 2* **74** 691–695 (1978).
CITED ON PAGE 139

232. Lawrence, C. J. and Winbaum, S., “The unsteady force on a body at low Reynolds number; the axisymmetric motion of a spheroid”, *Journal of Fluid Mechanics* **189** 463–489 (1988).
CITED ON PAGE 139

233. Bhiladvala, R. B. and Wang, Z. J., “Effect of fluids on the Q factor and resonance frequency of oscillating micrometer and nanometer scale beams”, *Physical Review E* **69**, 036307 (2004).
CITED ON PAGE 139

234. Savard, T. A., O’Hara, K. M., and Thomas, J. E., “Laser-noise-induced heating in far-off resonance optical traps”, *Physical Review A* **56**, 2 R1095–R1098 (1997).
CITED ON PAGES 140 AND 141

235. Gehm, M. E., O'Hara, K. M., Savard, T. A. et al., "Dynamics of noise-induced heating in atom traps", *Physical Review A* **58**, 5 3914–3921 (1998).
CITED ON PAGE 140

236. Romero-Isart, O., "Quantum superposition of massive objects and collapse models", *Physical Review A* **84**, 052121 (2011).
CITED ON PAGE 141

237. Rybicki, G. B. and Lightman, A. P., Radiative Processes in Astrophysics, Wiley-VCH (1979).
CITED ON PAGE 141

238. Ishida, T. and Yoshida, K., "Laser-Induced Damage and Environmental Stability of Thin Films Deposited by Ion-Assisted Electron-Beam Deposition", *Japanese Journal of Applied Physics* **46**, L16 (2006).
CITED ON PAGE 145

239. Bowen, W. P., "Experiments towards a Quantum Information Network with Squeezed Light and Entanglement", Ph.D. thesis, The Australian National University (2003).
CITED ON PAGE 149

240. Rao, S. R., "Mirror Thermal Noise in Interferometric Gravitational Wave Detectors", Ph.D. thesis, California Institute of Technology (2003).
CITED ON PAGE 152

241. Evans, M., Ballmer, S. W., Fejer, M. M. et al., "Thermo-optic noise in coated mirrors for high-precision optical measurements", *Physical Review D* **78**, 102003 (2008).
CITED ON PAGE 152

242. Carmon, T., Yang, L., and Vahala, K. J., "Dynamical thermal behavior and thermal selfstability of microcavities", *Optics Express* **12**, 20 4742–4750 (2004).
CITED ON PAGE 153

243. Chow, J. H., Sheard, B. S., McClelland, D. E. et al., "Photothermal effects in passive fiber Bragg grating resonators", *Optics Letters* **30**, 7 708–710 (2005).
CITED ON PAGES 153 AND 154

244. An, K., Sones, B. A., Fang-Yen, C. et al., "Optical bistability induced by mirror absorption: measurement of absorption coefficients at the sub-ppm level", *Optics Letters* **22**, 18 1433–1435 (1997).
CITED ON PAGE 153

245. Ilchenko, V. S. and Gorodetsky, M. L., "Thermal Nonlinear Effects in Optical Whispering Gallery Microresonators", *Laser Physics* **2**, 6 1004–1009 (1992).
CITED ON PAGE 161

246. Marino, F. and Marin, F., "Chaotically spiking attractors in suspended-mirror optical cavities", *Physical Review E* **83**, 015202 (2011).
CITED ON PAGE 161

247. Marino, F. and Marin, F., "Thermo-optical nonlinearities and stability conditions for high-finesse interferometers", *Physics Letters A* **364** 441–447 (2007).
CITED ON PAGE 161

248. Monifi, F., Zhang, J., Özdemir, . K. et al., “Optomechanically induced stochastic resonance and chaos transfer between optical fields”, *Nature Photonics* **10** 399–405 (2016).
CITED ON PAGE 161

249. Weng, W., Anstie, J. D., Abbott, P. et al., “Stabilization of a dynamically unstable opto-thermo-mechanical oscillator”, *Physical Review A* **91**, 063801 (2015).
CITED ON PAGE 162

250. Metcalfe, M., “Applications of cavity optomechanics”, *Applied Physics Reviews* **1**, 031105 (2014).
CITED ON PAGE 165

251. Rakich, P. T., Popović, M. A., and Wang, Z., “General Treatment of Optical Forces and Potentials in Mechanically Variable Photonic Systems”, *Optics Express* **17**, 20 18116–18135 (2009).
CITED ON PAGE 166

252. Braginsky, V. B., “Classical and Quantum Restrictions on the Detection of Weak Disturbances of a Macroscopic Oscillator”, *Journal of Experimental and Theoretical Physics* **26**, 4 831–834 (1968).
CITED ON PAGE 180

253. Caves, C. M., Thorne, K. S., Drever, R. W. P. et al., “On the measurement of a weak classical force coupled to a quantum-mechanical oscillator”, *Reviews of Modern Physics* **52**, 2 341–392 (1980).
CITED ON PAGE 180

254. Vahlbruch, H., Chelkowski, S., Hage, B. et al., “Coherent Control of Vacuum Squeezing in the Gravitational-Wave Detection Band”, *Physical Review Letters* **97**, 011101 (2006).
CITED ON PAGE 180

255. Kimble, H. J., Levin, Y., Matsko, A. B. et al., “Conversion of conventional gravitational-wave interferometers into quantum nondemolition interferometers by modifying their input and/or output optics”, *Physical Review D* **65**, 022002 (2001).
CITED ON PAGES 181, 188, 191, 192, AND 193

256. Unruh, W. G., “Quantum Noise in the Interferometer Detector”, in “Quantum Optics, Experimental Gravity, and Measurement Theory”, (Meystre, P. and Scully, M. O., editors), 647–660, Springer (1982).
CITED ON PAGES 181 AND 193

257. Harms, J., Chen, Y., Chelkowski, S. et al., “Squeezed-input, optical-spring, signal-recycled gravitational-wave detectors”, *Physical Review D* **68**, 042001 (2003).
CITED ON PAGE 181

258. Khalili, F. Y., “Optimal configurations of filter cavity in future gravitational-wave detectors”, *Physical Review D* **81**, 122002 (2010).
CITED ON PAGE 181

259. Evans, M., Barsotti, L., Kwee, P. et al., “Realistic filter cavities for advanced gravitational wave detectors”, *Physical Review D* **88**, 022002 (2013).
CITED ON PAGE 181

260. Kwee, P., Miller, J., Isogai, T. et al., "Decoherence and degradation of squeezed states in quantum filter cavities", *Physical Review D* **90**, 062006 (2014).
CITED ON PAGE 181

261. Corbitt, T. R., "Quantum Noise and Radiation Pressure Effects in High Power Optical Interferometers", Ph.D. thesis, Massachusetts Institute of Technology (2008).
CITED ON PAGE 181

262. Ma, Y., Danilishin, S. L., Zhao, C. et al., "Narrowing the Filter-Cavity Bandwidth in Gravitational-Wave Detectors via Optomechanical Interaction", *Physical Review Letters* **113**, 151102 (2014).
CITED ON PAGE 181

263. Qin, J., Zhao, C., Ma, Y. et al., "Classical demonstration of frequency-dependent noise ellipse rotation using optomechanically induced transparency", *Physical Review A* **89**, 041802 (2014).
CITED ON PAGE 181

264. Miao, H., Ma, Y., Zhao, C. et al., "Enhancing the Bandwidth of Gravitational-Wave Detectors with Unstable Optomechanical Filters", *Physical Review Letters* **115**, 211104 (2015).
CITED ON PAGE 181

265. Heidmann, A. and Reynaud, S., "Photon noise reduction by reflection from a movable mirror", *Physical Review A* **50**, 5 4237–4243 (1994).
CITED ON PAGE 181

266. Nunnenkamp, A., Børkje, K., Harris, J. G. E. et al., "Cooling and squeezing via quadratic optomechanical coupling", *Physical Review A* **82**, 021806 (2010).
CITED ON PAGE 181

267. Purdy, T. P., Yu, P.-L., Peterson, R. W. et al., "Strong Optomechanical Squeezing of Light", *Physical Review X* **3**, 031012 (2013).
CITED ON PAGE 182

268. Qu, K. and Agarwal, G. S., "Generating quadrature squeezed light with dissipative optomechanical coupling", *Physical Review A* **91**, 063815 (2015).
CITED ON PAGE 184

269. Kilda, D. and Nunnenkamp, A., "Squeezed light and correlated photons from dissipatively coupled optomechanical systems", *Journal of Optics* **18**, 014007 (2016).
CITED ON PAGE 184

270. Giovannetti, V. and Vitali, D., "Phase-noise measurement in a cavity with a movable mirror undergoing quantum Brownian motion", *Physical Review A* **63**, 023812 (2001).
CITED ON PAGE 184

271. Collett, M. J. and Walls, D. F., "Squeezing spectra for nonlinear optical systems", *Physical Review A* **32**, 5 2887–2892 (1985).
CITED ON PAGE 187

272. Weaver, M. J., Pepper, B., Luna, F. et al., “Nested Trampoline Resonators for Optomechanics”, *Applied Physics Letters* **108**, 033501 (2016).
CITED ON PAGE 188

273. Della Valle, F., Milotti, E., Ejlli, A. et al., “Extremely long decay time optical cavity”, *Optics Express* **22**, 10 11570–11577 (2014).
CITED ON PAGE 194

274. Zhang, G. and James, M. R., “Direct and Indirect Couplings in Coherent Feedback Control of Linear Quantum Systems”, *IEEE Transactions on Automatic Control* **56**, 7 1535–1549 (2011).
CITED ON PAGE 201

275. Hamerly, R. and Mabuchi, H., “Advantages of Coherent Feedback for Cooling Quantum Oscillators”, *Physical Review Letters* **109**, 173602 (2012).
CITED ON PAGE 201

276. Miao, Z., Hosseini, M., Guccione, G. et al., “Synchronisation of micro-mechanical oscillators inside one cavity using feedback control”, *Australian Control Conference* **4** 77–82 (2014).
CITED ON PAGE 201